

Dissertation zur Erlangung des Doktorgrades
der Fakultät für Chemie und Pharmazie
der Ludwig-Maximilians-Universität München

Investigations on the Administration of Dry Vaccines for Epidermal Powder Injection

Yibin Deng

aus

Yushan, China

2013

ERKLÄRUNG

Diese Dissertation wurde im Sinne von § 7 der Promotionsordnung vom 28. November 2011 von Herrn Prof. Dr. Gerhard Winter betreut.

EIDESSTATTLICHE VERSICHERUNG

Diese Dissertation wurde eigenständig und ohne unerlaubte Hilfe erarbeitet.

München, den 05. Juli 2013

(Yibin Deng)

Dissertation eingereicht am	05. Juli 2013
1. Gutachter:	Prof. Dr. Gerhard Winter
2. Gutachter:	Prof. Dr. Wolfgang Friess
Mündliche Prüfung am	30. Juli 2013

Acknowledgements

The present work was performed under the supervision of Prof. Dr. Gerhard Winter and Dr. Julia Engert at the Department of Pharmacy, Pharmaceutics and Biopharmaceutics, Ludwig-Maximilians-University (LMU), Munich.

First and foremost, I would like to express my deepest gratitude to my supervisor, Prof. Dr. Gerhard Winter, for the opportunity to join his research group and to work on the project of needle-free epidermal powder injection for vaccination. I am deeply indebted to his professional guidance, inspiring advices and kind encouragement. Furthermore, I am very grateful for giving me chances to take part in some scientific seminars and to present my work in international conferences.

I would also like to express sincere thanks to Dr. Julia Engert for her outstanding supervision, scientific support and a great deal of encouragement during the whole work. Thanks for her support and advices on the practical work of experiments and scientific writing, which did help me a lot to finish this thesis.

I want to thank Prof. Dr. Gerhard Winter and Prof. Dr. Wolfgang Friess for the efforts to provide excellent technical equipments and a harmonious atmosphere as one big working group, which made it an enjoyable time of my PhD work. I have learned a lot from the regular scientific seminars during semesters and enjoyed the activities such as ski camps and excursions.

In particular, I would like to thank the Chinese Scholarship Council (CSC) for the financial support and to thank the international office at LMU for the orientation course, language and culture programs helping me to get started to study and live in Munich.

Many thanks are expressed to all the colleagues I have worked with from the research groups of Prof. Winter and Prof. Friess for communications, discussions and numerous activities together. I want to thank Weiwei Tian for introducing me the lab and some equipments at the beginning and for sharing the experience she had. I want to thank Elsa Etzl and Cihad Anamur for working together on the Bio-Injection project and for many valuable discussions. Special thanks go to my lab-mate Raimund Geidobler for the happy time we had, for

scientific discussions, for the help on computer skills, for the introduction on German language and culture, for the rock music, for many soccer games we played. Many thanks are extended to Markus Hofer, Matthaeus Noga, Elisabeth Haertl, Sebastian Hertel, Roman Mathaes, Madeleine Witting, Matthias Lucke, Elisa Agostini, Eva-Maria Ruberg for all the help and discussions. I would also like to thank Gabi Hartl, Alice Hirschmann and Ayla Tekbudak for all the support.

I would like to acknowledge Dr. Barbara Kessler, LMU Munich, for supplying pig skin, to acknowledge Prof. Dr. Stefan Zahler, LMU Munich, for his assistance in using confocal laser scanning microscope, and to acknowledge Christian Minke for SEM measurements and Tina Reuther for pore size measurements.

Especially, I would like to thank Prof. G. Winter, Dr. J. Engert, Elsa Etzl, Markus Hofer, Matthaeus Noga, Raimund Geidobler, Christian Hildebrandt, Cihad Anamur and Thomas Bosch for providing transportation services when my ankle was injured.

Finally, I would love to thank my grandparents, parents, my sister and my brother for their dedicated encouragement and their full support throughout my life. They have been giving me constant enthusiasm and courage to go forward bravely.

Table of Contents

Chapter I. General Introduction.....	1
1. Structure and function of human skin	4
1.1 Epidermis	4
1.2 Dermis	5
1.3 Hypodermis	5
2. Mechanical properties of human skin	6
2.1 <i>In vivo</i> mechanical properties of human skin.....	10
2.2 <i>In vitro</i> measurement of skin mechanical properties	11
3. Powder and particle-mediated epidermal immunisation.....	13
3.1 Theoretical modelling of particle penetration into skin	15
4. Building of skin models for studying ballistic delivery of drugs and vaccines	16
5. Applications of confocal laser scanning microscopy for the investigations of intra- and transdermal drug/vaccine delivery	19
6. Nanoparticles and microparticles as vaccine delivery systems.....	22
6.1 Silica nanoparticles as a drug/vaccine delivery system	22
6.2 Particles targeting Langerhans cells	24
6.3 Microparticles for epidermal powder immunisation.....	25
7. Objectives of the project	25
Chapter II. Preparation and validation of a skin model for the evaluation of intradermal powder injection devices.....	28
1. Objectives.....	28
2. Materials and Methods	29
2.1 Materials.....	29
2.2 Methods	30
2.2.1 Preparation of human skin and pig skin	30
2.2.2 Preparation of gelatin based films	30
2.2.3 Preparation of silicone films	31
2.2.4 Preparation of agar gels.....	31
2.2.5 Preparation of polyacrylamide gels.....	31
2.2.6 Measurements of the mechanical properties of gelatin based films, silicone films, agar gel, polyacrylamide gels, human skin and pig skin.....	32
2.2.7 Storage conditions	32

2.2.8 Determination of the Young's modulus	33
2.2.9 Establishment of structural models and CLSM measurement	34
3. Results and Discussion.....	35
3.1 Indentation behaviour of biological skin and films as candidates of skin models....	35
3.2 Puncture of pig skin and candidates for skin models	39
3.3 Effect of the environmental relative humidity (RH) on the mechanical properties of the gelatin films.....	41
3.4 Effect of environmental temperature on the mechanical properties of the films	42
3.5 Stability of gelatin films under long-term storage	42
3.6 Direct determination of particle deposition depths by CLSM in layered structural models	43
4. Conclusions	45
Chapter III. Nano-in-micro particulate systems for epidermal powder injection	47
1. Objectives.....	47
2. Materials and Methods	49
2.1 Materials.....	49
2.2 Methods	50
2.2.1 Preparation of fluorescent PLGA nanoparticles.....	50
2.2.2 Preparation of fluorescent gelatin nanoparticles	51
2.2.3 Preparation of fluorescent spider silk nanoparticles	52
2.2.4 Preparation of fluorescent silica nanoparticles.....	52
2.2.5 Preparation of microparticles encapsulating different nanoparticles	53
2.2.6 Microscopic examination of microparticles	54
2.2.7 Measurements of hydrodynamic diameter and zeta-potential.....	55
2.2.8 Cellular uptake of nanoparticles by macrophage cells.....	55
2.2.9 Tap density of the microparticles	55
2.2.10 Measurements of the mechanical properties of freeze-dried matrix cakes by a texture analyser	56
3. Results	56
3.1 Encapsulation of nanoparticles in microparticles.....	56
3.1.1 Nanoparticles for the encapsulation in the sugar-based microparticles	56
3.1.2 Distribution of different nanoparticles in the sugar-based microparticles.	57
3.2 Stability of nanoparticles in TMD microparticles.....	64
3.3 Cellular uptake of nanoparticles.....	65

3.4 Enhancement of the density of microparticles by dense materials.	66
3.5 Indentation measurements of TMD/CaCO ₃ composite by a texture analyser	68
4. Discussion	69
4.1 Nano-in-micro system for drug delivery	69
4.2 Colloidal stability of nanoparticles processed by freeze-drying or spray-freeze-drying	69
4.3 Properties of nanoparticles for intracellular delivery	70
4.4 Effect of dense excipients on the density of the microparticles	71
5. Conclusion.....	71
Chapter IV. Encapsulation of antigen-loaded silica nanoparticles into microparticles for intradermal powder injection	72
1. Objectives.....	72
2. Materials and Methods	72
2.1 Materials.....	72
2.2 Methods	73
2.2.1 Preparation of mesoporous silica nanoparticles	73
2.2.2 Preparation of MSNP–ovalbumin conjugates	73
2.2.3 Ovalbumin loading and release from MSNP-NH ₂ nanoparticles	74
2.2.4 Preparation of microparticles with nanoparticles encapsulated by spray-freeze-drying	75
2.2.5 Preparation of microparticles containing fluorescently-labeled ovalbumin by spray-freeze-drying	75
2.2.6 Characterisation of the nanoparticles and microparticles	76
2.2.7 Ovalbumin concentration determination	77
2.2.8 Characterisation of ovalbumin	78
2.2.9 Cellular uptake of nanoparticles by macrophages.....	78
3. Results	78
3.1 Characterisation of mesoporous silica nanoparticles	78
3.2 Conjugation of mesoporous silica nanoparticles with ovalbumin	80
3.3 Ovalbumin (OVA) loading on the silica nanoparticles and release tests	81
3.4 Sugar-based microparticles encapsulating model antigens and nanoparticles.....	83
3.5 Epidermal powder injection of the microparticles on model skin and pig skin.....	88
3.6 Cellular uptake of ovalbumin-loaded silica nanoparticles	90
4. Discussion	93

4.1 Nanoparticles in microparticles (nano-in-micro) for epidermal powder immunisation	93
4.2 Silica nanoparticles for vaccine delivery	93
4.3 Microparticles with encapsulated silica nanoparticles and ovalbumin meeting the requirements for epidermal powder immunisation	94
4.4 Antigen-loaded nano-in-micro particles for epidermal powder immunisation	95
5. Conclusion.....	96
Chapter V. Formulation of H1N1 hemagglutinin and silica nanoparticles in sugar-based microparticles	98
1. Objectives.....	98
2. Materials and Methods	99
2.1 Materials.....	99
2.2 Methods	100
2.2.1 Concentrating of H1N1 hemagglutinin by ultrafiltration.....	100
2.2.2 Determination of H1N1 HA concentration	100
2.2.3 Size and zeta-potential measurements.....	102
2.2.4 Loading of H1N1 HA on silica nanoparticles (MSNP-NH2)	102
2.2.5 Encapsulation of H1N1 HA and silica nanoparticles in TMD microparticles by spray-freeze-drying	102
2.2.6 SDS-PAGE and western blot of H1N1 HA	103
2.2.7 Hemagglutinin inhibition (HAI) assay	104
3. Results and Discussion.....	105
3.1 Influenza hemagglutinin obtained from the vaccines	105
3.2 Interaction of H1N1 hemagglutinin and cationic mesoporous silica nanoparticles ..	106
3.3 Characterisation of H1N1 HA in TMD microparticles	108
3.4 Biological activity by hemagglutinin inhibition assay.....	112
3.5 Stability of influenza vaccines in a solid form	114
4. Conclusion.....	114
Chapter VI. Preparation of PLGA nanoparticles for vaccine delivery and their encapsulations in sugar-based microparticles	116
1. Objectives.....	116
2. Materials and Methods	118
2.1 Materials.....	118
2.2 Methods	119

2.2.1 Preparation of PLGA nanoparticles loaded with ovalbumin	119
2.2.2 Preparation of PLGA nanoparticles loaded with SIINFEKL.....	120
2.2.3 Determination of ovalbumin loading in PLGA nanoparticles	121
2.2.4 Determination of SIINFEKL loading in PLGA nanoparticles.....	121
2.2.5 Characterisation of OVA/SIINFEKL-loaded PLGA nanoparticles and the microparticles encapsulating the nanoparticles.....	122
2.2.6 Release of ovalbumin from PLGA nanoparticles	123
2.2.7 Encapsulation of OVA/SIINFEKL-loaded PLGA nanoparticles into microparticles	123
3. Results	124
3.1 Optimisation of conditions for the preparation of PLGA nanoparticles	124
3.1.1 Influence of the polyvinyl alcohol (PVA) concentration on the particle size ...	124
3.1.2 Cationisation of PLGA-OVA nanoparticles	124
3.2 Properties of OVA/SIINFEKL-loaded PLGA nanoparticles	125
3.2.1 OVA-loaded PLGA nanoparticles	125
3.2.2 SIINFEKL-loaded PLGA nanoparticles	127
3.3 Loading and encapsulation efficiency of OVA/SIINFEKL in PLGA nanoparticles	128
3.3.1 PLGA nanoparticles encapsulating ovalbumin	128
3.3.2 PLGA nanoparticles encapsulating SIINFEKL	128
3.4 Stability of PLGA nanoparticles during freeze-drying	129
3.5 Sugar-based microparticles encapsulating OVA/SIINFEKL-loaded PLGA nanoparticles.....	131
3.5.1 Microparticles encapsulating PLGA-OVA nanoparticles	131
3.5.2 Microparticles encapsulating PLGA-SIINFEKL nanoparticles	132
4. Discussion	134
4.1 Particle size control and cationisation of PLGA-based nanoparticles	134
4.2 OVA/SIINFEKL-loaded PLGA-based nanoparticles in the nano-in-micro particle systems	135
5. Conclusion.....	136
Chapter VII. Final Summary	138
Chapter VIII. References	141

Chapter I. General Introduction

The administration of vaccines is a huge success story in modern medicine. Since the first vaccination attempts of Jenner in 1796, the administration of vaccine formulations to prevent spreading of infectious diseases has become routine, at least in the developed world. The occurrence of some infectious diseases has been reduced due to widespread vaccination programmes in many countries [1-3].

However, one of the major drawbacks of most vaccine formulations is the need for administration by injection. Needle-stick injuries and transmission of blood-borne diseases due to re-use of disposable needles are a major issue in particular in developing countries. In addition, many commercially available vaccines require cold-chain transport and carefully controlled storage conditions due to the instability of vaccine antigens [4]. The conditions mentioned above may not be feasible in developing countries where supplies and costs are limiting factors.

Combating these limitations in vaccine formulation requires expertise in pharmaceutical technology to develop novel dry vaccine formulations that can be applied using alternative routes of administration.

Human skin is a target site for drug and vaccine delivery that is attracting more and more attention from researchers around the world. The epidermis of the skin, composed of live keratinocytes and immune cells, is a sensitive immune organ and a practical site for vaccine delivery. In addition, the epidermis lacks nerve endings and blood vessels which make this site of needle-free administration even more attractive [5]. Therefore, global health organisations are pushing for vaccination via the skin. As shown in **Figure I-1**, there are several needle-free methods for transcutaneous vaccine delivery, including liquid-jet injection, epidermal powder immunisation and topical applications [6]. These techniques are under development now and not yet applicable for replacing needle injection vaccination. Researchers are putting a lot of efforts into this field to investigate the feasibility of vaccination without needles, but more work still needs to be done.

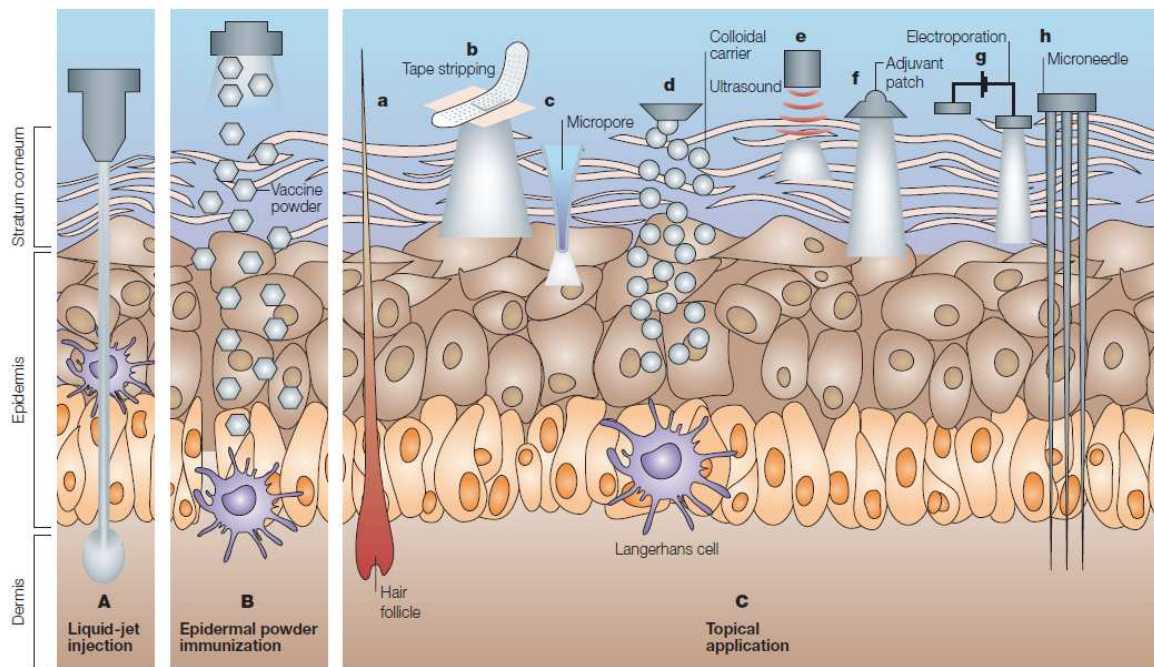


Figure I-1. Vaccine delivery to skin by transcutaneous routes. (A) Liquid-jet injection; (B) Epidermal powder immunization; (C) Topical applications of vaccines, including immunization through hair follicles, thermal or radio-wave-mediated vaccine penetration by creating micropore, colloidal carriers facilitation, low-frequency ultrasound mediated vaccine delivery, shallow microneedles assistance, etc. For all the routes, vaccines are delivered to the epidermis, and Langerhans cells will process and present the vaccines. Figure adopted from Ref. [6].

There are some important advantages for the epidermis as the target for immunisation. First, the epidermis contains a larger number of bone marrow-derived dendritic cells called Langerhans cells (LCs). Although LCs account for only about 1% - 3% of the epidermal cells, they cover about 25% of the entire surface of the skin [7]. About 500 - 1000 Langerhans cells exist in a square millimeter in most areas of the human skin, except the areas of sole and palm [8]. Langerhans cells are efficient antigen presenting cells (APCs) which can present antigen directly to the immune system when transfected by DNA or protein vaccines. The mechanism of presenting antigens introduced by the skin route is depicted in **Figure I-2**. Antigens penetrating into the epidermal layer are recognised and processed by LCs. The LCs carrying antigenic signals migrate to the draining lymph nodes under the stimulation of TNF α and IL-1 β . And then the LCs present the processed antigens to naïve T cell, resulting in either Th1 or Th2 types immune responses [8]; second, epidermal vaccine delivery is expected to decrease pain and suffering, as there are no nerves in the epidermal layer of skin. Compared to needle vaccination, needle-free vaccination is more comfortable for the patient; third, it is safer to

use a needle-free method for epidermal powder immunisation compared to needle vaccination because needle break and potential infection of blood-borne diseases may be harmful to the patient. Especially in developing countries, the reuse of disposable needles for vaccination may result in the transmission of blood-borne diseases; fourth, use of powders make the storage easy and improve the stability of vaccine. The “cold chain” for the transportation of vaccines may be not necessary which could reduce the cost and increase the convenience for extensive use. However, there are some disadvantages of the present devices for powder injection, such as the high cost of devices, occasional bleeding and limited clinical history [4]. The controllability of powder injection devices needs to be improved and the efficiency of vaccination should be evaluated systematically.

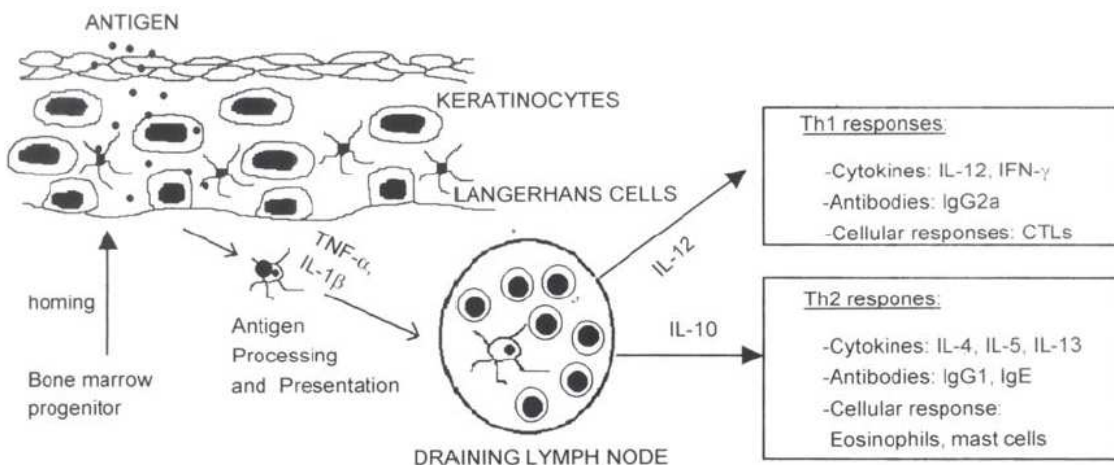


Figure I-2. A schematic diagram of antigen processing and presenting by Langerhans cells. The antigens penetrate through skin and are recognized by LCs in the epidermis. LCs with antigens migrate to the draining lymph nodes under the influence of TNF α and IL-1 β . And then LCs induce either Th1 or Th2 types immune responses by presenting processed antigen to naïve T cells. Figure adopted from Ref. [8].

Due to the skin barrier function, especially the protection of the stratum corneum of the most superficial layer of epidermis, it is not easy to deliver drugs or vaccines into epidermis or dermis. Efforts to improve the efficiency of drug or vaccine delivery into skin by needle-free methods have been made. So far, common needle-free techniques to achieve penetration of antigens into the skin are tape-stripping and electroporation. Researchers try to design the formulations which can penetrate through the skin barrier by encapsulating vaccines into colloidal carriers such as microemulsions and transfersomes. However, these techniques are time-consuming, elaborate, and may not result in an increase in patient compliance. Micro-

needle mediated penetration is another option which proves to be a possible minimal invasive method [9].

Another option is to deliver vaccine antigen either in liquid or solid form into the skin by exhibiting large acceleration forces on either liquid or the solid vaccine formulation. These techniques are called liquid jet injection and epidermal powder immunisation, respectively [6]. The liquid injection device uses the kinetic energy of a high-velocity jet, whereas powdered vaccine devices usually contain helium gas cartridges that accelerate the powder particles to the required high speed [10]. The helium-related device is been used to administer DNA HIV vaccine (Phase I) and Herpes simplex type 2 (HSV2, Phase I) and DNA cancer vaccine (Phase I) by ballistic microparticle injection [11]. The use of helium results in an increase in costs per immunisation and thus limits the applicability of this approach in developing countries. Epidermal powder immunisation (EPI) is a promising method for delivery of vaccines by transcutaneous route [12, 13], but a more economic, elegant and effective device without helium is required.

A novel device for EPI is being developed by our collaborator. A skin model for the evaluation of the device and vaccine powders/microparticles for EPI is needed. In this circumstance, the project was proposed to address these problems. Several areas such as the skin properties, skin models, vaccine particles for epidermal immunisation and detection of delivered vaccines are involved in this project and will be introduced further.

1. Structure and function of human skin

The skin is the largest organ in the human body. For the average adult human, the skin has a surface area of about 1.8 m^2 , most of it is between 1 - 2 mm thick and the average thickness is 1.2 mm. The average square inch (6.5 cm^2) of skin holds 650 sweat glands, 20 blood vessels, 60,000 melanocytes, and more than a thousand nerve endings [14]. The general skin structure is constituted of the stratum corneum (about 0.02 mm thickness), the viable epidermis (about 0.1 mm thickness), the dermis (about 1.1 mm thickness) and hypodermis (0.1 to several centimetres) [14].

1.1 Epidermis

The epidermis is the outer layer of the skin, composed of stratum corneum and viable epidermis with a total average thickness of about 0.12 mm [14]. It is the body's major

biological barrier against an inhospitable environment or viruses. The epidermis is avascular and composed of four types of cells, i.e. keratinocytes, melanocytes, Langerhans cells, and the Merkel cells. Keratinocytes are the major constituent, constituting 95% of the epidermis. The epidermis is composed of 4 - 5 layers depending on the region of skin considered.

The stratum corneum with a thickness between 10 and 40 μm is the outermost layer of the epidermis, composed of large, flat, polyhedral, plate-like envelopes (15 - 20 layers of dead cells) filled with keratin. Keratin keeps the skin to stay hydrated by preventing water evaporation. These dead cells can also absorb water, further aiding in hydration. This is why humans and other animals experience wrinkling of the skin on the fingers and toes when immersed in water for prolonged periods. The mechanical properties of skin are decreased when hydrated.

The viable epidermis with an average thickness of 60 μm is the target for drug or vaccine delivery by transcutaneous routes. The professional antigen presenting cells, Langerhans cells, are uniquely present in the viable epidermis of skin. The density of LCs in most areas of human skin with the exception of sole and palm is approximately 500 - 1000 cells/ mm^2 [15]. LCs take up epicutaneous antigens, emigrate into the regional skin-draining lymph nodes and present the processed antigens to the T cells. In all, LCs initiate, maintain, and regulate adaptive immunities in the skin.

1.2 Dermis

The dermis is the layer of skin beneath the epidermis that consists of connective tissue and cushions the body from stress and strain. The dermis is tightly connected to the epidermis by a basement membrane. It also harbours many mechanoreceptor and nerve endings that provide the sense of touch and heat. It contains the hair follicles, sweat glands, sebaceous glands, apocrine glands, lymphatic vessels and blood vessels. The blood vessels in the dermis provide nourishment and waste removal from its own cells as well as from the stratum basale of the epidermis.

1.3 Hypodermis

The hypodermis is not part of the skin, and lies below the dermis. Its purpose is to attach the skin to underlying bone and muscle as well as supplying it with blood vessels and nerves. It consists of loose connective tissue and elastin. The main cell types are fibroblasts,

macrophages and adipocytes (the hypodermis contains 50% of body fat). Fat serves as padding and insulation for the body.

2. Mechanical properties of human skin

Mechanical properties of human skin are important for its function such as protecting tissues under the skin and forming the structure of organs. To measure the biomechanical properties of human skin is necessary to develop drug delivery methods through skin. It is difficult to describe the mechanical properties of skin due to the anisotropic properties and layered structures. In fact, different results of mechanical properties will be obtained when the same skin is measured by different methods. Furthermore, the skin *in vivo* and that *in vitro* display different mechanical properties. Therefore, one should be careful to use the skin *in vitro* to evaluate the cutaneous drug delivery and administration.

There are some kinds of methods for measuring the mechanical properties of soft materials including tissues. For transdermal delivery of drugs by a physical method, it is necessary to know the mechanical properties, i.e. storage modulus, Young's modulus, shear modulus, tensile strength. The measurement methods include mainly suction, indentation, torque and extension.

(1) Suction

The suction method is one of the most extensively used ways to measure skin mechanical properties. The principle of the suction method is the measurement of skin elevation caused by application of a partial vacuum (usually in the range of 5 - 50 kPa or 50 - 500 mbar) via a circular aperture in a measuring probe. The deformation is measured with an ultrasound system (dermis) or optical coherence tomography (OCT) (epidermis and dermis) [16, 17]. Two different instruments are commercially available: Dermaflex (Cortex, Denmark) and Cutometer (Courage & hazaka Electronic GmbH, Germany).

Hendriks *et al.* [18] studied the contributions of different skin layers to the mechanical behaviour of human skin *in vivo* using suction methods. They assumed that the measurement was based on the hypothesis that experiments with different length scales represent the mechanical behaviour of different skin layers (epidermis and papillary dermis, reticular dermis). For example, the upper layer is measured when the small sized (0.3 mm in diameter) aperture is used. Attention should be paid to that they just considered the skin with two layers: one is the upper layer including epidermis and papillary dermis, the other is the reticular dermis. The

mechanical properties of single epidermis have not been achieved by the present settings due to the limited resolution of the imaging systems, but may be obtained by measuring the skin using even smaller aperture sizes [18].

(2) Indentation

A rigid indenter is used to apply a known force or deformation to the skin in indentation experiments, and then the relation between the penetration depths and normal load is obtained, which could give the information of elastic mechanical properties. Zahouani *et al.* [19] used a device for indentation experiments named bio-tribometer (**Figure I-3**) to characterize the mechanical properties of a dermal equivalent and human skin. The conical probe can be changed into spherical probe if necessary [19].

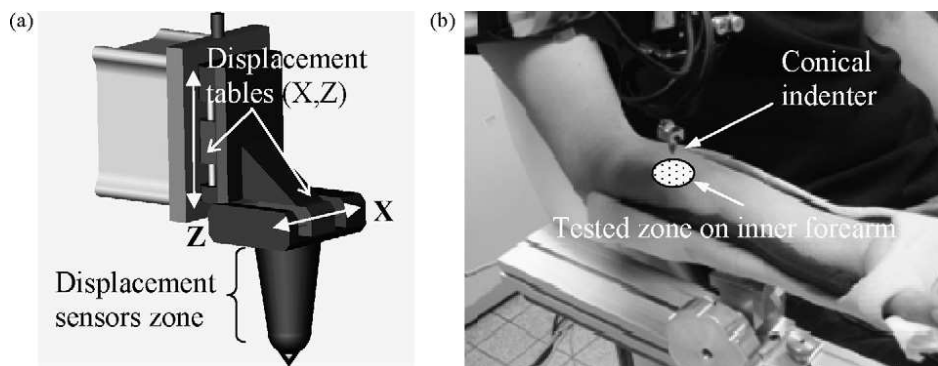


Figure I-3. Skin tribometer device: (a) schematic diagram of the indentation device; (b) indentation system and positioning of the subject's arm. The tests were performed on the inner forearm. Figure adopted from Ref. [19].

The nano-indenter® XP (MTS Nano Instruments, 1001 Larson Drive, Oak Ridge, TN, USA) can also be used for indentation experiments of skin, applying the continuous stiffness measurement (CSM) technique. By decreasing the diameter of the probe, the mechanical properties of the skin epidermis can be obtained [20]. Kendall *et al.* [20] used custom tungsten probes fabricated with nominally 5 and 2 μm diameters with nano-scale tips to measure the mechanical properties by penetrating through the intact stratum corneum and viable epidermis (**Figure I-4**). In the theory of viscoelastic properties, the elasticity of elastic solids and the viscosity of viscous fluid are combined to describe the characteristics of mechanical properties of viscoelastic materials [21]. The elastic portion is described by the storage modulus and the viscous portion is described by the loss modulus. Loss tangent describes the phase angle between the storage modulus and the loss modulus. Young's modulus can be calculated from the storage modulus and the probe properties [20]. They

obtained the storage modulus, Young's modulus, loss modulus and loss tangent for the viable epidermis of murine ear skin for the first time (**Table I-1**).

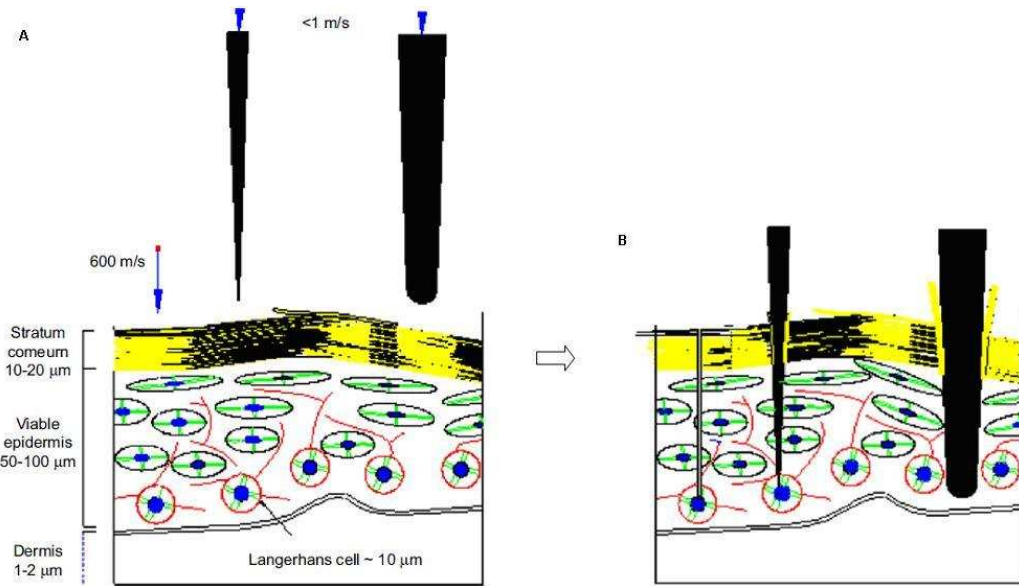


Figure I-4. The schematic diagram of the skin epidermis structure under micro-projections for gene and drug delivery [20]. **(A)** A single 2 μm micro-particle was accelerated to a speed of $\sim 600 \text{ m}\cdot\text{s}^{-1}$ before penetrating into the epidermis, while simplified profiles of 2 μm and 5 μm probes will be gradually inserted into the skin with a speed lower than $<1 \text{ m}\cdot\text{s}^{-1}$; **(B)** The respective positions of the ballistically delivered micro-particle and the two probes following insertion. Figure adopted from Ref. [20].

Table I-1 Murine ear skin viable epidermis mechanical properties [20]

Probe diameter (μm)	5		2	
Parameters	Average	S.D.	Average	S.D.
Young's modulus (MPa)	2.9	NA	11.1	NA
Storage modulus (MPa)	3.587	2.35	13.974	2.49
Loss modulus (MPa)	0.263	0.81	2.452	9.2
Loss tangent	1.206	0.49	0.834	0.11

The texture analyzer (TA) can be applied to measure the mechanical properties of skin and skin model materials. Jachowicz *et al.* [22] utilized the model TA-XT2 from Texture Technologies Corp. (Scarsdale, NY, USA) which was equipped with smooth stainless-steel spherical indenters characterized by diameters of 5/16, 5/8, 5/4 inch to obtain indentation curves (force vs penetration depth). They interpreted the experimental data with the Hertz theory of contact mechanics that describes the deformation of contacting solids and calculated

the fundamental parameters such as the modulus of elasticity [22]. The schematic represent is shown in **Figure I-5**, the equivalent Young's modulus (E^*) of elasticity between the bodies is defined as

$$\frac{1}{E^*} = \frac{1-v_1^2}{E_1} + \frac{1-v_2^2}{E_2} \quad (1)$$

where E_1 , E_2 and v_1 , v_2 are modulus and Poisson' Ratios of the spherical probe and the spherical object, respectively. The load of compression P can be expressed as a function of indentation depth σ

$$P = \frac{4}{3} E^* R^{0.5} \delta^{1.5} \quad (2)$$

By fitting the experimental data of indentation force with penetration depth, the mechanical parameters can be obtained.

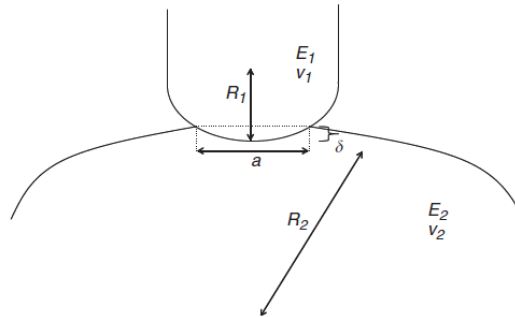


Figure I-5. A scheme of the indentation of a spherical probe with a diameter R_1 (Young's modulus E_1 and Poisson's Ratio v_1) into a spherical object with a diameter R_2 (Young' modulus E_2 and Poisson's Ratio v_2). An a denotes the indentation diameter and σ is the indentation depth. Figure adopted from Ref. [22].

(3) Torsion

In torsion tests a guard ring and an intermediary disc are attached to the skin. A constant torque or rotation is applied by the disc. According to Escoffier *et al.* [23], this method has two advantages: 1) hypodermis and underlying tissues do not affect the measurements and 2) the anisotropic character of the skin is minimized. However, it is difficult to differentiate the mechanical properties of epidermis and dermis, no such work has been reported yet.

Agache *et al.* [24] studied skin stiffness using a torsional apparatus [25]. Application of a torque of 28.6×10^{-3} N·m during 2 minutes to the dorsal forearm skin resulted in a rotation of 2 - 6°. The torsional moment was applied by a 25 mm diameter disc surrounded by a 35 mm diameter guard ring. Young's moduli (E) were calculated for the linear part of the stress-strain

curve and were found to be $E = 4.2 \times 10^5$ Pa for people aged less than 30 years old, and $E = 8.5 \times 10^5$ Pa for people over 30 years.

(4) Extension

In tensile testing the skin is mainly loaded parallel to its surface. Two tabs are attached to the skin and then pulled apart. The attachment of the tabs to the skin may significantly influence the results as many of the double-sided adhesive tapes exhibit creep deformation. Rapidly bonding cyanoacrylate adhesives can be used to avoid these effects. The simplest method by extension tests is the *in vitro* tensile testing, but the *in vivo* test is a challenge.

A typical example of a uniaxial tensile test is described by Manschot and Brakkee [26, 27]. They performed uniaxial tensile tests on human calf, both across and along the tibial axis. Two square tabs ($10 \times 10 \text{ mm}^2$) were attached to the skin with cyanoacrylate adhesive with a distance of 5 mm in between. A skin thickness of 1.2 mm was measured with ultrasound. Four sawtooth shaped loads (maximum 12 N) were applied with a loading and interval time of respectively 10 and 20 seconds. Preconditioning is left out of consideration by neglecting the response to the first load cycle. A clear non-linear stress-strain relationship was observed. Across the tibia axis a maximum strain of 0.32 and a maximum Young's modulus of 4 MPa were found. Along the tibia axis the maximum observed strain and Young's modulus were 0.3 and 20 MPa, respectively.

2.1 *In vivo* mechanical properties of human skin

The mechanical properties of human skin *in vivo* are summarized in **Table I-2**, and the results by different studies vary distinctly. Basically, the mechanical properties of human skin are related to age, individuals, body sites, and environmental factors such as relative humidity and temperature. Meanwhile, different methods always give distinct different results of Young's moduli. In the literature, the Young's modulus of the human skin *in vivo* varies between 0.05 and 0.15 MPa for the suction tests [16, 25], 1 and 10 kPa for the indentation tests [19, 20], 4.6 - 20 MPa for the extension tests [27], 0.42 and 0.85 MPa for the torsion tests [24]. Therefore, caution should be paid when comparing the data of mechanical properties of skin.

Table I-2 *In vivo* Young's modulus of human skin

Skin sample	Young's modulus	Method	Descriptions	Ref.
Forearm outside	2.5 MPa	Suction		[28]
Forearm	18 - 57 MPa	Suction	20 to 70 years old	[29]
Forearm (man)	0.14 MPa	Suction	Before 25 years old	[30]
Forearm (woman)	0.16 MPa	Suction	Before 25 years old	[30]
Forearm (man)	0.11 MPa	Suction	28.3 ± 6.2 years old	[31]
Forearm (woman)	0.12 MPa	Suction	27.8 ± 8 years old	[31]
Forearm inside	2.20 ± 4.48 MPa (average 3.52)	Suction (dermaLab)	9 - 29 years old	[31]
Forearm	1.09 - 1.51 kPa	Indentation		[32]
Forearm	14.0 ± 5.0 kPa	Indentation	Relaxation	[33]
Forearm (man)	2.7 - 3.3 kPa	Indentation	28 - 65 years old	[22]
Forearm (woman)	1.1 - 2.2 kPa	Indentation	28 - 65 years old	[22]
Inner forearm (man)	4.5 - 8 kPa	Indentation (tribometer)	About 30 years old	[19]
Inner forearm (woman)	8.3 ± 2.1 kPa	Indentation (tribometer)	55 - 77 years old	[19]
Forearm outside	0.42 - 0.85 MPa	Torque	0.42 MPa before 30, 0.85 MPa after 30	[23, 32, 33]
Forearm outside	23 - 107 kPa	Torque	6 - 61 years old	[34]
Forearm	1.1 - 1.32 MPa	Torque		[23]
Human skin	4.6 - 20 MPa	Extention		[27]
Human skin	28.42 MPa	Extension	7 months to 3 years	[35]
Human skin	65.66 MPa	Extension	15 – 30 years old	[35]
Human skin	79.38 MPa	Extension	30 – 50 years old	[35]
Human skin	107.80 MPa	Extension	50 – 80 years old	[35]
Human skin	0.5 MPa	Extension		[36]
Human skin	0.42 - 0.75 MPa	Extension		[37]
Forearm	457.8 kPa	Extension	strain 40%	[38]

2.2 *In vitro* measurement of skin mechanical properties

The removal of the skin samples from the body is involved in the *in vitro* measurement methods of mechanical properties. The skin *in vitro* could be considered to be a viscoelastic material. Due to the distinct effect of environments on the mechanical properties, the conditions for measurements of skin mechanical properties should be well controlled. Edwards and Marks summarized the measurements of biomechanical properties of human skin and discussed the *in vitro* methods with some considerations about the comparison *in vitro* with *in vivo* measurements [39]. Tensile testing is commonly used, including uniaxial

and biaxial tests. Typical stress versus stain relationships under uniaxial and biaxial tension are shown in **Figure I-6**, respectively [40]. Three obviously different regions can be observed for uniaxial tests as follows: (1) small strain stage (0 - 30%), the stress increases slowly with the strain increasing. It is caused by the gradual straightening of an increasing fraction of the wavy collagen fibers and the stretching of elastic fibers; (2) middle strain stage (30% - 60%), the stress changes linearly with the increase of strain. It is attributed to the stretching and slippage of collagen molecules within crosslinked collagen fibers and collagen fibril slippage; (3) large strain stage (>60%), the final yield region, which is attributed to the loss of fibrillar structure resulting from the defibrillation of collagen fibrils. Compared with uniaxial stretch, the stress-strain curve is shifted left in biaxial stretch due to the two-directional stretch of collagen fibers, as shown in **Figure I-6B**. **Table I-3** summarizes some of the *in vitro* Young's modulus of human skin. Apparently, the skin *in vitro* is different from the status of the skin *in vivo*.

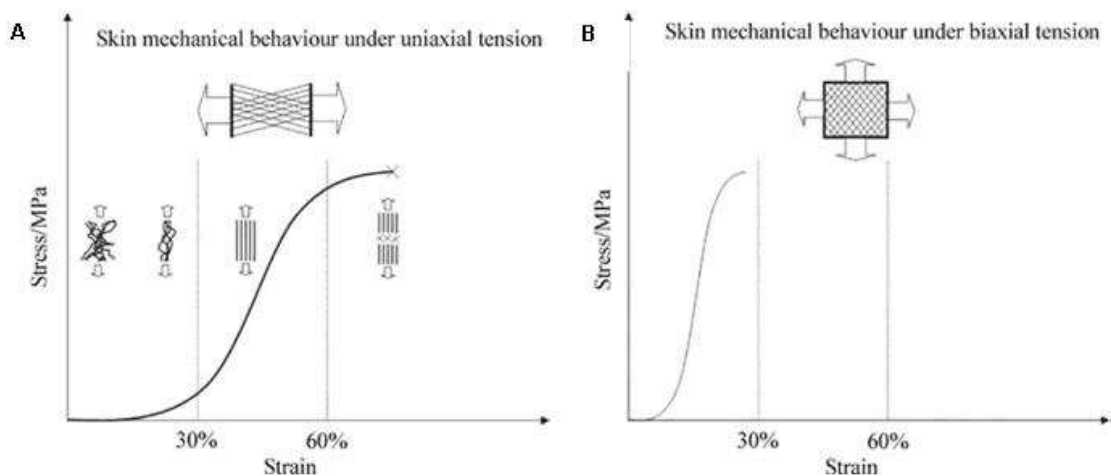


Figure I-6. Schematic diagrams of skin mechanical behavior under (a) uniaxial and (b) biaxial tension. Figure adopted from Ref. [40].

Table I-3 *In vitro* Young's modulus of human skin

Skin sample	Young's modulus	Method	Description	Ref.
Human skin	2.16 kPa	Uniaxial stretch	0% strain	[41]
Human skin	26.5 kPa	Uniaxial stretch	50% strain	[41]
Human skin	5.0 kPa	Uniaxial stretch	NA	[42]
Human skin	0.1 MPa	Extension	47 - 86 years old	[43]
Human skin	0.3 MPa	Extension	NA	[44]

3. Powder and particle-mediated epidermal immunisation

Epidermal powder immunisation (EPI), also known as a ballistic method, is carried out by delivering antigen-loaded particles or powders into the upper layer of the skin and depositing in the epidermis or the superficial layer of the dermis [6]. The delivered antigens can be processed by LCs and then presented to naïve T cells, leading to the immune responses [6]. Dean *et al.* [45] have reviewed powder and particle-mediated approaches for delivery of DNA and protein vaccines into the epidermis. They differentiate the intracellular and extracellular particle delivery (**Figure I-7**) as the mechanisms of epidermal powder immunisation.

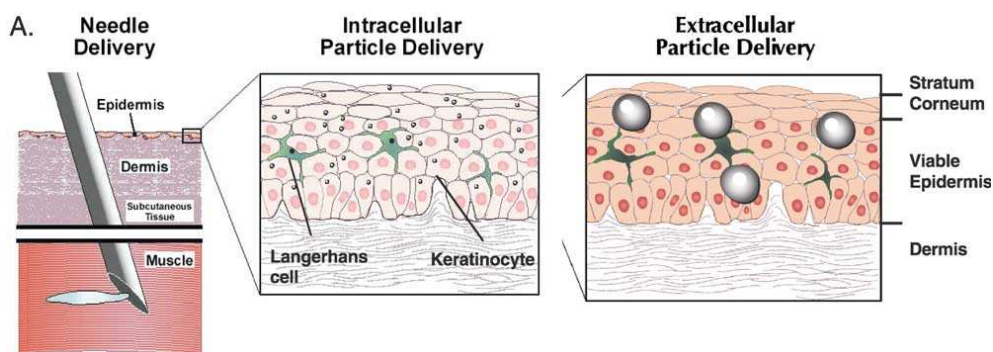


Figure I-7. A schematic represent of immunisation by transcutaneous routes. 1) Intracellular particle delivery depicts that 1 - 3 μm gold particles penetrate through the stratum corneum and directly transfect both Langerhans cells and keratinocytes of the viable epidermis; 2) Extracellular particle delivery depicts that dense particles of 20 - 70 μm in diameter containing protein antigens penetrate the stratum corneum and are deposited in the intracellular spaces of the viable epidermis. Figure adopted from Ref. [45].

The PowderJect® delivery system (**Figure I-8**) was developed especially for powder and particle injection into epidermis [45]. The device is a metal instrument that accelerates particles or powders at a high speed by regulating a burst of helium with an electrical solenoid. The particles or powders with DNA or proteins are contained in a cartridge [45]. The cartridge is inserted into a disposable nozzle linked to the device by a snap lock. When the compressed helium is released by activating the trigger, the gas bursts into the cartridge with vaccines and accelerates the particles or powders to a high velocity. Particles or powders are then ejected from the nozzle and injected into the epidermis of the skin.

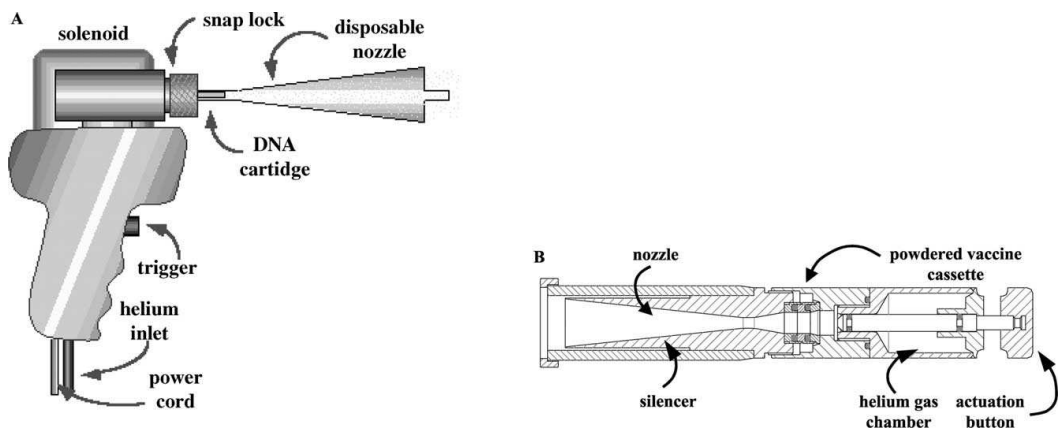


Figure I-8. Particle-mediated delivery system for epidermal immunisation: (A) the prototype delivery device used for particle-mediated DNA vaccination and epidermal powder immunization; (B) cross-sectional view of the rechargeable PowderJect ND device used for epidermal powder immunization of 20 - 70 μm protein powders. Figure adopted from Ref. [45].

The PowderJect Centre for Gene and Drug Delivery Research at University of Oxford has investigated PowderJect® device or similar devices [45]. Kendall *et al.* [13] found the effects of relative humidity and ambient temperature on the ballistic delivery of microparticles into excised porcine skin are distinct, and calculated the theoretical penetration depths based on the properties of stratum corneum and viable epidermis and particles. Kendall *et al.* [12] revealed that the particle penetration depth in the excised human skin strongly depends on the particle density and impact velocity. Chen *et al.* [46] have proven the efficiency of the PowderJect device for epidermal immunisation by studying the immunogenicity of influenza vaccine and protection in mice. Drape *et al.* [47] described a phase I clinical trial to evaluate a monovalent influenza DNA vaccine by particle-mediated epidermal delivery using the PowderJect device. In the mean time, different devices for powder injection have been developed. Roberts *et al.* evaluated the clinical safety and efficacy of a powdered Hepatitis B nucleic acid vaccine delivered to the epidermis by using the XR-1 clinical research and the commercial prototype ND5.5 devices [48]. When vaccine particles are delivered into the epidermis with the powder injection device, the damage to targeted cells by microparticles may influence transfection efficiencies, which was studied by Raju *et al.* [49]. In fact, the ballistic delivery of microparticles to the viable epidermis can result in localised cell death to some degree. It is a compromise of microparticle payload and cell death for optimizing the transfection by epidermal immunisation [49]. The work about the epidermal immunisation

with ballistic delivery and the device is still ongoing [50, 51], and much more work needs to be done on the development of the application of epidermal vaccination.

3.1 Theoretical modelling of particle penetration into skin

Based on the unified theory of penetration [52], the relationship between the theoretical penetration depth in skin and the properties of the particle, skin and the particle velocity has been proposed [12, 13, 53]. The mechanisms of particle impact were explored with a theoretical model attributing the particle resistive force (D) to plastic deformation and target inertia [12, 13, 53]

$$D = \frac{1}{2} \rho_t A v^2 + 3A \sigma_y \quad (3)$$

where ρ_t and σ_y are the density and yield stress of the target, A is the particle cross-sectional area, and v is the particle velocity. The yield strength or yield point of a material is defined in engineering and material science as the stress at which a material begins to deform plastically. Integration of expression (3) produces the theoretical penetration depth (d): [12]

$$d = \frac{4\rho_p r_p}{3\rho_t} \left\{ \ln \left(\frac{1}{2} \rho_t v_i^2 + 3\sigma_t \right) - \ln(3\sigma_t) \right\} \quad (4)$$

Kendall *et al.* [13] proposed a two-layer model using expression (3) shown in **Figure I-9**. There are two kinds of penetration denoted **A** and **B** in **Figure I-9**. Penetration case **A** denotes particle delivery into the stratum corneum (d_{sc}), whereas in case **B** the stratum corneum is fully breached (t_{sc}) and the final particle location is within the viable epidermis (d_{ve}). The impact velocity is v_i and the input velocity for the viable epidermis is $v_{i,ve}$.

Case A: particle delivery only to stratum corneum

$$d_{sc} = \frac{4\rho_p r_p}{3\rho_{sc}} \left\{ \ln \left(\frac{1}{2} \rho_{sc} v_i^2 + 3\sigma_{sc} \right) - \ln(3\sigma_{sc}) \right\} \quad (5)$$

Case B: particle delivery to viable epidermis

The velocity of the particle at the SC-viable epidermis boundary ($v_{i,ve}$) can be calculated from expression (5)

$$v_{i,ve} = \left\{ \left(v_i^2 + \frac{6\sigma_{sc}}{\rho_{sc}} \right) e^{\frac{-3\rho_{sc}t_{sc}}{4\rho_p r_p}} - \frac{6\sigma_{sc}}{\rho_{sc}} \right\}^{1/2} \quad (6)$$

And then d_{ve} can be obtained. The total particle penetration depth (d_t) is thus

$$d_t = t_{sc} + d_{ve} \quad (7)$$

However, the calculated depths in excised porcine skin are distinctly larger than the experimental results [13], which may be due to the deviations of the parameters and assigned values used in the theoretical calculations of the particle penetration depths.

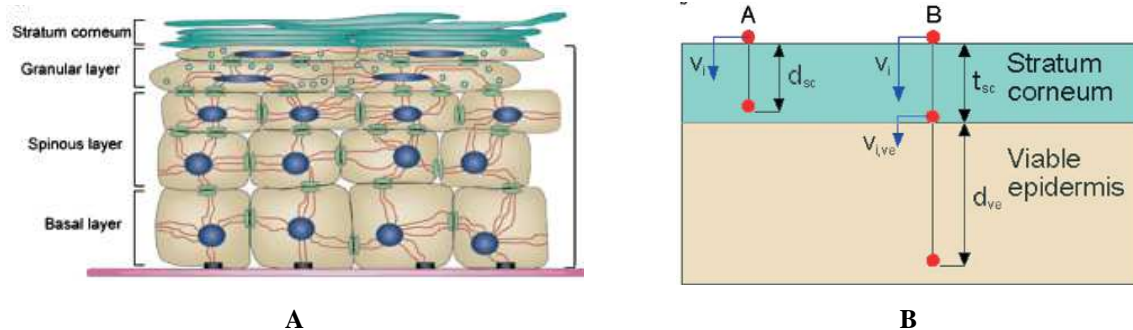


Figure I-9. Schematic diagrams of the epidermal structure of human skin (A) and the description of the corresponding bilayer approximation of the epidermis in the theoretical penetration model (B). Figure adopted from Ref. [13].

It is a challenge to deliver particles to specific skin layers due to the complicated mechanical properties of the skin. From the above theoretical modelling, we can predict the particle penetration depth with the mechanical properties of skin and parameters of device and particle properties. Therefore, it is necessary to know the structure and properties of the skin for the powder injection into skin. In fact, the studies of the penetration into skin model materials with stable mechanical properties will help the evaluation of vaccine formulations and powder injection devices.

4. Building of skin models for studying ballistic delivery of drugs and vaccines

Skin models or artificial skins are useful for adhesion-to-skin testing [54], studying modification by cosmetic treatment [55], wound healing [55] and evaluation of needle-free transcutaneous delivery of drugs and vaccines [56]. According to the composition and structure of natural skin, the best way to build a skin model is to establish a structure mimicking the function of real skin. Biomacromolecules such as gelatin, collagen, alginate, etc. have been used to make artificial skin [57]. Collagen fibrils are the main components in dermis responding to the mechanical properties. Lir *et al.* [54] synthesized a film modelling human skin considering skin composition, structure, functions, mechanical properties and surface properties. They used collagen-derived skin protein gelatin to provide skin mechanical integrity, glycerol as a plasticizer to increase the film flexibility, hydroxyethylcellulose as polysaccharide component to tailor film mechanical properties, formaldehyde as cross-linking

agent to regulate film hydrolytic stability and lipid to create film hydrophobic surface [54]. Due to the layered structure including epidermis, dermis and hypodermis of natural skin, multilayer membrane composed of different layers was developed by Yannas *et al.* [58]. Skin tissue engineering is another way to obtain skin equivalents [59]. Usually, single- and multi-layer skin models can be used with different intentions.

(1) Single-layer skin model

Skin has a layered and anisotropic structure. A single-layer skin model will not produce an exact model, but still can be used if the intention is to mimic the average properties. Skin is a typical soft tissue and soft tissue modelling is applied extensively. Dermis is the main contribution of mechanical properties of skin, thus single-layer skin models may just simulate the properties of dermis in skin. The development of all diagnostic imaging system and most physical therapeutic interventions has required the use of tissue-simulating objects to mimic the properties of tissues. Pogue and Patterson reviewed tissue simulating “phantoms” for optical spectroscopy, imaging and dosimetry [60]. Matrix materials typically used for phantom include gelatin, agar, polyester or epoxy and polyurethane resin, room-temperature vulcanizing (RTV) silicone, polyvinyl alcohol gels and so on.

Gelatin is one of the most commonly used materials for skin modelling. Lir *et al.* synthesized a gelatin-based film with thickness of $100 \pm 10 \mu\text{m}$ as a substrate for adhesion-to-skin testing [54]. They also imitated the topography of a real skin with the silicone replica technique employed. **Figure I-10** shows the surface topographies. Polyacrylamide gels can be used as a model system for the investigation of jet injection mechanics into skin [56, 61, 62]. The best advantage of polyacrylamide gels is the transparency, making it possible to imaging the evolution of jet penetration (**Figure I-11**). RTV silicone-based materials may be a good choice for preparing skin models. The material is prepared by mixing the RTV with its hardener that initiates a chemical process which solidifies the compound. Heat and gas generation during the process requires pumping the material under vacuum. Mansy *et al.* evaluated the elastic properties of silicone-based materials for soft tissue modelling [63]. Polyvinyl chloride (PVC) phantoms can be used for tissue model in the investigation of needle insertion [64]. PVC gels with Young’s modulus ranging from 10 kPa to well over 100 kPa could be prepared by varying the amount of plasticizer, a phthalate ester added to the PVC.

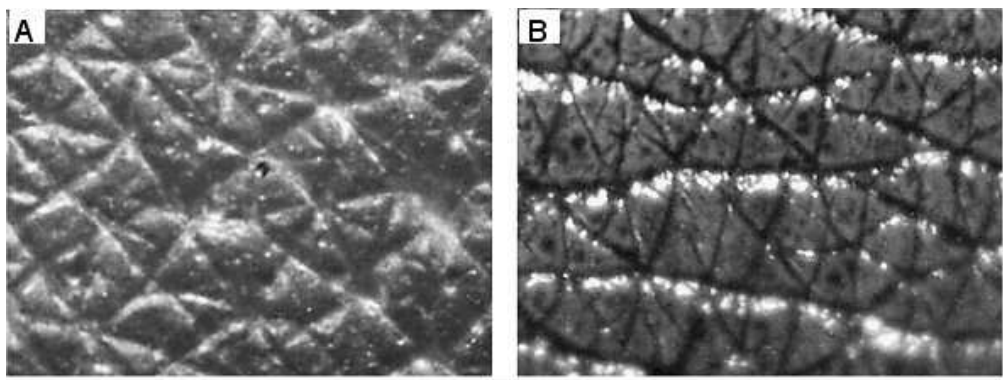


Figure I-10. Surface topographies of the model material (**A**) and real human skin (**B**) from the forearm zone (optical images, $\times 60$). Figure adopted from Ref. [54].

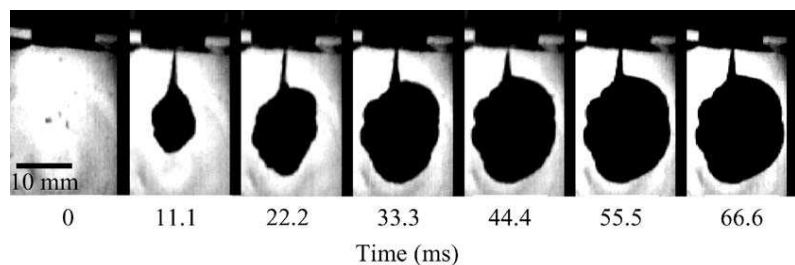


Figure I-11. Imaging of jet penetration with different injection time during the injection into 20% acrylamide gels. The jet enters the gel at the black/white interface. The black parts in the middle of the gels are the jets. Figure adopted from Ref. [56].

(2) Multi-layer skin model

Due to the layered structures of skin, multilayer membranes may be a good option for building a skin model. Yannas *et al.* [58] patented the method to prepare multilayer membranes, as shown in **Figure I-12**. The first layer, mimicking the dermis, is insoluble in the presence of body fluids, and nondegradable in the presence of body enzymes. According to the composition of dermis, preferred materials for the first layer are crosslinked collagen-mucopolysaccharide composites, which are synthesized by intimately contacting collagen with a mucopolysaccharide and subsequently crosslinking the resultant product [58]. For the simple double-layer skin model, the outmost layer mimicking the epidermis is a moisture transmission control layer which is adherently bonded to the first layer. Suitable materials for this layer include synthetic polymers such as silicone resins, polyacrylate or polymethacrylate esters or their copolymers, and polyurethanes [58]. One of the polymeric materials is silicone polymer, such as Silastic® Medical Adhesive (Dow Corning), a mixture of a hydroxyl terminated silicone polymer and methyl triethoxy silane which cures into a flexible, tough layer that adheres very well to the first layer materials such as crosslinked collagen-mucopolysaccharide composites. For example, a double layer skin model proposed in the

literature is composed of a 381 μm thick layer of collagen-mucopolysaccharides and a 127 μm thick silicone film [58]. Multilayer membrane can be prepared by using a moisturecured silicone elastomer as the agent bonding the collagen-mucopolysaccharide layer to another material layer. The materials for the added layer include synthetic polymers such as the segmented polyurethanes, hydroxyethyl methacrylate and other hydrogels, polyethylene terephthalate and polytetrafluoroethylene or modified natural polymers such as cellulose acetate or natural polymers such as elastin [58].

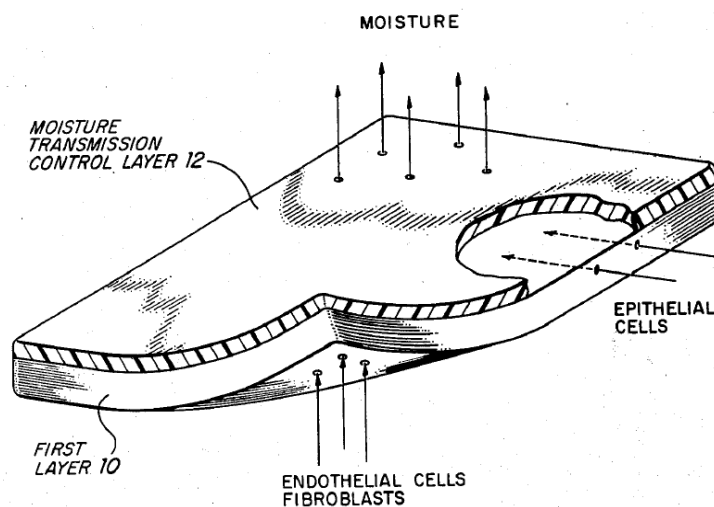


Figure I-12. Schematic represent of multilayer membrane as a skin model [58]. Layer **12** is the outmost layer controlling the moisture, while the layer **10** is the layer mimicking dermis in skin. Multilayer membrane can be made by using silicone adhesive as the agent bonding layer **10** to layer **12**. Figure adopted from Ref. [58].

5. Applications of confocal laser scanning microscopy for the investigations of intra- and transdermal drug/vaccine delivery

Confocal laser scanning microscopy (CLSM) is a technique for obtaining high-resolution optical images with depth selectivity [65]. The key feature of confocal microscope is its ability to acquire in-focus images from selected depths by a process known as optical sectioning. Images are acquired point-by-point and reconstructed with a computer, allowing three-dimensional reconstructions of topologically-complex objects. For opaque specimens, this is useful for surface profiling, while for transparent specimens, interior structures can be imaged. For interior imaging, the quality of the image is greatly enhanced over simple microscope because image information from multiple depths in the specimen is not superimposed. A conventional microscope sees as far into the specimen as the light can

penetrate, while a confocal microscope only images one depth level at a time. In effect, the CLSM achieves a controlled and highly limited depth of focus.

Human skin is a good target for drug and vaccine delivery and has been attracting considerable interest in recent years. CLSM is an appropriate method to visualize skin structure and determine the mechanisms of diverse skin penetration enhancement strategies [66]. CLSM is a no-invasive method both *in vitro* and *in vivo* conditions and can obtain the visualization of images parallel to the surface of the sample, at multiple depths, without mechanical sectioning. **Figure I-13** shows the confocal optical sectioning of porcine skin. The structures of different depth in skin are visualized clearly.

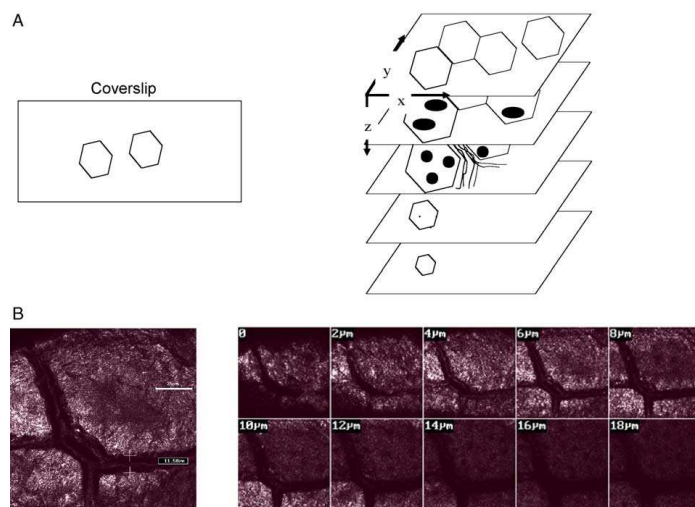


Figure I-13. Confocal optical sectioning. (A) A schematic of a z-series (sequential xy sections as a function of depth (z)), and (B) confocal images of sequential xy sections of a z-series through porcine skin, the depth is 0, 2, 4, 6, 8, 10, 12, 14, 16, 18 μm , respectively. Figure adopted from Ref. [66].

The distribution of a fluorophore in hair follicles has been determined by CLSM, and the relative accumulation in the SC, epidermis, dermis, outer root sheath, inner root sheath, cuticular area and hair shaft in non-fixed fresh human scalp skin was determined semi-quantitatively [67]. CLSM was used to visualize the distribution of calcein, a charged (-4), hydrophilic dye, and nile red, a lipophilic, neutral compound in hairless mouse skin, and the permeation of nile red was greatly enhanced by the application of iontophoresis [68]. Tuner *et al.* studied the extent and distribution of a series of model peptides (poly-L-lysine, PLL) coupled to the fluorescent probe FTIC under iontophoretic skin penetration [69]. CLSM images revealed that iontophoresis increased transport via follicular pathways only slightly

more than that through non-follicular regions for the 4 and 7 kDa FTIC-PLL [69]. Pharmaceutical applications of confocal laser scanning microscopy have been summarised by Pygall *et al.* [70].

Brus *et al.* [71] studied fluorescence-labelled polyethylenimine oligodeoxynucleotide (PEI/ODN) complexes in human skin after iontophoretic delivery using confocal scanning laser microscopy and visualized and quantified the penetration properties of double labelled PEI/ODN complexes across full thickness human skin. **Figure I-14** shows the CLSM results of human skin after treatment with different substances.

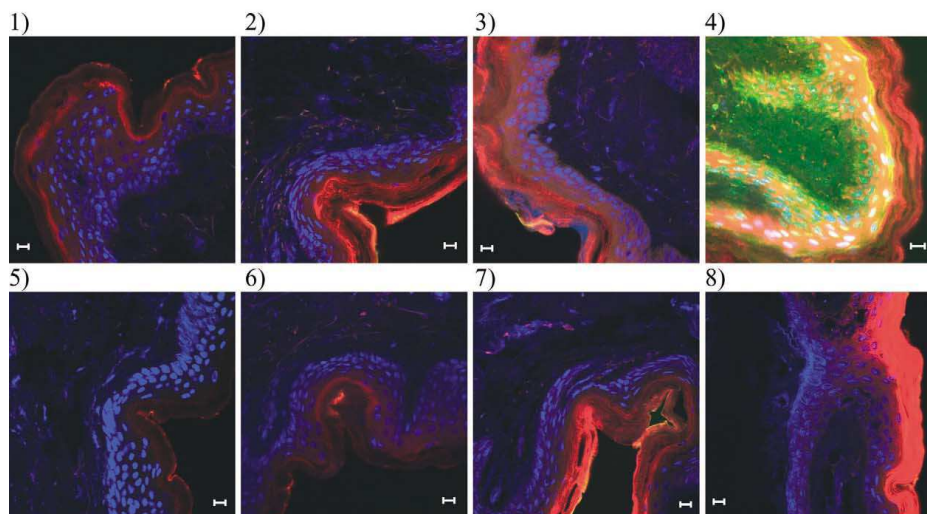


Figure I-14. The effect of anodal iontophoresis on the penetration of TAMRA-ODN and Oregon Green-PEI complexes. The human skins were treated with TAMRA-labelled ODN (red) and Oregon Green-labelled PEI (green) complexes. Upper panel shows the distribution of complexes in the skin layers after anodal iontophoresis for **1)** 1 h, **2)** 4 h, **3)** 10 h, and **4)** 24 h, and lower panel shows the results for passive diffusion for **5)** 1 h, **6)** 4 h, **7)** 10 h, and **8)** 24 h. The scale bar is 10 μ m. Figure adopted from Ref. [71].

CLSM has successfully been applied on the visualization of skin and the distribution of drugs or vaccines across skin. CLSM provides a possible way to track the drug delivery into skin. Compared to normal wide field microscopy, CLSM enhances the resolution distinctly. Meanwhile, selecting a suitable fluorescence probe is important for the investigation of the distribution and flow of particles and/or drugs.

6. Nanoparticles and microparticles as vaccine delivery systems

The applications of nano- and microparticles used for vaccine and drug delivery are well documented [72-77]. Particulate delivery systems have the advantages of controlled and targeted delivery, and can act as vaccine adjuvants [78-80]. Polymeric particles, inorganic nanoparticles and hybrid particles are the main research focus for such vaccine/drug delivery systems. Various nanoparticles have been designed and functionalized for delivering antigens/drugs with different purposes. Reddy *et al.* used Pluronic-stabilized polypropylene sulphide (PPS) nanoparticles conjugated to ovalbumin to exploit lymphatic transport and complement activation [81]. Ultra-small PPS nanoparticles (25 nm) have been reported to show stronger immune response than 100-nm PPS nanoparticles because the former can be efficiently taken up by lymphatic vessels and then transported to the draining lymph node [81]. Bourquin *et al.* studied gelatin nanoparticles for delivering immunostimulatory RNA oligonucleotides in mouse tumor models, successfully triggering an efficient antitumoral immune response [82]. Poly(lactic acid) (PLA) nanoparticles modified with polyvinyl alcohol (PVA), alginate (ALG) and glycolchitosan (GCS) were prepared and investigated as *Streptococcus equi* antigen carriers [83]. Trimethyl chitosan-hyaluronic acid nanoparticles loaded with ovalbumin showed enhanced immunogenicity after nasal and intradermal vaccination [84]. Biodegradable poly(γ -glutamic acid) nanoparticles loaded with ovalbumin effectively induced innate and adaptive immunity, suggesting antigen carrier capacity and potential adjuvant function. Some inorganic nanoparticles have also been considered for vaccine/drug delivery. Gold nanoparticles for loading DNA antigens are often used for particle-mediated epidermal delivery [85-87]. Calcium phosphate nanoparticles have been reported as a promising vaccine delivery system and adjuvant [88].

6.1 Silica nanoparticles as a drug/vaccine delivery system

Mesoporous silica nanoparticles are potential useful drug delivery systems attracting a lot of interests for many biomedical applications (**Figure I-15**) [75, 89, 90]. The development of the technology for the synthesis has greatly improved the controllability of the properties of mesoporous silica nanoparticles with different mesostructures and pore sizes [91]. The porosity of silica nanoparticles and surface modifications enable the possibility of drug loading and release under a controlled manner [92, 93]. Stimuli-responsive mesoporous silica nanoparticles can be obtained by surface modification using some macromolecules. Park *et al.* prepared pH-sensitive silica nanoparticles by coating the surface with PEI and cyclodextrin,

which can release guest molecules at an acidic pH (5.5) [94]. Hybrid chitosan modified silica nanospheres also show very good pH-controlled release of loaded model proteins [95].

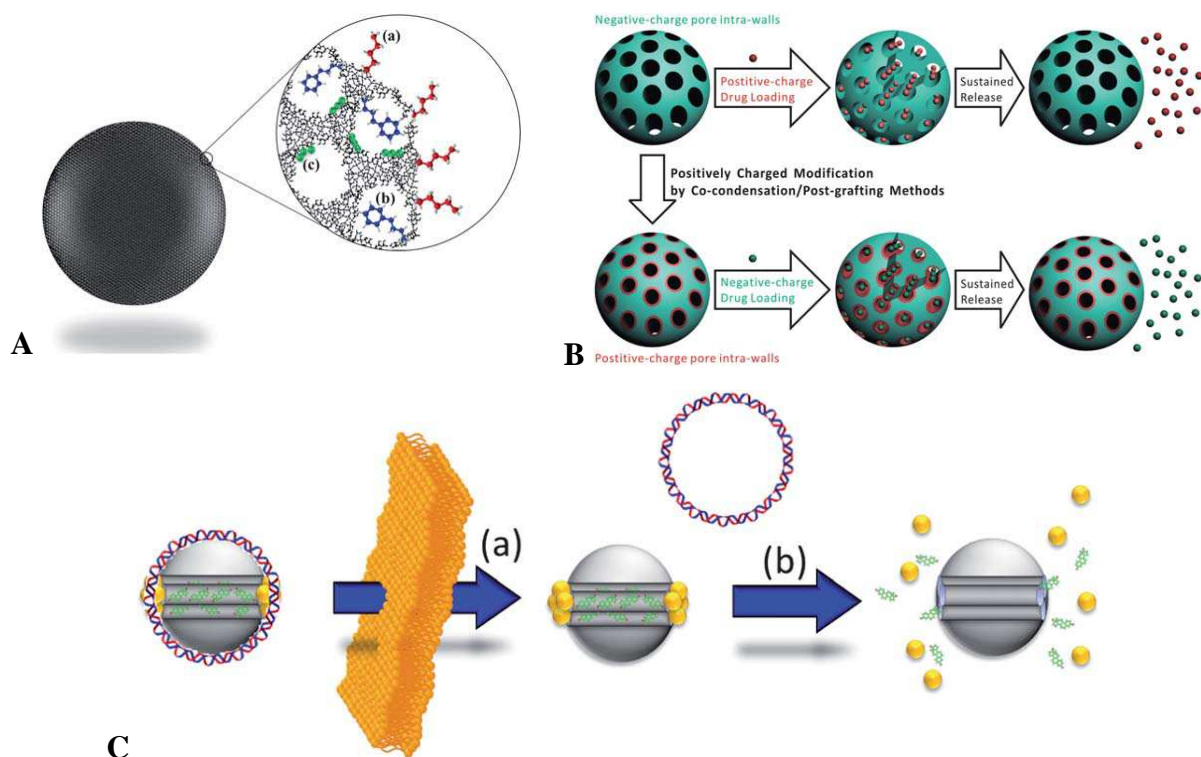


Figure I-15. Mesoporous silica nanoparticles as a drug delivery system. (A) Functional groups (a) at the external surface, (b) at the pore entrances and (c) within the walls; (B) Counterpart charge modification for loading different drugs: negative surface for loading positively-charged drugs and positive surface for loading negatively-charged drugs; (C) Intracellular delivery by penetrating cell membrane: (a) plasmid DNA is release in cells and (b) release of activator β -estradiol stimulated by a reducing agent. Figure adopted from Ref. [89, 90].

However, silica nanoparticles have not received sufficient attention as a vaccine delivery system. In fact, silica showed an adjuvant effect in the immunological response of the guinea pig [96]. Vallhov *et al.* studied the effects of mesoporous silica particles (270 nm and 2.5 μm) on human monocyte-derived dendritic cells (MDDC) and found good cellular uptake of both particles and low-toxicity profiles on MDDC [97]. Recently, Vallhov *et al.* suggested that mesoporous silica particles have adjuvant properties of tuning effect T cell development according to cell culture experiments [98]. Furthermore, mesoporous silica nanoparticles can enhance mucosal and systemic immune responses when applied by oral immunisations in

mouse models [99]. Although silica nanoparticles show potential as a vaccine delivery system, there is no study investigating their applications for epidermal powder immunisation.

6.2 Particles targeting Langerhans cells

Langerhans cells (LCs) in the epidermal layer covering about 25% of the entire surface of human skin [7] are responsible for the antigen presenting process. Particles carrying antigens can be accelerated into the epidermal layer to target LCs, subsequently inducing immune responses. Ginsberg *et al.* showed that particle-mediated epidermal delivery (PMED) of melanosomal antigens (Xenogeneic gp100 DNA) adsorbed on gold particles in melanoma patients produced similar immune response compared to intramuscular delivery, even though a significant smaller dose of DNA was used for PMED injection [100]. A phase I clinic trial of PMED for delivering Hantaan virus and Puumala virus M-segment DNA showed positive results in humans having hemorrhagic fever with renal syndrome [86]. Gold particles are well suitable for DNA vaccines, but gold is a high-cost and non-biodegradable material.

Chitosan particles loaded with DNA vaccines was shown to be efficacious in mice using transdermal immunisation [101]. Skin Langerhans cells were promoted to migrate to lymph node and then to spleen after being bombarded with chitosan/DNA particles, confirming the function of LCs as antigen presenting cells [101]. The migration of Langerhans cells challenged by vaccines was better using core-shell polymeric nanoparticles by Lee's work [102]. Targeting of antigens delivered by the intradermal route to skin dendritic cells makes it possible to enhance vaccine efficacy, even better than with the conventional subcutaneous or intramuscular route [103, 104]. Mesoporous silica nanoparticles as a drug delivery system have never been used as a vaccine delivery system for epidermal powder immunisation. The pores of silica particles provide a controlled space for loading adjuvants, peptide antigens, and protein antigens if silica particles with large pores are used. Therefore, we hope we can contribute to this point and open the door to apply silica or silica-based nanoparticles for better epidermal immunisation.

Silica nanoparticles cannot be delivered into epidermal layer of human skin by direct powder injection because smaller particles require higher velocity [12], which is limited by the particle-accelerating device. Kendall *et al.* proposed a relation between the particle penetration depth and the particle impact parameters (ρvr) that are determined by particle density (ρ), velocity (v) and radius (r) [12]. As indicated from the penetration of gold particles

into human skin, ρ_{vr} should be 7 - 12 kg/m·s for delivering them into the viable epidermal layer [12]. Therefore, it is necessary to formulate silica nanoparticles and antigens into microparticles that meet the requirements of powder injection. Meanwhile, formulation of the nanoparticles into microparticles can improve the long-term stability of nanoparticles and protein antigens.

6.3 Microparticles for epidermal powder immunisation

The methods for epidermal powder immunisation include intracellular particle delivery of small particles such as 1 - 3 μm gold particles and extracellular particle delivery for micro-scale particles (20 - 70 μm) [10, 45]. Sugar-based microparticles prepared by spray-freeze-drying (SFD) were used for epidermal powder immunisation against influenza, resulting humoral immune responses in humans [105]. The formulations of sugar-based microparticles were optimized for better particle morphology and higher density that are required for powder injection [106-108]. Insulin as a polypeptide commonly used for treating diabetes is required to be injected regularly. Schiffter *et al.* developed insulin-encapsulated microparticles consisting of trehalose, mannitol and dextran for needle-free ballistic powder injection [109]. There are some other methods to prepare microparticles that may be useful as delivery systems for powder injection, for example, PLGA microparticles [110] and gelatin-hydroxyethyl cellulose microspheres [111].

The idea to encapsulate nanoparticles in microparticles for epidermal powder immunisation is novel, even though some composite microparticles were developed for other purposes. PLGA-mesoporous silica microspheres were prepared for DNA prime-protein boost vaccination [112]. Inorganic nanocrystals were encapsulated into PLGA microsphere to study their intracellular localisation in dendritic cells by transmission electron microscopy and confocal laser scanning microscopy [113]. However, nanoparticles encapsulated in the biocompatible sugar-based microparticles have not yet been investigated.

7. Objectives of the project

A locally based company is dedicated to establish a useful accelerating device by Dr. Peter Lell (Pyroglobe GmbH, Hettenshausen, Germany). Dr. Lell patented a needleless injection device with pyrotechnic drive [114], which can be modified for injection particles into a body tissue such as skin [115]. As shown in **Figure I-16**, the gas-generating material (19) was ignited to produce a high pressure; the pressure is directly or indirectly transmitted to the

membrane (9) and the pulse is transferred to the substance particles (3); the particles detached from the membrane are accelerated to a high speed and then penetrate into the tissue such as skin. The penetration depth can be controlled by adjusting the energy produced from the gas-generating material. Active ingredients can be formulated in the particles for powder injection into skin using this device.

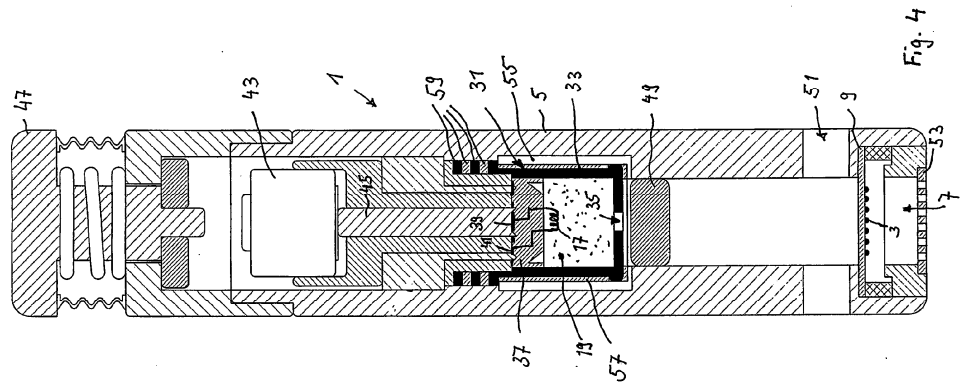


Figure I-16. Representative diagram of the device for needle-free powder injection [115]. A longitudinal section of a reusable apparatus with a separate gas generator (33) and a sliding piston (49) for generating pulses are shown. The accelerated piston can transfer the energy to the membrane (9), accelerating the particle on the membrane to a high speed. The particles can penetrate into a body tissue through the window (53).

With their expertise in extremely simple and cheap novel actuators it is thought to improve the delivery device by a small actuator device unit that is not dependent on helium gas. Experiments to formulate suitable powdered formulations that can be loaded into a surrogate device mimicking the later envisioned vaccine delivery device can be carried out. In order to achieve successful vaccination using powdered vaccines, it is inevitable to determine the penetration depths of particles. This can be determined and analysed using different skin models, ranging from simple gel-based skin surrogates to animal cadaver skin. Formulation of vaccines into microparticles with a suitable size and density is also very important for the subsequent animal experiments and clinical investigations.

The aim of the research project is to develop suitable skin models which can be utilised to determine penetration of particles or powders of vaccines delivered by epidermal powder injection (EPI) and to create an antigen-loaded delivery system which can be used for epidermal powder immunisation.

Skin models simulating the mechanical properties of human skin will be studied for the purpose of evaluating the device for powder injection which is developed by a local company. The simple and cheap novel actuator used here is not dependent on helium gas, and is thought to improve the epidermal delivery. The skin models will be used to determine the parameters of the device for the experiments on living animals and clinic studied in the future. The acceleration force necessary for the delivery of model particles into a certain depth in the skin will be correlated with the mechanical properties of skin and the characteristics of particles. The determination of particles delivered into skin models or skins will be studied. Confocal laser scanning microscopy will be used for the detection and imaging of fluorescently-labelled particles in skin models or skins.

Particles carrying antigens for epidermal powder immunisation will be investigated. Considering the requirements of particle size, density and robustness for EPI delivery [12], the optimisation of the formulation containing antigens is necessary. The particles with sizes of 20 - 70 μm in diameter [10, 45] are preferably delivered into skin by epidermal powder injection. Sugar-based matrices including trehalose, mannitol and dextran will be incorporated to prepare water-soluble microparticles loaded with antigens. Nanoparticles have shown some advantages as good vaccine delivery systems [116-119], but nanoparticles are too small to be directly used for epidermal powder immunisation. Therefore, a nanoparticles-in-microparticles (nano-in-micro) system is proposed to take advantage of nanoparticles for vaccine delivery and simultaneously meet the requirements for effective epidermal powder injection. Nanoparticles for loading antigens will be used in the formulations of the sugar-based microparticles. Mesoporous silica nanoparticles (MSNP) and poly(lactic-co-glycolic acid) (PLGA) nanoparticles will be used for loading ovalbumin (OVA) and OVA peptide. MSNP nanoparticles will also be used for loading influenza vaccine H1N1 hemagglutinin. The encapsulation of antigen-loaded nanoparticles into the sugar-based microparticles will be achieved by spray-freeze-drying.

Finally, the nano-in-micro particles carrying antigens will be applied on the skin models and porcine skin by powder injection using the novel device. The depths and distribution of injected particles will be studies by CLSM.

Chapter II. Preparation and Validation of a Skin Model for the Evaluation of Intradermal Powder Injection Devices

1. Objectives

Epidermal powder immunisation is a promising needle-free method for vaccination [6]. It can overcome the risk of needle-stick injuries and transmission of blood-borne diseases resulting from re-use of disposable needles [6]. A novel intradermal powder injection device has been developed by our collaborating partner. It is necessary to evaluate the new device on human/animal skin or skin models before it can be applied in animal studies. Human skin is preferred for the evaluation, but human skin *in vivo* has complex mechanical properties, e.g. sex and site-dependent variation and ageing effects [17, 31, 120]. Moreover, human skin *in vitro* is not easy to obtain and also requires careful handling because it cannot be stored for a long period of time after it has been removed from the human body. Animal skin, for example pig skin, can be obtained more easily but faces similar problems as regards storage and handling. In addition, animal skin may display very different mechanical properties depending on the animal species. Skin models mimicking the mechanical properties of real skin are needed. The mechanical properties of human skin *in vivo* or *in vitro* are considered the gold standard for developing model skin for the purpose of the evaluation of intradermal powder injection devices. Therefore, a skin model mimicking the mechanical properties of human skin needs to be developed that will be an appropriate option for evaluating powder injection devices and particles for injection.

The most appropriate way to build a skin model is to establish a structure mimicking the function of real skin. Biomacromolecules such as gelatin, collagen, or alginate have been used to prepare artificial skin [57]. In the study of Condliffe *et al.*, a 3% (w/w) agar gel was used as a model skin for evaluating the particle size distribution following powder injection [109], but this agar gel cannot be used as the evaluation base for injection of soluble microparticles in our study because of its high water content. Skin tissue engineering is another possibility to obtain skin equivalents [59]. A dermal equivalent built by tissue engineering displays identical mechanical properties as the skin *in vivo* from 20 subjects ranging 55 to 77 years old [121], but that such extremely costly skin for graft is not an option for our purpose.

Gelatin with a random coil conformation containing 3000 - 4000 amino acids residues is an irreversibly hydrolysed form of collagen that has a triple-helix structure [55, 122]. Gelatin based films have also been used for food and drug packaging due to a melting point close to the body temperature [123]. The mechanical properties of gelatin film can be tailored by adding plasticisers such as glycerol, polyethylene glycols (PEG), or mannitol [124, 125]. However, only a few publications about gel films used as a skin model for the purpose of the evaluation of powder injection devices can be found in the literature [109, 126, 127].

The aim of this study was to prepare and compare films made of different materials and investigate their potential to be used as a skin model for ballistic powder immunisation. Furthermore, storage stability of the prepared films was analysed. In addition, the localisation of particles in the skin gel models was determined by confocal laser scanning microscope (CLSM). The typical method for particle depths determination is cryo-sectioning of skin samples [72]. One of the drawbacks of this method is the time-consuming preparation procedure for each sample. Meanwhile, there is always the risk of creating artefacts simply due to the fact that the blade of the instrument can move particles in the gel/skin. Also, cryo-sections must be cut very thin to allow for an observation under the microscope. If the particle size is larger than the maximum thickness of the cryo-section, particles must be cut and artefacts can be produced. Moreover, the determination depth of fluorescent particles in real skin by CLSM is limited to 50 μm for high resolved observation [66]. Therefore, there is a need to develop a novel, simple and easy-to-use technique to determine particle distribution in the skin models within a range of large depth (up to 150 μm) and visualise them.

2. Materials and Methods

2.1 Materials

GELITA Pharmaceutical Gelatin made from pig skin with a strength of 180 Bloom was purchased from DGF STOESS AG (Eberbach, Germany). 1,2,3-Propantriol (Glycerol) (purity, 99%) was obtained from AppliChem GmbH (Darmstadt; Germany). Agar was purchased from Sigma-Aldrich Chemie GmbH (Steinheim, Germany). Elastosil® RT 604 A and Elastosil® RT 604 B were provided by Wacker Chemie AG (Munich, Germany) as a gift. Acrylamide solution (40(w/v)%) (29:1 ratio of mono- and bis-acrylamide) was purchased from Carl Roth GmbH (Karlsruhe, Germany). 10% ammonium persulfate (APS) and *N,N,N',N'*-tetramethylethylenediamine (TEMED) were purchased from SERVA Electrophoresis GmbH (Heidelberg, Germany). Moisture barrier bags (aluminium bags)

including a static dissipative nylon outer layer and a static dissipative polyethylene inner layer with a centre layer of aluminium foil were obtained from Advantek, Inc. (Freiburg, Germany). Fluorescein isothiocyanate (FITC) labeled poly(methyl methacrylate) (PMMA) spheres were kindly provided by microParticles GmbH (Berlin, Germany). Tetramethyl rhodamine B isothiocyanate-Dextran (TRITC-Dextran) (average molecular wt. ~70 kDa) was obtained from Sigma-Aldrich (Steinheim, Germany). Petri dishes of μ -Dish 35mm high ibiTreat were obtained from ibidi GmbH (Munich, Germany).

2.2 Methods

2.2.1 Preparation of human skin and pig skin

Human skin samples were obtained from the Plastic Surgery Department of a renowned clinic after patient's consent and in line with the regulations of the German law on transplantation ("Gesetz über die Spende, Entnahme und Übertragung von Organen und Geweben (Transplantationsgesetz - TPG)"). The skin sample was obtained from the abdomen of an individual (37 years old). The working instructions for handling human skin were followed according to the appropriate regulations. The skin was stored in a sealed aluminium bag at -80°C. It was thawed at room temperature for 4 hours before use. The measurements of mechanical properties were carried out after removing the subcutaneous fat of the skin.

Piglet skin was provided by the Veterinary Faculty, Ludwig-Maximilians-University, Munich, Germany. After excision from the dead animal, full abdominal skin and ear skin were placed on ice. The subcutaneous fatty tissue was removed with a scalpel. The piglet skin without fat was covered with aluminium foil and stored in a sealed plastic bag in a -80 °C freezer until use. All samples were used within 6 months. Before measuring the mechanical properties, a part of the skin was cut out from the frozen skin and placed in a desiccator with a relative humidity of 43% for about 3 hours. The thickness of pig ear and abdominal skin was $750 \pm 50 \mu\text{m}$ and $1050 \pm 50 \mu\text{m}$, respectively, according to the observations by a digital microscope.

2.2.2 Preparation of gelatin based films

Gelatin was dissolved in hot deionized water (~55°C), and a gelatin aqueous solution was obtained. Ten percent (by mass) gelatin aqueous solution was used for the preparation of all films. A specific amount of glycerol (as outlined in **Table II-1**) was added into 10% (w/w) gelatin solution, and mixed together by stirring and degassed by ultrasound for 5 min. 45 g of

each mixture was cast in plastic Petri dishes having a diameter of 8.6 cm. The gelatin-based films formed after drying in a chemical hood for three days at ambient condition. The films were peeled from the Petri dishes, turned over and placed in the chemical hood for one more day. The films were stored at a relative humidity (RH) of 43% for one week. At last, one film was cut into five pieces (discs) with each film having a diameter of 3.0 cm as shown in **Figure II-1**. The small discs were stored in a sealed plastic bag at 4 °C. Gelatin films with gelatin/glycerol (gel/gly) weight ratios of 5/5, 4.5/5.5, 4/6 and 3.5/6.5 were prepared (**Table II-1**). The thicknesses of all the films were between 1.1 - 1.4 mm as measured by an electronic micrometer IP54 from Messmittelonline (Kloster-Lehnin, Germany).

Table II-1 Gelatin films with different contents of glycerol as skin models

Gelatin/glycerol (gel/gly)	gel1	gel2	gel3	gel4
Weight ratio	5/5	4.5/5.5	4/6	3.5/6.5

2.2.3 Preparation of silicone films

36.0 g Elastosil RT 604 A and 4.0 g Elastosil RT 604 B were mixed together under gentle stirring. After 5 min, the mixture was poured into a plastic Petri dish with a diameter of 8.6 cm, and then the dish was placed in a vacuum dryer with a vacuum pressure of 11 mbar and a temperature of 30 °C for 24 h. The silicone film was punched into small pieces with a diameter of 3.0 cm as shown in **Figure II-1**, and a thickness of around 1.3 mm.

2.2.4 Preparation of agar gel

Three percent agar gel was prepared according to [109]. 0.44 g agar was dissolved in 14.8 g deionised water under gentle stirring in a water bath at 80 °C. After 20 min, the stirring was stopped and the agar solution was stored at 80 °C for another 10 min. After that, the solution was poured into Petri dishes with a diameter of 3.4 cm. The Petri dish with agar gel was sealed with parafilm and stored at 4 °C for at least 24 hours to ensure formation of the gel. For measurements by texture analyser, the agar gel was removed from the Petri dish and cut into a film with a diameter of 3.0 cm as shown in **Figure II-1**.

2.2.5 Preparation of polyacrylamide gels

Polyacrylamide gels were prepared according to the work of Schramm-Baxter *et al.* [56]. Briefly, four kinds of gels ((w/v)% acrylamide: 10 - 40) were created with 10% ammonium

persulfate (APS) and *N,N,N',N'*-tetramethylethylenediamine (TEMED) as initiators. 10 - 30% acrylamide solutions were obtained by dilution with DI water from 40% acrylamide solution. For polymerization, 30, 60, 45, and 24 μ l of APS solution, and 6, 12, 12, and 6 μ l of TEMED solution were added into the 10%, 20%, 30%, and 40% acrylamide solution, respectively. Cylindrical tubes with a diameter of 13 mm were used as the moulds for the gels. 1 ml mixtures were added into the tubes respectively. The tubes with gels were sealed with parafilm and stored at 4 °C for about 24 h before measurements.

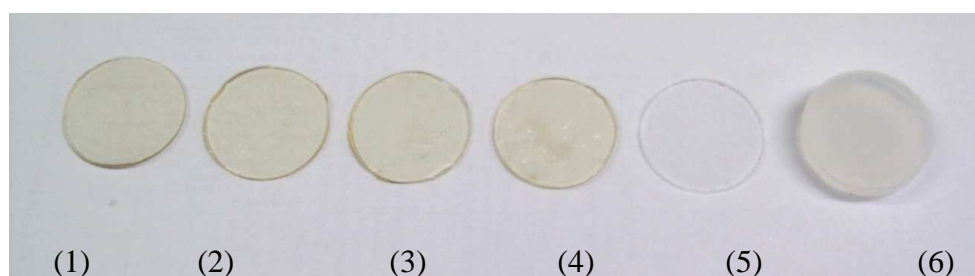


Figure II-1. Photograph of gelatin films, silicone film and agar gel. From left to right, (1) gel/gly = 5/5, (2) gel/gly = 4.5/5.5, (3) gel/gly = 4/6, (4) gel/gly = 3.5/6.5, (5) silicone film and (6) agar gel.

2.2.6 Measurements of the mechanical properties of gelatin based films, silicone films, agar gel, polyacrylamide gels, human skin and pig skin

A texture analyser TA.XTplus from EXPONENT Stable Micro Systems Ltd. (Godalming, Surrey GU7 1YL, UK) was used to measure the force versus indentation distance curve. A custom-made conical probe with a cone angle of 60° ($2\alpha = \pi/3$) was used for the measurement of indentation behaviour under a force of 0.08 N. The indentation speed for all the tests was set to 0.5 mm/s. The curve for each sample was obtained by calculating the average of three indentation results on different locations of the film surface ($n = 3$). A custom-made spherical probe consisting of a ball with a diameter of 0.98 mm attached to a cylinder with a diameter less than 0.98 mm was used to measure the puncture force of pig skin and skin models. The maximal force in the puncture tests was 20 N.

2.2.7 Storage conditions

The films were stored in the desiccator with a RH of 33 ± 3%, 43 ± 3% or 75 ± 3% at room temperature for one week after they had been dried in the chemical hood. Saturated salt solutions were used to control the relative humidity inside the desiccators [128]. Saturated potassium carbonate maintains an equilibrium relative humidity of 43% between 10 - 30 °C.

The desiccator with a RH of 43% was used to store the films for humidity controlling. After 7 days of storage at RH 43%, the gelatin films were packaged in sealed plastic bags first, and then the bagged films were sealed in aluminium bags, and finally placed in the freezer (-80 °C) until use.

2.2.8 Determination of the Young's modulus

The calculation was based on the Hertz theory of contact between a rigid conical indenter and an elastic solid [129]. The indentation distance (δ) and the contact radius (a) are related by

$$\delta = \frac{\pi}{2} a \tan \theta = \frac{\pi}{2} a \tan\left(\frac{\pi}{2} - \alpha\right) \quad (1)$$

where θ is the angle between the side surface of the cone and the plane, and the pressure distribution is proposed as

$$p(r) = -\frac{E\delta}{\pi a(1-v^2)} \ln\left(\frac{a}{r} + \sqrt{\left(\frac{a}{r}\right)^2 - 1}\right) \quad (2)$$

And then the total force is

$$F_N = \frac{2}{\pi} E^* \frac{\delta^2}{\tan \theta} \quad (3)$$

where E^* is defined as

$$\frac{1}{E^*} = \frac{1-v_1^2}{E_1} + \frac{1-v_2^2}{E_2} \quad (4)$$

where E_1, E_2 are the elastic moduli and v_1, v_2 the Poisson's ratios of the rigid indenter and elastic solids, respectively. In this case, $E_1 \gg E_2$, and thus,

$$E_2 = E^* (1 - v_2^2) \quad (5)$$

Considering the relation between the rigid indenter and the elastic solid in equation (3), indentation force/distance curves were all simulated with

$$F_N = F_0 + \frac{2E^*}{\pi \tan \theta} \cdot \delta^2 \quad (6)$$

F_0 was considered to reduce the systematic error and improve the simulation quality. Finally the Young's modulus of the skin and skin models were obtained. All the correlation

coefficients (R^2) are between 0.95 and 0.99. A Poisson's ratio of 0.495 was used for all the skin and skin models as they could be assumed to approximate incompressible materials.

2.2.9 Establishment of structural models and CLSM measurement

Two layered structures were built as the models for the validation of a method to determine the depth of a particle in a skin sample using Confocal Laser Scanning Microscope (LSM 510 META, Carl ZEISS, Germany). Two layered structural models were established as described in **Figure II-2**. Glycerol was added to prepare gelatin films having a composition of gelatin/glycerol of 4/6 by mass which increases the adhesiveness of the films. For the first model structure, two species of thin gelatin films including unlabeled and fluorescently labeled ones were stacked in an alternating manner to obtain a layered composite with a total thickness of about 840 μm . For the second model, unlabeled films and FITC-PMMA particles were stacked in an alternating manner to simulate the location of particles at different depths, and one TRITC labeled gelatin film (TRITC-gel) layer was placed on the top for determining the surface. In order to make sure the layers hold together tightly, transparent adhesive tape (Tesa[®] film) was used to cover the entire layered models by wrapping from the top layer to the bottom layer. First of all, 20 ml of a 2.5% gelatin solution of the composition of gel/gly of 4/6 (gel 3) was prepared and cast in the Petri dish with a diameter of 8.6 cm. After 3 days in the chemical hood, a dry flexible gelatin film was obtained with a thickness of $140 \pm 20 \mu\text{m}$. Second, in order to prepare a TRITC labeled gelatin film, 50 μl of a 4.0 mg/ml TRITC-Dextran was added into 15 ml of a 2.5% gelatin solution of the composition of gel/gly of 2/1, and then 50 μl of a 18.0 wt% formaldehyde solution was added into the solution to crosslink the gelatin film. The mixture solution was cast in a Petri dish and a TRITC labeled gelatin film was obtained after drying of 3 days. The thickness of TRITC-gel was determined as $70 \pm 10 \mu\text{m}$.

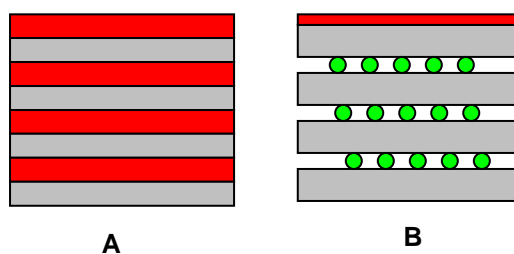


Figure II-2. Schematic of layered structural model **A** (left) and model **B** (right). The red part represents the TRITC-gel layer, while the grey part represents the unlabeled gelatin film with gel/gly of 4/6. The green circles represent PMMA particles.

A LSM 510 META Invert Laser Scan Microscope (Carl Zeiss, Germany) equipped with an Argon laser and a HeNe1 laser for excitation was used to observe the two structural models. The excitation and emission wavelengths for FITC-PMMA are 488 nm and 505 - 530 nm, while those for TRITC-Dextran labeled films are 543 nm and 560 - 615 nm, respectively. The objectives of Plan-Neofluar 10 \times /0.3 and LD-Achroplan 40 \times /0.6 corr were used to observe model **A** and model **B**, respectively. Z-stacking mode was used to obtain 3D images of the samples, orthogonal sections and galleries can be displayed with the Zeiss LSM Image Browser software. A specially designed Petri dish of μ -Dish was used as the sample holder (ibidi, Munich, Germany). The bottom is made of microscopic plastic with a thickness of 180 μ m, and the objective of the CLSM detects samples from the bottom of the Petri dish. The two structural models were placed inside the Petri dishes with the fluorescent surfaces facing the bottom.

3. Results and Discussion

3.1 Indentation behaviour of biological skin and films as candidates of skin models

Measurements of the indentation behaviour of different skin models (**Figure II-1**) were taken in order to determine their mechanical properties and to assess their relative quality. Pig skin has been extensively used as a surrogate of human skin for the study of topical drug delivery and has been identified as one of the most appropriate *in vitro* and *in vivo* human skin models[130, 131]. Herein, pig skin is used as a mechanical model for comparison with human skin *in vitro*. Human abdominal skin samples were used as a reference criterion for mechanical properties in the development of skin models. For a skin model for powder injection, the mechanical properties are the main factors to be considered which will determine the penetration depth after powder injection. The *in vivo* properties, including immune reactions to vaccine delivery, have to be studied *in vivo* later, when the technical setup of the delivery device has been defined by means of the *in vitro* models. The indentation results of pig abdominal and ear skin are shown in **Figure II-3** which indicates that pig abdominal skin is much softer than the ear skin. One of the most important factors affecting the mechanical properties of the skin is the water content in the skin which depends on the environmental relative humidity for storage.

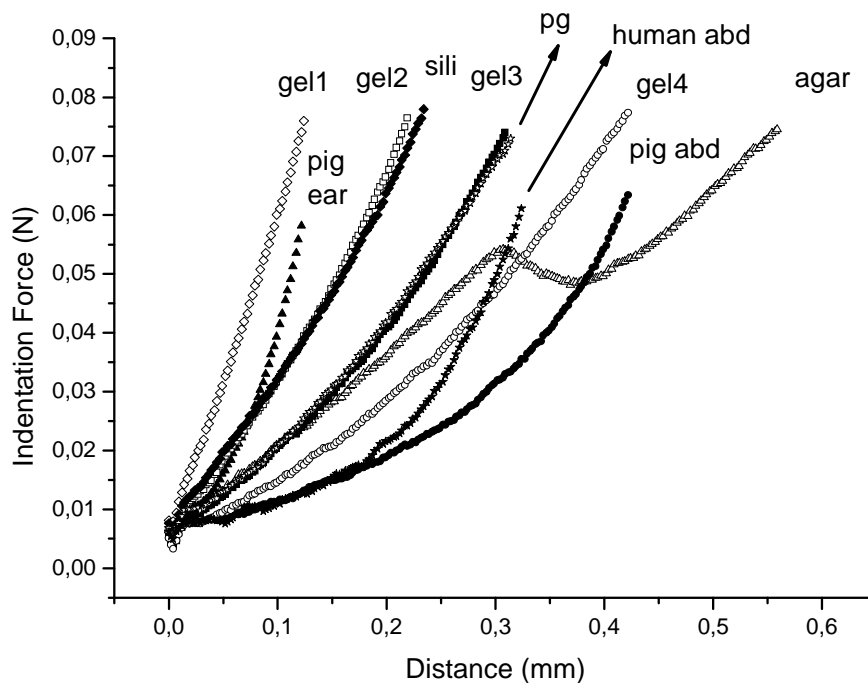


Figure II-3. Indentation curves of human skin, pig skin, agar gel, silicone film, and gelatin films using a conical probe. Gelatin films were stored at a relative humidity of 43%. Curve **gel1** (gel/gly of 5/5) open diamonds, **gel2** (gel/gly 4.5/5.5) open squares, **gel3** (gel/gly 4/6) black squares, and **gel4** (gel/gly 3.5/6.5) open circles. Curve **human abd** (black stars), **pig ear** (black triangles), **pig abd** (black circles), **sili** (black diamonds), **agar** (open triangles), and **pg** (open stars) correspond to human abdominal skin, pig ear skin, pig abdominal skin, silicone film, agar gel, and polyacrylamide gel (40% acrylamide), respectively. All the measurements were averaged by four measurements on different locations ($n = 4$).

In the following, skin models were prepared, analysed and compared to the data obtained from the measurements of pig and human skin. All indentation results of skin and skin models are shown in **Figure II-3** and the corresponding Young's moduli (E) were obtained by the Hertz theory as shown in **Table II-2**.

Table II-2 Mechanical parameters of skin and skin models

Young's Modulus	human abd.	pig abd.	pig ear	gel1	gel2	gel3	gel4	silicone film	polyacrylamide gel	agar gel
E (MPa)	0.7	0.6	6.8	8.6	2.8	1.4	0.8	2.5	1.6	1.2

Human abd., pig abd. and pig ear are referred to human abdominal skin, pig abdominal skin and pig ear skin, respectively.

The silicone film is a good soft tissue mimicking material because of its elastic properties. In our study, a transparent silicone film was made from Elastosil® RT 604 by addition-curing of two-part silicone rubber that vulcanises at room temperature. The Young's modulus of the silicone is 2.5 MPa which is larger than that of human abdominal skin with an E of 0.7 MPa. Agar gels of a concentration of 3% were prepared as they had been reported in the literature as a base for powder injection [109, 132]. The indentation curve of 3% agar gel ($E = 1.2$ MPa) showing a distinct break point around the indentation distance of 0.3 mm is therefore very different from pig skin and gelatin films. Polyacrylamide gels have already been used as a base for jet injection [56] which leads us to also use this system for powder injection. Interestingly, 40% polyacrylamide gels ($E = 1.6$ MPa) show almost the same indentation curve under small indentation forces as gelatin film of the composition gel/gly 4/6 ($E = 1.4$ MPa). However, 40% polyacrylamide gels are quite fragile and easily break into small pieces when removed from the mould.

From the results in **Table II-2** it can be concluded that gelatin films including **gel2**, **gel3**, and **gel4** cover the range of mechanical properties of pig abdominal and ear skin. The Young's modulus of human abdominal skin ($E = 0.7$ MPa) is close to those of pig abdominal skin ($E = 0.6$ MPa) and **gel4** ($E = 0.8$ MPa). Both **gel4** and pig abdominal skin are good skin models for mimicking the mechanical properties of *in vivo* human abdominal skin. It is necessary to keep in mind that the properties of human skin *in vitro* may differ from the *in vivo* situation [40]. The human skin could be hydrated after excision which would reduce their strength. The gelatin film **gel3** ($E = 1.4$ MPa) shows a larger Young's modulus than that of human skin *ex vivo* ($E = 0.7$ MPa) used in the current study. Geerligs *et al.* used a similar *in vitro* indentation method to obtain the Young's moduli of both the stratum corneum and epidermis varying between 1 and 2 MPa [133]. Papini *et al.* found an elastic modulus of 2.25 MPa for the consideration of penetration of high speed particles [127]. Some studies on *in vivo* indentation tests reported Young's moduli of human skin in the range of 7 - 33 MPa [19, 22, 121]. The Young's modulus of human abdominal skin ($E = 0.7$ MPa) as we obtained is quite close to the one measured by Geerligs *et al.* [133], (approximately 1 MPa for both stratum corneum and viable epidermis). The Young's modulus of skin can vary much when measured by different methods such as indentation tests, torsion tests, extension tests, etc. [121]. Therefore, the mechanical properties of skin can be comparable only if the similar method for measurements is used. The difference of the reported Young's moduli for skin may be attributed to the complexity and several heterogeneous layered structure of skin. The large indentation test

distance and the large size indenters could make the Young's moduli come from the combination layer of epidermis and dermis, and even part of hypodermis. Actually, due to the variation of mechanical properties of human skin [31], three gelatin films having different mechanical properties with gel/gly of 4.5/5.5 (**gel2**), 4/6 (**gel3**) and 3.5/6.5 (**gel4**) were studied further as a series of skin models. The film with gel/gly of 5/5 (**gel1**) was not considered further because it's Young's modulus ($E = 8.6$ MPa) is too far from that of human skin ($E = 0.7$ MPa). The gelatin films can be obtained easily and are easy to store compared to human skin and animal skin. The transparency of gelatin films is another advantage for microscopic observation such as CLSM after powder injection. Though agar gels can be easily sliced into slices for microscopic observation with a normal scalpel at room temperature [109], they can be punctured too easily as there is a break point as shown in **Figure II-3**. Three percent agar gel has a high viscosity and it is difficult to remove air bubbles inside. To improve the hardness of agar gel with a larger concentration is not easy because of the high viscosity of agar solution at a concentration higher than 3%. Therefore, a series of gelatin films seem to be preferable skin models.

Double-layer gelatin films were prepared as well by varying the composites of the two layers. The first layer (inside layer) was prepared using formaldehyde crosslinked gelatin, while the second layer (outside layer) of around 100 μm , which should be harder than the first one according to the composition, was added. However, the indentation behaviour of the double-layer film shows no much difference compared to the single layer gel. In the case of human skin, the stratum corneum has a higher Young's modulus than dermis, but the thickness is not large enough to affect the global mechanical properties of skin [134]. Likewise, double-layer films are more difficult to handle and to control the mechanical properties. Thus all the gelatin films used further in this study have a single layered structure.

The silicone film is hydrophobic and contains no water inside which suggests that relative humidity will not affect the properties of the silicone film. However, the silicone film is not flexible for preparing different mechanical properties of skin models. As shown in **Figure II-3**, the gelatin films with gel/gly of 5/5 (**gel1**), 4.5/5.5 (**gel2**), 4/6 (**gel3**) and 3.5/6.5 (**gel4**) display different mechanical properties when the glycerol content is varied. The more glycerol the film contains, the more flexible the film is. In fact, water residues in the gelatin films function as another plasticiser, which makes the mechanical properties of gelatin films sensitive to relative humidity which is further described in section 3.3.

Besides force/distance measurements, force relaxation behaviour is another relevant mechanical parameter as it describes the elastic properties of different materials. As shown in **Figure II-4**, the visco-elasticities of silicone and polyacrylamide gel are close to that of a perfect elastomer as the force holding a certain indentation does not decrease over time. Oppositely, the force relaxation of the agar gel is strong, which is consistent with its little elastic behaviour as indicated from its indentation curve in **Figure II-3**. Human abdominal skin has a similar force relaxation as the agar gel, indicating the agar can simulate the visco-elasticities of human skin very well. Pig ear and abdominal skin have lower force relaxations compared to human abdominal skin and the agar gel. Human skin, pig skin, and gelatin films have much stronger force relaxations than silicone and polyacrylamide gel. Gelatin films show different relaxation curves, where an inverse correlation between glycerol content and high/fast/relaxation exists. In a certain range, gelatin films can be adjusted to a relaxation according to different skin types.

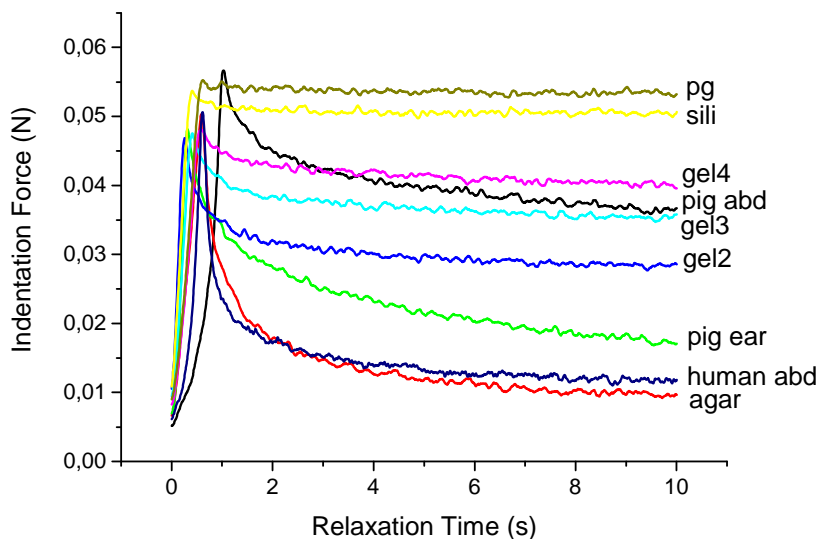


Figure II-4. Force relaxation of human skin, abdominal skin, ear skin, gelatin films, agar gel, silicone film, and polyacrylamide gel under constant penetration depths. Curve **gel2** with gel/gly of 4.5/5.5, **gel3** with 4/6 and **gel4** with 3.5/6.5. Curve **human abd**, **pig ear**, **pig abd**, **sili**, **agar**, and **pg** correspond to human abdominal skin, pig ear skin, pig abdominal skin, silicone film, agar gel, and 40% polyacrylamide gels, respectively. All the measurements were repeated 3 or 4 times.

3.2 Puncture of pig skin and candidates for skin models

An indentation test using small forces of less than 0.08 N as described in our previous experiments is a non-invasive way which can be used to measure mechanical properties of

human skin *in vivo* [19]. The indentation curves obtained describe the differences for different skin model candidates. For powder injection, the true aim of the application mode is that particles will penetrate the stratum corneum and enter the epidermis of the skin. A puncture test with a ball-shaped probe may therefore well simulate the situation for particle penetration into skin or model skin. The custom-made spherical probe with a diameter of 980 μm was used for all the puncture tests. As shown in **Figure II-5**, the turn points of the curves representing break points for gelatin films, silicone film, agar gel, pig ear skin, and abdominal skin can be identified by the maximal force before they are punctured, while for human skin it is not easy to determine the break points. Human skin and pig skin can be punctured with the spherical probe at an indentation force of less than 5 N which was observed from the skin samples after testing. All break points are shown in **Table II-3** and no exact break point for human skin was observed. The break point for agar under the spherical probe is too small to simulate the break point for pig skin, even though the agar gel has a force relaxation close to human skin. Gelatin films and silicone films have break points at the same order of magnitude, but the silicone films do not meet the force relaxation properties of human skin. The gelatin films with gel/gly of 4.5/5.5 (**gel2**), 4/6 (**gel3**) and 3.5/6.5 (**gel4**) have break points of 9.1 N, 6.8 N and 4.6 N, respectively. The variations of gelatin films resulting from the glycerol content are useful to simulate real skin with a specific mechanical property. Therefore, the puncture properties of gelatin films provide another evidence to support them as skin models in powder injection delivery.

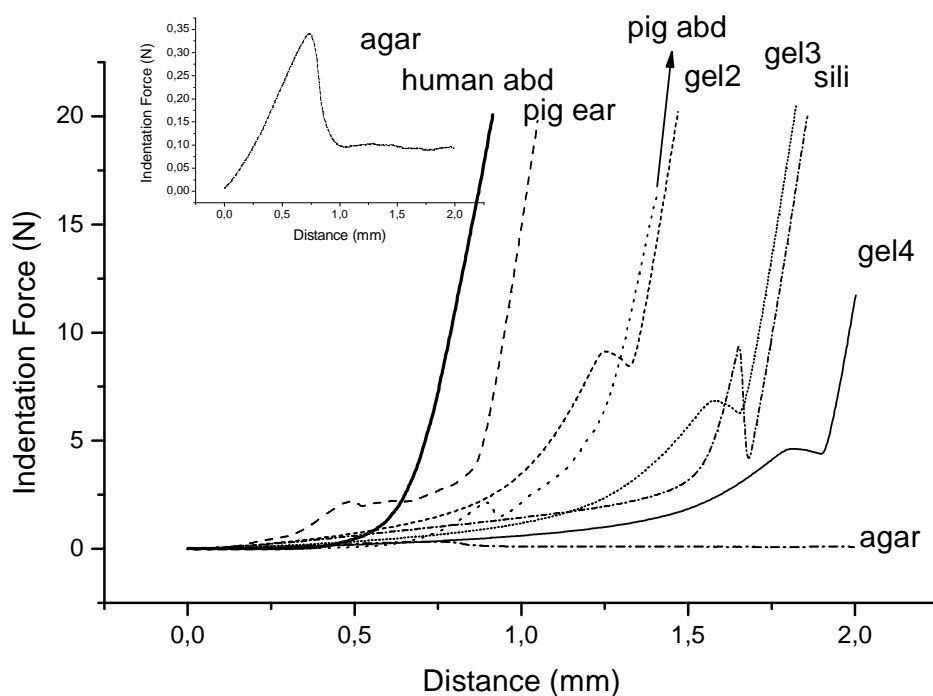


Figure II-5. Results from puncture tests of human skin, pig ear skin, pig abdominal skin, and

skin models including gelatin films, silicone films, and agar gels. Curve **gel2** (short dash), **gel3** (short dot) and **gel4** (solid) correspond to gelatin films with gel/gly of 5/5, 4.5/5.5, 4/6 and 3:5/6.5, respectively. Curve **human abd** (bold solid), **pig ear** (dash), **pig abd** (dot), **sili** (short dash dot), and **agar** (dash dot) correspond to human abdominal skin, pig ear skin, pig abdominal skin, silicone film, and agar gel, respectively. The inset shows the enlarged curve for agar gel. All the measurements were repeated 3 or 4 times.

Table II-3 Break points of pig skin and candidates of skin model

Sample	human abd.	pig ear	pig abd.	gel2	gel3	gel4	Silicone	agar
Break point (N)	Less than 5	2.2	2.1	9.1	6.8	4.6	9.3	0.3

Human abd., pig abd. and pig ear are referred to human abdominal skin, pig abdominal skin and pig ear skin, respectively.

3.3 Effect of the environmental relative humidity (RH) on the mechanical properties of the gelatin films

The relative humidity during measurements may have important implications on the results as the mechanical properties of the skin models may vary when a change in RH occurs. Therefore, the effect of the RH on the mechanical properties was investigated. **Figure II-6** shows the mechanical properties of the gelatin films with gelatin/glycerol ratios of 4.5/5.5, 4/6 and 3.5/6.5 stored in a desiccator at a RH of 33%, 75%, and at ambient condition (35%<RH<45%). The data in **Figure II-6** demonstrate that the mechanical properties can be varied and controlled as long as a control over RH during storage and experiment is in place. A RH of 43% for conditioning is used as this is close to typical conditions in our lab.

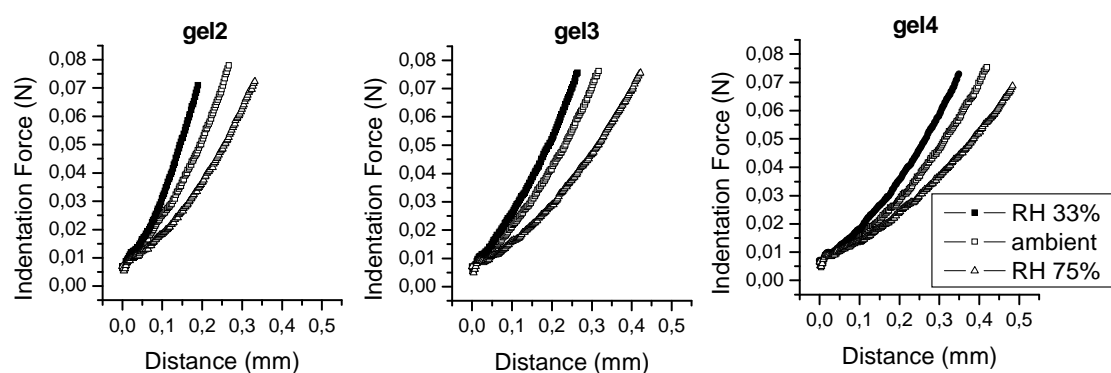


Figure II-6. Effect of relative humidity (RH) on the mechanical properties of the gelatin films. The films were stored for 4 days in the desiccator at RHs of 33% (black squares) and 75% (open triangles), and ambient condition (open squares), respectively.

3.4 Effect of environmental temperature on the mechanical properties of the films

Temperature is another factor affecting the mechanical properties of gelatin films besides relative humidity. Considering the films as model skin will be usually used under ambient conditions, the mechanical properties of gelatin films at 20 - 35 °C were measured. As shown in **Figure II-7**, the higher the test temperature was, the weaker the films became. The indentation force at the same indentation distance decreases a little when the test temperature increases between 20 and 30 °C. Above 30 °C, the indentation force at a certain indentation distance decreases more distinctly. Therefore, it is suggested to use the films as skin model at ambient conditions with 20 - 30 °C which is the normal room temperature range. Therefore, no special temperature control is needed when using the films at a typical condition of 22 ± 2°C.

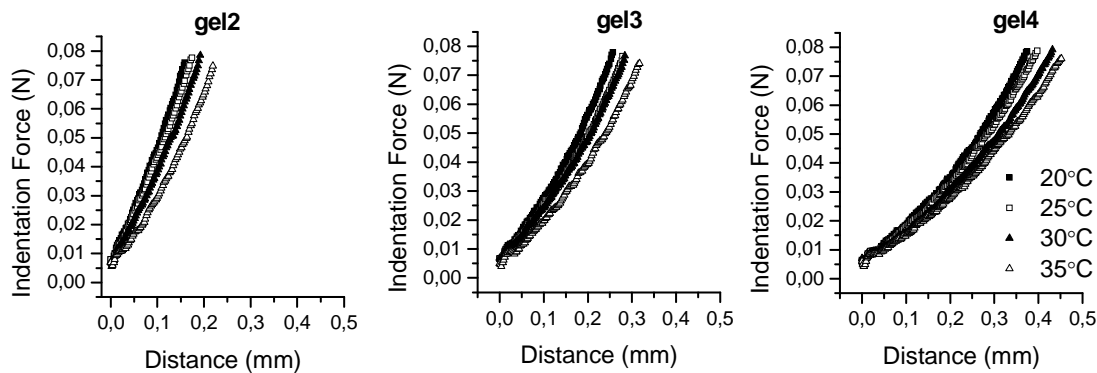


Figure II-7. Temperature dependence of the mechanical properties of gelatin films with gel/gly of 4.5/5.5 (**gel2**), 4/6 (**gel3**), 3.5/6.5 (**gel4**). All the films were stored in the desiccator with RH of 43% for at least one week before measurement. The mechanical properties of the films at 20 (black squares), 25 (open squares), 30 (black triangles) and 35 °C (open triangles) were measured.

3.5 Stability of gelatin films under long-term storage

Freshly prepared gelatin films were stored in the desiccator with RH of 43% for 7 days, and then the films were placed in a sealed plastic bag and stored in the freezer at a temperature of -80 °C. After each week, the films were thawed in the desiccator with a RH of 43% for about 4 hours, and then the mechanical properties were measured. All the films measured were frozen and thawed once only. The results for the films with different storage times in -80 °C are shown in **Figure II-8A**. All the tests were carried out at ambient conditions, and the room temperature was between 20 - 30°C. The curves in **Figure II-8A** are classified into three

groups corresponding to the results of **gel2**, **gel3** and **gel4**, respectively. The different curves in one group are the results of the specified film at different storage times. The indentation forces of the gelatin films with gel/gly of 4.5/5.5 (**gel2**), 4/6 (**gel3**) and 3.5/6.5 (**gel4**) under indentation distances of 0.129 mm, 0.209 mm and 0.289 mm, respectively are used to track the change of gel strength of the films over the storage time as shown in **Figure II-8B**. The force for each film in **Figure II-8B** varies within amplitude of only 0.01 N over time (12 weeks). **Figure II-8B** shows that 22 of 24 data points over 12 weeks storage show only very minor deviations from the starting value. Data for **gel 2** after 6 and 8 weeks fall below the average but after 10 and 12 weeks gel strength of this system reaches the starting level again. Considering the variation of test temperature, the films and those after frozen storage up to 12 weeks have almost the same mechanical properties. Therefore, the gelatin films can be stored in the -80 °C for at least 12 weeks until use without observing relevant changes in the properties of the films. For longer storage, they can be packed in sealed moisture barrier bags (Advantek®).

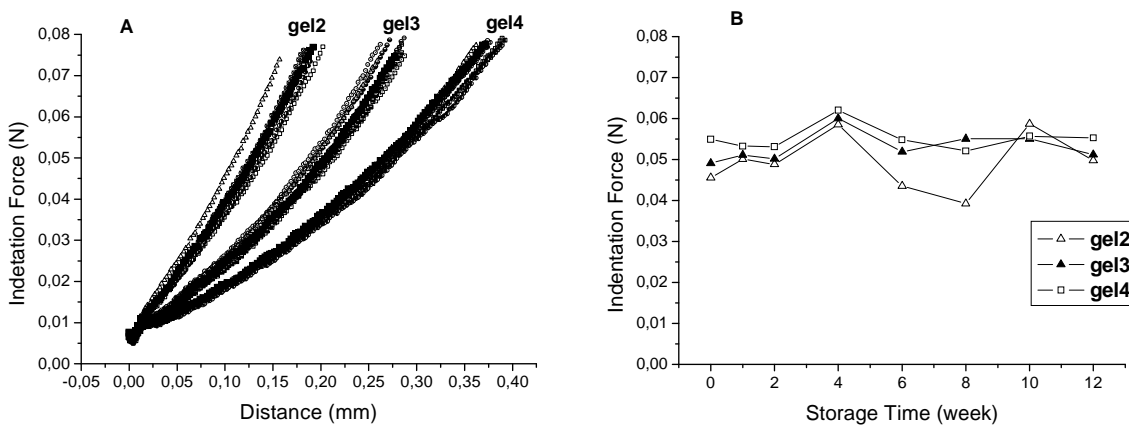


Figure II-8. The stability of the gelatin films in a plastic bag stored at -80°C. Week 0 represents the samples before storage in the freezer. The duration of storage is up to 12 weeks. (A) Indentation curves of gelatin films with gel/gly of 4.5/5.5 (**gel2**), 4/6 (**gel3**) and 3.5/6.5 (**gel4**); (B) Indentation forces of gelatin films of **gel2**, **gel3** and **gel4** under indentation distances of 0.129 mm, 0.209 mm and 0.289 mm, respectively.

3.6 Direct determination of particle deposition depths by CLSM in layered structural models

Confocal laser scanning microscopy was used as a modern tool to investigate the presence of fluorescently labeled model particles in a layered skin model. This technique was used to validate the method in order to later use it for the determination of particle penetration depths

that have been injected into skin or skin models by epidermal powder immunisation. The layered model is depicted in **Figure II-2** and the results of the investigations are shown in **Figure II-9**. The four red lines in the cross section of model A in **Figure II-9A** correspond to the four red layers depicted in **Figure II-2A**. The first sub-photo which shows a red color in **Figure II-9B** corresponds to the top red layer in **Figure II-2B**, while the yellow particles in different sub-photos in **Figure II-9B** correspond to the particle layers as shown in **Figure II-2B**.

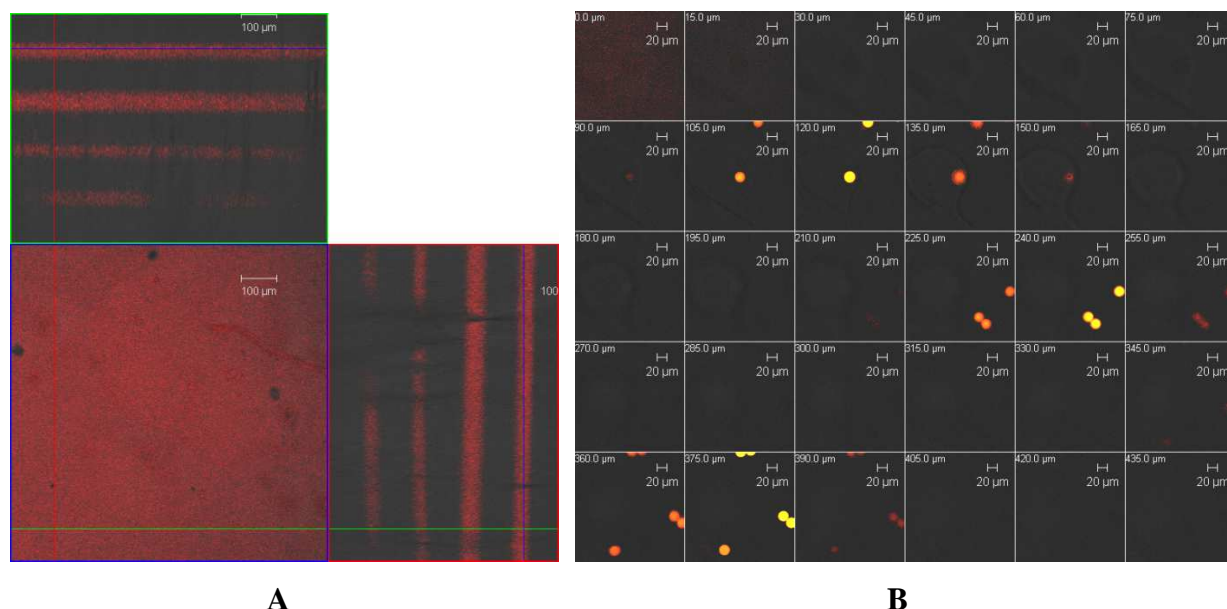


Figure II-9. CLSM images of layered structural model **A** (left) and model **B** (right). The CLSM images of the established layered structural models confirm the validation of the depth measurement by the non-invasive CLSM method. The dye used for labelling gelatin film is Rhodamine B isothiocyanate-Dextran, while the PMMA particles were labeled with Fluorescein isothiocyanate. The brighter part is the area closer to the lens of CLSM. The scale bar of the left one is 100 μm, while that of the right one is 20 μm. For the CLSM measurement of model **A** structure, the pinhole of Ch3 (BP 560-615) is 164 μm. For the CLSM measurement of model **B** structure, the pinholes of Ch2 (BP 505-530) and Ch3 (BP: 560-615) are 184 μm and 480 μm, respectively.

Orthogonal sections of structural model **A** are shown. Four red layers of TRITC-gel films can be observed from the cross section. This result is in coherence with the composition of the model. It is worth noting that the deeper the layer, the weaker the intensity of fluorescence is. The laser intensity decreases with the increase of depth inside the gelatin films, especially when the laser passes through the upper-layer of TRITC-gel films before arriving at the deeper layer. That is to say that the fluorescence intensity at different depths is not directly

related to the concentration of the fluorescent probe. The gallery image of structural model **B** is displayed in **Figure II-9** (right). The first subset image showing red is the fluorescent surface of model **B**. It is a major advantage for measuring the depth of the particles that the surface can be distinguished. The FITC-PMMA spheres at the specific layer can be excited by both excitations of 488 nm (green) and 543 nm (red). The merged photograph is shown in **Figure II-9B** (right) and the yellow circles are the positions where the PMMA spheres reside. The depths of the particles can be determined in relation to the surface ($z = 0$). The depth of the first layer containing two PMMA particles is 120 μm . The second and the third layer are 240 and 375 μm underneath the surface. The shape and size of the PMMA particles are the same as specified by the manufacturer. It means that the CLSM used here is a valid method to determine the depths of fluorescent particles inside model skin or real skin.

CLSM has been extensively applied to visualise transdermal drug delivery into skin [66]. The penetration and distribution of polystyrene nanoparticles containing fluorescein 5-isothiocyanate across porcine skin has been visualised using CLSM [135]. Even though the skin colour and auto-fluorescence can make it difficult to observe deeper layers inside, it is still attractive as a non-invasive method. Usually, the detecting depth of skin after topical drug delivery using CLSM is around 50 μm which is deep enough for evaluating whether drugs can penetrate the skin barrier stratum corneum or not [66]. The special morphology characteristic of stratum corneum surface can be used to define skin surface [135]. In the case of powder injection, we need to measure the depth under skin surface up to 120 μm or even deeper. From the results of the structural models established with gelatin films, the detection depth can be up to 400 μm . Gelatin films seems to be promising skin models for the visualisation of the penetration and distribution of particles delivered by powder injection devices.

4. Conclusions

Different skin models including gelatin films, silicone film and agar gel were analysed as skin models for powder injection delivery. The transparent silicone film may be a good candidate as model skin, but the mechanical properties of the silicone films are difficult to tailor, resulting in the difficulty to simulate different properties of the skin. Agar gels can be applied as model skin for powder delivery as proven by others, but the high water content in agar gel would make injected water-soluble microparticles dissolve away quickly, and then result in ambiguous distribution of particles. A series of gelatin films seems to be good model skin according to our research. Gelatin films with gel/gly ratios of 4.5/5.5 (**gel2**), 4/6 (**gel3**) and

3.5/6.5 (**gel4**) which can be easily prepared at low cost could simulate the skin with different mechanical properties. Young's modulus of the gelatin film with a gel/gly of 3.5/6.5 (**gel4**) ($E = 0.8 \text{ MPa}$) is close to that of *in vitro* human abdominal skin ($E = 0.7 \text{ MPa}$) making that this is favoured as a skin model. The reproducibility of the gelatin films can be controlled and the stability during storage is good. Furthermore, gelatin films are transparent for CLSM measurements, which is a major advantage for observing the penetration and distribution of fluorescent particles after powder injection. As seen from the CLSM image of the structural layered model **B**, the FITC-PMMA particles at a depth of 400 μm can be well visualised. In all, gelatin films will be simple and effective skin models for powder delivery research, which may facilitate the development of powder injection devices and the evaluation of powder or particles for injection.

Chapter III. Nanoparticles-in-Microparticulate Systems for Epidermal Powder Injection

1. Objectives

As described in the first chapter, there are requirements for the particles to be used for epidermal powder injection (EPI), including the right size, sufficient density and good robustness. In fact, nanoparticles and microparticles have been extensively used as drug/vaccine delivery systems, but nanoparticles are not suitable for EPI due to the limitation of size and density [12]. The definition of “nanoparticles” used in this thesis describes especially the particles in the size range of 100 nm to 1000 nm. Due to their small size and therefore low mass, it is necessary to formulate nanoparticles into microparticles in order to achieve a particle that can be delivered by EPI. The microparticles should optimally have sizes ranging from 20 μm to 70 μm that are best for EPI delivery [10, 45]. The particles lower than 20 μm may not penetrate into skin effectively if the density is not high enough, while the particles larger than 70 μm could induce blood bleeding and pain when impacted on human skin [10, 45].

The idea of the work described in this chapter is to combine the advantages of nanoparticles for vaccine delivery and microparticles for EPI. The concept of nanoparticles-in-microparticles (nano-in-mico) systems for EPI delivery is shown in **Figure III-1**. Antigens are loaded in nanoparticles or on the surface of nanoparticles, and then these nanoparticles are formulated in microparticles by using spray-freeze-drying (SFD). The sugar-based microparticles are then delivered into the viable epidermis layer or upper layer of dermis by EPI. The sugar and polysaccharide matrices are water-soluble and will subsequently be dissolved in the tissue, and then antigen-loaded nanoparticles are released. The Langerhans cells (LCs) distributed in skin can recognise and process the antigens, and then migrate to lymph nodes via lymphatic vessels to induce immune response [6, 136].

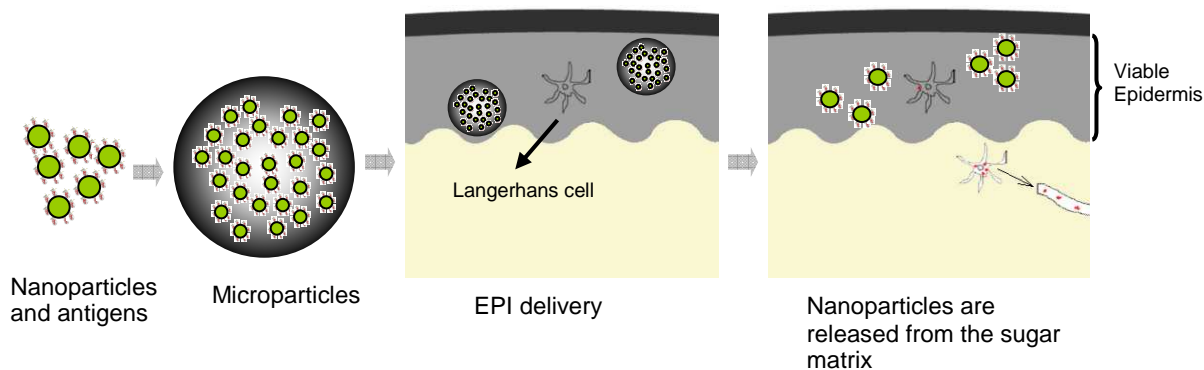


Figure III-1. Schematic diagram of the concept of nano-in-micro particles for epidermal powder immunisation. The green circles represent the nanoparticles and red dots represent antigens. The antigens can be absorbed on the surface of nanoparticles, or encapsulated inside nanoparticles. The antigen-loaded nanoparticles are then encapsulated in microparticles that can be delivered into skin by epidermal powder injection (EPI). The antigens and nanoparticles are released in the viable epidermis where the inherent Langerhans cells can recognise the antigens and process them. The Langerhans cells carrying the antigens migrate to the lymph node by the lymphatic vessels. Finally, a systemic immune response will be induced.

The strategies for encapsulating nanoparticles in microparticles depend on the properties of the nanoparticles and microparticles, and also the applications. Poly(epsilon-caprolactone) (PCL) microparticles containing gelatin nanoparticles have been prepared by emulsification and investigated for oral delivery [137, 138]. Poly(e-caprolactone) (PCL) nanoparticles with loaded hydrocortisone acetate (HA) were incorporated in PLGA microparticles by a double emulsion method [139]. The PCL nanoparticles were trapped on the layer close to the surface of the microparticles resulting in a hollow core [139]. Microgels (microparticles) containing nanoparticles were fabricated by a new Michael addition during (water-in-oil) emulsion (MADE) method, and they are suitable for intracellular delivery into the deep lung [140]. PLGA microparticles containing mesoporous silica nanoparticles have been prepared for the use of DNA prime-protein boost vaccination [112]. Dexamethasone acetate-loaded PLGA nanoparticles were encapsulated into microparticles by spray-drying of the mixture of the nanoparticles, 1,2-Dipalmitoyl-sn-Glycero-3-Phosphocholine (DPPC) and hyaluronic acid [141]. In our studies, spray-freeze-drying will be used to prepare nano-in-micro particles.

To my knowledge, nano-in-micro particles have been used for oral and lung delivery [137, 138, 140, 142, 143], but there are no reports on the application for EPI delivery. The particle

size for oral and lung delivery is usually smaller than 10 μm , which could be achieved by spray-drying. Spray-freeze-drying can produce larger sized particles around 10 - 50 μm as in our case here, even though the density may be reduced. In fact, the density can be improved by controlling the conditions for the freeze-drying step [132]. Furthermore, sugars could protect nanoparticles from aggregating during freeze-drying [144-147]. Sugar-based microparticles are suitably produced by spray-drying or SFD, while the SFD method is more suitable for formulating thermal-sensitive biological ingredients. The encapsulation of nanoparticles in sugar-based microparticles might be achieved by spraying the mixture of nanoparticles and the sugar-based matrix into a liquid nitrogen bath. The frozen microparticles encapsulating nanoparticles can be freeze-dried, and then nano-in-micro particles would be obtained.

The objectives of this chapter are to investigate the encapsulation of different nanoparticles in microparticulate formulations and to increase the density of microparticles by including dense materials in the formulation. Inorganic, polymeric and protein nanoparticles are going to be used, including mesoporous silica, poly(lactic-co-glycolic acid) (PLGA), recombinant silk, gelatin nanoparticles. Trehalose, mannitol, dextran (TMD) are used as the sugar-based matrix for microparticles. A spray-freeze-drying method will be used to manufacture the TMD microparticles encapsulating nanoparticles. The distribution of fluorescently labelled nanoparticles encapsulated in TMD microparticles will be observed by confocal laser scanning microscope (CLSM). To improve the density and robustness of TMD microparticles, dense inorganic materials have been added to the formulation.

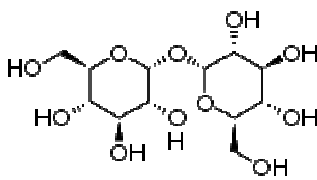
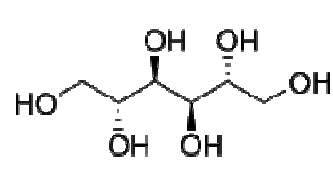
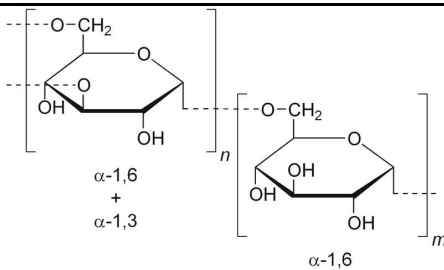
2. Materials and Methods

2.1 Materials

The copolymer poly(lactic-co-glycolic acid) (PLGA) (RESOMER RG 752S) was obtained from Evonik Industries AG (Darmstadt, Germany). Poly(vinyl alcohol) (PVA) (Mw 9000-10000, 80% hydrolyzed), tetraethyl orthosilicate (reagent grade, 98%) (TEOS), (3-aminopropyl)trimethoxysilane (97%) (APTMS), hexadecyltrimethylammonium bromide (BioUltra, $\geq 99\%$) (CTAB), fluorescein isothiocyanate (FITC), glutaraldehyde solution (25.0%), N-(3-dimethylaminopropyl)-N-ethylcarbodiimide hydrochloride (EDC), (2-aminoethyl)trimethylammonium (Cholamin) chloride hydrochloride (99%), gelatin, Type A (175 Bloom), dextran from *Leuconostoc mesenteroides* (average mol wt 9 000-11 000),

dextran from *Leuconostoc mesenteroides* (average mol wt 100 000), dextran from *Leuconostoc mesenteroides* (average mol wt 150 000) were purchased from Sigma-Aldrich Chemie GmbH (Steinheim, Germany). D(+) -trehalose dehydrate (for biochemistry) was purchased from VWR International (Darmstadt, Germany). Mannitol was obtained from Boehringer Ingelheim (Ingelheim, Germany).

Table III-1 Summary of the molecular structures of the sugar-based matrices

Trehalose	Mannitol	Dextran
		

Recombinant silk protein (eADF) was a gift from AMSilk GmbH (Munich, Germany). Fluorescent dye Alexa Fluor® 633 carboxylic acid, succinimidyl ester (ex.632/em.647) was purchased from Molecular Probes (Oregon, USA). Dimethyl sulfoxide (DMSO) was obtained from Gruessing GmbH (Wahrenholz, Germany). Monodispersed polystyrene nanoparticles labelled with Rhodamine B (PS-RhB) with a diameter of 167 nm and a PDI of 0.08 (2.5 w/v% suspension in water) was purchased from Microparticles GmbH (Berlin, Germany).

2.2 Methods

2.2.1 Preparation of fluorescent PLGA nanoparticles

Fluorescent dye was encapsulated into poly(lactic-co-glycolic acid) (PLGA) nanoparticles by a modified method from Sarti *et al.*[148]. 20 mg/ml of Rhodamine B isothiocyanate (RITC) in Dimethyl sulfoxide (DMSO) was prepared. 150 mg of PLGA (RESOMER RG 752S) was dissolved in 5.0 ml of dichloromethane (DCM). 50 μ l of the 20 mg/ml RITC was added into the PLGA solution, and then the mixture was added to 20.0 ml of PVA solution (1.0% w/v). The mixture was emulsified by sonicating for 90 s at an amplitude of 40% using the probe type MS 73 (Sonopuls HD 2200, Bandelin electronic, Berlin, Germany). Finally, it was stirred overnight to remove DCM. The PLGA-RITC nanoparticles were obtained by centrifugation at 12000 rpm for 10 min (Sigma 4K15 centrifuge, SIGMA Laboratory Centrifuges, Shropshire, UK) and washed three times with highly purified water (HPW). The suspension of

nanoparticles was obtained by resuspending them in 8.0 ml of HPW water. A microbalance (METTLER TOLEDO, Giessen, Germany) was used to determine the particle concentration. 0.050 ml of the suspension was added to an aluminium 100 DSC crucible (NETZSCH, Selb, Germany) and dried at 40 °C overnight. The dried weight of added suspension was calculated from the empty crucible weight and the weight of the crucible with dry particles.

2.2.2 Preparation of fluorescent gelatin nanoparticles

The method for preparing gelatin nanoparticles has been developed previously [149, 150]. 1.25 g of gelatin (Type A) was dissolved in 23.75 g of sterile HPW water under stirring at 500 rpm at 50 °C. 25 ml of acetone was added quickly (within 1 min) to the gelatin solution. 20 s later, the supernatant was removed, and then the rest inside the 250-ml flask was weighed. Sterile HPW water was added to the flask until the total amount reached to 25.0 g. The gelatin inside the flask was dissolved again at 50 °C under stirring. The pH was adjusted to 7.0-8.0 using 1 M NaOH. 50 µl of Alexa Fluor® 633 was added into the solution and the mixture was stirred for 2h at room temperature (RT). After that, the gelatin solution was heated to 50 °C under stirring, and then the pH was adjusted to 2.5 - 3.0. The gelatin solution was incubated at 50 °C for a while, and then 50-75 ml acetone was added slowly (3 - 5 ml/min) in while stirring at 500-700 rpm. After 15 min, 175 µl of glutaraldehyde (25.0%) was added to crosslink the nanoparticles. The suspension was stirred overnight to remove acetone.

The obtained gelatin nanoparticles (GNP) suspension was transfer to a 15-ml falcon tube and centrifuged at 17,500×g for 15 min. The obtained particles were resuspended in 10 ml of sterile HPW by shaking or pipetting. The washing step was repeated three times. Finally, the particles were resuspended in 1-2 ml of sterile HPW to obtain the suspension of plain GNP nanoparticles. A microbalance (METTLER TOLEDO, Giessen, Germany) was used to determine the particle concentration. 0.050 ml of the suspension was added to an aluminium 100 DSC crucible (NETZSCH, Selb, Germany) and dried at 40 °C overnight. The dried weight of added suspension was calculated from the empty crucible weight and the weight of the crucible with dry particles.

In order to prepare cationic GNP nanoparticles, the dispersion of plain GNP particles was diluted with 20 ml of sterile HPW water. The pH was adjusted to 4.5-5.0 before adding 50 mg of cholamin under constant stirring. 50 mg of N-(3-dimethylaminopropyl)-N-ethylcarbodiimide hydrochloride (EDC) was added when cholamin was totally dissolved. The

mixture was stirred at RT at 500 rpm for 30 min. The particles were obtained by using the same process as above. 1.0 ml of sterile HPW was added to resuspend the cationic GNP nanoparticles. The dispersion was filtered with a 1.2 μ m syringe filter (Sartorius Stedim Biotech S.A., Aubagne, France) to obtain the final product of cationic GNP nanoparticles. A microbalance was used to determine the particle concentration.

2.2.3 Preparation of fluorescent spider silk nanoparticles

The recombinant spider silk protein eADF4 (C16) comprising 16 repeats of GSSAAAAAAAASGPGGYGPENQGPGSGPGGYGPGGP ($M_w = 47.7$ kDa) was provided by Prof. Dr. Thomas Scheibel, University of Bayreuth. The eADF4 powder was dissolved in 6 M guanidinium thiocyanate first and then the solution was dialysed in tris(hydroxymethyl)aminomethane/HEPES buffer (20 mM, pH 8.0) using tube membranes with a molecular weight cut-off of 6000-8000 Da (Spectrum Laboratories Inc., Rancho Dominguez, USA). 5 mg/ml of fluorescein isothiocyanate (FITC) in DMSO was prepared, 653 μ l of which was added into 10 ml of 2 mg/ml eADF4 in HEPES buffer (20 mM, pH 8.0). The solution was incubated for 1h at RT in the dark. FITC labelled eADF (eADF-FITC) in solution was obtained by dialysis against HEPES buffer at 4 °C overnight to remove the excess FITC.

The particle preparation was carried out using the method by Hofer *et al.* [151]. Briefly, eADF in Tris buffer and eADF-FITC in Hepes buffer were mixed together with a mass ratio of 3/1. A micromixing system (model 100 DX, Teledyne Isco Inc., USA) consisting of two channels was used to mix the silk protein solution and potassium phosphate buffer (2 M, pH 8.0). The precipitated silk particles were collected by centrifugation (7500 g for 10 min and 12 500 g for 15 min). The particles were washed three times with HPW. The dispersion of resuspended particles in HPW was sonicated for a maximum of 15 min (cycle 6, amplitude 50%) using a probe sonifier (SonoPuls HD 2200, Badelin electronic, Berlin, Germany) and filtered using a 5 μ m syringe filter (Sartorius Stedim Biotech S.A., Aubagne, France). A microbalance was used to determine the particle concentration.

2.2.4 Preparation of fluorescent silica nanoparticles

The synthesis method of mesoporous silica nanoparticles (MSNP) was modified from Xia *et al.* [152]. Briefly, 27.5 mg of FITC was dissolved in 18 ml of absolute ethanol and then 0.100 ml of APTMS was added. The APTMS-FITC mixture was stirred for 24 h at room

temperature in dark. 1.60 g of CTAB was dissolved in a mixture of 11.20 ml of 1 mol/l NaOH aqueous solution and 768 ml of deionised (DI) water under stirring. The temperature of the solution was increased to 80 °C in 30 min. 8.00 ml of TEOS was added dropwise while stirring at 700 rpm, and then 8.0 ml of the prepared APTMS-FITC mixture was added. After 2 h stirring, fluorescein 5(6)-isothiocyanate (FITC) labelled silica nanoparticles (FITC-MSNP) were obtained by centrifugation and washed with ethanol once. In order to remove CTAB, fresh prepared silica nanoparticles FITC-MSNP were refluxed overnight in 160 ml of ethanol containing 8 ml of 37% (w/v) HCl aqueous solution and then washed with adequate water and ethanol. The surfactant extracting process was repeated once. Finally, the nanoparticles were dried overnight at 20 °C in a vacuum dryer.

2.2.5 Preparation of microparticles encapsulating different nanoparticles

Trehalose, mannitol, dextran (10 kDa) and dextran (100 kDa) or dextran (150kDa) (TMD) were mixed with a weight ratio of 3:3:3:1, and were then dissolved in sodium phosphate buffer (PB) (10 mM, pH 7.4) under stirring to obtain 35 wt% sugar-based solutions. The TMD solution was filtered with a 0.2 µm syringe filter (VWR, Darmstadt, Germany) before use. Each kind of nanoparticles was added into the formulation of the TMD matrix according to **Table III-2**. The mixtures were shaken occasionally by hand. The solid content of nanoparticles in microparticles is 3-4 µg/mg, which was calculated on the basis of the dry mass of sugar matrices.

Table III-2 Formulations of microparticles encapsulating nanoparticles

Sample	TMD 35%(w/w) solution (g)	Nanoparticle concentration (mg/ml)	Nanoparticle volume (µl)	Particle content (µg/mg)
TMD/PS-Rhd	1.0	25	50	3.6
TMD/PLGA-Rhd	1.0	15	100	4.3
TMD/MSNP-FITC	2.0	50	50	3.6
TMD/GNP-Alexa(-)	1.0	19	63	3.4
TMD/GNP-Alexa(+)	1.0	18	66	3.4
TMD/silk-FITC	2.0	15	168	3.6

The prepared formulations of TMD and nanoparticles were sprayed into liquid nitrogen by an ultrasonic atomizing nozzle (120 kHz, Sono-Tek, Milton, USA). The power for spraying was set to 4.0-4.5 watts and the flow rate of a peristaltic pump (IsmaTec IPC 78001-20, Wertheim, Germany) to 0.6 ml/min. The custom-made set-up for spray-freezing is shown in **Figure III-2**.

The sprayed microparticles were collected in vials and transferred to a pre-cooled lyophilizer (Martin Christ EPSILON 2-6D, Harz, Germany). The freeze-drying sequence was carried out by 24 h of primary drying at -10 °C and 20 h of secondary drying at 25 °C. The chamber pressure was kept at 0.12 mbar during the whole drying process.

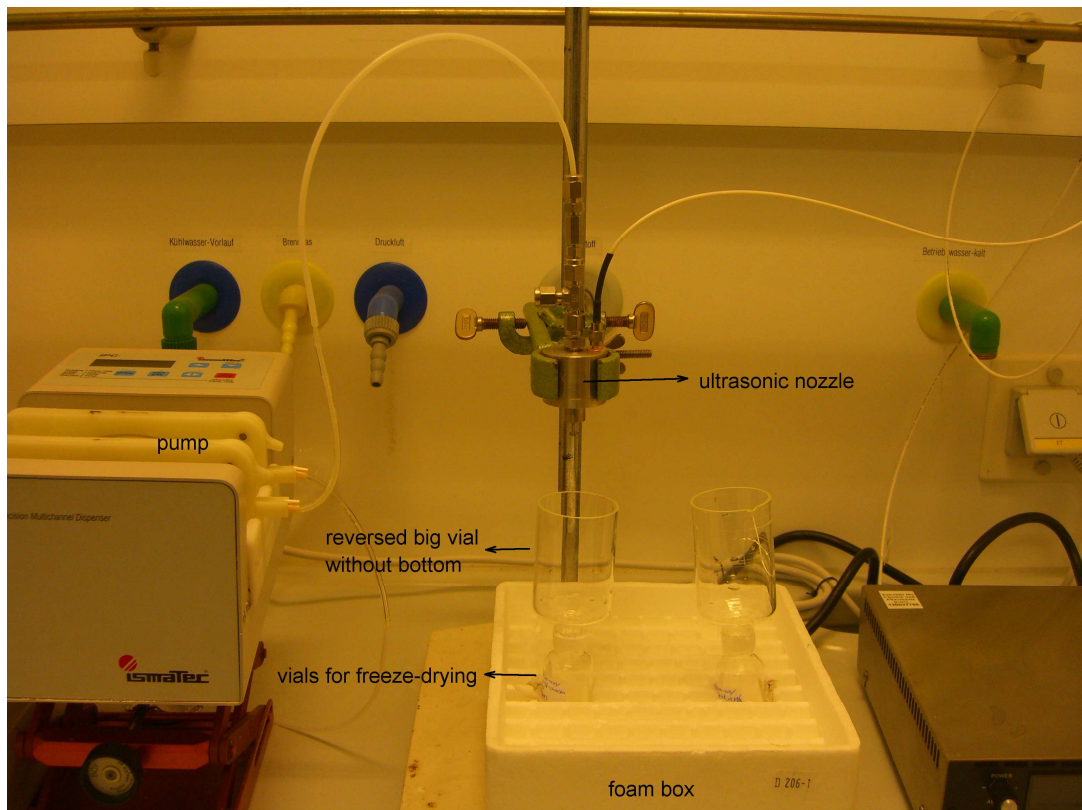


Figure III-2. Set-up of a spray-freezing system. A peristaltic pump is used to feed the solution for spraying. The vial for freeze-drying and the reversed big vial without bottom are connected by a Teflon tape and adhesive plastic film. Liquid nitrogen is filled into the white foam box and the vials. The ultrasonic nozzle (120 kHz) sprays the solution into the special vial. Atomized liquid drops are frozen quickly as they meet liquid nitrogen. The frozen particles are collected in the small vials. The upper part of the vial is removed and then the small vial containing frozen particles is freeze-dried subsequently.

2.2.6 Microscopic examination of microparticles

Confocal Laser Scanning Microscopy (CLSM)

A confocal Laser Scanning Microscope (LSM 510 META, Carl ZEISS, Germany) was used to observe the microparticles encapsulating fluorescent nanoparticles. Argon laser (488 nm) and HeNe laser (543 nm) were used as excitation wavelengths, corresponding the emissions of BP 505-530 nm and LP 560 nm, respectively. Different objectives were used, including

Plan-Neofluar 40 \times /1.3 Oil, Plan-Apochromal 63 \times /1.4 Oil DIC and Plan-Neofluar 100 \times /1.3 Oil Ph3. Z-stacking mode was used to observe the distribution of nanoparticles in the microparticles.

Scanning electron microscopy (SEM)

Microparticles were placed on Leit adhesive carbon tabs (Plano GmbH, Wetzlar, Germany) and then coated with a thin layer of carbon before observed under a JEOL JSM-6500F scanning electron microscope (SEM) (Joel Inc., Peabody, USA). Samples were viewed at a magnification of 300.

2.2.7 Measurements of hydrodynamic diameter and zeta-potential

The hydrodynamic diameter and zeta-potential of nanoparticles were determined using a Zetasizer Nano ZS (Malvern Instruments, Herrenberg, Germany). The reflective index (RI) of all nanoparticles used for the size measurement was 1.59. The dispersant phase is water with RI of 1.330 and viscosity of 0.8872 cP. The particle concentration was kept around 0.05 mg/ml for dynamic light scattering (DLS) measurements.

2.2.8 Cellular uptake of nanoparticles by macrophage cells

A macrophage cell line J774.A1 with a concentration of 7 \times 10⁵ cells/ml in Dulbecco's modified eagle's serum with 10% Fetal Bovine Serum (FBS) was used. 300 μ l of the cell suspension was added to each well of 8-well ibidi μ -sildes (ibidi, Martinsried, Germany) and incubated at 37 °C for 4 hours prior to particle treatment. 20 μ l of a 0.25 mg/ml of nanoparticles suspension was added in duplicates, homogenized and incubated for 30 min in the dark. After that, the wells containing cells were carefully washed with PBS to remove the excessive particles. The cells were fixed by 4% paraformaldehyde and stained by bisBenzimide H 33342 trihydrochloride. The resultant samples were observed by Confocal Laser Scanning Microscope LSM 510 META (Carl ZEISS, Göttingen, Germany) as described above.

2.2.9 Tap density of the microparticles

Tap density was measured by using a small custom-made cylinder with a volume of 1.5 ml. About 0.5 g of powder was added into the cylinder, and then it was tapped for 1000 times using a Stampfvolumeter (JEL STAV, 2003 model, Engelsmann AG, Ludwigshafen, Germany). The volume after tapping and the mass were used to calculate tap density.

2.2.10 Measurements of the mechanical properties of freeze-dried matrix cakes by a texture analyser

A texture analyser TA.XTPlus from EXPONENT Stable Micro Systems Ltd. (Godalming, Surrey GU7 1YL, UK) (**Figure III-3**) was used to measure the force versus indentation distance curve. A custom-made steel cylinder probe was used for the measurement of indentation behaviour. The indentation speed for all the tests was set to 0.5 mm/s. The maximal force in the puncture tests was about 60 N.

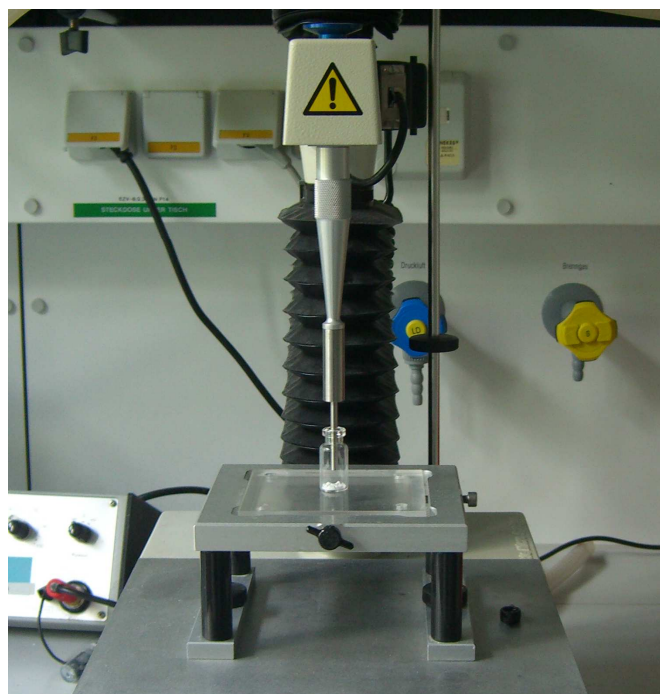


Figure III-3. The set-up of a texture analyser for the measurements of freeze-dried cakes.

3. Results

3.1 Encapsulation of nanoparticles in microparticles

3.1.1 Nanoparticles for the encapsulation in the sugar-based microparticles

Several kinds of nanoparticles (NPs) made of polystyrene (PS), poly(lactic-co-glycolic acid) (PLGA), gelatin (GNP), recombinant spider silk were prepared. **Table III-3** shows the sizes and surface properties of the nanoparticles measured by dynamic light scattering (DLS). The polymer nanoparticles have very narrow particle size distributions as the PDI is low than 0.1. The zeta-potential of PS nanoparticles is -70.6 mv in PB (10 mM, pH 7.4), indicating a negatively charged surface. PLGA nanoparticles in the PB buffer shows a zeta-potential of -1.8 mv. Gelatin nanoparticles with positive (ZP = 6.5 mv) and negative (ZP = -3.1 mv)

surfaces have a similar size of about 300 nm. As another protein particle, silk NPs have a Z-average size (Z-Ave) of 334.9 and a PDI of 0.154. The negative ZP (-26 mv) indicates a negative surface of silk NPs in the PB buffer.

Table III-3 Sizes and zeta-potentials (ZPs) of different nanoparticles

Sample	Chemical structure	Z-Ave (d.nm)	PDI	ZP (mv)
PLGA NPs		216	0.072	-1.8
PS NPs		155	0.016	-70.6
Cationic GNP	protein	295	0.276	6.5
Plain GNP	protein	300	0.269	-3.1
Silk NPs	protein	335	0.154	-26.0

The nanoparticles were suspended in PB (10 mM, pH 7.4) at a concentration of 0.1 - 0.2 mg/ml.

These nanoparticles made of different materials have a size range from 150 nm to 350 nm. The surface properties of the nanoparticles are different. They were used as model particles for investigating the encapsulation of nanoparticles in the sugar-base microparticles by spray-freeze-drying.

3.1.2 Distribution of different nanoparticles in the sugar-based microparticles.

These nanoparticles were used in the sugar-based microparticles to study the encapsulation of nano-sized particles into micro-sized particles (nano-in-micro). The nanoparticles in aqueous suspension were added to the TMD solution (35 wt%). The mixture was mixed thoroughly before spray-freeze-drying. In order to observe the nanoparticles in microparticles using CLSM, all nanoparticles were fluorescently labelled.

TMD microparticles without nanoparticles inside were prepared as a control. FITC labelled dextran (Dextran-FITC) was used in the formulation at a content of 1 wt% of the solid microparticles. As shown in **Figure III-4**, the microparticles can be well visualised by labelling the matrix. **Figure III-4A** shows a single scan of CLSM, while Z-stacking micrographs are shown as the 3D view in **Figure III-4B** and gallery model in **Figure III-4C**.

One of the advantages of CLSM is the optical slicing by focusing on a specific layer. The green fluorescence is distinctly strong when the surface of the microparticles was illuminated. There are two particles in **Figure III-4A** showing green circles and black centres. Dextran-FITC could be on the surface or in the matrix.

The different intensities on the single scan layer of one particle can be contributed to the point-by-point scanning of CLSM. The matrices of the microparticles are non-transparent materials which can decrease the intensity of fluorescence transmitting through them [153]. When the middle layer of microparticles is observed under CLSM, the edge is brighter because it is more close to surface and the centre shows less intensity because the light needs to pass the matrixes causing some loss of the intensity. This can explain the observation of microparticles with a green circle and black centre in **Figure III-4A**. Furthermore, the rough surface can also lead to heterogeneous appearance of an optical layer of CLSM observation.

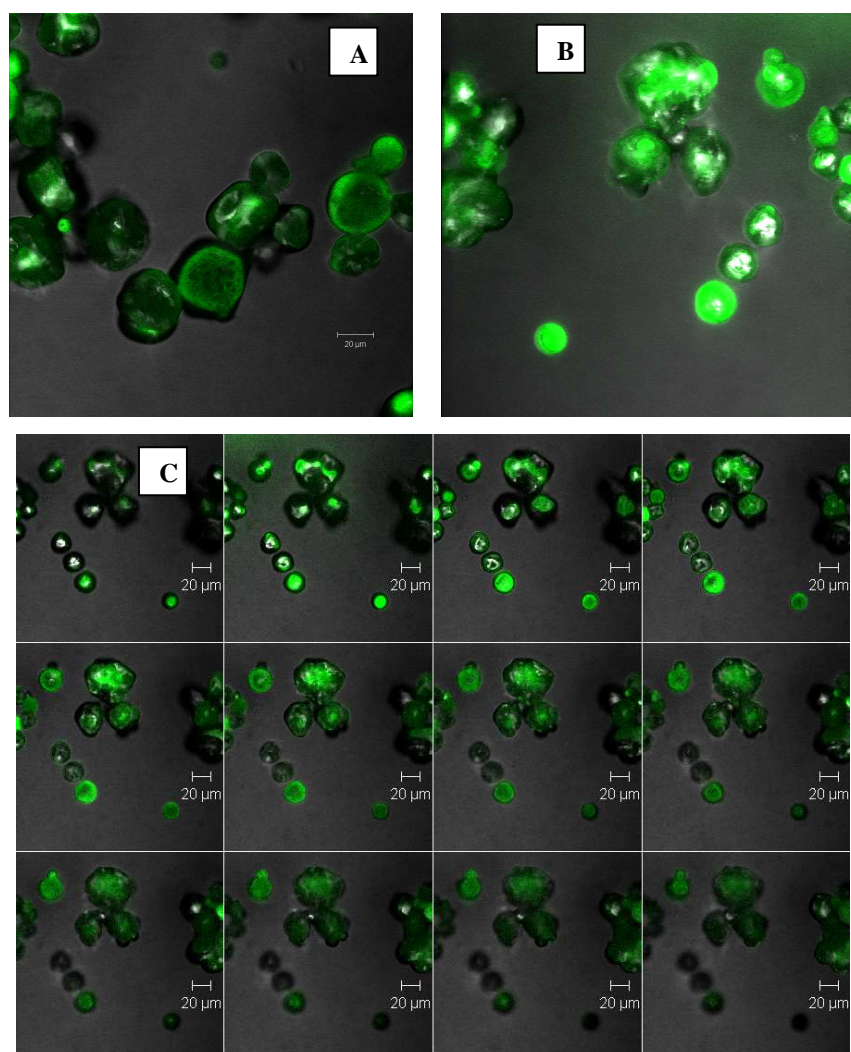


Figure III-4. TMD/FITC-Dextran microparticles. (A) Single scan micrograph; (B) 3D micrograph produced from Z-stacking scan; (C) Gallery displaying Z-stacking micrographs.

The microparticles containing PS nanoparticles have a size of 10-40 μm in diameter and a wrinkled surface as shown in the SEM micrograph (**Figure III-5A**). PS-RhB nanoparticles (**Figure III-5**) were observed and the fluorescent microparticles indicate that the PS (167 nm in diameter) nanoparticles can be encapsulated very well. With CLSM micrograph of microparticles containing only Dextran-FITC (**Figure III-4**), brighter edge of each particle was observed at both magnifications (40 \times and 63 \times). This does not mean that PS-RhB nanoparticles are just located on the layer close to surface. As explained above, this phenomenon results from the decrease of light after transmitting the middle part of the microparticle. The wrinkles on the surface of the microparticles are very bright in the 3D view of Z-stacking micrographs (**Figure III-5D**), indicating a morphology consistent with the SEM micrograph.

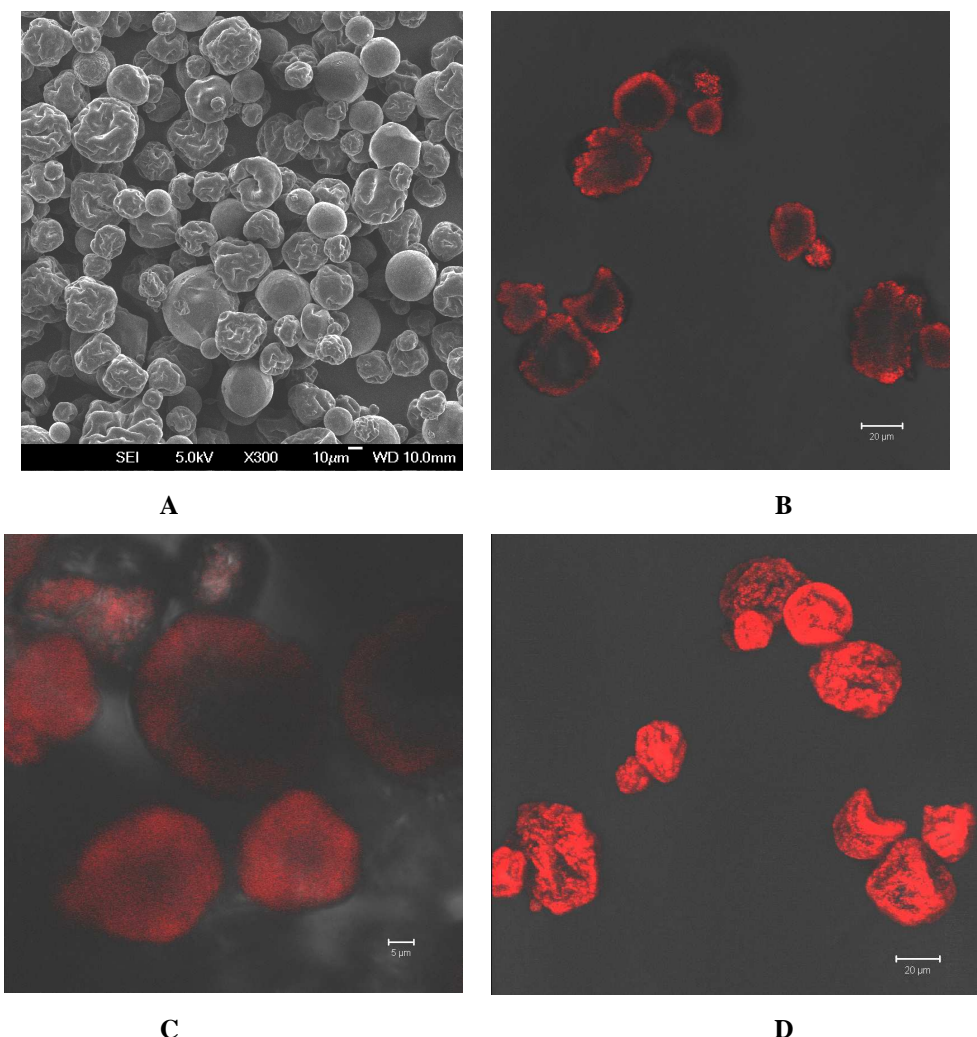


Figure III-5. Sugar-based microparticles containing PS-RhB nanoparticles. (A) SEM micrograph; (B) CLSM micrograph with a magnification of 40 \times ; (C) CLSM micrograph with a magnification of 63 \times ; (D) 3D view produced from z-stacking micrographs.

PLGA nanoparticles (216 nm in diameter) are encapsulated in the microparticles as shown in **Figure III-6**. The surface of the microparticles containing PLGA-RITC nanoparticles is very bright. The PLGA nanoparticles are distributed in the whole particles as indicated by the homogeneous distribution of fluorescence.

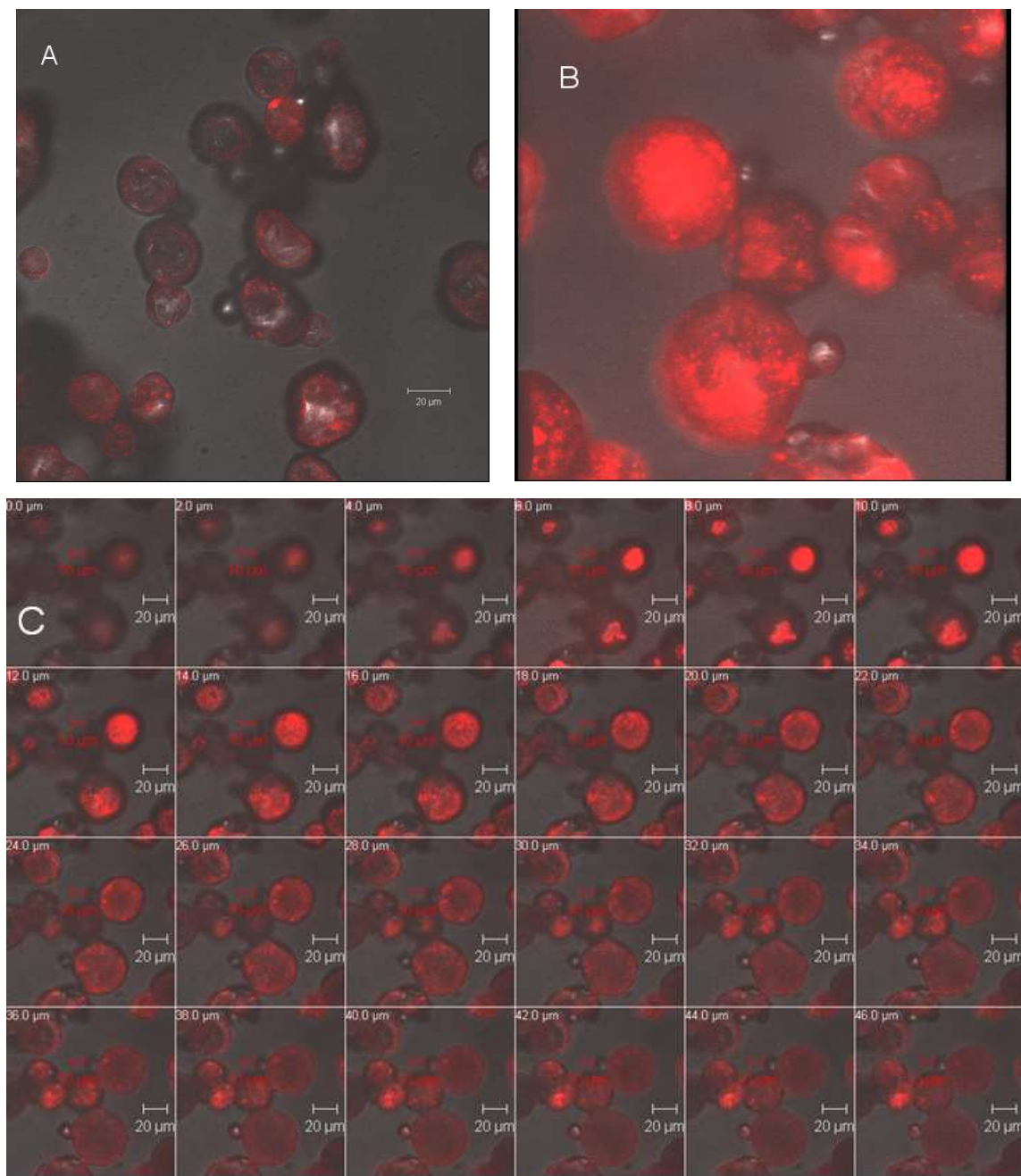


Figure III-6. CLSM micrographs of TMD microparticles containing PLGA-RITC nanoparticles. (A) Single scan micrograph; (B) 3D micrograph produced from Z-stacking scan; (C) gallery displaying of Z-stacking micrographs.

In the case of silica nanoparticles (MSNP-FITC) with a size of ~130 nm, the distribution is not as homogeneous as for PS and PLGA. There are some bright spots in the area of microparticles as shown in **Figure III-7B**. However, the silica nanoparticles are still distributed in the whole space as can be observed in **Figure III-7C**. The 3D view shows green spots everywhere in the microparticles. Therefore, silica nanoparticles can also be encapsulated in the TMD microparticles.

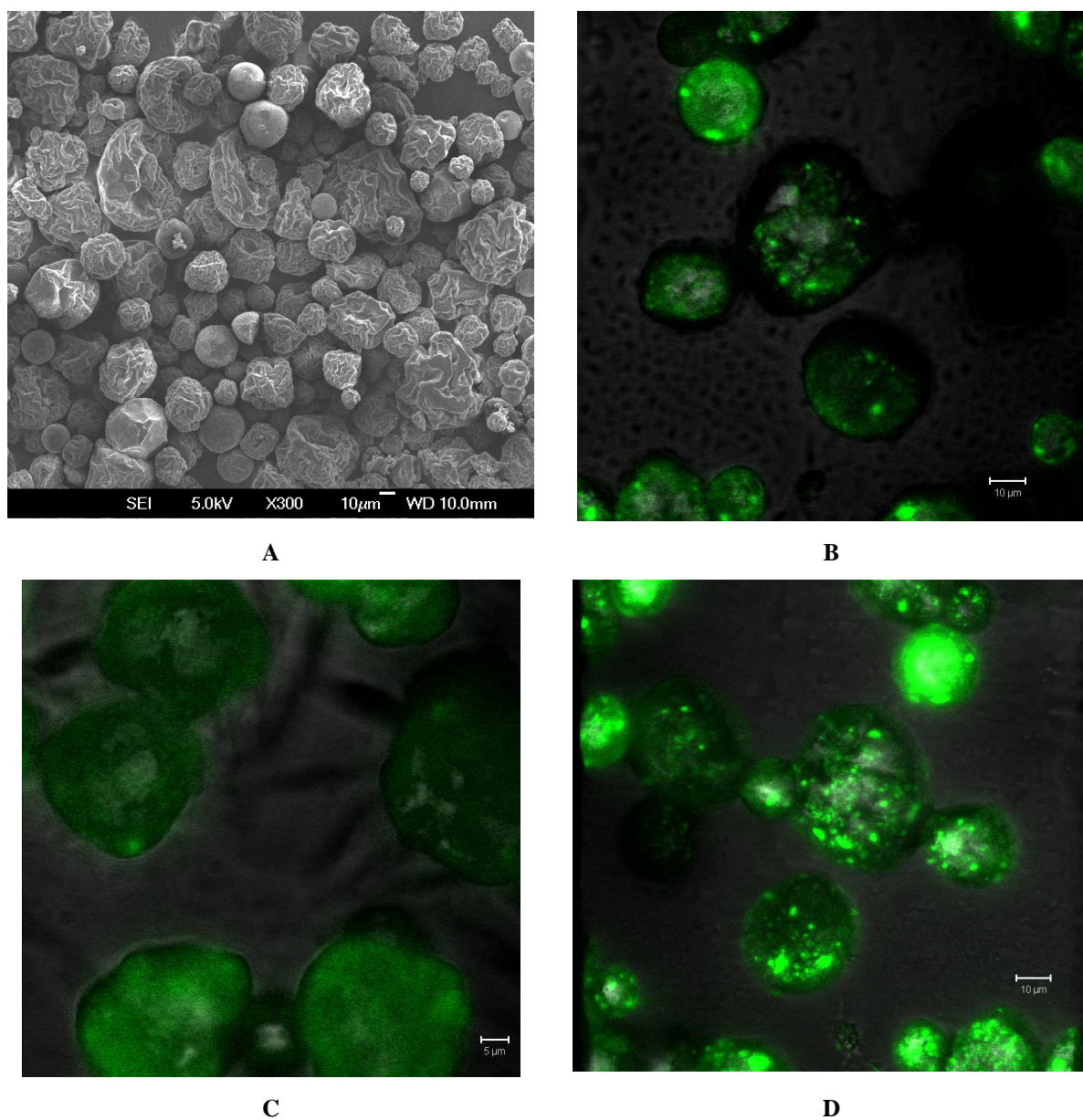


Figure III-7. Sugar-based microparticles containing MSNP-FITC nanoparticles. **(A)** SEM micrograph; **(B)** CLSM micrograph with an objective of Plan-Apochromal 63 \times /1.4 Oil DIC; **(C)** CLSM micrograph with an objective of Plan-Neofluar 100 \times /1.3 Oil Ph3; **(D)** 3D view produced from z-stacking micrographs.

Until now, we have successfully encapsulated polymer and inorganic nanoparticles in the sugar-based microparticles. It is also interesting to investigate whether protein-based nanoparticles can be encapsulated in the microparticles using this method. Considering the availability in our group, gelatin nanoparticles and recombinant spider silk nanoparticles were used. Plain gelatin nanoparticles (GNP(-)) have a negative surface, which can be cationized to a positively charged surface (GNP(+)). Both have been encapsulated in the TMD microparticles. As shown in **Figure III-8**, GNP(-) are distributed evenly and the 3D view micrograph displays many wrinkles on the particle surface. The distribution of GNP(+) was not as good as that of GNP(-). Although red GNP(+) can be seen in the microparticles, the surface morphology is not well resolved as for GNP(-).

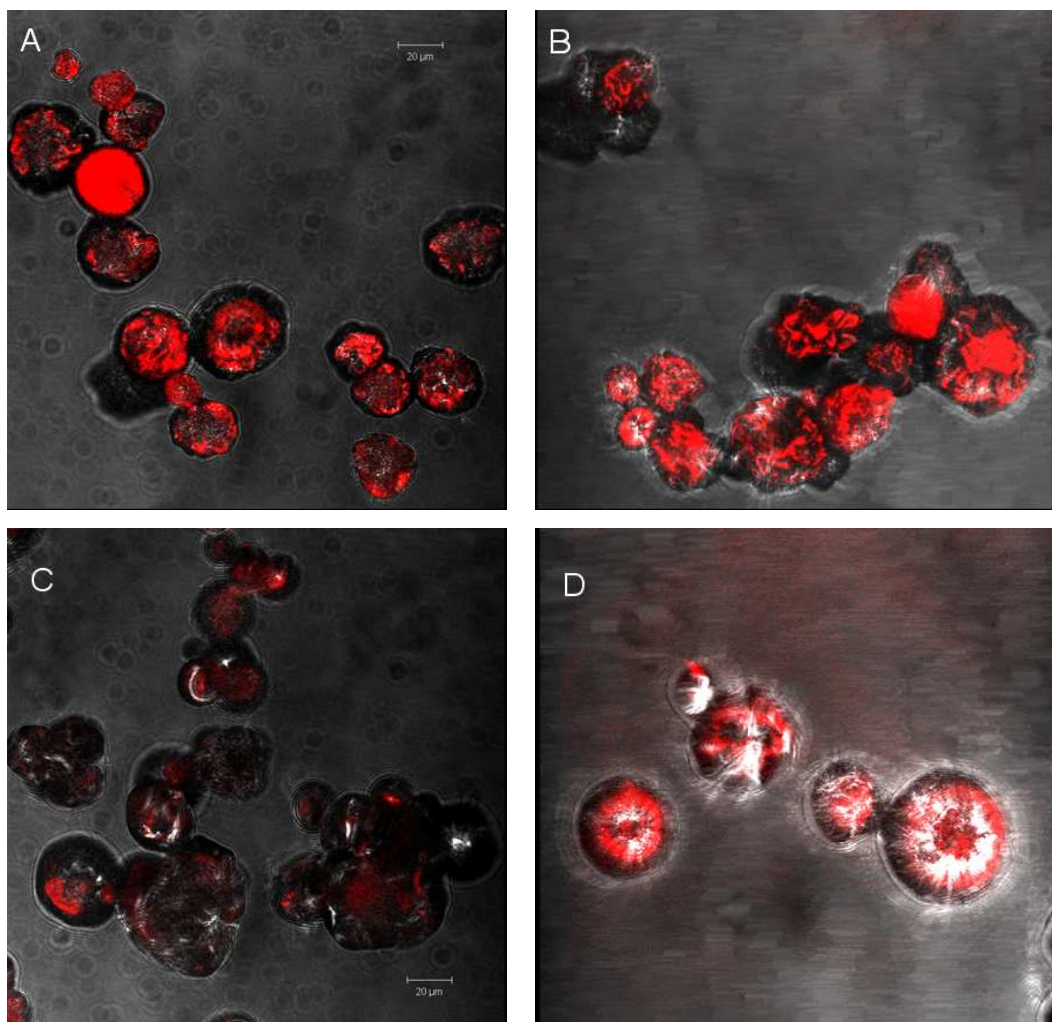


Figure III-8. SEM micrographs of microparticles containing gelatin nanoparticles. **(A, B)** Plain gelatin nanoparticles (negative surface); **(C, D)** Cationic gelatin nanoparticles (positive surface). **A** and **C** are single scan micrographs, while **B** and **D** are 3D micrographs produced from Z-stack scanning.

FITC-labelled recombinant spider silk nanoparticles were distributed in TMD microparticles as green fluorescence can be observed allover the microparticles. Micrographs with different magnifications (10 \times , 40 \times , 63 \times) were scanned (**Figure III-9**). The silk nanoparticles are obviously encapsulated in all microparticles. The 3D view was obtained by processing the Z-stacking micrographs with projections, confirming the spatial distribution of the silk nanoparticles in microparticles.

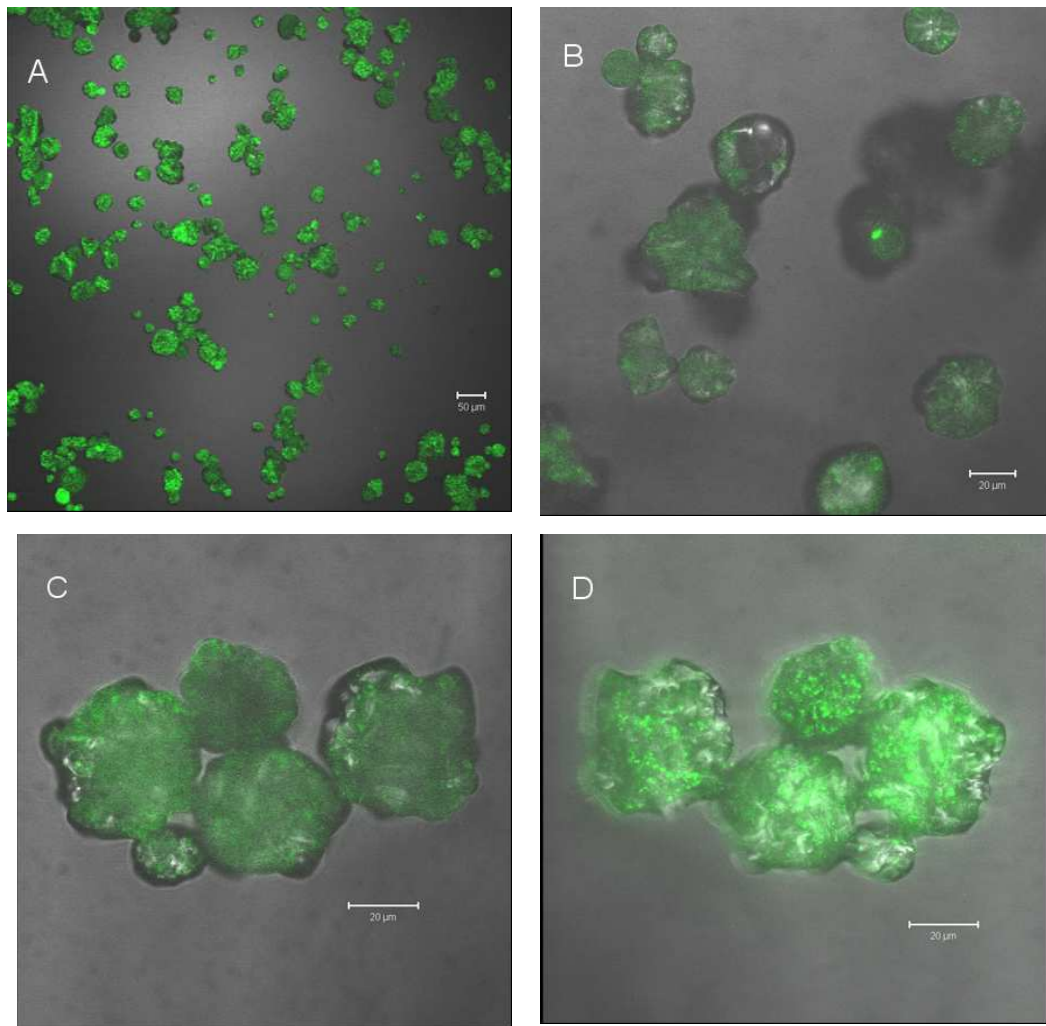


Figure III-9. TMD microparticles silk-FITC at magnifications of 10 \times (**A**), 40 \times (**B**) and 63 \times (**C**). 3D view (**D**) was produced from Z-stacking scan.

All the nanoparticles we have used in the formulations have been successfully encapsulated in microparticles fabricated by spray-freeze-drying. The mixing of the nanoparticles and sugar-based matrix was done by occasional hand-shaking. Furthermore, labelled nanoparticles and labelled dextran were both added into the formulation, in order to distinguish the matrix and nanoparticles. As shown in **Figure III-10**, nanoparticles (red) and matrix (green) appear

together and also overlap to each other to produce a yellow area. The 3D photos of the microparticles are vivid and a cave under the surface has been visualised (**Figure III-10B**).

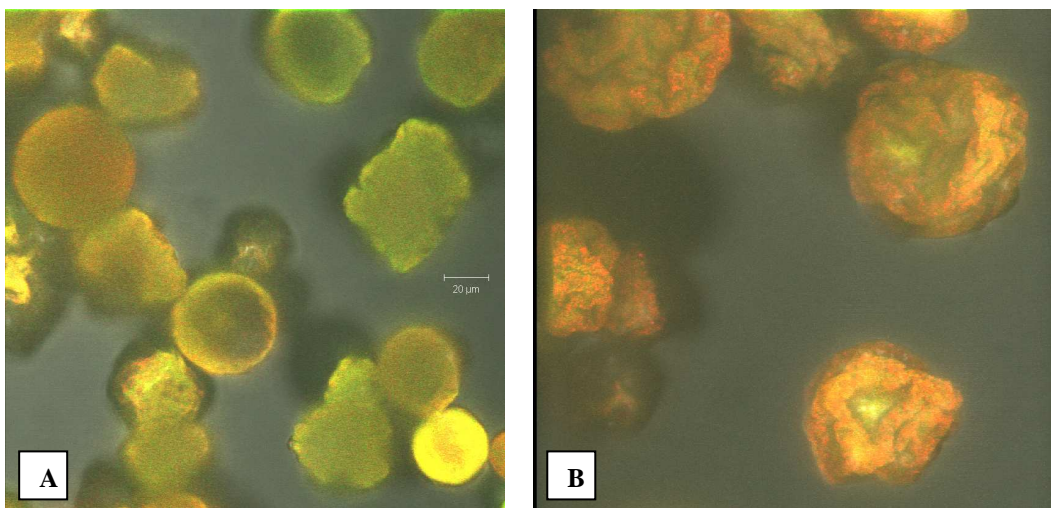


Figure III-10. TMD/FITC-Dextran/PS-Rhd microparticles. 3 $\mu\text{g}/\text{mg}$ of FITC-Dextran and 3.6 $\mu\text{g}/\text{mg}$ of PS-Rhd nanoparticles in the microparticles. **(A)** Single scan micrograph; **(B)** 3D view was produced from Z-stacking scan.

3.2 Stability of nanoparticles in TMD microparticles

Size is an important parameter when nanoparticles are used in a drug formulation. It is necessary to investigate the colloidal stability of the nanoparticles encapsulated in the TMD formulation. 15 mg of the microparticles containing different kinds of nanoparticles were redissolved in 1 ml of PB (10 mM, pH 7.4). The size and zeta-potential were then measured.

Table III-4. Sizes and zeta-potentials of nanoparticles before and after being formulated in microparticles ($n = 3$)

sample	Before formulation			After formulation in microparticles		
	Z-Ave (d.nm)	PDI	ZP (mv)	Z-Ave (d.nm)	PDI	ZP (mv)
PLGA NPs	216	0.072	-1.8	263	0.269	-3.5
PS NPs	155	0.016	-70.6	173	0.030	-45.1
Cationized GNP	295	0.276	6.5	1162	0.818	-5.5
Plain GNP	300	0.269	-3.1	687	0.718	-7.7
Silk NPs	335	0.154	-26.0	550	0.423	-23.7

The sizes of the nanoparticles before being formulated in TMD matrix and those resuspended after formulated in TMD microparticles are shown in **Table III-4**. The PS nanoparticles are the most stable ones, showing a size of 155 nm and PDI of 0.016 before formulating and a size of 173 nm and PDI of 0.030 after formulated in microparticles. PLGA nanoparticles have a size of 216 nm and PDI of 0.072, while the size increases to 262 nm and PDI to 0.269. Two kinds of dextran with molecular weight of about 10 kDa and 100 kDa are in the formulations. The dextran may increase the size in a small degree when adsorbed to the nanoparticles, as in the cases of PLGA and PS nanoparticles. Both plain GNP and cationized GNP have a size around 300 nm and PDI around 0.27 before added into the matrix, but the size and PDI increase distinctly in the resuspended suspension of microparticles. Recombinant silk nanoparticles are moderately stabilised in the microparticles as the size and PDI increases slightly, from 335 nm and 0.154 to 550 nm and 0.423, respectively. The zeta-potentials of all nanoparticles except cationic GNP were negative but absolute values changed at different levels.

3.3 Cellular uptake of nanoparticles

Cell penetration properties of nanoparticles determine the usability as a vaccine delivery system. As a general investigation, we applied the formulations containing PS-Rhd, PLGA-RITC, MSNP-FITC, plain GNP and cationic GNP to macrophage cells. This is basically used to study the properties of the nanoparticles as systems for intracellular drug delivery. The fluorescently-labeled nanoparticles can be observed near the nuclei area stained as blue if they are successfully delivered into cells. Strong fluorescence of nanoparticles observed in cells indicate good cellular uptake of the nanoparticles into the cells.

Figure III-11 shows CLSM results of macrophages respectively treated with the labeled nanoparticles and sodium phosphate buffer as a negative control. The same settings for obtaining the micrographs were used to ensure that fluorescence intensity represents the concentration of delivered nanoparticle. PS-Rhd nanoparticles cannot penetrate into the macrophage cells within 30 min (**Figure III-11A**), because the reddish background is similar to the negative control, indicating no sufficient amount of PS-RhD in the cells. On the contrary, PLGA-RITC nanoparticles penetrate very well (**Figure III-11B**), as red dots (particles) were obviously observed in macrophages. The green color around the blue nuclei (**Figure III-11C**) indicates that MSNP-FITC nanoparticles were taken up by the cells. Plain and cationic gelatin nanoparticles can also be delivered into the cells as some particles appear

around the blue cell nuclei (**Figure III-11 D** and **E**). More cationic gelatin nanoparticles were observed in macrophages than the plain gelatin nanoparticles. As a negative control, the phosphate buffer was added to the macrophage cells. Only blue cell nuclei can be observed for the negative control (**Figure III-11F**).

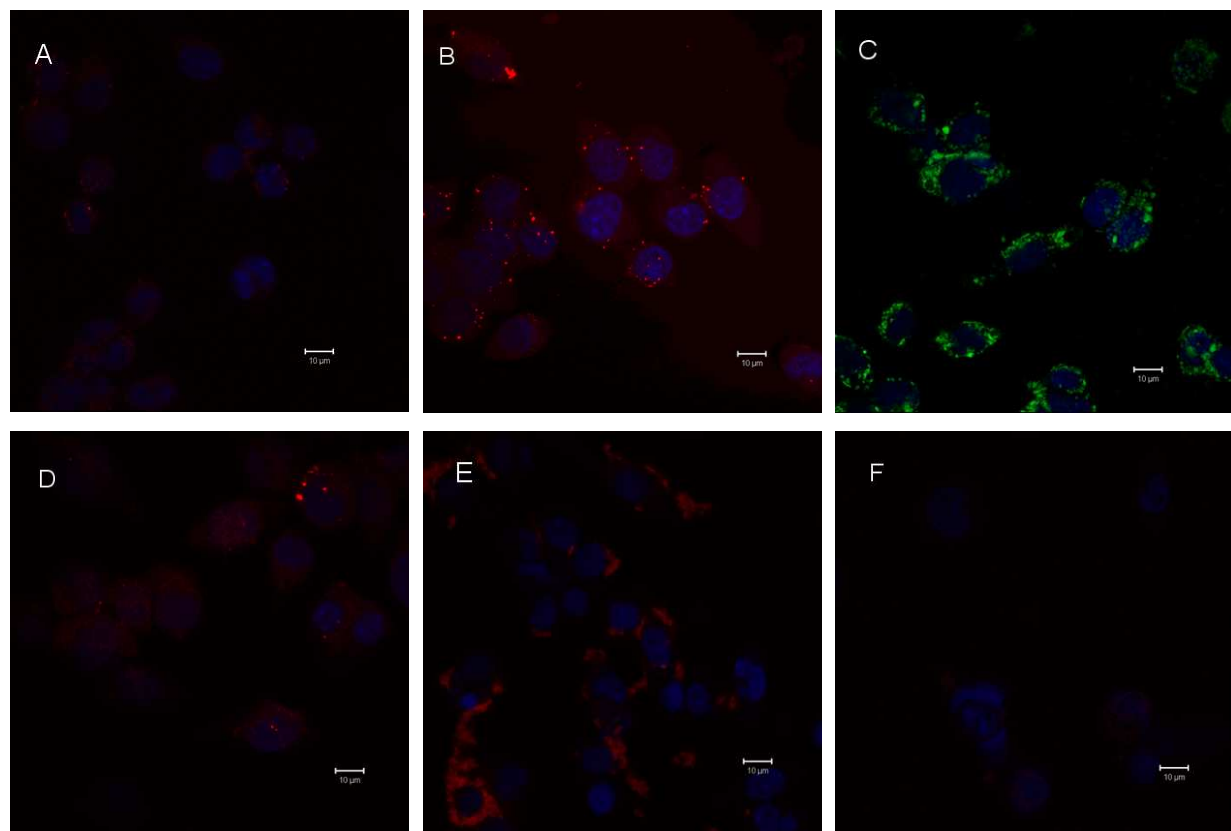


Figure III-11. CLSM results of macrophage cells incubated in different substances. **(A)** PS-Rhd (TMD matrix); **(B)** PLGA-Rhd nanoparticles (TMD matrix); **(C)** FITC-MSNP-NH2 (TMD matrix); **(D)** plain gelatin nanoparticles (negatively charged) (TMD matrix); **(E)** cationic gelatin nanoparticles (TMD matrix); **(F)** negative control. The scale bar is 10 μ m.

3.4 Enhancement of the density of microparticles by dense materials.

Normally, sugar-based particles prepared by spray-freeze-drying have a low density due to the high porosity. The density can be improved by increasing the solid content of the solution for spraying and controlling the shrinkage during the freeze-drying step. 35 wt% of matrix solution was used in our experiments. It is limited by the solubility of sugar and polysaccharides and the viscosity increases. Another way to improve the density could be achieved by adding dense materials in the formulation. Considering the biocompatibility of calcium carbonate (CaCO_3), it was used in the formulations of microparticles. Different amounts of CaCO_3 were added as shown in **Table III-5**. In the formulation of TMD (100

kDa), the tap density was increased from 670 to 831 kg/m³ when the weight ratio of TMD and CaCO₃ comes to 2.5/1. For the case of TMD (150 kDa), the tap density was increased from 618 to 770 kg/m³ when the weight ratio of TMD and CaCO₃ is 5/1. When TMD and CaCO₃ are used at a weight ratio of 1/1, the density of TMD (100 kDa) and TMD (150 kDa) increases to 850 (Figure III-12) kg/m³. Unfortunately, there are many aggregates for the formulation of TMD/CaCO₃ = 1/1 (by mass) because the spraying is not working well.

Table III-5 Tap density of sugar-based microparticles

Sample	Dextran (100 kDa)	Dextran (150 kDa)
	Tap density (kg/m ³)	Tap density (kg/m ³)
TMD (35%(w/w))	670	618
TMD/CaCO ₃ = 10/1	669	627
TMD/CaCO ₃ = 5/1	671	765
TMD/CaCO ₃ = 2.5/1	831	770
TMD/CaCO ₃ = 1/1*	853	848

*many aggregates

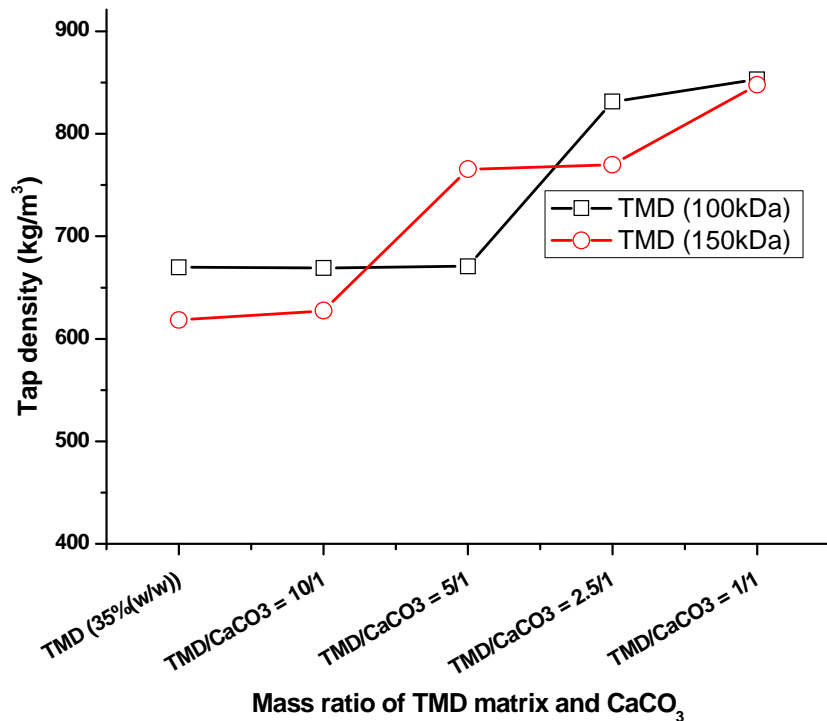


Figure III-12. Effect of calcium carbonate particles on the tap density of the sugar-based microparticles.

3.5 Indentation measurements of TMD/CaCO₃ composite by a texture analyser

CaCO₃ can not only enhance the density of TMD microparticles, but it could also increase the robustness which is very important for powder injection. It is very difficult to measure the force of breaking for one microparticle due to the small size and small force. Therefore, we prepared composites by freeze-drying the mixtures of TMD and CaCO₃ at different weight ratios under the same conditions for SFD process. The freeze-dried composites were measured by a texture analyser using a custom-made steel cylinder probe. As shown in **Figure III-13**, the force for indenting the pure TMD matrix increases firstly and then decreases a little before increasing again. All the composites containing CaCO₃ similarly show straight increase of force against increasing indentation distance. The indentation force on TMD stays at one level or even decreases a little bit before increasing again, indicating the higher porosity of the pure TMD matrix. This is reasonable considering that CaCO₃ can fill some gaps or pores in the TMD matrix. The difference between the different mass ratios of TMD and CaCO₃ can not be figured out because the curves of the samples with a TMD/CaCO₃ mass ratio of 9/1 to 5/5 overlap. Even though the enhancement of TMD robustness by CaCO₃ was just observed in freeze-dried composites, it also indicates that TMD microparticles containing CaCO₃ could have higher robustness due to that the same freeze-drying process was used for SFD.

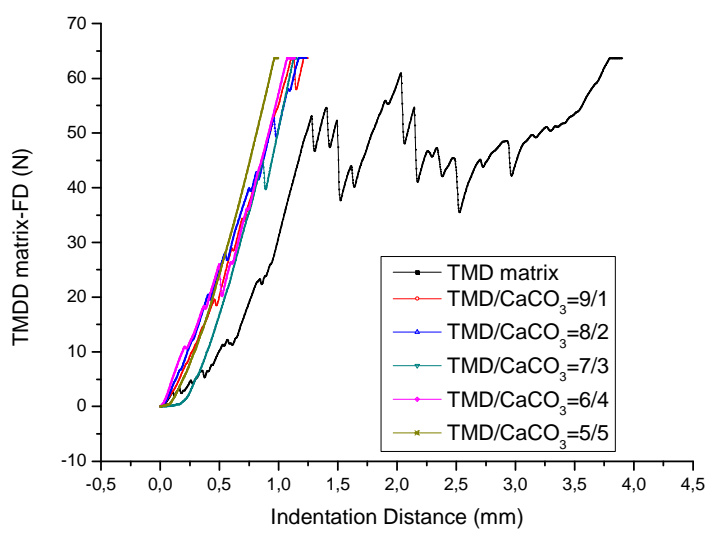


Figure III-13. Indentation results of the composites of TMD and CaCO₃. Maximal force for indentation was limited to 65 N according to the specifications of the texture analyser.

4. Discussion

4.1 Nano-in-micro systems for drug delivery

Different nanoparticles have been encapsulated into TMD microparticles fabricated by spray-freeze-drying. CLSM observations of the nano-in-micro particles confirm the encapsulation and distribution of the nanoparticles in the microparticles. Most of the microparticles have a size range of 20 - 40 μm and a shrunken surface morphology, making them suitable for epidermal powder injection. There are some advantages of this nano-in-micro system for EPI. First, nanoparticles in microparticles can be delivered into the skin by epidermal powder injection. Second, labile substances such as proteins, peptides etc. could be formulated in the nanoparticles to protect them from the physical stress during SFD process. Third, two or even more kinds of nanoparticles providing different functions can be simultaneously encapsulated in the same microparticle, e.g. antigens loaded in one kind of nanoparticles and adjuvants loaded in another kind of nanoparticles may be formulated into the same microparticle for vaccination purpose. Fourth, formulations of nanoparticles in sugar-based microparticles may reduce the aggregation of some unstable nano-sized particles during long-term storage.

Our aim is to develop microparticles applicable for EPI and also make use of nanoparticles as drug/vaccine delivery systems. As there are requirements of the particles concerning particle size (r), density (ρ) and velocity (v) [12], more effort has been put on the preparation of optimal particles for EPI. As shown in **Figure III-1**, nanoparticles in the microparticles made of water-soluble materials are accelerated into skin, and then the matrix is dissolved while the antigen-loaded nanoparticles are released to target Langerhans cells.

The density can be improved for SFD microparticles by improving the solid concentration of the solution for SFD and inducing the shrinkage of the microparticles during the freeze-drying process. Furthermore, dense materials such as CaCO_3 can be added to improve the density. Spray-freeze-drying has been favoured because the nanoparticles of PS, PLGA, silk and gelatin are evenly encapsulated in TMD microparticles.

4.2 Colloidal stability of nanoparticles processed by freeze-drying or spray-freeze-drying

Herein, stability of nanoparticles is understood as referring to the particle size. The freeze-drying of nanoparticles can lead to distinct increase of the particle hydrodynamic size if there is no matrix for protection [144]. Mannitol, sucrose or trehalose has been used to protect

PLGA nanoparticles from aggregation during freeze-drying or spray-drying process [144-147]. The stability of colloid nanoparticles depends on the interaction forces including van der Waals attraction, electrostatic attraction and steric attraction [154]. In aqueous solution, the repulsive effect of the electrostatic barrier plays an important role on the stability. The absolute value of zeta-potential (ζ) determines the repulsive force. Normally if the $|\zeta|$ is larger, the dispersion is more stable. Steric effects can be used to improve the stability of dispersion by coating the nanoparticles with polymers. The polymer layer induces steric hindrance when two particles come close to each other [154]. The matrix used for protecting nanoparticles acts as a spacer between the nanoparticles to stop the agglomeration.

In the formulation of TMD microparticles encapsulating nanoparticles, the matrix plays a role of protecting the nanoparticles from aggregation. The polymeric nanoparticles such as PS and PLGA are well protected because only small increase of particle sizes was observed. The gelatin nanoparticles have a distinct larger size in TMD microparticles. This probably results from the low absolute value of zeta-potentials. Gelatin nanoparticles in lactose microparticles prepared by spray-drying also show increased sizes [142]. The silk nanoparticles in the TMD matrix are more stable than GNP as the size increases at a moderate level. It seems that zeta-potential is very important for the stability of protein-based nanoparticles.

4.3 Properties of nanoparticles for intracellular delivery

Though Langerhans cells could be the first choice for investigating the intracellular delivery of nanoparticles considered as vaccine delivery systems for EPI, it is rather complicated to culture Langerhans cells [155]. In fact, macrophage cells are also involved in the immune response. As macrophage cell lines are commercially available, we use it for initial experiments for intracellular delivery of different nanoparticles. Almost no PS-Rhd nanoparticles penetrated into microphage cells, while PLGA, silica nanoparticles and gelatin nanoparticles penetrated. The surface properties such as charge, hydrophobicity, coating, and particle size determine the uptake of them by cells. As the membrane of cells is negatively charged, the nanoparticles with low negative charge or positive charge on surface could be taken up more easily. This could explain that PS-Rhd nanoparticles ($\zeta = -45.1$ mv) were not delivered into macrophage cells because of the high negative charge on the particle surface. Cationisation is one popular method for coating particles used for intracellular delivery, e.g. cationic PLGA nanoparticles [148, 151].

4.4 Effect of dense excipients on the density of the microparticles

It is rational to use dense materials to increase the density of TMD microparticles. The density of SFD microarticles depends very much on the solid concentration of the solution for SFD. 35 wt% of TMD used in our experiments is too viscous to add more absolute amounts of any component. Solid CaCO_3 powder with a size around 1 μm in diameter was added into the TMD solution to obtain a composite which can still be sprayed by the ultrasonic probe. The true density of CaCO_3 ($\sim 2.7 \text{ g/cm}^3$) is much higher than the sugar-based matrix ($\sim 1.4 \text{ g/cm}^3$) [156]. The density should increase as the amount of CaCO_3 increases. This is consistent with that the tap density of TMD microparticles increased when efficient amount of CaCO_3 was added. On the other hand, CaCO_3 is insoluble in aqueous solution so that it can fill some small pores which may exist in the TMD microparticles. It can make the microparticles denser which is beneficial for EPI delivery.

In the formulation of TMD, dextran as a polysaccharide is used to increase the robustness that is necessary for EPI delivery. The robustness of TMD matrix has been further enhanced by adding CaCO_3 as proved here. The indentation force for each composite of TMD and CaCO_3 increases faster than that of pure TMD (**Figure III-13**). The TMD/ CaCO_3 can stand a larger force at the same indentation distance compared to the pure TMD matrix.

5. Conclusion

Sugar-based microparticles consisting of trehalose, mannitol, dextran have been fabricated by spray-freeze-drying. The compact morphology ensures the potential application for EPI delivery. Nanoparticles-in-microparticle systems have been investigated by formulating different kinds of nanoparticles in the TMD matrix. Each type of nanoparticles including PS, PLGA, gelatin, silica and silk has been encapsulated in TMD microparticles from the CLSM observation, but the stability of PS and PLGA can only be best preserved. Silica and PLGA nanoparticles for loading antigens will be investigated in the next chapters. PLGA, gelatin, silk, silica nanoparticles can be taken up by macrophages after redissolution from TMD microparticles, suggesting that they can be used for intracellular delivery. Addition of CaCO_3 in TMD microparticles can increase the tap density and enhance the robustness, which are positive for EPI delivery.

Chapter IV. Encapsulation of Antigen-loaded Silica Nanoparticles into Microparticles for Intradermal Powder Injection

1. Objectives

Silica-based nanoparticles have been extensively used for drug delivery and biomedical applications [75, 93], but are not well investigated as a vaccine delivery system. In fact, silica showed an adjuvant effect in the immunological response in guinea pigs [96]. Vallhov *et al.* studied the effects of mesoporous silica particles (270 nm and 2.5 μ m) on human monocyte-derived dendritic cells (MDDC) and found good cellular uptake of both particles and low-toxicity profiles on MDDC [97]. Recently, Vallhov *et al.* suggested that mesoporous silica particles have adjuvant properties of tuning effect T cell development according to cell culture experiments [98]. Furthermore, mesoporous silica nanoparticles can enhance mucosal and systemic immune responses when applied orally in mouse models [99]. Although silica nanoparticles show potential as a vaccine delivery system, there is no study investigating their applications for epidermal powder immunisation.

The objective of this work was to prepare microparticles encapsulating antigen-loaded silica nanoparticles, i.e. nanoparticles-in-microparticles (nano-in-micro) system integrating the advantages of nanoparticles as vaccine delivery vehicles and microparticles for epidermal powder immunisation (EPI). Cationic mesoporous silica nanoparticles (MSNP-NH₂) were prepared and used for loading a model antigen, ovalbumin (OVA). The surface of MSNP-NH₂ is positively charged in solution with near neutral pH, while ovalbumin is negatively charged at that pH. Thus the OVA protein can be absorbed on the surface of the silica nanoparticles driven mainly by electrostatic interactions.

2. Materials and Methods

2.1 Materials

Tetraethyl orthosilicate (reagent grade, 98%) (TEOS), (3-Aminopropyl)trimethoxysilane (97%) (APTMS), hexadecyltrimethylammonium bromide (BioUltra, $\geq 99\%$) (CTAB), ovalbumin from chicken egg white (Grade V, lyophilized powder, $\geq 98\%$) (OVA), N,N'-carbonyldiimidazole (CDI), Fluorescein isothiocyanate–dextran (FITC-dextran) (average mol

wt 70 000, FITC:Glucose = 1:250), Dextran (average mol wt 9 000-11 000) from *Leuconostoc mesenteroides* and Dextran (average mol wt 10 000) from *Leuconostoc mesenteroides* were purchased from Sigma-Aldrich (Steinheim, Germany). D(+)-Trehalose dehydrate (for biochemistry) was obtained from VWR (Darmstadt, Germany). Mannitol was obtained from Boehringer Ingelheim (Ingelheim, Germany). Rhodamine B isothiocyanate-labeled ovalbumin (RITC-OVA) were prepared by conjugation of Rhodamine B isothiocyanate (Sigma-Aldrich, St. Louis, USA) and ovalbumin according to the instructions where the method is adapted from Larsson (www.piercenet.com/instructions/2162081.pdf) [157].

2.2 Methods

2.2.1 Preparation of mesoporous silica nanoparticles

The synthesis method of mesoporous silica nanoparticles (MSNP) was modified from Xia et al. [152]. Briefly, 1.60 g of CTAB was dissolved in a mixture of 11.20 ml of 1 mol/l NaOH aqueous solution and 768 ml of deionised (DI) water under stirring. The temperature of the solution was increased to 80 °C within 30 min. For preparing plain MSNP nanoparticles with hydroxyl groups on the surface, 8.00 ml of TEOS was added dropwise while the solution was stirred at 700 rpm. After 2 hours of stirring, plain MSNP nanoparticles (MSNP-OH) were obtained by centrifugation and washed with ethanol once. For preparing MSNP nanoparticles with amine groups on the surface, 7.60 ml of TEOS and 0.40 ml of APTMS were mixed together and then added into the solution containing CTAB and NaOH at 80 °C drop by drop while stirring at 700 rpm. After 15 min of stirring, 0.656 ml of APTMS was added dropwise, and then the complete suspension was stirred for another 2 hours. MSNP nanoparticles with positive charges on the surface (MSNP-NH₂) were obtained by centrifugation and washed with ethanol once. In order to remove CTAB, fresh prepared silica nanoparticles MSNP-OH and MSNP-NH₂ were refluxed overnight in 160 ml of ethanol containing 8 ml of 37% (w/v) HCl aqueous solution and then washed with ethanol three times and water three times using 120 ml for each time. The surfactant extracting process was repeated once. Finally, the nanoparticles were dried overnight at 20 °C in a vacuum dryer. The fluorescently-labeled silica nanoparticles (FITC-MSNP-NH₂) were prepared as described in Chapter III.

2.2.2 Preparation of MSNP-ovalbumin conjugates

Ovalbumin (OVA) was chemically conjugated to MSNP-OH according to a N,N'-carbonyldiimidazole-mediated functionalization method [158]. 45 mg of MSNP-OH was

suspended in 3 ml of DI water under probe sonication (Bandelin UW 3200, Berlin, Germany). The nanoparticles were separated by centrifugation at 10000×g for 5 min, and then washed with anhydrous Tetrahydrofuran (THF) four times, 9 ml of THF each time. The MSNP-OH nanoparticles were resuspended in 9 ml of THF again under probe sonication. 450 mg of carbonyldiimidazole (CDI) was added into the particles suspension, and the mixture was stirred for 2 hours at 700 rpm at room temperature. The particles were washed with THF twice and subsequently with 20 ml each of ice-cold sodium phosphate buffer (PB) (100 mM, pH 8.5) three times within 40 min. The CDI-activated MSNP-OH was resuspended in 4.5 ml of PB (100 mM, pH 8.5), and then 45 mg of ovalbumin was added into the suspension. The mixture was stirred gently for 24 hours at 4 °C. Finally, excess OVA was removed by washing three times with PB (100 mM, pH 8.5). MSNP-ovalbumin conjugates (MSNP-OVA) was obtained and stored at 4 °C for subsequent use. Fourier transform infrared spectroscopy (FTIR) and sodium dodecyl sulfate polyacrylamide gel electrophoresis (SDS-PAGE) were used to characterise the conjugates.

2.2.3 Ovalbumin loading and release from MSNP-NH2 nanoparticles

The ovalbumin loading process was carried out as following: 50 mg/ml suspension of nanoparticles in sodium phosphate buffer (PB) (10 mM, pH 4.8 or 6.8) was prepared by probe sonicating (Bandelin UW 3200, Berlin, Germany) twice, each for 1 min (amplitude 30%, pulse 1s/1s). Ovalbumin was dissolved in PB (10 mM, pH 4.8 or 6.8) under occasional shaking. After centrifugation at 12000×g for 5 min, the supernatant was obtained as 100 mg/ml ovalbumin stock solution. 0.5 ml of the particle suspension and specific volume of the stock OVA solution were mixed together. Specific volume of PB buffer (10 mM, pH 4.8 or 6.8) was added if necessary to make the final volume for loading 1 ml in a 2-ml Eppendorf tube. The final ovalbumin concentrations for loading were 1, 2, 5, 10, 25 and 50 mg/ml, respectively while keeping the MSNP-NH2 concentration at 25 mg/ml. The 1 ml loading suspension in 2 ml EP tube was gently shaken at RT under 30 rpm for 4 hours. The tubes were centrifuged and the supernatants were removed. The particles were washed with PB (10 mM, pH 4.8 or 6.8) twice. The loaded amount was calculated by subtracting the OVA concentration in supernatants from the original OVA concentration.

The determination of ovalbumin release is described briefly here. 5 mg of MSNP-NH2 nanoparticles loaded with OVA were resuspended in 1 ml 1×PBS buffer (150 mM, pH 7.4) in 2-ml EP tubes. After a specific release time, the tubes were centrifuged and 0.5 ml

supernatant was replaced with 0.5 ml of fresh PBS buffer. The process was repeated at each time point for release test. The supernatants were measured using a Nanodrop (Thermo Scientific, Wilmington, USA) to obtain OVA concentration. The amounts of accumulated released ovalbumin were calculated. The same process was used for all the release experiments in other buffers.

2.2.4 Preparation of microparticles with nanoparticles encapsulated by spray-freeze-drying

50 mg/ml of MSNP-NH₂ in sodium phosphate buffer (PB) (10 mM, pH 5.8) was prepared under probe sonication. 200 mg/ml of ovalbumin in the same PB buffer was obtained after removing the non-dissolvable part by centrifugation. Trehalose, mannitol, dextran (10 kDa) and dextran (100 kDa) (TMD) were mixed with a weight ratio of 3:3:3:1, and were then dissolved in sodium phosphate buffer (PB) (10 mM, pH 7.4) under stirring to obtain 35 wt% sugar-based solution. The TMD solution was filtered through a 0.2 μ m syringe filter before use. TMD solution and OVA solution were mixed together by a short vortex-shaking (Heidolph, Schwabach, Germany) to prepare microparticles with 25 μ g per 1 mg (25 μ g/mg) of dry microparticles. MSNP-NH₂ suspension and OVA solution were mixed together under gentle shaking for 1 hours at RT before mixed with TMD solution. MSNP-NH₂/OVA mixture was then mixed with TMD solution by a short vortex-shaking. In the formulations, ovalbumin was kept at 25 μ g/mg of dry sugar-based microparticles and the MSNP-NH₂ amount was varied.

The prepared formulations of TMD, OVA and MSNP-NH₂ were sprayed into liquid nitrogen by an ultrasonic atomizing nozzle (120 kHz, Sono-Tek, Milton, USA). The power for spraying was set to 4.0 watts and the flow rate of peristaltic pump to 0.6 ml/min. The sprayed microparticles were collected in vials and transferred to a pre-cooled Christ lyophilizer (Martin Christ EPSILON 2-6D, Harz, Germany). The freeze-drying sequence was carried out by 24 hours of primary drying at -10 °C and 20 hours of secondary drying at 25 °C. The chamber pressure was kept at 0.12 mbar during the whole drying process.

2.2.5 Preparation of microparticles containing fluorescently-labeled ovalbumin by spray-freeze-drying

10 mg of Rhodamine B isothiocyanate-labeled ovalbumin (RITC-OVA) and 30 mg of OVA were dissolved in 0.2 ml PB buffer (10mM, pH 5.8), resulting in OVA/RITC-OVA solution.

0.0438 ml of OVA/RITC-OVA solution and 0.0875 ml of 50 mg/ml MSNP-NH2 in PB buffer (10 mM, pH 5.8) were mixed. Then, 1.0 g of 35 wt% TMD solution was added into the mixture to prepare TMD microparticles containing MSNP-NH2 and protein with a mass ratio of 1/2 by the same SFD process as described previously. Similarly, TMD microparticles containing MSNP-NH2 and protein with a mass ratio of 1/4 were prepared.

2.2.6 Characterisation of the nanoparticles and microparticles

Measurements of hydrodynamic diameter and zeta-potential

The hydrodynamic diameter and zeta-potential (ζ) were determined by dynamic light scattering (DLS) using a Zetasizer Nano ZS (Malvern Instruments, Herrenberg, Germany). The reflective index (RI) of silica nanoparticles used for the size measurement was 1.47 as suggested in the literature [159]. Before DLS measurements, the suspensions of MSNP nanoparticles sodium phosphate buffer were diluted to 0.25-0.5 mg/ml, which can produce effective signals. MSNP-NH2 loaded with OVA and MSNP-OVA conjugated were also measured using the same conditions.

Scanning electron microscopy (SEM)

Silica nanoparticles and sugar-based microparticles were coated with a thin layer of carbon before observed using a JEOL JSM-6500F scanning electron microscopy (SEM) at magnifications of 18000-20000 for silica nanoparticles and 300 for microparticles.

Pore size distribution and surface area

Pore size distribution of MSNP-NH2 was determined from absorption and desorption of nitrogen gas using Autosorb-1 (Quantachrome, Odelzhausen, Germany). The sample was outgassed at 250 °C for 36 hours before each measurement. The specific surface area and pore size distribution (PSD) was calculated by the Brunauer-Emmett-Teller (BET) and Barrett-Joyner-Halenda (BJH), respectively, using the Autosorb-1 software.

Measurements of particle size

Microparticles obtained from spray-freeze-drying were suspended in Miglyol 812 (Sasol, Witten, Germany) under stirring. A Partica LA-950 (HORIBA, Kyoto, Japan) was used to measure the particle size distribution. The reflective indexe (RI) of sugar-based microparticles is 1.530, which was approximated by the RI of the sugar (sucrose) as described in the 'Sample

Dispersion & Refractive Index Guide' from Malvern Instruments; the RI of Miglyol 812 is 1.449 as described by the manufacturer.

Confocal Laser Scanning Microscopy (CLSM)

An invert Confocal Laser Scanning Microscope (LSM 510 META, Carl ZEISS, Germany) was used to observe the microparticles encapsulating fluorescent nanoparticles. Argon laser (488 nm) and HeNe laser (543 nm) were used as excitation wavelengths, corresponding to the emissions of BP 505-530 nm and LP 560 nm, respectively. Three different oil lenses were used, including Plan-Neofluar 40 \times /1.3 Oil, Plan-Apochromal 63 \times /1.4 Oil DIC and Plan-Neofluar 100 \times /1.3 Oil Ph3. The Z-stacking mode was used to observe the distribution of nanoparticles in the microparticles. 3D view of Z-stacking micrographs was obtained by processed with projection under a Turning Axis of Y, First Angle of 180°, Number Projections of 16 and Difference Angle of 1°.

TMD microparticles containing MSNP-NH2 and OVA/RITC-OVA were ballistically injected into a gelatin film and pig skin by a custom-made device. The distribution and depths of fluorescent microparticles in model skin and pig skin after injection were determined as follows. 4 mg/ml of FITC-dextran in PBS (150 mM, pH 7.4) was prepared and then glycerol was added into the solution to obtain 2 mg/ml FITC-dextran in solution, which was used to distinguish the surface of model skin or pig skin. 50% (v/v) of glycerol in the solution was used to increase the viscosity. A petri dish for imaging with a diameter of 35 mm and thin bottom (ibidi GmbH, Martinsried, Germany) was used. One drop of the FITC-dextran solution was added on the bottom of the petri dish, and then the model skin or pig skin was placed in by facing the layer with injected particles to bottom. The FITC-dextran solution fills the space between the bottom and the skin surface. This is particularly advantageous for determining rough surfaces, e.g. of biological skin samples.

2.2.7 Ovalbumin concentration determination

The application "Protein A280" of NanoDrop 2000 (Thermo Scientific, Wilmington, USA) was used for the determination of ovalbumin concentrations. The absorbance at 280 nm (A_{280}) and OVA concentration has a very good linear correlation over a broad range between 0.02 mg/ml and 200 mg/ml with an R^2 -value of 0.99993. In order to obtain a more precise determination of ovalbumin concentration, a standard curve between A_{280} and OVA concentration over the range of 0.5-50 mg/ml was measured to calculate the extinction

coefficient ($E^{1\%}$). $E^{1\%} = 6.3$ was obtained by linear fitting of the A_{280} and OVA concentration. Finally, OVA concentration (C , unit of mg/ml) was calculated as follows:

$$C = \frac{10 \times A_{280}}{E^{1\%}} \quad (1)$$

Micro BCATM protein assay reagent kit (PIERCE, Thermo Scientific, Rockford, USA) was also used to confirm the results from NanoDrop and determine the amount of ovalbumin conjugated to MSNP-OH. Diluted albumin (BSA) standards were prepared with final BSA concentrations between 0.5 and 200 µg/ml. The standards and samples were measured at 562 nm in a microplate well using a plate reader (Fluostar Omega, BMG LABTECH GmbH, Ortenberg, Germany).

2.2.8 Characterisation of ovalbumin

NuPAGE[®] 10% Bis-Tris precast gels (Life Technologies, Darmstadt, Germany) were used for SDS-PAGE. Non-reducing conditions were used and the proteins were stained with coomassie blue (Life Technologies, Darmstadt, Germany). Size-exclusion high-performance liquid chromatography (SEC-HPLC) was carried out to determine the molecular size of ovalbumin. A TSK-GEL[®] column (TOSOH BIOSCIENCE, Stuttgart, Germany) and Thermo Scientific System equipped with a UV1000 detector were applied. The running buffer was 50 mM sodium phosphate buffer (pH 7.2, 300 mM of NaCl). Data analysis was done using ChromQuestTM 4.1 (Thermo Scientific, Dreieich, Germany).

2.2.9 Cellular uptake of nanoparticles by macrophages

The cell experiments were carried out using the same method as described in Chapter III. Cellular uptakes of each sample were performed at 37 and 0 °C, respectively.

3. Results

3.1 Characterisation of mesoporous silica nanoparticles

Mesoporous silica nanoparticles (MSNP) were synthesized using CTAB as the surfactant and NaOH as the catalyst. MSNP around 130 nm in diameter were obtained as shown by SEM micrographs in **Figure IV-1**. The plain MSNP (MSNP-OH) and cationic MSNP (MSNP-NH₂) have almost the same spherical shape and size that are close to the results by Xia *et al.* [152]. The mesopore size of MSNP-NH₂ is 2.3 nm calculated from the BJH method, and the estimated specific surface area by the BET method is 1170.27 m²/g.

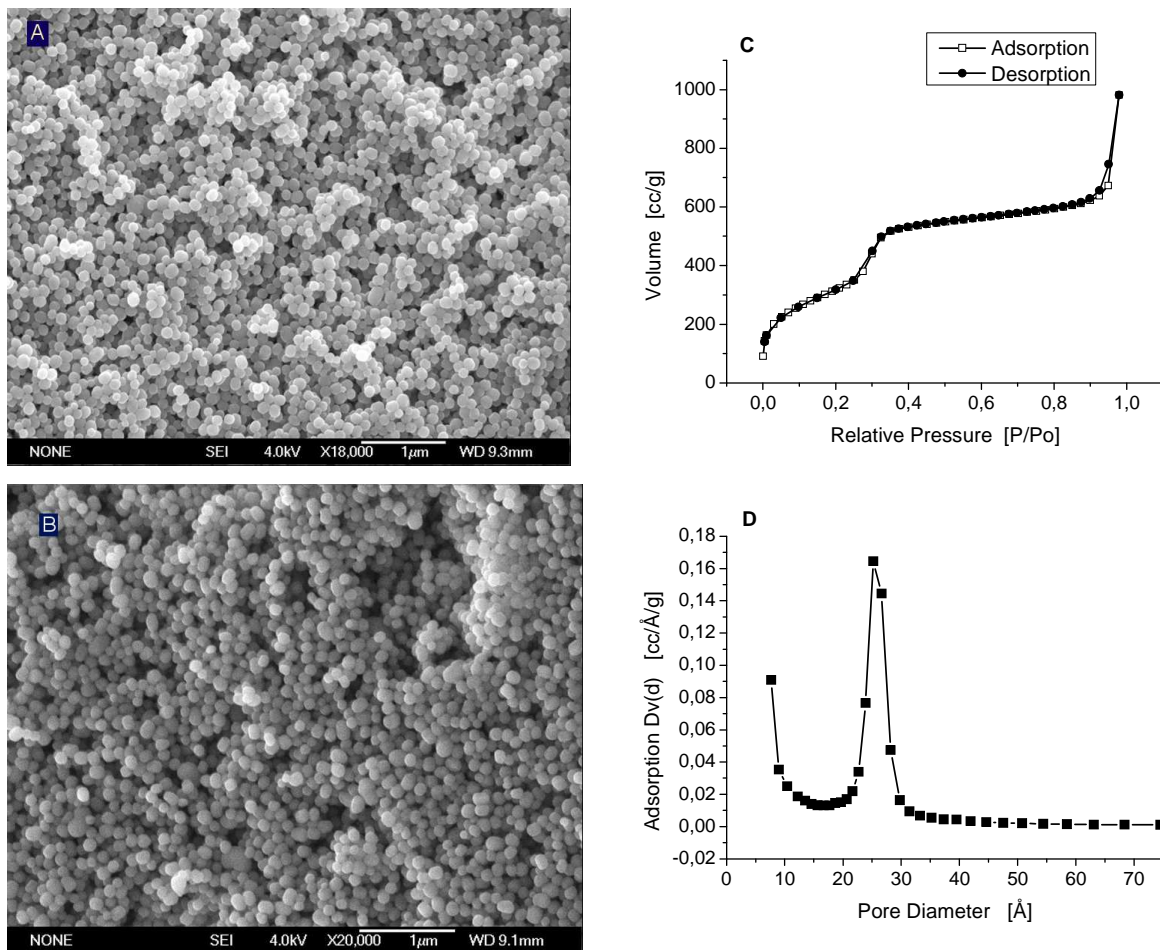


Figure IV-1. Results of mesoporous silica nanoparticle analysis. SEM micrographs of MSNP-OH (A), MSNP-NH2 (B) (the scale bar is 1 μ m); Nitrogen physisorption isotherm (C) and corresponding pore size distribution of MSNP-NH2 (D).

MSNP nanoparticles were dispersed in 15 mM PBS (pH 6.2) and DLS measurements were carried out. As shown in **Table IV-1**, MSNP-NH2 particles have a hydrodynamic size of 111 nm which is consistent with the results from the SEM observation. The cationic MSNP-NH2 particles have a positive charge on the surface at pH 6.2, while plain MSNP-OH have a slightly negative surface. The Z-average size of MSNP-OH is much larger than that from the SEM micrograph, which indicates the aggregation due to the ζ -potential (-5.5 mV) which is close to neutrality. The positive surface of MSNP-NH2 enables the particles to be a possible delivery system for negatively charged drugs or antigen as absorption of negatively charged antigens may take place due to electrostatic interactions. [152].

Table IV-1 Size distribution of MSNP in 15 mM PBS (pH 6.2) buffer

Silica nanoparticles	Z-Ave (nm)	PDI	ζ -potential (mv)
MSNP-NH2	111	0.244	30.8
MSNP-OH	670	0.510	-5.5

3.2 Conjugation of mesoporous silica nanoparticles with ovalbumin

Ovalbumin was considered to be conjugated to MSNP as this method has already been proved effective for vaccine delivery [81]. We used the same method for the conjugation of OVA onto inorganic nanoparticles as the one developed by Ho, *et al.* [158]. OVA was successfully conjugated to MSNP-OH as shown by SDS-PAGE and FTIR results (**Figure IV-2**). SDS-PAGE was performed to determine if the conjugation of ovalbumin onto silica nanoparticles was successful or not. From lane 4 and lane 10 in **Figure IV-2**, there is no OVA band as obviously all OVA was chemically bound to MSNP, but a narrow blue band can be seen at the starting points. For physically absorbed OVA on silica, OVA bands (lane 6 and lane 12) are very clear. MSNP-OH was used as a control showing no protein bands. For FTIR measurements (**Figure IV-2B**), MSNP-OVA and MSNP-NH2 with physically adsorbed OVA (MSNP-NH2/OVA) were washed with sufficient DI water. As expected, physically adsorbed OVA has been washed away, and as a result no OVA signals were detectable in **Figure IV-2B**. The curve of MSNP-OVA shows distinct signals (as annotated with an arrow) resulted from OVA.

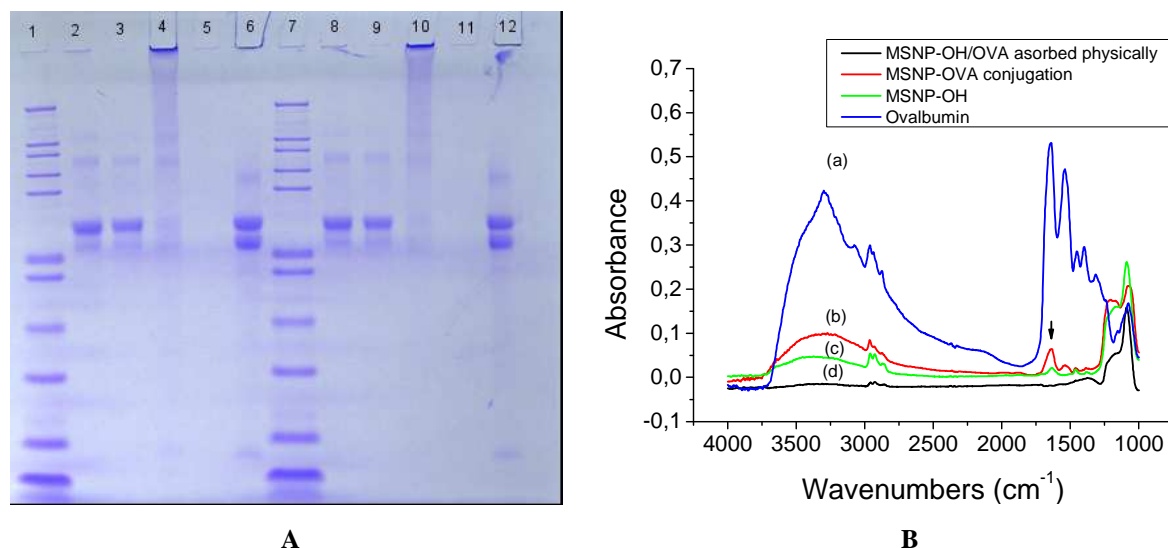


Figure IV-2. Conjugates of MSNP-ovalbumin. (A) SDS-PAGE of ovalbumin at different conditions. From right to left (lane 1-12), they are marker (lane 1), OVA control (lane 2), supernatant after conjugated onto silica nanoparticles (lane 3), conjugation of MSNP-OH and OVA (lane 4), MSNP-OH particles (lane 5), MSNP-NH2 with physically adsorbed OVA (lane 6), marker (lane 7), OVA control (lane 8), supernatant after conjugated onto silica nanoparticles (lane 9), conjugation of MSNP-OH and OVA (lane 10), MSNP-OH particles (lane 11) and MSNP-NH2 with physically adsorbed OVA (lane 12), respectively. (B) FT-IR spectra of (a) ovalbumin, (b) MSNP-ovalbumin conjugates, (c) pure MSNP-OH, (d) MSNP-OH/OVA absorbed physically.

OH absorbed with ovalbumin physically and washed with adequate buffer. (Transmission mode of FT-IR-microscope)

3.3 Ovalbumin (OVA) loading on the silica nanoparticles and release tests

BSA loading on silica nanoparticles and release behaviour have been investigated by Want *et al.* [99], aiming to use them as an oral vaccine adjuvant. It is necessary to study loading capacity of OVA on MSNP and release behaviour before this type of delivery system can be used in the formulation of microparticles. The effect of loading time was investigated from four hours to three days. No further increase in OVA loading was observed for loading times longer than 4 hours. Thus 4 hours was kept as the loading time. The effect of the pH on loading was studied as shown in **Table IV-2**. A larger amount of OVA can be loaded on MSNP-NH2 at PB loading buffer with a lower pH. The hydrodynamic sizes of silica nanoparticles and OVA-loaded ones are very dependent on the zeta-potentials. All protein loaded particles are aggregated except MSNP-NH2 at pH 6.8, which are already aggregated before loading. Thus, the loading was only achieved with aggregates.

Table IV-2 The effect of pH on ovalbumin loading capacity

Sample	PB Buffer	Before loading			After loading			Loading capacity (mg/mg)
		Z-Ave (nm)	PDI	Z (mv)	Z-Ave (nm)	PDI	Z (mv)	
MSNP-NH2	pH = 4.8	88	0.278	29.0	1129	0.273	-3.5	0.37±0.05
MSNP-NH2	pH = 6.8	746	0.297	13.2	710	0.382	-14.4	0.30±0.01
MSNP-OH	pH = 4.8	181	0.345	-4.9	1856	0.429	-7.4	0.18±0.02
MSNP-OH	pH = 6.8	110	0.227	-17.7	249	0.305	-17.6	0.12±0.01

OVA concentration is another important factor affecting loading amounts and loading efficiencies, as shown in **Table IV-3** and **Figure IV-3**. The amount of OVA loaded on MSNP-NH2 increases with the increasing concentration of OVA for loading, while the efficiency decreases. As antigens for vaccination are usually expensive, it is necessary to balance loading amount and efficiency.

Table IV-3 Ovalbumin loading on silica nanoparticles in different concentrations of OVA

OVA Concentration (mg/ml)	1.0	2.0	5.0	10.0	25.0
Loaded OVA (mg/mg)	0.028±0.002	0.057±0.003	0.117±0.002	0.168±0.006	0.218±0.037
Loading efficiency (%)	71	71	58	41	22

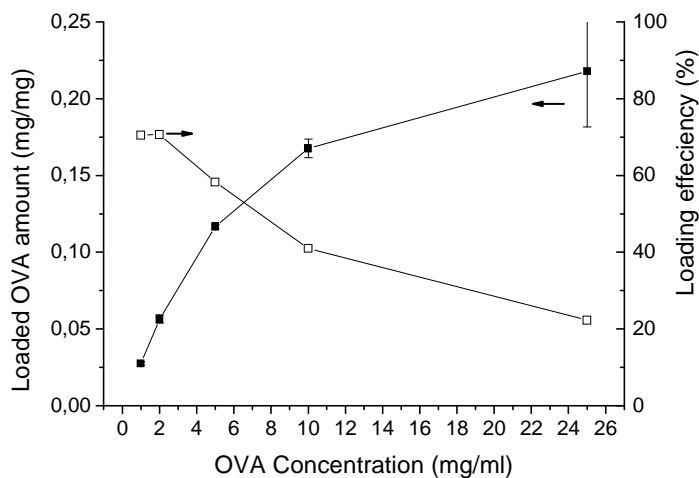


Figure IV-3. Effect of OVA concentration on the loading amount on silica nanoparticles and loading efficiency.

The release tests were carried out in PBS (150 mM, pH 7.4) which is a commonly used buffer simulating the physiological environment in humans. MSNP-NH₂ particles loaded with OVA at 10 mg/ml were used for release tests in **Figure IV-4A**, while the same nanoparticles in **Figure IV-4B** were loaded at 25 mg/ml of OVA. All particles show a distinct burst effect during the first few hours of the release. Different frequencies for refreshing release buffer have been tested in order to study the effect of sampling time on the release. As we can see from **Figure IV-4**, fast release was observed when changing the release buffer at a shorter time span (2 hours compared 24 hours at the beginning stage). In other words, the speed of OVA release from MSNP-NH₂ depends on the distribution of OVA in the liquid phase. The release tests were also carried out in different buffers such as 1×PBS (150 mM, pH 7.4), 1×PBS (150 mM, pH 9.8), 10×PBS (1500 mM, pH 7.4) and 10×PBS (1500 mM, pH 9.8). It is not surprising that fast release of OVA in the release buffers with higher pH and higher ionic strength considering the main interaction force between OVA and MSNP-NH₂ is electrostatic attraction. Therefore, the OVA release is just controlled by the displacement from electrostatic bindings by salt and no sustained release was observed.

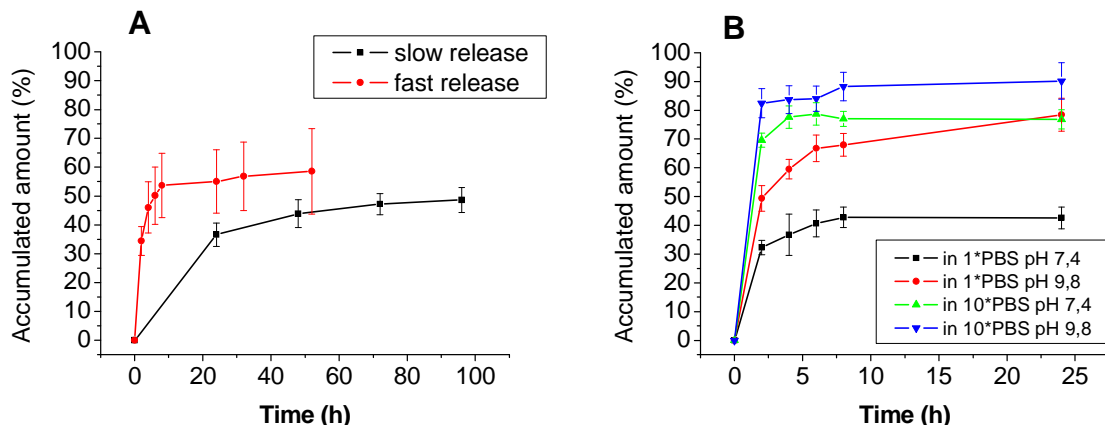


Figure IV-4. OVA release from the OVA-loaded silica particles. (A) OVA release in 1×PBS buffer (pH 7.4); (B) Effect of pH and ionic strength on OVA release behaviour.

3.4 Sugar-based microparticles encapsulating model antigens and nanoparticles

Before using the MSNP-NH₂ in the formulation for preparing microparticles, it is necessary to investigate the stability of MSNP-NH₂ before and after loading with OVA in the sugar-based matrix. Aggregation of silica nanoparticles is a major challenge for the application. Much effort was put to minimize the aggregation tendency of MSNP-NH₂ for OVA delivery. MSNP-NH₂ particles dispersed in PB buffer (10 mM, pH 4.8) have no aggregation before loading OVA, but MSNP-NH₂/OVA particles at pH 4.8 show big aggregates. Moreover, this pH (4.8) is too close to isoelectric point (pI = 4.5 or 4.9) as specified in the product information that may result in the tendency of OVA precipitation. At a pH 6.8, MSNP-NH₂ particles show aggregation before loading OVA, even though the size of OVA-loaded MSNP-NH₂ does not increase more. As a compromise, PB (10 mM, pH 5.8) was chosen. Different amounts of OVA were mixed with specific amounts of MSNP-NH₂ in PB (10 mM, pH 5.8), and then DLS measurements were carried out after the samples were diluted with PB buffer (10 mM, pH 5.8). As depicted in **Table IV-4**, the hydrodynamic sizes increase when MSNP-NH₂ nanoparticles were mixed with OVA. The aggregation is very distinct for MSNP-NH₂/OVA mixtures with mass ratios of 4/1, 2/1 and 1/1. In the mixture of MSNP-NH₂/OVA = 1/2 and 1/4, the sizes were increased from 116 nm to 472 nm and 187 nm, respectively, after mixing for 24 h. Therefore, the mass ratios of MSNP-NH₂/OVA = 1/2 and 1/4 were used in the next formulation of TMD, OVA and MSNP-NH₂. Higher stability of the mixtures MSNP/OVA = 1/2 and 1/4 was also observed from the optical images (data not shown). Similar results were obtained when TMD dissolved in PB (10 mM, pH 7.4) was added (data not shown). The formulations with MSNP-NH₂/OVA = 1/2 and 1/4 were investigated further.

Table IV-4 Effect of OVA on the colloidal stability of MSNP-NH2

Sample	Fresh mixture			Mixture after 24h		
	Z-Ave (nm)	PDI	ζ (mv)	Z-Ave (nm)	PDI	ζ (mv)
MSNP-NH2	116	0.259	22.8	128	0.290	19.2
MSNP-NH2/OVA = 4/1	1800	0.352	-9.1	1007	0.303	-9.3
MSNP-NH2/OVA = 2/1	1049	0.236	-9.4	870	0.386	-11.0
MSNP-NH2/OVA = 1/1	772	0.208	-12.2	1180	0.279	-11.7
MSNP-NH2/OVA = 1/2	243	0.344	-12.0	472	0.340	-12.0
MSNP-NH2/OVA = 1/4	171	0.335	-11.6	187	0.374	-12.5

The samples were diluted to about 0.2 mg/ml of particles with PB buffer (10 mM, pH 5.8) for DLS measurements.

The effect of TMD on the size of MSNP-NH2/OVA particles was also studied. 5 mg/ml of silica nanoparticles and 20 mg/ml of ovalbumin in PB buffer (10 mM, 5.8) were used to prepare the mixture. Considering the situation for using MSNP-NH2/OVA in the TMD formulation, the mixtures of TMD, OVA and MSNP-NH2 were prepared by keeping constant OVA contents at 25 μ g per 1 mg of absolute TMD mass. OVA can be loaded onto MSNP-NH2 at pH 5.8 and the OVA-loaded particles are supposed to be used at a physiological pH (7.4). Thus each formulation was diluted in PB buffer (10 mM, pH 7.4) for DLS measurements (Table IV-5). MSNP-NH2 was mixed with OVA for 4 hours under gentle shaking, and then the MSNP-NH2/OVA was mixed with TMD solution. After a short vortex-shaking, the formulations of TMD and MSNP-NH2/OVA were diluted in PB (10 mM, pH 7.4) for DLS measurements. As shown in **Table IV-5**, the sizes of the MSNP-NH2/OVA do not change when the OVA loaded nanoparticles are mixed with TMD solution, while the PDIs increase. The zeta-potentials were maintained during the mixing of MSNP-NH2/OVA and TMD. Thus TMD matrices containing MSNP-NH2/OVA (1/2 and 1/4) are acceptable for preparing TMD-based nano-in-micro particles.

Table IV-5 Effect of TMD solution on the the stability of MSNP-NH2

Sample	Before TMD mixing			After TMD mixing		
	Z-Ave (nm)	PDI	ζ (mv)	Z-Ave (nm)	PDI	ζ (mv)
MSNP-NH2	2194	0.242	8.5	1763	0.433	5.4
OVA	21	0.534	-8.3	24	0.589	-8.1
MSNP-NH2/OVA = 1/2	709	0.125	-13.3	529	0.332	-12.9
MSNP-NH2/OVA = 1/4	448	0.211	-12.9	431	0.492	-15.5

The samples were diluted to about 0.2 mg/ml of particles with PB buffer (10 mM, pH 7.4) for DLS measurements.

The colloidal stability of nanoparticles is limited by the properties of the nanoparticles and the media for suspension. To increase the long-term stability on storage is one of the reasons we incorporate the silica nanoparticles into formulations of dry microparticles. Spray-freeze-drying (SFD) is a promising method for the preparation of microparticles for ballistic delivery [106-109]. The main concern of SFD methods is to obtain dense (non-porous) microparticles with strong mechanical stability for bombardment on skin. Several formulations (**Table IV-6**) were prepared. The SEM results are shown in **Figure IV-5**. Most of the microparticles were in the size range between 20 μm and 40 μm , and are well suitable for powder injection. Some parameters of the microparticles are shown in **Table IV-6**. The span of particle size determined by laser diffraction is close to 1.0, indicating a narrow size distribution. TMD/MSNP-NH₂/OVA (S1), TMD/MSNP-NH₂/OVA (S2) and TMD/OVA (S3) correspond to the TMD formulations containing MSNP-NH₂/OVA (1/2), MSNP-NH₂/OVA (1/4) and free OVA without nanoparticles (25 $\mu\text{g}/\text{mg}$), respectively.

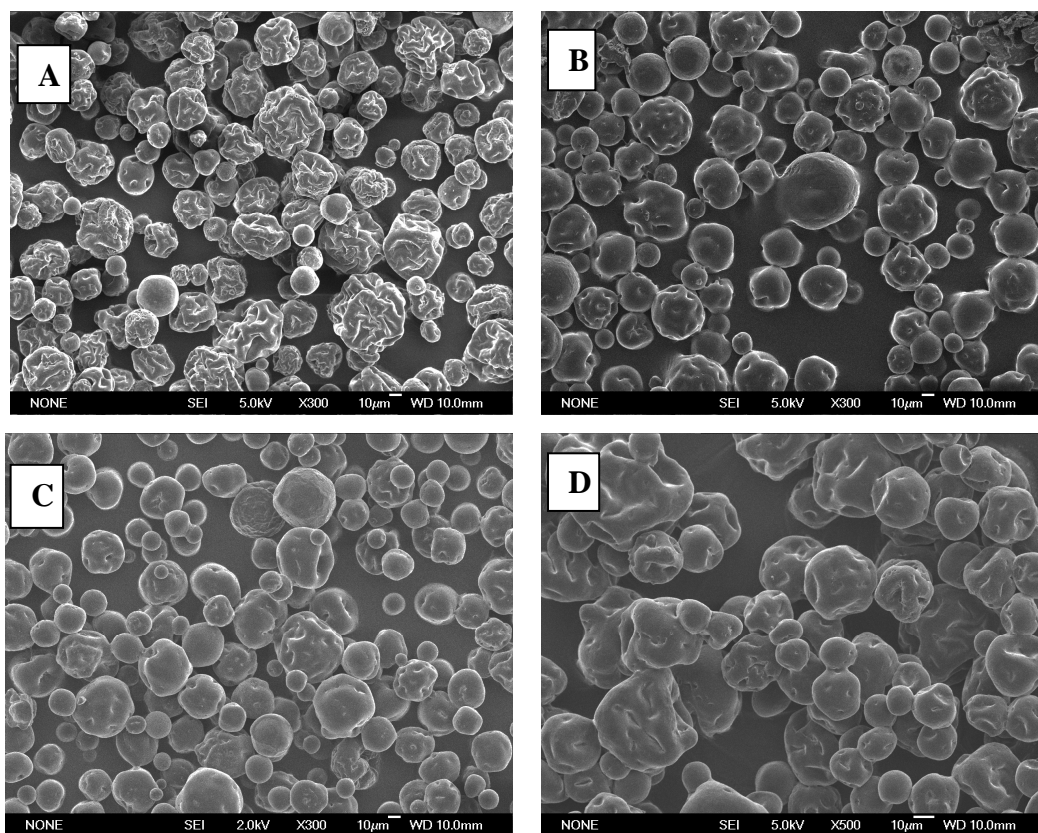


Figure IV-5. SEM micrographs of sugar-based microparticles by SFD. **(A)** TMD; **(B)** TMD/OVA (S3); **(C)** TMD/MSNP-NH₂/OVA (S1); **(D)** TMD/MSNP-OVA. The scale bar is 10 μm .

Table IV-6 Results of microparticles prepared by spray-freeze-drying

Formulation	OVA ($\mu\text{g}/\text{mg}$)	MSNP-NH2 ($\mu\text{g}/\text{mg}$)	Median Size (μm)	Span	Tap density (mg/ml)	Residual water (%)
TMD/MSNP-NH2/OVA (S1)	25	12.5	43.47	0.902	533 \pm 23	0.25 \pm 0.04
TMD/MSNP-NH2/OVA (S2)	25	6.25	42.35	0.775	580 \pm 17	0.23 \pm 0.05
TMD/OVA (S3)	25	0	43.92	0.87	583 \pm 80	0.26 \pm 0.07

It is necessary to investigate the nanoparticle size after a resuspension of the microparticles. The SFD microparticles were dissolved in sodium phosphate buffer (10 mM, pH 7.4) before DLS measurements. The MSNP-NH2 physically coated with OVA in the TMD formulation before spray-freeze-drying process have hydrodynamic sizes of 681 nm (PDI = 0.204) and 307 nm (PDI = 0.250) for MSNP-NH2/OVA = 1/2 and 1/4 (**Table IV-7**), respectively. After re-dissolution in the buffer, the apparent particle sizes decrease to 139 nm (PDI = 0.281) for MSNP-NH2/OVA = 1/2 and 118 nm (PDI = 0.258) for MSNP-NH2/OVA = 1/4. It indicates that SFD process seems to disaggregate MSNP-NH2/OVA nanoparticles. The MSNP-NH2 particles in the re-suspensions of both TMD/MSNP-NH2/OVA microparticles have negative zeta-potentials, indicating that at least a major part of loaded OVA is still attached to the surface of the silica nanopartilces.

Table IV-7 Stability of MSNP-NH2 in the sugar-based SFD microparticles

Sample	Suspension before SFD			Re-suspended after SFD		
	Z-Ave (nm)	PDI	ζ (mv)	Z-Ave (nm)	PDI	ζ (mv)
MSNP-NH2	1398	0.276	6.8	2550	1.000	0.5
TMD/MSNP-NH2/OVA (S1)	681	0.204	-15.4	139	0.281	-17.2
TMD/MSNP-NH2/OVA (S2)	307	0.250	-16.8	118	0.258	-15.5
TMD/OVA (S3)	18	0.574	-7.7	21	0.548	-16.3

Samples were resuspended in PB (10 mM, pH 7.4) for DLS measurements.

The ovalbumin released from the dissolution of SFD microparticles was analysed using SDS-PAGE and SEC-HPLC (**Figure IV-7**). The bands of the SDS-PAGE indicate that the recovered ovalbumin samples from SFD microparticles show no difference to the ovalbumin control. The major band locates between 36.5 kDa and 55.4 kDa, consistent with the specification (~43 kDa) of the producer. Another band located between 66.3 kDa and 97.4 kDa represents the dimers of ovalbumin, which was confirmed by the SEC results (**Figure**

IV-6). There are no obvious bands for additional fragments or oligomers. As seen in **Figure IV-7B**, the ovalbumin monomer contents in different formulations are almost the same, indicating that there is no harmful stress during the SFD process in the formulations.

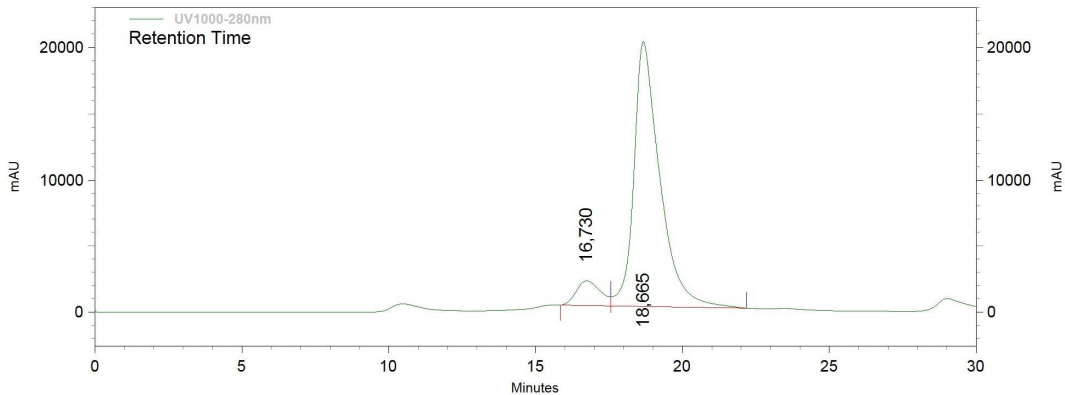


Figure IV-6. SEC-HPLC spectrum of ovalbumin recovered from the TMD/MSNP-NH2/OVA (S1) microparticles.

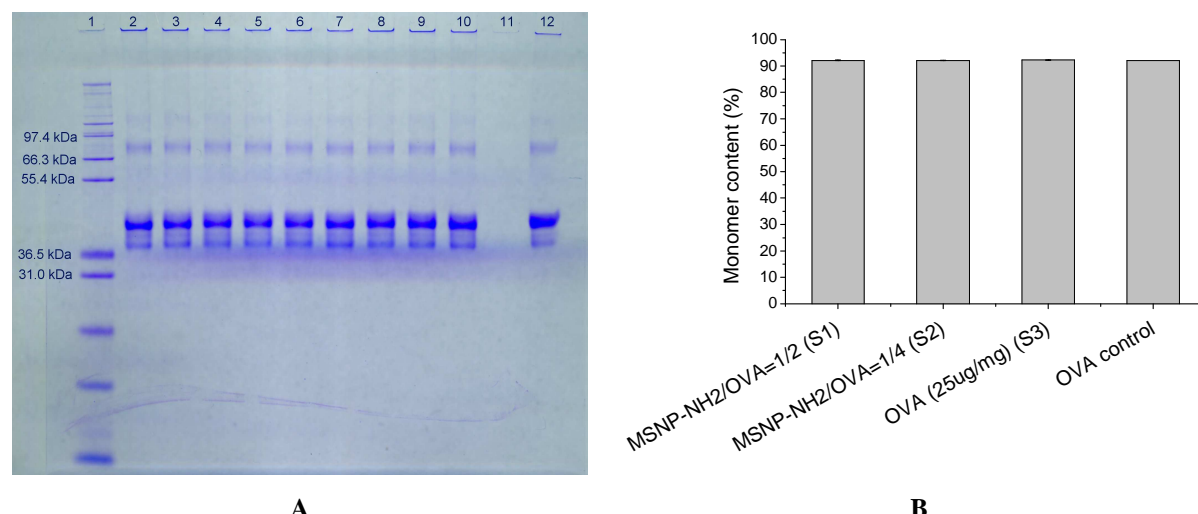


Figure IV-7. Characterisation of ovalbumin in the microparticles. (A) SDS-PAGE of the released ovalbumin formulated in TMD microparticles; (B) Monomer contents of ovalbumin obtained from SEC results. Lane 1 is the Mark12TM(Invitrogen); lanes (2, 5, 8) and lanes (3, 6, 9) correspond to the ovalbumin in the formulation of TMD/MSNP-NH2/OVA (S1) and TMD/MSNP-NH2/OVA (S2), respectively; lane 11 represents formulation of MSNP-NH2 and TMD; lane 12 represents ovalbumin as a control. Three repeats were carried out.

3.5 Epidermal powder injection of the microparticles on model skin and pig skin

Rhodamine B isothiocyanate labeled ovalbumin (RITC-OVA) was added to the formulations of microparticles containing MSNP-NH₂ to visualise the distribution of the added antigen. Both of the formulations containing MSNP-NH₂ and without MSNP-NH₂ were prepared. 20% of the antigen of the formulations was replaced by RITC-OVA. The fluorescence is strong enough to allow observation of the particles. RITC-OVA is evenly dispersed in the TMD/MSNP-NH₂/OVA formulation (**Figure IV-8A**) and the 3D view shows the shrinking on the surface (**Figure IV-8B**). As for the formulation without MSNP-NH₂, the distribution of RITC-OVA is also very good and the surface of microparticles wrinkles as shown in **Figure IV-8 (C, D)**. These microparticles were used for powder injection, enabling observation of depth and distribution by CLSM.

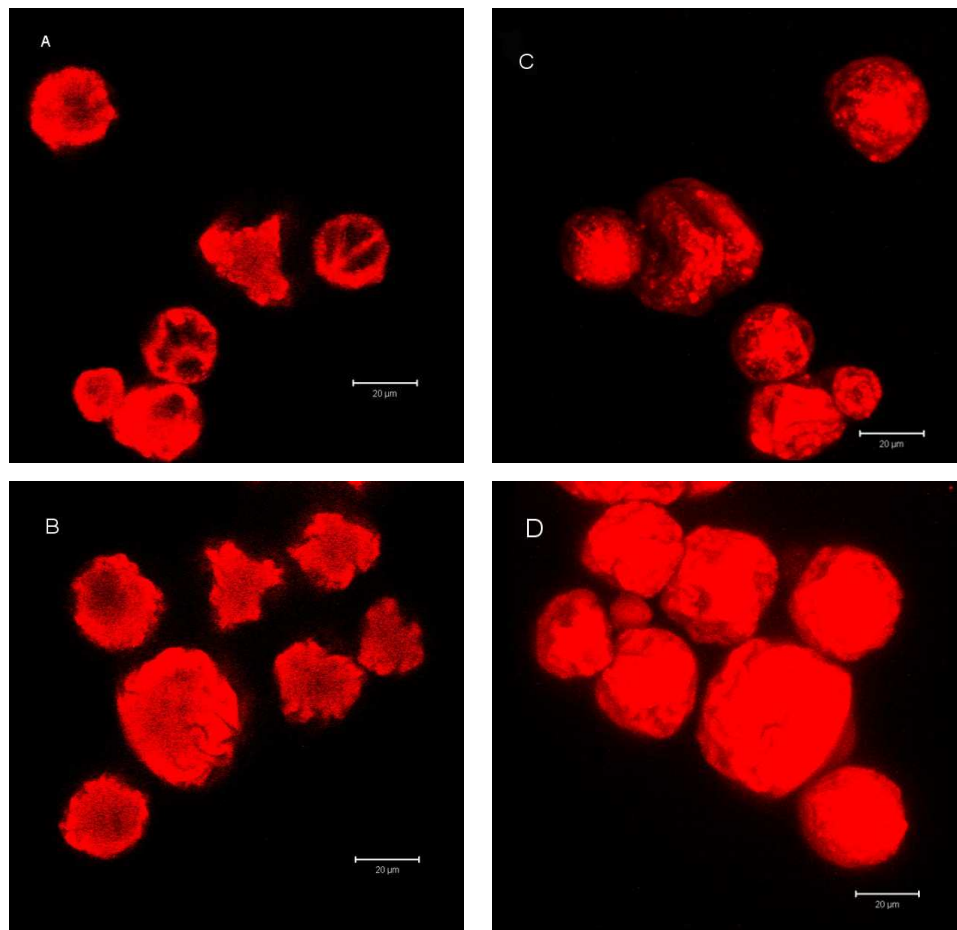


Figure IV-8. CLSM micrographs of fluorescent microparticles. **(A)** Single scan of TMD microparticles containing MSNP-NH₂/(OVA/RITC-OVA) (1/2); **(B)** Single scan of TMD microparticles containing OVA/RITC-OVA; **(C)** 3D view of Z-stacking micrographs of TMD microparticles containing MSNP-NH₂/(OVA/RITC-OVA) (1/2); **(D)** 3D view of Z-stacking

micrographs of TMD microparticles containing OVA/RITC-OVA. The objective of Plan-Apochromal 63 \times /1.4 Oil DIC was used. The scale bar is 20 μ m.

The injection of the microparticles into a gelatin film skin model (see Chapter II) with a gelatin/glycerol (gel/gly) mass ration of 4/6 and pig abdominal skin was carried out by using a custom-made device developed by Dr. Lell (Pyroglobe GmbH, Hettenhausen, Germany). The gelatin film or pig skin surface was labeled by putting a drop of FITC-dextran solution onto the surface showing green colour as seen in **Figure IV-9**. The position and depth of injected particles could then be simply determined as the position of the surface is defined by the FITC-dextran solution. The gelatin film has a smooth surface as the interface between green and black areas is linear. Parts of TMD microparticles have penetrated in the gelatin film, while the shape of the injected particles is preserved as spheres. As for the pig skin, the surface is very rough that can be told from the interface of green and black parts in **Figure IV-9B**. The TMD microparticles dissolved, leaving the diffusion of OVA into the pig skin. The depths of injected TMD microparticles in the gelatin film and pig skin are quite similar. The penetration is not as deep as expected probably due to the too low velocity (about 250 m/s) because model polystyrene (PS) microparticles (42 μ m in diameter) did not penetrate better under the same conditions for delivery. More work on the optimization of the device was needed at that point of the device development.

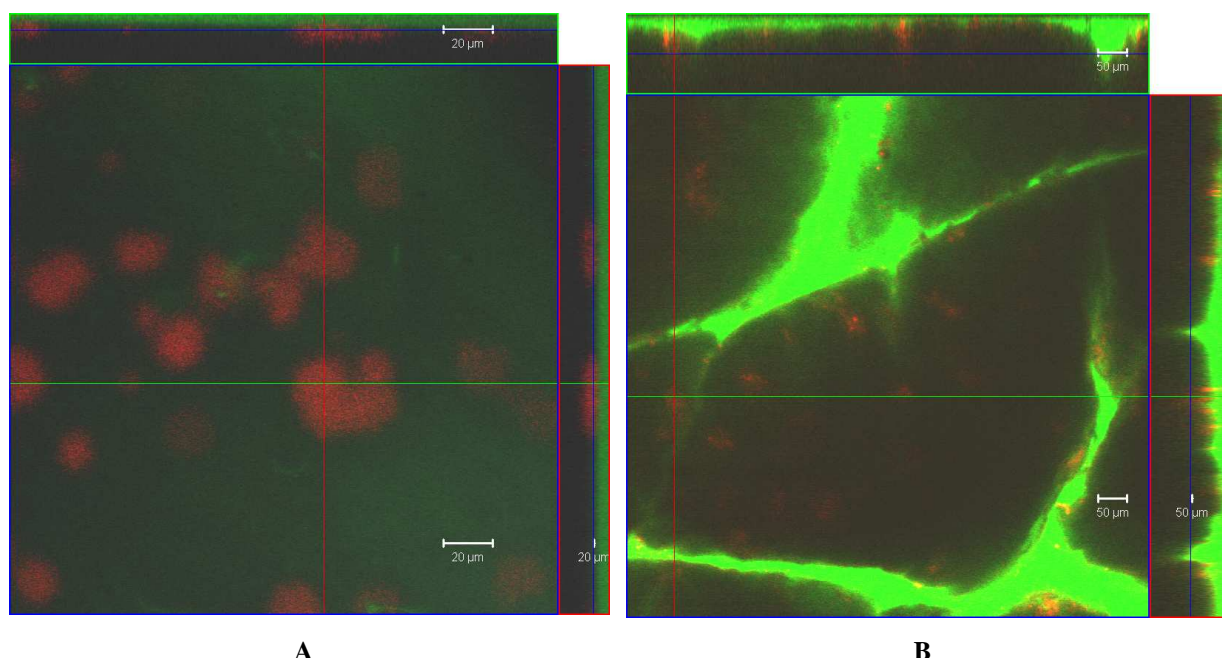


Figure IV-9. Orthogonal sections of Z-stacking micrographs of the microparticles injected into gelatin films (gel/gly = 4/6) (A) and pig abdominal skin (B). TMD microparticles

containing MSNP-NH2 and OVA/RITC-OVA were used. Red represents RITC-OVA and green represents FITC-dextran.

3.6 Cellular uptake of ovalbumin-loaded silica nanoparticles

Cellular uptake of antigens is very important for the process of presentation of the antigen to induce immune response. As an initial test, ovalbumin-loaded silica nanoparticles in the TMD matrix were incubated together with macrophages to study particle uptake. The cell nuclei are stained by 4',6-Diamidino-2-phenylindole (DAPI) showing blue fluorescence under excitation of 364 nm. The substance delivered into the cells should be close to the blue nuclei. The cellular uptake results of fluorescently-labeled OVA or silica nanoparticles (**Table IV-8**) by macrophages at 37 °C are shown in **Figure IV-10**. For samples **A**, **B** and **C**, the solutions were obtained by redissolution of TMD microparticles in PB (10 mM, pH 7.4). For sample **D**, RITC-OVA was loaded on MSNP-NH2 at a mass ratio of 1/10 firstly in HPW and the loaded particles were then added into TMD in PB (10 mM, pH 7.4). For sample **E**, it was prepared as sample **D**, but no TMD was used.

Table IV-8 Summary of the samples for cellular uptake by macrophages

Sample	Particle Con.	RITC-OVA Con.
A : resuspension of TMD/MSNP-NH2/OVA/RITC-OVA	1.0 mg/ml	1.0 mg/ml
B : redissolution of TMD/OVA/RITC-OVA	0	1.0 mg/ml
C : resuspension of TMD/FITC-MSNP-NH2	0.2 mg/ml	0
D : suspension of MSNP-NH2/RITC-OVA (10/1) + TMD	1.2 mg/ml	0.12 mg/ml
E : suspension of MSNP-NH2/RITC-OVA (10/1) without TMD	1.2 mg/ml	0.12 mg/ml

10 µl of solution was added to macrophages and then incubated for one hour at 37 or 0 °C.

RITC-OVA loaded on MSNP-NH2 particles recovered from TMD microparticles was delivered into the cells (**Figure IV-10A**). On the contrary, RITC-OVA recovered from TMD microparticles was not sufficiently taken up by macrophages (**Figure IV-10B**). FITC-labeled MSNP-NH2 (FITC-MSNP-NH2) alone resuspended from TMD microparticles can penetrate into macrophages (**Figure IV-10C**). The MSNP-NH2/RITC-OVA (10/1) in TMD solution (**Figure IV-10D**) can be delivered into macrophages, but the amount of delivered RITC-OVA is low. Almost no RITC-OVA was observed in macrophages for MSNP-NH2/RITC-OVA (10/1) particles in solution without TMD (**Figure IV-10E**). The RITC-OVA amount in samples **D** and **E** is much lower than in sample **A**, which could explain much less RITC-OVA was found in macrophages treated with sample **D** and **E** compared to sample **A**. In a word, it

is reasonable to conclude that cellular uptake of OVA by macrophages can be enhanced by MSNP-NH₂ nanoparticles.

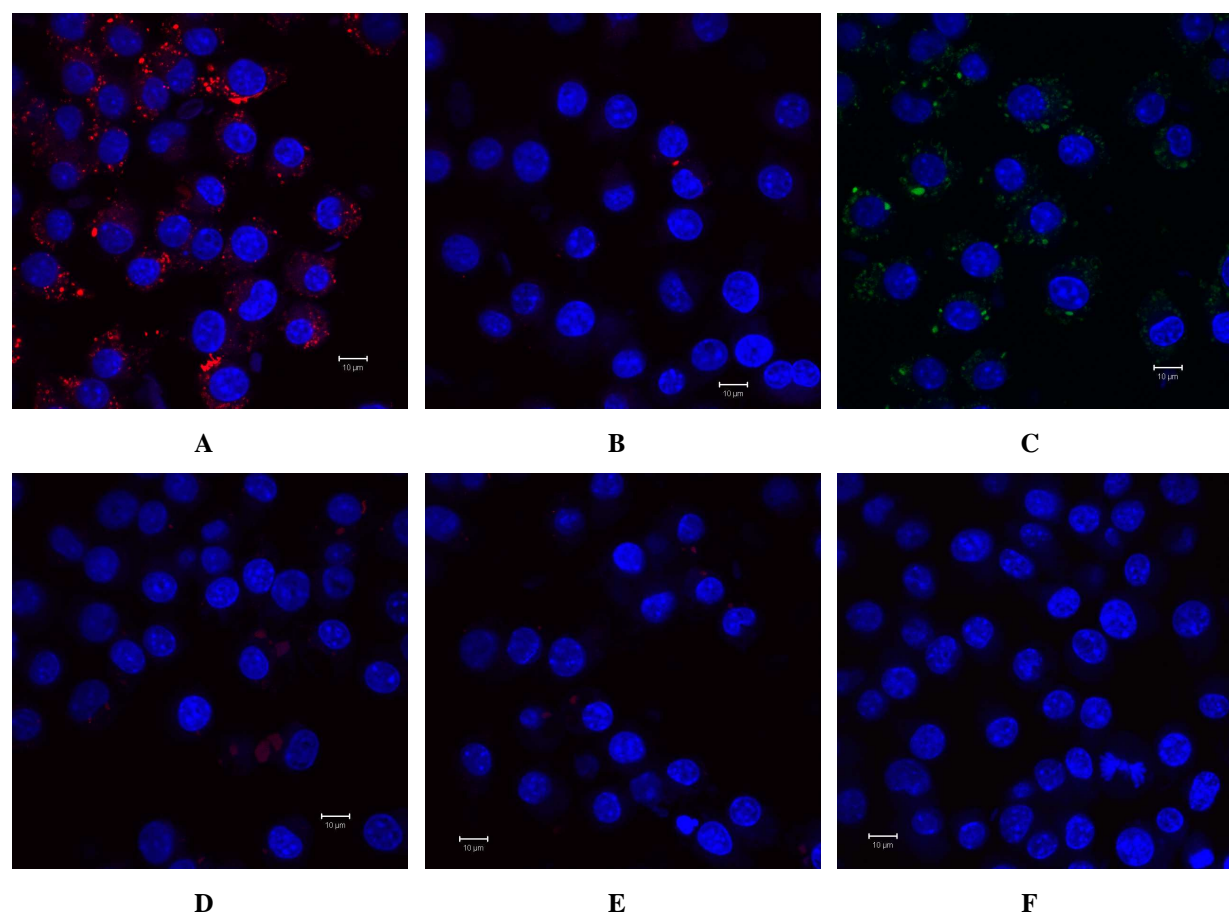


Figure IV-10. Uptake of fluorescent substances by macrophage cells at 37 °C. (A) incubated in resuspension of TMD microparticles containing MSNP-NH₂/OVA/RITC-OVA; (B) incubated in redissolution (1 mg/ml of RITC) of TMD microparticles containing OVA/RITC-OVA; (C) incubated in FITC-MSNP-NH₂ nanoparticles resuspension; (D) incubated in a mixed solution of MSNP-NH₂/RITC-OVA (10/1) and TMD in HPW; (E) incubated in MSNP-NH₂/RITC-OVA (10/1) solution without TMD; (F) incubated in PB (10 mM, pH 7.4) as a negative control. Green indicates FITC-MSNP, red indicates RITC-OVA and blue indicates cell nuclei. The scale bar is 10 µm.

Each sample described in **Table IV-8** was also used for macrophage uptake at 0 °C (**Figure IV-11**). The RITC-OVA loaded on MSNP-NH₂ in TMD particles was taken up by macrophages at 0 °C (**Figure IV-11A**), while no RITC-OVA was found in the formulation without MSNP-NH₂ (**Figure IV-11B**). Very weak signals were observed for MSNP-NH₂/RITC-OVA (10/1) in TMD solution (**Figure IV-11D**) and there are almost no signals for the MSNP-NH₂/RITC-OVA (10/1) suspension without TMD (**Figure IV-11E**). No

signals were observed for the in PB (10 mM, pH 7.4) as a negative control. Less RITC-OVA was found in macrophages at 0 °C than at 37 °C (**Figure IV-10A** and **Figure IV-11A**). It indicates that OVA absorbed on silica nanoparticles are taken up by macrophages at passive and active modes. For FITC-MSNP-NH2 without protein, both passive and active modes were found for cellular uptake (**Figure IV-10C** and **Figure IV-11C**).

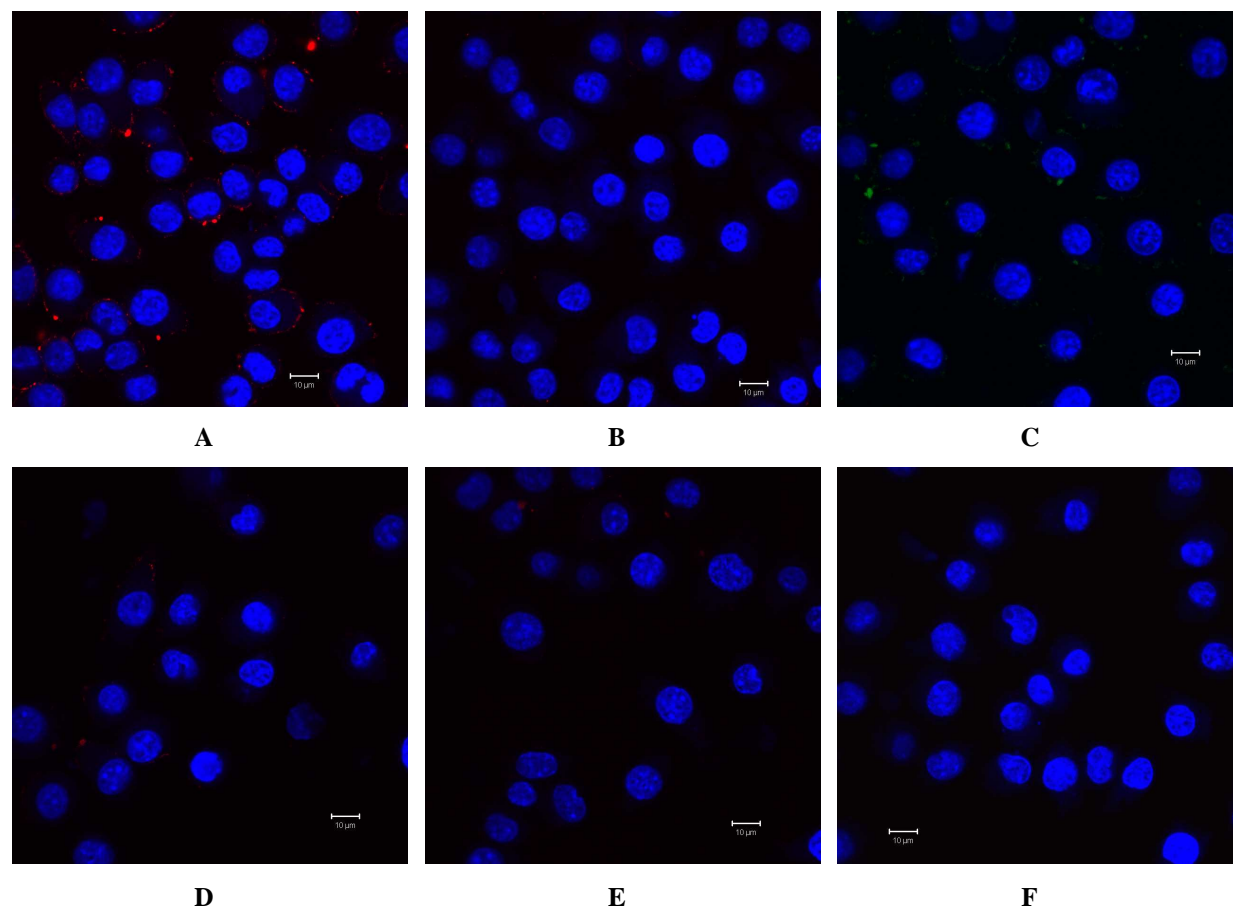


Figure IV-11. Uptake of fluorescent substances by macrophage cells at 0 °C. (A) incubated in resuspension of TMD microparticles containing MSNP-NH2/OVA/RITC-OVA; (B) incubated in redissolution of TMD microparticles containing OVA/RITC-OVA; (C) incubated in FITC-MSNP-NH2 nanoparticles resuspension; (D) incubated in a mixed solution of MSNP-NH2/RITC-OVA (10/1) and TMD in HPW; (E) incubated in MSNP-NH2/RITC-OVA (10/1) solution without TMD; (F) incubated in PB (10 mM, pH 7.4) as a negative control. Green indicates MSNP-FITC, red indicates RITC-OVA and blue indicates cell nuclei. The scale bar is 10 μm.

4. Discussion

4.1 Nanoparticles in microparticles (nano-in-micro) for epidermal powder immunisation

Mesoporous silica nanoparticles with positively charged surface are coated by negatively charged ovalbumin, and then they are encapsulated in sugar-based microparticles. After powder injection into skin, the matrix of the microparticles is dissolved and nanoparticles and antigens are released. The released antigens can then be processed and presented by LCs.

In a first experimental setup, rhodamine B labeled polystyrene (PS-RhB) nanoparticles as model nanoparticles were formulated into TMD microparticles by spray-freeze-drying. The PS nanoparticles were well formulated in the sugar-based matrix (**Figure III-5** in Chapter III) by a simple mixing method. This method for preparation of nano-in-micro systems also works for silica nanoparticles. The small hydrodynamic size of MSNP-NH₂/OVA in TMD microparticles after resuspended (**Table IV-7**) from the microparticles indicates that they are well dispersed in the sugar-based matrix.

4.2 Silica nanoparticles for vaccine delivery

Silica nanoparticles show positive results as a novel adjuvant [98, 99], promoting us to use it as an antigen delivery system. Considering that the model antigen we are using is negatively charged, the mesoporous silica nanoparticles with positively charged surface (130 nm, $\zeta = +22.8$ mv at pH of 5.8) have been chosen. Ovalbumin is too large to enter into the pores, but it can be absorbed on the surface. The plain MSNP has a negatively charged surface and only adsorbed very small amounts of OVA. The loading capacity of MSNP-NH₂ is larger at pH of 4.8 than that at pH of 6.8 because the zeta-potential at pH of 4.8 is more positive. More ovalbumin could be loaded onto MSNP-NH₂ when higher concentration of OVA solution was used, while the loading efficiency decreased with the increasing of OVA concentration (**Table IV-3**). The release of ovalbumin is very fast due to that the main interaction force is electrostatic attraction. This is also the reason why the release is even faster at higher pH and higher concentration of PBS (**Figure IV-4**) because high pH would decrease the zeta-potential of MSNP-NH₂ and high ionic strength would shield the electrostatic interaction to some degree. As an alternative to silica nanoparticles with physically absorbed ovalbumin, ovalbumin was chemically conjugated to the silica nanoparticles by other authors. MSNP-OVA may induce better immune response when processed by LCs as particulate systems could be more easily recognised as dangerous signals [81].

MSNP-NH₂ has a positive zeta-potential (+22.8 mv) in PB (10 mM, pH 5.8) making a well dispersed suspension. The zeta-potential becomes close to neutral when more and more ovalbumin is adsorbed to the surface and thereby the aggregation propensity is increased. The aggregation is expectedly high when less ovalbumin is used, as in the case of MSNP-NH₂/OVA mixtures with mass ratios of 4/1 and 2/1 (**Table IV-4**). In this circumstance, ovalbumin may act like a glue to bind MSNP-NH₂ together. The aggregation problem can be minimized by increasing the amount of OVA relative to MSNP-NH₂, as in the case of MSNP-NH₂/OVA mixtures with mass ratios of 1/2 and 1/4 (**Table IV-4**). On the other hand, a centrifugation process needs to be avoided not to increase amount of the aggregates further. That is why MSNP-NH₂ and ovalbumin were mixed directly and formulated together into sugar-based microparticles without removing the free ovalbumin. Actually, the excessive amount of ovalbumin can ensure the particles are entirely surrounded by OVA. It may increase the stability of MSNP-NH₂/OVA as a protection layer surrounding the particles is formed. The mixing of MSNP-NH₂/OVA and TMD has no obvious effect on the size but increases the PDI (**Table IV-5**). Interestingly, the MSNP-NH₂/OVA resuspended from the SFD microparticles have smaller sizes (~130 nm) (**Table IV-7**) than MSNP-NH₂/OVA and TMD in solution before SFD (~450 nm) (**Table IV-5**). OVA is still absorbed on MSNP-NH₂ as the zeta-potential of the particles in redissolution of the TMD microparticles is negative (-16 mv). It seems that spray-freeze-drying process can improve the stability of MSNP-NH₂/OVA in the formulation.

4.3 Microparticles with encapsulated silica nanoparticles and ovalbumin meeting the requirements for epidermal powder immunisation

The matrix of trehalose, mannitol and dextran is water soluble so that the microparticles can be dissolved after EPI delivery into skin. The ovalbumin and MSNP-NH₂ can be released like “sub-bullets” as shown in the schematic diagram (**Figure III-1** in Chapter III). This matrix has already shown the ability of stabilizing protein structures and functions [106, 107, 109]. The same fact was observed in our formulations, as indicated from the SDS-PAGE and SEC results of recovered ovalbumin. Furthermore, the low water residue (around 0.25 wt%) in the formulations (**Table IV-6**) could increase the storage stability in a long-term period. As elucidated by the mechanisms of particle impact on skin using a theoretical model, particle impact parameter $\rho v r$ (unit in kg/m·s, ρ is the density of particles, v is the particle impact velocity, r is the radius of particles) determines the penetration [12], estimated 7 kg/m·s as a threshold for breaching the stratum corneum. Most of the microparticles we prepared have

diameters around 40 μm and tap density around 580 mg/ml. $\rho v r$ can be calculated as 8.7 kg/m \cdot s assuming the speed of the microparticles is 750 m/s.

$$\text{Impact parameter} = \rho \times v \times r \quad (2)$$

The microparticles are expected to breach the stratum corneum of skin as the impact parameter (8.7 kg/m \cdot s) is larger than the threshold (7 kg/m \cdot s). Once the skin barrier is breached, the antigens and silica nanoparticles can be dissolved and diffuse into the viable epidermis.

The shrinkage of the particles during drying as seen from the SEM micrographs is very important for increasing the density and mechanical robustness. In order to increase the density of microparticles, high concentration of TMD (35.0 wt%) was used to prepare the formulations for spray-freeze-drying. The cause of the shrinking was attributed to the plastic flow of the TMD phase when the shelf temperature ($T_s = -10^\circ\text{C}$) for primary freeze-drying exceeds the glass transition temperature (T_g') of the frozen SFD microparticles [132]. As seen in **Figure IV-5**, the TMD without ovalbumin shows more obvious shrinkage compared to the formulations containing ovalbumin, indicating that added ovalbumin could increase the T_g' . Increasing the temperature for primary freeze-drying can increase the degree of shrinkage, but may result in collapse of the product that is not good for the flowability of the microparticles.

4.4 Antigen-loaded nano-in-micro particles for epidermal powder immunisation

The encapsulation of ovalbumin and MSNP-NH₂ nanoparticles in TMD microparticles is very efficient as proved by observing the formulations containing RITC-OVA. The fluorescence intensity of RITC-OVA is so strong that the surface of microparticles is clearly imaged.

The TMD microparticles containing RITC-OVA have been accelerated to penetrate gelatin films and pig skin by our custom-made device, but the penetration depth is still too low. The same result has been obtained when using PS microparticles by the same device. Therefore, the insufficient penetration of TMD microparticles may result from the velocity of the accelerated particles, which is not high enough due to the limitation of the device at that moment. The optimisation of the device is still going on, and progress is expected in the short term. Due to the high water content in pig skin, the TMD microparticles were dissolved after injection. This is useful especially when the sudden penetration is not as deep as required. If

the stratum corneum (about 15 μm for human skin) could be penetrated, the ovalbumin may diffuse deep itself because the main biological barrier has already been broken.

Ovalbumin has been delivered into macrophage cells at 37 and 0 $^{\circ}\text{C}$ with the assistance of MSNP-NH2 in one hour as indicated in **Figure IV-10**. More RITC-OVA in the TMD/MSNP-NH2/OVA/RITC-OVA formulation was delivered into macrophages at 37 $^{\circ}\text{C}$ than at 4 $^{\circ}\text{C}$, indicating that active uptake exists. On the other hand, RITC-OVA was also taken up with MSNP-NH2 in the TMD matrix by macrophages at 0 $^{\circ}\text{C}$. It means that a passive mode is also the route for uptake by macrophages. For FITC-MSNP-NH2 nanoparticles without protein, they have also been taken up by macrophages at both passive and active modes. Therefore, silica nanoparticles play a major role in enhancing the cellular delivery of ovalbumin. In fact, silica nanoparticles helping to deliver macromolecules into cells was also found by others [152]. These results support the idea of using silica nanoparticles for vaccine delivery in the TMD microparticles for EPI.

5. Conclusion

Cationic mesoporous silica nanoparticles have been prepared as a vaccine delivery system. Negatively charged antigens such as ovalbumin can be loaded on the surface through electrostatic interactions. The release of ovalbumin is mainly a displacement process from electrostatic bindings by salt, depending on the elimination speed of ovalbumin, the pH and ionic strength of solution. Ovalbumin and MSNP-NH2 have been formulated in sugar-based microparticles that are suitable for epidermal powder immunisation. The silica nanoparticles resuspended from the spray-freeze-dried (SFD) microparticles show a hydrodynamic size close to the actual size, indicating that the sugar matrix can stop the aggregation of nanoparticles when they are dried. In the redissolution of TMD microparticles containing MSNP-NH2/OVA, OVA is still coated on the surface of MSNP-NH2 as the zeta-potential is negative. The ovalbumin recovered from the microparticles maintains the integrity as well. Therefore, nanoparticles-in-microparticles (nano-in-micro) systems, combining the advantages of nanoparticles for vaccine delivery and the method of needle-free epidermal powder immunisation, can be prepared by spray-freeze-drying and used for EPI.

In the present study, silica nanoparticles and TMD matrix were used to prepare the microparticles for epidermal powder immunisation. In fact, the nano-in-micro idea is not limited to the materials used in this study. Other nanoparticles for vaccine delivery and matrix

materials can be chosen to obtain the nano-in-micro microparticles which can release antigens in an appropriate timeline. In a word, this method gives the possibility to deliver nanoparticulate vaccine delivery systems and adjuvants via ballistic delivery into skin.

Chapter V. Formulation of H1N1 Hemagglutinin and Silica Nanoparticles in Sugar-based Microparticles

1. Objectives

As described in Chapter IV, cationic mesoporous silica nanoparticles (MSNP-NH₂) have been successfully used for a model antigen, ovalbumin (OVA), in the sugar-based microparticles made of trehalose, mannitol, dextan (9-10 kDa) and dextran (100 kDa) (TMD). The TMD microparticles encapsulating OVA and MSNP-NH₂ particles have a size range of 10-40 µm, mainly of 20-30 µm. They are suitable for epidermal powder immunisation (EPI). The stability of the nanoparticles and OVA in the formulation of microparticles has been proved to be good. Ovalbumin is a good model antigen for studying the formulation and immune response, but it is more stable than some real protein antigens such as influenza hemagglutinin [160, 161]. The formulation stabilising OVA must not necessarily be applicable to some real antigens.

Influenza vaccines are the most popular and extensively used in the world. The occurrence of influenza is impossible to predict, thus a large amount of influenza vaccines needs to be formulated, produced, and reserved every year in case it happens. Until now, the influenza vaccines on the market are all liquid formulations, leading to some disadvantages such as cold-chain transportation and storage, short shelf life, etc. [162-164]. For example, influenza subunit vaccine showed a strongly increased degradation rate of haemagglutinin when the storage temperature was increased from 5 °C to 25 °C [162]. Therefore, it is necessary to develop solid formulations of influenza vaccines that have better stability during a long-term stability and economic distributions. Furthermore, influenza vaccines in a solid form of powder or microparticles give some chances for novel administration routes, i.e. nasal delivery, intradermal or epidermal delivery.

Influenza hemagglutinin is an antigenic glycoprotein, found on the surface of the influenza viruses. The viruses bind to cells by the interaction of HA proteins and the sialic acid on the membranes [160]. Influenza virus or HA proteins separated from viruses have the ability to cause agglutination of erythrocytes (red blood cells). There are many subtypes of HA antigens depending on the species where the viruses were found, e.g. H1, H2 and H3 are found in

human influenza viruses. The monomers of HA have a molecular weight of about 62 kDa, dimers and trimers also exist as indicated from SDS-PAGE bands [165, 166]. HA monomers (HA0) can be cleaved into two smaller subunits of the HA1 and HA2, under reducing conditions of SDS-PAGE [165].

A real vaccine was chosen to study the stability and biological activity of the antigens in TMD formulation. The Pandemrix® suspension as an influenza vaccine (H1N1) (split virion, inactivated, adjuvanted), produced by GlaxoSmithKline (GSK), has been used in Germany in 2011. Pandemrix® was obtained from the Bavarian State Ministry of Environment and Public Health. The antigen suspension before mixing with an adjuvant contains 15 µg of hemagglutinin (HA) per 1.0 ml. This antigen suspension and the suggested adjuvant emulsion AS03 are mixed at a volume ratio of 1:1. 0.5 ml of the mixture is used as the dose for humans. The H1N1 HA has been used to study the formulation of microparticles for EPI due to its sensitivity and the availability of the vaccine. The main objective of this chapter is to encapsulate H1N1 HA and silica nanoparticles in TMD microparticles and to investigate the stability of H1N1 HA in the formulation. The interaction between H1N1 HA and MSNP-NH2 was studied and the biological activity of HA in TMD microparticles was determined.

2. Materials and Methods

2.1 Materials

Pandemic influenza vaccine, Influenza A/California/7/2009 (H1N1)v-like strain (X-179A), known as Pandemrix®, was produced by GlaxoSmithKline Biologicals s.a. (Rixensart, Belgium). One pack of Pandemrix® consists of one pack containing 50 vials of 2.5 ml suspension (antigen) (15 µg/ml HA) and two packs containing 25 vials of 2.5 ml emulsion (adjuvant). Pandemrix® requires mixing of the antigen suspension and adjuvant emulsion with the same volume. A volume of 0.5 ml of Pandemrix® after mixing has been suggested for adults. The adjuvant of AS03 contains squalene, DL-a-tocopherol and polysorbate 80. The other ingredients in Pandemrix® are octoxynol 10, thiomersal, sodium chloride, disodium hydrogen phosphate, potassium dihydrogen phosphate, potassium chloride, magnesium chloride, water. The antigen suspension (15 µg/ml HA) before mixing is used for our research herein.

Micro BCA™ Protein Assay Reagent Kit (PIERCE) was purchased from Thermo Fisher

Scientific (Rockford, IL Campus, USA). VivaSpin® 20 (5kDa cut-off) tubes were purchased from Sartorius Stedim Biotech GmbH (Goettingen, Germany). Polysorbate 80, TritonX-100 and Tween 20 were obtained from Sigma-Aldrich (Steinheim, Germany). Phenomenex Jupiter 300 (5 µm, C18) was purchased from Phenomenex (Aschaffenburg, Germany). NuPage 10% Bis-Tris-Gel and Nitrocellulose membranes were obtained from Invitrogen, Life Technologies Corporation (Carlsbad, USA). An Anti-influenza A H1N1 Hemagglutinin (HA) monoclonal antibody (MAb) was obtained from Sino Biological (Beijing, China). IRDye 800CW conjugated goat Anti-Mouse IgG, was from LI-COR Biosciences (Lincoln, USA). Chicken erythrocytes (25% whole blood suspension in Alsever's buffer), also called red blood cells (RBCs), Dextrose-gelatin-veronal (DGV) buffer and Agglutest buffer (for haemagglutination inhibition tests) was purchased from LABOR DR.MERK & KOLLEGEN GmbH (Ochsenhausen, Germany).

2.2 Methods

2.2.1 Concentrating of H1N1 hemagglutinin by ultrafiltration

The H1N1 HA protein has molecular weight above 50 kDa [165], thus VivaSpin 20 with a molecular cut-off of 5 kDa was used to concentrate the H1N1 HA protein. VivaSpin tubes containing about 20 ml of Pandemrix® vaccine for each were centrifuged for 2 hours under a swing-out mode at a speed of 5000×g (Sigma 4K15 centrifuge, SIGMA Laboratory Centrifuges, Shropshire, UK). More original vaccine solution was added after the previous concentrating process. 250 ml of original vaccine solution was concentrated to about 3 ml. Finally, the buffer was changed into a freshly prepared KH₂PO₄-Na₂HPO₄-MgCl₂-polysorbate 80-tritonX-100 (KNaMgPT) buffer (pH 7.0), which was prepared by dissolving 0.694 g of KH₂PO₄, 1.0705 g of Na₂HPO₄·2H₂O, 0.025 g of MgCl₂·6H₂O, 0.4 g of polysorbate 80 and 0.2 g tritonX-100 in 1L of high-purified water (HPW) and filtering with 0.2 µm membrane (Sartorius Stedim Biotech GmbH, Goettingen, Germany). The concentrated H1N1 HA in KNaMgPT buffer was stored at 4 °C for subsequent use.

2.2.2 Determination of H1N1 HA concentration

2.2.2.1 Bicinchoninic acid assay (BCA) assay

2.0 mg/ml BSA was used to prepare the standards for BCA assay, including BSA concentrations of 180, 90, 22.4, 11.2, 5.6, 2.8, 1.4 and 0 µg/ml. The concentrated HA was diluted 10 fold before used for BCA assay. The micro BCA working reagent (WR) was

prepared according the instructions of the assay kit. 150 µl of each standard and sample was added to the 96-well plate and then 150 µl of WR was added into the wells. The 96-well plate was shaken at 600 rpm (Thermo Scientific Sorvall ST 16R, Dreieich, Germany) for about 30 s before incubated at 37 °C (UL 50, Memmert, Schwabach, Germany) for 2 hours. After that, the plate was cooled at room temperature and centrifuged at 1000×g in case some air bubbles were observed. The absorbance at 562 nm of each well was measured using a plate reader (Fluostar Omega, BMG LABTECH GmbH, Ortenberg, Germany).

2.2.2.2 Reversed phase high-performance liquid chromatography (RP-HPLC)

RP-HPLC was used to determine the H1N1 HA concentration. A Phenomenex Jupiter 300 (5 µm, C18 column) was used. 0.1%TFA in highly purified water was used as the mobile phase A (Eluent A), while 0.1% TFA in 75% isopropanol and 25% acetonitrile as the mobile phase B (Eluent B). Flow rate is 1.0 ml/min. The elution gradient is shown in **Figure V-1**. A fluorescence detector (excitation 280 nm / emission 335 nm) (DIONEX RF 2000, Idstein, Germany) was used, with a sensitivity that is sufficient to measure the vaccine concentration as low as 3.75 µg/ml. The spectrum of each sample was obtained by subtracting the signals from the buffer. The original vaccine with a H1N1 HA concentration of 15 µg/ml was used as the standard. The concentrated H1N1 HA was diluted 10 fold before used for measurement in case the high concentrated protein may overload the column.

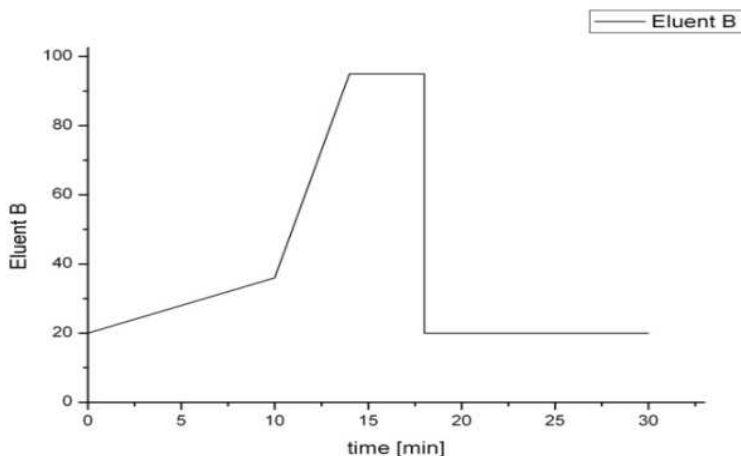


Figure V-1. Gradient of mobile phase A (Eluent A) and mobile phase B (Eluent B) for elution.

2.2.3 Size and zeta-potential measurements

The details for the measurement of the sizes and zeta-potentials have been described in Chapter IV. Briefly, 1.0 ml of 0.2 mg/ml MSNP-NH2 in PB buffer (10 mM, pH 5.8) was used to mix with a specific volume (0.114 ml, 0.228 ml or 0.457 ml) of 1.75 mg/ml HA in KNaMgPT buffer (10 mM, pH 7.0). The mass ratios of MSNP-NH2 and HA include 1/1, 1/2 and 1/4. The obtained mixtures were directly used for DLS measurements. To study the silica nanoparticles in TMD microparticles, 15 mg of microparticles was dissolved in 1 ml of KNaMgPT buffer (10 mM, pH 7.0) before DLS measurements.

2.2.4 Loading of H1N1 HA on silica nanoparticles (MSNP-NH2)

0.2 ml of 2 mg/ml MSNP-NH2 in PB buffer (10 mM, pH 5.8) and 0.2 ml of H1N1 HA in KNaMgPT buffer (10 mM, pH 7.0) were mixed together in a 1.5ml-EP tube by gentle hand-shaking. HA solutions including 0.180, 0.325 and 0.548 mg/ml were used to study the loading under different concentrations of HA. One hour after the mixing, the EP tubes were centrifuged at 14 000 rpm for 10 min (Sigma 4K15 centrifuge, SIGMA Laboratory Centrifuges, Shropshire, UK). The HA concentration in the supernatant of each sample was measured by BCA assay. The loading amount was calculated as following:

$$\text{Loading capacity} = \frac{\text{added HA amount} - \text{supernatant HA amount}}{\text{MSNP - NH2 amount}} \quad (1)$$

2.2.5 Encapsulation of H1N1 HA and silica nanoparticles in TMD microparticles by spray-freeze-drying

Concentrated H1N1 HA solution was used to prepare TMD microparticles. Trehalose·2H₂O, Mannitol, Dextran (9-10 kDa) and Dextran (150 kDa) were mixed at a mass ratio of 3:3:3:1 and then H1N1 HA solution was added to dissolve the matrix by occasional shaking. The solid content of H1N1 HA in the TMD microparticles was kept to about 4 µg/mg. For the formulation containing silica nanoparticles, 0.010 ml of 50 mg/ml MSNP-NH2 in PB buffer (10 mM, pH 5.8) was added to obtain a MSNP-NH2/HA mass ratio of 1/4. The mixtures were then spray-freeze-dried using the same process as described in Chapter IV. Briefly, an ultrasonic atomizing nozzle (120 kHz, Sono-Tek, Milton, USA) was used. The power for spraying was set to 4.5 watts and the flow rate of the peristaltic pump to 0.6 ml/min. The microparticles sprayed into liquid nitrogen were collected in vials and transferred to a pre-cooled lyophiliser at -55 °C (Martin Christ EPSILON 2-6D, Harz, Germany). The freeze-drying step includes 24 hours of primary drying at -10 °C and 20 hours of secondary drying at

25 °C. The chamber pressure was kept at 0.12 mbar during the whole drying process. After that, dry nitrogen gas was filled into the chamber before closing the vials.

2.2.6 SDS-PAGE and western blot of H1N1 HA

HA was formulated in TMD microparticles by SFD. 10 mg of the microparticles were dissolved in 0.2 ml of KNaMgPT buffer (10 mM, pH 7.0). Concentrated HA solution was diluted 10 fold before used as a control.

Buffers for SDS-PAGE:

Electrophoresis running buffer was obtained by mixing 30 ml of NuPage® MES SDS Running Buffer (20×) and 570 ml of HPW water. Sampling (loading) buffer for non-reducing conditions was prepared by mixing 25 ml of 1.0 M Tris, 4 g of SDS; 23 ml of glycerol (87%) and 1.0 ml of bromophenol blue (0.1%), and adjusting the pH to 6.8 and total volume to 100 ml with HPW water. Sampling buffer for reduced condition was prepared by dissolving DL-dithiothreitol (DTT) in the non-reducing sampling buffer at a concentration of 50 µg/ml.

40 µl of each sample and 60 µl of sampling buffer were mixed and then incubated at 95 °C for 20 min. 10 µl of each sample was added to the NuPage® 10% Bis-Tris-Gel (Invitrogen) and 4 µl of Marker 12™ Unstained Protein Standards (Life Technologies) was added. For the gel used for western blot afterwards, the same amount of each sample was added and 2 µl of the MagicMark™ XP Western Protein Standard (Life Technologies) was added. After running about 1.5 hours at 80 mA, the gel for SDS-PAGE was stained with Imperial™ Protein Stain (Thermo Scientific) and the other gel was used for western blot.

After the SDS-PAGE step, transferring of protein from the gel to nitrocellulose membrane was carried out. Different layers including a nitrocellulose membrane, a fiber pad and a filter paper were stacked together and then placed in the chamber for electrophoretic transferring under a cooled condition. The transferring was done by adding a voltage of 75 V for 2h. After transfer, the membrane was placed into a small box with the protein side facing up. Ponceau red staining solution was added to check if the blotting is successful (about 1 min). The membrane was washed once using water and subsequently blocking buffer was added. The blocking was done by shaking at RT for 90 min. The membrane was washed once with TBST washing buffer. The primary antibody was added to the small box containing the membrane. The box was shaken gently overnight at a 4 °C room. On the second day, the primary antibody

solution was poured into a tube for reuse next time and the membrane was washed three times using TBST buffer to get rid of excessive unbound antibodies. The membrane was incubated in the solution of the secondary antibody in dark under shaking for 1 hour at room temperature (RT). The secondary antibody was recovered for reuse and the membrane was washed 4 times (5 min for each) at RT with PBS+0.1% Tween 20 under gentle shaking. The membrane was rinsed in PBS to remove residual Tween 20. Finally, the membrane was scanned using an odyssey imaging system (LI-COR Biosciences, Lincoln, USA). The buffers and antibodies used include are shown in **Table V-1**.

Table V-1 Buffers and antibodies for western blot

Buffer or antibody	Description
Transferring buffer	25 mM tris-HCl, 192 mM glycine and 20% methanol, pH 8.3: Add 200 ml methanol in 700 ml HPW H ₂ O. Dissolve 3.03g Tris base (Mwt. 121.2 g/mol), 14.42g Glycine (Mwt. 75.07 g/mol) in this water-methanol solution. Adjust pH to 8.3 by concentrated HCl and complete the final volume to 1 L with water.
Blocking buffer	TBST + 5% skim milk (i.e. 2.5g skimmed milk in 50ml TBST)
1X TBS buffer	Tris-HCl buffer saline, pH 7.6 2.42 g Tris base and 8 g NaCl were in 1 L of HPW H ₂ O. Adjust pH to 7.6 (with concentrated HCl).
TBST (Washing buffer):	1X TBS + 0.1% Tween 20 (i.e. 1 ml Tween 20 in 1L 1X TBS)
Primary antibody	Anti-influenza A H1N1 Hemagglutinin (HA) monoclonal antibody (MAb) (Sino Biological, 1.5 g/μl)
Secondary antibody	IRDye 800CW conjugated goat Anti-Mouse IgG (Licor, 1.0 g/μl)

2.2.7 Hemagglutinin inhibition (HAI) assay

Hemagglutinin inhibition (HAI) assay was firstly developed by Hirst [167]. Biologically active HA will bind to red blood cells, causing the formation of a lattice. Inactive HA can not bind the red blood cells, which will sink to the bottom and form a button. Fresh red blood cells (RBCs) (LABOR DR.MERK & KOLLEGEN GmbH, Ochsenhausen, Germany) were diluted to 0.5% (v/v) for subsequent use. A 96-well plate with round-bottom wells was used for the assay. 50 μl of PBS buffer was added into each well except the first column (A1-H1). One row of the 96-well plate is used for one sample with different dilutions. 100 μl of samples and controls were added into the first column (A1-H1). 50 μl solution of each well from the first column was transferred to the second column (A2-H2) to obtain the 1/2 diluted sample. After mixing in the wells (A2-H2), 50 μl solution of each well was added to the wells

(A3-H3) to obtain the 1/4 diluted sample. By this way, a series of dilutions from 1 to 1/2048 for each sample was prepared. Afterwards, 50 μ l suspension of RBCs (0.5%, v/v) was added into each well. The 96-well plate was shaken for a short time (around 1 min) (Heidolph, Schwabach, Germany) and then stored in an incubator (Memmert, Schwabach, Germany) at 25 °C for 30 min. Subsequently, the microplate was put at RT for 10 min before a photo was taken by a camera (CASIO, Japan) to observe the red buttons formed on the bottom of the wells.

3. Results and Discussion

3.1 Influenza hemagglutinin obtained from the vaccines

Influenza A/California/7/2009 (H1N1)v-like strain (X-179A), split-virion inactivated influenza vaccine Pandemrix® was used to prepare concentrated H1N1 HA by ultrafiltration. The concentrated H1N1 HA was diluted 10 fold and then was used for concentration determination by micro BCA assay. Considering the disturbance of polysorbate 80, the absorption resulting from the buffer containing polysorbate 80 was subtracted. Afterwards, HA concentration was calculated from the standard curve of BSA standards. Three batches of concentrated H1N1 HA were prepared as shown in **Table V-2**.

Table V-2 Concentration of concentrated H1N1 HA solution

Sample	Batch 1	Batch 2	Batch 3
Concentrated H1N1 HA	2.00 mg/ml	1.50 mg/ml	1.75 mg/ml

The HA concentration of the samples obtained in our study by ultrafiltration is about 1-2 mg/ml. This concentration can be used to prepare TMD microparticles containing a HA content lower than 5 μ g/mg, is still too low to prepare TMD microparticles with a higher content of HA. Ultrafiltration is good for concentrating a small amount of HA, but is not convenient for scaling up. Tangential flow filtration (TFF) is more suitable for preparing a large batch of concentrated vaccine antigens [168]. Highly concentrated HA (up to 28 mg/ml) has been reported to be prepared by TFF without compromising HA stability [168]. This ensures that HA concentration can be used to prepare TMD microparticles or other solid formulations containing a HA content up to 80 μ g/mg, which is sufficient for intradermal immunization [169].

3.2 Interaction of H1N1 hemagglutinin and cationic mesoporous silica nanoparticles

The interaction of H1N1 HA and cationic mesoporous silica nanoparticles (MSNP-NH2) was investigated to estimate the loading amount of HA on MSNP-NH2 and the effect of HA on the particle size. MSNP-NH2 nanoparticles, having a size of 130 nm and pore size of 2.5 nm, were prepared as described in Chapter IV. 2.0 mg/ml of MSNP-NH2 in PB buffer (10 mM, pH 5.8) was prepared. 0.2 ml of the MSNP-NH2 suspension was mixed with 0.2 ml of HA solution having different concentrations of antigens, which were diluted from concentrated HA stock (1.75 mg/ml). **Table V-3** shows the loading amounts determined by supernatant analysis at different HA concentrations. The mixtures of HA and MSNP-NH2 with mass ratios of 1/30, 1/15, 1/7.5 and 1/3.75 were prepared, respectively. The load amount of HA on MSNP-NH2 increases with the increasing HA concentration, while the loading efficiency changes slightly.

Table V-3 Summary of loading of HA on silica nanoparticles

Sample	MSNP-NH2 (mg/ml)	HA Con. (μ g/ml)*	Loading amount (mg/mg)	Loading efficiency (%)
HA/silica = 1/30 (w/w)	1.0	34	0.009	25.6
HA/silica = 1/15 (w/w)	1.0	67	0.020	29.6
HA/silica = 1/7.5 (w/w)	1.0	142	0.047	32.8
HA/silica = 1/3.75 (w/w)	1.0	296	0.112	37.8

*HA Con. represents the HA concentration in the mixed solution of 0.2 ml MSNP-NH2 particles and 0.2 ml HA solution.

H1N1 HA can be absorbed on the silica nanoparticles, but the effect of HA on the size and zeta-potential of MSNP-NH2 needs more investigation. The mixture solutions of different ratios of HA and MSNP-NH2 were prepared by adding different volumes of 1.75 mg/ml HA into 1.0 ml of 0.2 mg/ml MSNP-NH2 in PB buffer (10 mM, pH 5.8). DLS results including Z-Ave size, PDI and zeta-potential (ZP) are shown in **Table V-4**. MSNP-NH2 nanoparticles have a positive ZP, but change to a negative ZP when H1N1 HA was added in the formulation. HA protein is negatively charged around neutral pH, it could be absorbed on positive surfaces of MSNP-NH2, leading to negative surfaces of MSNP-NH2/HA. This is similar to the case of ovalbumin as described in Chapter IV. The loading tests reported above confirm that HA can be absorbed onto MSNP-NH2 nanoparticles.

Table V-4 DLS results of silica nanoparticles in different concentrations of HA

Sample	Z-Ave (d.nm)	PDI	ZP (mV)
H1N1 HA/MSNP-NH2 = 1/1 (w/w)	782±22	0.576±0.035	-(15.2±0.9)
H1N1 HA/ MSNP-NH2 = 2/1 (w/w)	402±8	0.579±0.047	-(16.1±0.4)
H1N1 HA/ MSNP-NH2 = 4/1 (w/w)	210±3	0.498±0.010	-(16.0±0.6)
MSNP-NH2 in PB buffer (10 mM, pH 5.8)	175±2	0.161±0.024	20.5±0.5
Concentrated HA protein (1/10× diluted)	154±4	0.414±0.055	-(16.9±0.9)
Original vaccine	142±3	0.314±0.004	-(6.1±1.8)

The PDI of MSNP-NH2 particles was increased from about 0.2 to 0.5 when HA was absorbed on the surface. The size and PDI of the HA from original vaccines are 142 nm and 0.314, indicating HA agglomerates itself. The concentrated HA has a size of 154 nm and PDI of 0.414. HA protein not only could increase the size and PDI of MSNP-NH2, but also could bind MSNP-NH2 nanoparticles together, leading to the increase of particle size. As the relative amount of HA compared to MSNP-NH2 amount increases, the size of MSNP-NH2/HA decreases even though the ZP does not change. The excessive HA in the suspension seems to play a role in stabilising MSNP-NH2 nanoparticles. When the mass ratio of H1N1 HA and MSNP-NH2 comes to 4/1, the MSNP-NH2 nanoparticles have a size of about 210 nm and a PDI of about 0.5. Thus a mass ratio of at least 4/1 for HA vs MSNP-NH2 is suggested when both are used together in one formulation.

TMD microparticles containing H1N1 HA at a content of about 4 µg/mg (HA/TMD) and TMD microparticles containing 4 µg/mg of HA and 1 µg/mg of MSNP-NH2 (HA/MSNP-NH2/TMD) were prepared. The sizes of HA protein and MSNP-NH2 nanoparticles re-dissolved from the TMD microparticles are shown in **Table V-5**. The HA recovered from TMD microparticles has a size of 93 nm and PDI of about 0.8. The size of HA is low, but the PDI is very high, probably due to the TMD matrix having a PDI of about 0.6. The particle size and PDI of the HA/MSNP-NH2/TMD formulation are 140 nm and about 0.6. Therefore, cationic silica nanoparticles in the TMD microparticles containing the HA antigen do not produce big particles/aggregates.

Table V-5 DLS of the re-dissolved microparticles containing HA and/or silica nanoparticles

Sample	Z-Ave (d.nm)	PDI	ZP (mV)
H1N1 HA/TMD	93±12	0.832±0.221	-(10.7±1.2)
H1N1 HA/MSNP-NH2/TMD	140±3	0.610±0.011	-(14.5±1.1)

5 - 8 mg of TMD microparticles were dissolved in 1 ml of KNaMgPT buffer.

3.3 Characterisation of H1N1 HA in TMD microparticles

H1N1 HA was formulated in TMD microparticles by spray-freeze-drying (SFD). The HA content in the TMD microparticles can be calculated from the HA amount added and the TMD amount. Concentrated HA solutions from batch 1 (2.00 mg/ml) and batch 2 (1.50 mg/ml) were used. 50 mg/ml MSNP-NH2 in PB buffer (10 mM, pH 5.8) was used in the formulations for TMD microparticles. On the other hand, HA content in the TMD microparticles can be directly determined by dissolving TMD microparticles and measuring HA concentration using RP-HPLC. As shown in **Table V-6**, the concentrations of all the samples obtained from RP-HPLC measurements are comparable to those calculated (**Table V-2**). The RP-HPLC method for determining HA concentration was considered as the standard. The calculated HA concentrations are obtained from the concentrated HA solutions whose concentrations were determined by micro BCA assay. Therefore, both RP-HPLC and protein micro BCA assay are suitable for the determination of HA concentration.

Table V-6 Concentration of HA solution redissolved from the TMD microparticles

Sample	RP-HPLC (mg/ml)	Calculated (mg/ml)
H1N1 HA/TMD	0.190	0.175
H1N1 HA/MSNP-NH2/TMD	0.135	0.175

The HA solution recovered from TMD microparticles and the concentrated HA that was used to prepare TMD microparticles were studied by SDS-PAGE. As seen from the SDS-PAGE result in **Figure V-2**, there are mainly four bands including HA monomer (ca. 66 kDa), HA dimer (ca. 130 kDa), HA trimer (ca. 190 kDa) and subunit (HA1) protein of HA (ca. 50 kDa). The bands of HA monomer, HA dimer and HA trimer are consistent with the results found in the literature [165]. The lane for the concentrated HA shows a distinct high concentration of protein.

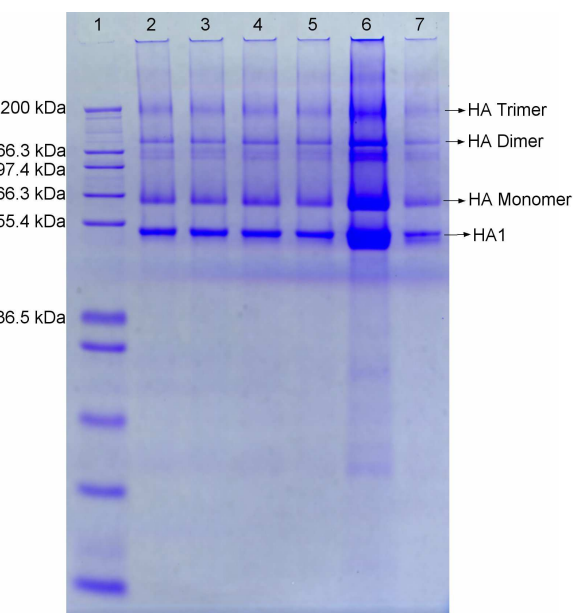


Figure V-2. SDS-PAGE of concentrated HA and recovered HA from TMD microparticles.

Lane 1 - Marker, **lane 2 and lane 4** - HA from the HA/TMD formulation, **lane 3 and lane 5** - HA from the HA/MSNP-NH₂/TMD formulation, **lane 6** - concentrated HA, **lane 7** - 5-fold dilution of the concentrated HA.

SDS-PAGE and western blot of H1N1 HA under non-reducing and reducing conditions were further studied. The SDS-PAGE and western blot results in **Figure V-3** confirms that the three bands (ca. 66, 130, 190 kDa) belong to H1N1 HA. A very light band of the subunit HA1 appears on the blotting membrane for the samples under reducing conditions, but the HA1 band for the samples under non-reducing conditions is hardly observed. The HA proteins from the TMD microparticles have the bands as the original vaccine, except that the HA concentration in the original vaccine is lower than the HA reconstituted from TMD microparticles.

Under reducing conditions, the HA monomer band becomes slightly broad and goes up a little bit to the higher molecular direction. According to the properties of HA protein, HA monomer (HA0) includes two subunits bound together by a disulfide bond [165]. The HA monomer can be cleaved into two parts (HA1 and HA2) under reducing conditions. HA1 appears on the SDS-PAGE (**Figure V-3A**), but HA2 is hardly seen. The subunit HA1 was observed in **Figure V-3B**, showing a molecular weight of ca. 50 kDa. The bands corresponding to HA dimers and trimers under reducing conditions on the SDS-PAGE gel and western blot membrane have less concentration than those under no-reducing conditions. It indicates that

HA dimers and trimers can be changed to HA monomers under reducing conditions due to the reversible balance between HA monomers, dimers and trimers.

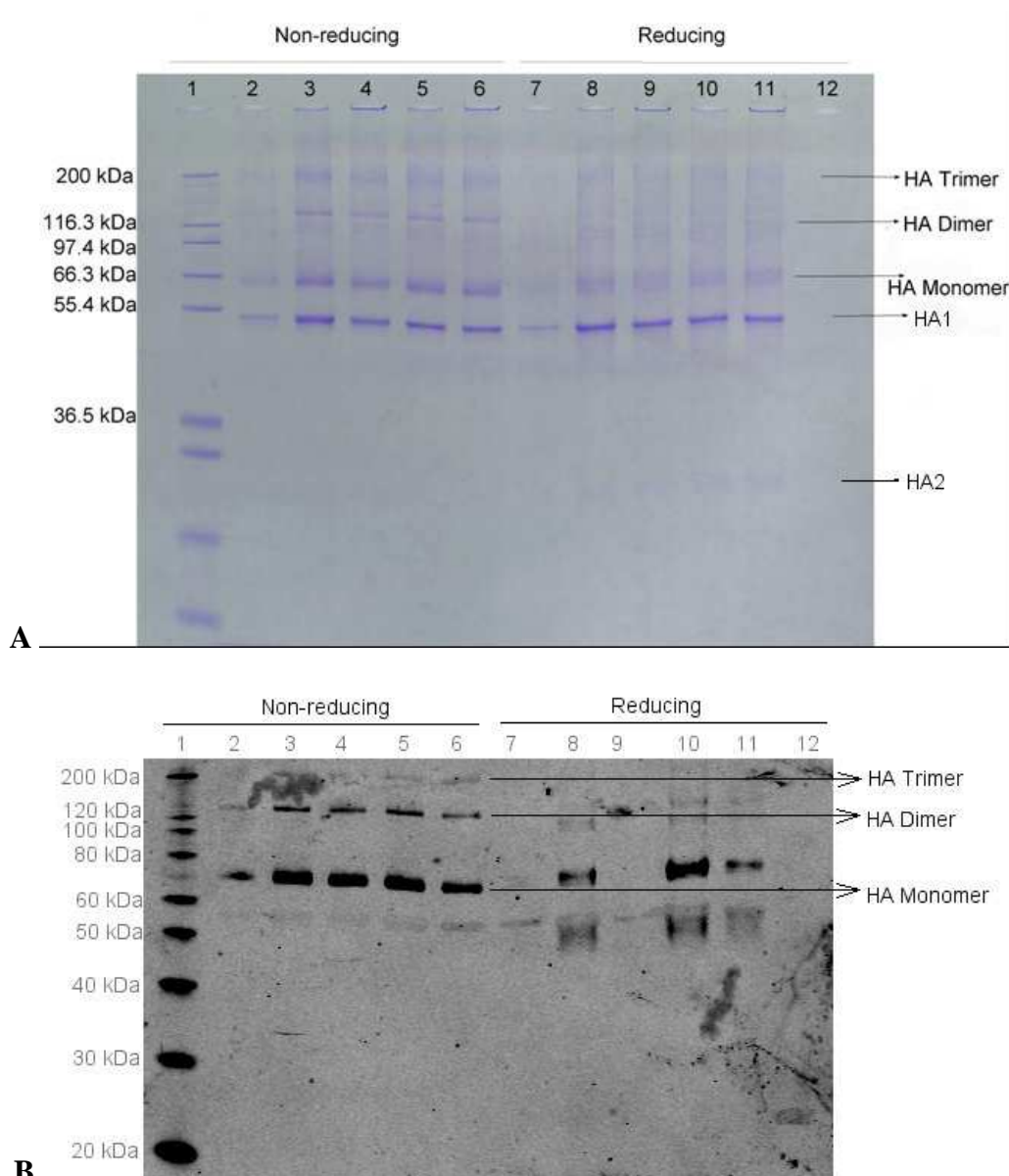


Figure V-3. Reducing and non-reducing SDS-PAGE and western blot results of H1N1 HA. **Lane 1** - Marker, **lane 2** - original vaccine, **lane 3** and **lane 5** - HA from the HA/TMD formulation, **lane 4** and **lane 6** - HA from the HA/MSNP-NH2/TMD formulation, **lane 7** - reduced original vaccine, **lane 8** and **lane 10** - reduced HA from the HA/TMD formulation, **lane 9** and **lane 11** - reduced HA from the HA/MSNP-NH2/TMD formulation, **lane 12** - TMD matrix.

H1N1 HA protein in TMD microparticles maintains the molecular integrity and binding specificity in spite of the formulations containing MSNP-NH2 or not. Two conclusive aspects

could be drawn from the above results. One aspect is that TMD formulations and the spray-freeze-drying process for preparing microparticles have no detriment effects on H1N1 HA. The other one is that silica nanoparticles in the formulation have no obvious negative effects on the HA antigen. Considering HA protein is sensitive to physical stresses [170], the process for manufacturing the nano-in-micro particle systems made of TMD matrices and silica nanoparticles is useful for producing vaccine microparticles for epidermal powder immunisation.

More experiments were carried out to obtain better quality of western blot results. The non-reducing SDS-PAGE of HA protein is shown in **Figure V-4A**; the corresponding western blot result of each lane is shown in **Figure V-4B**. Compared to the conditions in the experiments of **Figure V-3**, double amount of each sample was added into the lane. It is clear that the HA protein recovered from TMD microparticles containing or without silica nanoparticles shows the same bands as the H1N1 HA control, including monomers, dimers and trimers. The subunit HA1 appears on the SDS-PAGE gel, but is hardly observed on the western blot membrane. It indicates that the bind affinity of HA1 with the primary antibody is very low. The bands in **Figure V-4** are more clear than those in **Figure V-3** because the HA amount added into the lane doubles. The concentration of HA monomers is distinctly larger than that of HA dimers, which is larger than that of trimers. TMD matrices have no protein bands on the gel and no binding bands on the membrane.

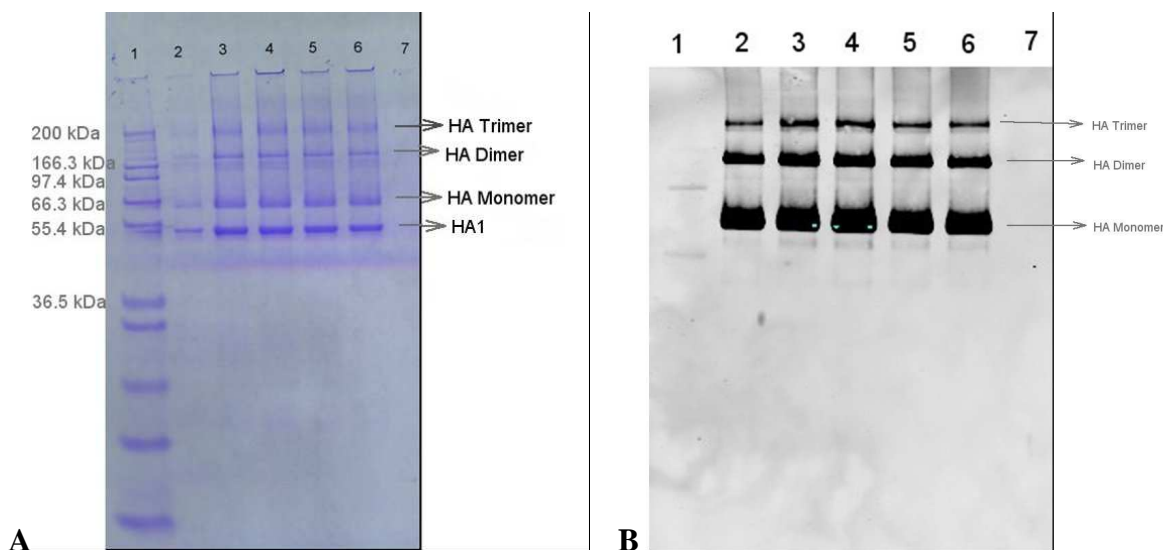


Figure V-4. Non-reducing SDS-PAGE (A) and western blot (B) results of H1N1 HA. **Lane 1**

- Marker, **lane 2** - H1N1 HA (control), **lane 3** and **lane 5** - HA from the HA/TMD formulation, **lane 4** and **lane 6** - HA from the HA/MSNP-NH2/TMD formulation, lane 7 - TMD matrix. The right photo was imaged by ODYSSEY system using the channel of 800 nm.

3.4 Biological activity by hemagglutinin inhibition assay

The biological activity of H1N1 HA was determined by hemagglutinin inhibition (HAI) assay using chicken red blood cells (RBCs) [167]. The results are shown in **Figure V-5** and summarized in **Table V-7**. The HA concentration of samples **D** and **E** is estimated to be 0.120 mg/ml by multiplying the original vaccine concentration (0.015 mg/ml) 8 fold. The value 0.120 mg/ml is consistent with the calculated HA protein concentration (0.118 mg/ml) calculated from the HA content in the microparticles. Therefore, the biological activity of HA in the TMD microparticles can be preserved during the spray-freeze-drying step. In addition, MSNP-NH2 particles have no negative effect on the activity of HA.

A: Standard HA
(positive control)

B: Stressed HA (negative control)

C: DGV buffer

D: HA from HA/TMD

E: HA from HA/MSNP-NH2/TMD

F: HA from HA/TMD
(repeat)

G: HA from HA/MSNP-NH2/TMD (repeat)

H: TMD matrix

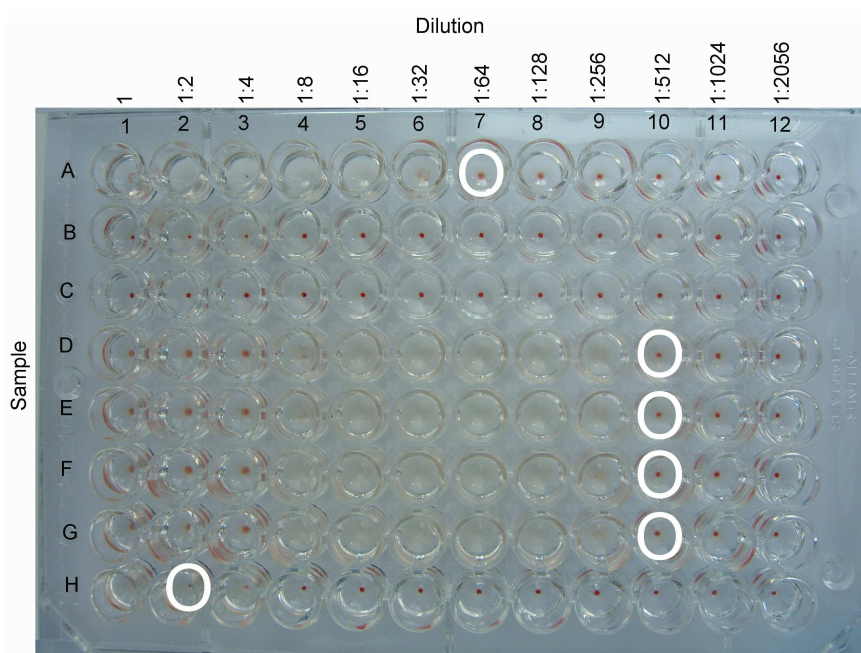


Figure V-5. The results of HAI assay of H1N1 HA proteins from different formulations. The white circle indicates the first red button appearing among the dilutions of each sample.

More studies were carried out to investigate the storage effect of the concentrated HA stock solution and the storage effect of the reconstituted HA from TMD microparticles on the biological activity of HA. Concentrated freshly prepared H1N1 HA and aged H1N1 HA (two weeks at 4 °C) were diluted 20 fold before used for HAI assay (**Table V-7**). The calculated concentration (Con.) of HA was obtained from the concentrated HA stock concentration that was obtained by protein micro BCA assay, while the estimated concentration of HA was

calculated according to the HAI assay. Calculated HA concentrations, calculated from the protein content in the microparticles, were comparable to those estimated from the biological activity. The HA stock solutions and the freshly reconstituted HA solutions show very good biological activity.

Table V-7 Summary of the concentrations of concentrated HA stock solutions and freshly reconstituted HA (unit, mg/ml)

Sample	HA standard	Fresh HA stock (diluted)	Aged HA stock (diluted)	Fresh HA from HA/TMD	Fresh HA from HA/silica/TMD
Calculated HA	0.015	0.088	0.075	0.118	0.118
Estimated HA	0.015	0.06	0.06	0.12	0.12

Calculated HA was calculated from the HA content in the microparticles. Estimated HA was obtained from HAI assay.

H1N1 HA solutions from TMD microparticles were prepared by reconstitution in the KNaMgPT buffer. The HAI assay results are summarized in **Table V-8**. Distinct decreased activities of the aged reconstituted HA samples were observed after storage at 4 °C for one week. The dextran (10 kDa and 150 kDa) in TMD matrix could be detrimental to HA in solution by interacting with HA, resulting activity loss of the aged reconstituted HA.

Table V-8 Effect of storage (4 °C) on the reconstituted HA (unit, mg/ml)

Sample	HA standard	Aged HA, HA/TMD	Aged HA, HA/silica/TMD	Aged HA, HA/TMD	Aged HA, HA/silica/TMD
Calculated HA Con.*	0.015	0.118	0.118	0.088	0.088
Estimated HA Con.*	0.015	0.002	0.015	0.015	0.03

*Con. = concentration.

For the concentrated HA stock solution, two weeks storage in the fridge has no obvious effect on the activity of HA antigens. HA biological activities of all the freshly reconstituted samples from TMD microparticles are as good as the original vaccine. However, the aged reconstituted HA (one week at 4 °C) has much lower activity than the original vaccine. That is to say, the HA antigens in TMD microparticles are stable in a solid form, but not very stable in solution containing TMD matrices. Original HA vaccines on market are stable at 4 °C for about one year, but the HA in TMD solution is not stable. Trehalose and mannitol are sugar

matrices that can stabilise proteins in solution, but dextran as a polysaccharide, especially the type with a high molecular weight (150 kDa), can destabilise vaccines such as HA.

3.5 Stability of influenza vaccines in a solid form

In our experiments, trehalose, manitol and dextran were used to formulate H1N1 HA into microparticles by SFD. Because we have already proved the suitability of these TMD microparticles regarding size, density and robustness for EPI delivery previously, the stability of HA in the formulation is the main research focus of this chapter.

We have successfully prepared TMD microparticles containing biologically active HA by spray-freeze-drying. The H1N1 HA in the TMD microparticles shows the same molecular integrity as the standard. The binding affinity (**Figure V-4**) and the biological activity (**Table V-7**) of HA have no distinct change in the microparticles. The trehalose and mannitol act as a role of stabilising HA in the formulation, an appropriate amount of dextran can increase the particle density and robustness without destabilising the vaccines in a solid form. We found the biological activity of HA in dry TMD microparticles is good but reconstituted HA loses its activity in one week at 4 °C (**Table V-8**). In other studies, the stability of influenza vaccines in TMD microparticles has been maintained for at least 6 months at 25 °C and for 3 months at 40 °C [169]. The conformational changes of HA can be prevented by using fast freezing, Hepes buffer and carbohydrates (trehalose, inulin or dextran) during freeze-drying [171], the HA potency in the vaccine powder keeps stable as long as at least 6 months at room temperature.

The silica nanoparticles we used in the formulation have no negative impact on the HA stability. HA can be adsorbed on the cationic silica nanoparticles (MSNP-NH₂) as seen from the above results. As the H1N1 HA stability can be preserved in TMD microparticles when silica nanoparticle are also included in the formulation, the nano-in-micro particle systems composed of MSNP-NH₂, HA and TMD matrices are practical for epidermal powder immunisation.

4. Conclusion

H1N1 hemagglutinin protein solution with a concentration of 1 - 2 mg/ml has been prepared from the original vaccines with a HA concentration of 15 µg/ml. The concentrated HA solution is stable for at least two weeks at 2 - 8 °C. This HA solution has been used to prepare

TMD microparticles by spray-freeze-drying. Cationic silica nanoparticles can adsorb HA protein very well mainly by electrostatic interaction. HA was loading onto MSNP-NH2 nanoparticles by absorption and then both were formulated into the TMD matrix to create nano-in-micro particle systems containing antigens. These nano-in-micro particles are pursued for the purpose of epidermal powder immunisation. The H1N1 HA reconstituted from the TMD microparticles maintains the integrity and shows the same binding affinity to the antibody as the HA standard. The biological activity of the HA from TMD microparticles is as good as that of concentrated HA. Silica nanoparticles encapsulated in TMD microparticles have no obvious negative effects on the stability of HA antigen. TMD microparticles containing HA and MSNP-NH2 have been successfully prepared, which could be used for epidermal powder injection.

For now, the obtained TMD microparticles have a HA content of about 4 $\mu\text{g}/\text{mg}$. This content seems to be low for the application on animals or even human. As for the epidermal powder injection, about 1 mg of microparticles can be delivered into the epidermal layer or dermal up-layer. 10 - 50 μg of vaccines are needed for one shot. Therefore, it is necessary to develop TMD microparticles with a HA content of 10 - 50 $\mu\text{g}/\text{mg}$. These microparticles could be achieved by using a higher concentration of HA stock solution.

Chapter VI. Preparation of PLGA Nanoparticles for Vaccine Delivery and Their Encapsulations in Sugar-based Microparticles

1. Objectives

Poly(lactic-co-glycolic acid) (PLGA) is a copolymer of lactic acid and glycolic acid linked by ester linkages. It has been approved for manufacturing therapeutic devices by the Food and Drug Administration (FDA), owing to its good biodegradability and biocompatibility [172]. PLGA nano/microparticles have been extensively used for drug/vaccine delivery of therapeutics as a sustained-release system [110, 173]. The rapid endo-lysosomal escape of PLGA nanoparticles after delivery into cells indicates good implications for intracellular delivery of genes and drugs [174]. Some products based on PLGA are on the market, e.g. Lupron Depot®, Sandostatin® LAR Depot, Zoladex®, Vivitrol®, etc. [175-179]. PLGA particles are typically prepared by emulsification methods, the encapsulation of proteins or peptides can be achieved [110, 180]. The controlled release of encapsulated ovalbumin from PLGA particles on a long term (up to 3 months) facilitates a long-term memory T cell response and efficacy in pathogen recall, which is very attractive for vaccine delivery [181].

PLGA-based particles with different sizes can be fabricated for multiple applications [182, 183]. Tuskada *et al.* have prepared sterile PLGA nanoparticles with a mean size of 100 nm-160 nm [182]. Protein-loaded PLGA-based particles have been investigated concerning the encapsulation efficiency and protein stability [173, 184, 185]. The surface charges and functional groups on the surface of PLGA nano/microparticles can be tailored by surface modification. Cationic PLGA nanoparticles have been prepared by incorporating or coating positively charged molecules, such as chitosan, PEI, CTAB, DEAE-dextran, etc. [144, 186, 187]. Chitosan is the most popular substance for cationizing PLGA nanoparticles [146, 186, 188-191]. PEI is another option for cationization of PLGA particles [144, 187, 192]. Coating methods such as PEGylation are often used for surface modification of PLGA nanoparticles to stabilise the dispersion and reduce unspecific interactions with cells [79, 193, 194]. There is an alternative method for stabilizing PLGA nanoparticles by using hydroxyethyl starch or pluronic [193]. PEG-PPO-PEG block polymers such as Pluronic F127, P103, P105 were coated on PLGA nanoparticles, thereby accelerating penetration of the particles into human

mucus [194]. In a word, PLGA-based nanoparticles have already been widely recognised as a useful drug/vaccine delivery system.

PLGA-based particles have been shown in literature to be a good candidate as a vaccine delivery system for parenteral, nasal and oral routes of administration. Cruz *et al.* found that nano-sized PLGA particles but not microparticles can specifically deliver antigen to human dendritic cells [79]. Wang *et al.* loaded the foot and mouth disease virus (FMDV) DNA vaccine on chitosan-coated PLGA nanoparticles, which can induce protective immunity again FMDV challenge by intranasal delivery [146]. Prasad *et al.* optimized PLGA nanoparticles containing B16-tumor antigen lysate for the study of anti-tumor responses [195]. PLGA microparticles (3 - 5 μm) containing the immune potentiators of monophosphoryl lipid A (MPLA) and the synthetic LPS mimetic RC529 were coated with antigens and then used for immune stimulation [196]. PLGA nanoparticles containing ovalbumin and MPLA were demonstrated to promote systemic and mucosal responses administered orally [148]. However, antigen-loaded PLGA nanoparticles have never been used for intradermal immunisation by powder injection.

As described in Chapter III, PLGA nanoparticles can be encapsulated into the sugar-based microparticles by spray-freeze-drying. PLGA nanoparticles (100 nm-1000 nm) will be further investigated as nanocarriers for antigens. According to the concept of nano-in-micro particle systems investigated in this thesis, it is reasonable to create TMD microparticles containing antigen-loaded PLGA nanoparticles for the purpose of epidermal powder immunisation. Ovalbumin (OVA) has been used as a model protein for the study of encapsulation into PLGA microparticles [185]. Only a few examples investigated ovalbumin-loaded PLGA nanoparticles [148, 181]. As an alternative to protein antigens, peptides may induce more direct and specific immune response. OVA 257-264 peptide (SIINFEKL) is the natural H-2K^b-restricted epitope of ovalbumin presented by MHC class I molecules [197, 198]. SIINFEKL can induce a much stronger H-2K^b-restricted response compared to OVA [197], but the main disadvantage of peptide antigens is that the immunogenicity is so poor that adjuvants or particulate delivery systems are needed to induce effective immune response [198, 199]. To my knowledge, the encapsulation of SIINFEKL into PLGA nanoparticles has not been performed yet.

The aim of this chapter is to use a long-term sustained release system, PLGA nanoparticles, in place of the fast release system, silica nanoparticles, to prepare nano-in-micro particles for the

purpose of epidermal powder immunisation. The objectives include 1) loading of ovalbumin into plain (anionic) and cationic PLGA nanoparticles and investigation of ovalbumin release, 2) loading of OVA peptide (SIINFEKL) into plain and cationic PLGA nanoparticles, 3) encapsulation of OVA- or SIINFEKL-loaded PLGA nanoparticles into the sugar-based TMD microparticles. OVA and SIINFEKL will be loaded into PLGA nanoparticles by a water-in-oil-in-water (W/O/W) double emulsion method. The antigen-loaded nanoparticles will be characterised including the determination of the loaded amount. The release of ovalbumin from PLGA nanoparticles will be determined by a protein micro BCA assay. The stability of PLGA nanoparticles in TMD microparticles will be investigated.

2. Materials and Methods

2.1 Materials

Poly(lactic-co-glycolic acid) (PLGA) (RESOMER® RG502H) was obtained from Evonik Industries AG (Darmstadt, Germany). Ovalbumin (OVA), albumin from chicken egg white (Grade V), PEI (polyethylenimine, Mw~25.000, Branched), chitosan (low/medium molecular weight), and polyvinyl alcohol (PVA) (80% hydrolyzed, Mw: 9000-10000) were purchased from Sigma-Aldrich Chemie GmbH (Steinheim, Germany). Ethylacetate (EA) was from Merck kGaA (Darmstadt, Germany). Carboxyfluorescein (FAM) labeled SIINFEKL (FAM-SIINFEKL) with a sequence of SIINFEKL was purchased from AnaSpec (Seraing, Belgium). The polymers used in the experiments are summarized in **Table VI-1**.

Table VI-1 Summary of the polymers for the preparation of PLGA nanoparticles

Product	Chemical structure	Description of properties
PLGA, RESOMER® RG502H		Mw: 7 000-17 000; End group: free carboxylic acid; Molar ration of D,L-lactide and glycolide: 50:50
polyvinyl alcohol (PVA)		80% hydrolyzed, Mw: 9 000-10 000
Chitosan, low molecular weight		Viscosity (1% solution in 1% acetic acid): 20-200 cps; Deacetylation: 75-85%
Chitosan, high molecular weight		Viscosity (1% solution in 1% acetic acid): 200-800 cps; Deacetylation: 75-85%
Polyethylenimine (PEI)		average Mw ~25,000 by LS, average Mn ~10,000 by GPC, branched

2.2 Methods

2.2.1 Preparation of PLGA nanoparticles loaded with ovalbumin

The method for the preparation of cationic OVA-loaded PLGA nanoparticles was modified from Kumar, *et al.* [186]. 90 mg of PLGA (RG 502H) was dissolved in 3.0 ml of ethyl acetate (EA) in an eppendorf (EP) tube. 0.1-0.3 ml of 100 mg/ml ovalbumin in PB buffer (10 mM, pH 7.4) was added into the solution of PLGA in EA, and then the mixture was treated with a probe ultrasonicator (Bandelin UW 3200, Berlin, Germany) (Sonotrode MS 73, 20% amplitude) for 60 seconds in an ice bath. The obtained emulsion was quickly added into a 12 ml solution of 1.0% (w/v) PVA in highly purified water (HPW). The solution was mixed and instantly ultrasonicated (Sonotrode MS 73, 20% amplitude) for 180 seconds in an ice bath. The obtained emulsion was then stirred at room temperature (RT) overnight to remove the solvent. The PLGA particles were collected by centrifugation at 14 000 rpm for 10 min at 10 °C (Sigma 4K15 centrifuge, SIGMA Laboratory Centrifuges, Shropshire, UK), and were subsequently washed twice with 12 ml of HPW. Finally, the PLGA particles encapsulating OVA (PLGA-OVA) were re-suspended in 1.5 ml of HPW. The suspension was ultrasonicated for 30 seconds to ensure that the PLGA-OVA nanoparticles were fully suspended. The particle concentration was determined by microbalance. 50 µl of the suspension was dried in an aluminium crucible and the dry amount was measured to calculate the particle concentration. PLGA nanoparticles loaded with different amounts of OVA were prepared by varying the added OVA stock volume (**Table VI-2**).

Table VI-2 Composition of OVA-loaded PLGA nanoparticles

Sample	PLGA (30 mg/ml)	OVA stock (100 mg /ml)	Theoretical OVA loading
PLGA-OVA(10%)	3.0 ml	0.100 ml	10 wt%
PLGA-OVA(20%)	3.0 ml	0.225 ml	20 wt%
PLGA-OVA(25%)	3.0 ml	0.300 ml	25 wt%
PLGA-OVA(10%)-chitosan	3.0 ml	0.100 ml	10 wt%
PLGA-OVA(20%)-chitosan	3.0 ml	0.225 ml	20 wt%
PLGA-OVA(25%)-chitosan	3.0 ml	0.300 ml	25 wt%

2.2.1.2 Cationic PLGA nanoparticles loaded with ovalbumin

The emulsion of OVA solution dispersed in PLGA in EA was prepared using the same method as above. PVA and chitosan (low molecular weight) were dissolved in an acetate buffer (50 mM, pH 4.5) to obtain a PVA-chitosan solution containing 1.0% (w/v) of PVA and 0.2% (w/v) of chitosan. The freshly prepared emulsion was added to 12 ml of a PVA-chitosan solution. The solution was mixed instantly and ultrasonicated (Sonotrode MS 73, 20% amplitude) for 180 seconds in an ice bath. The resulting emulsion was stirred overnight. The particles were collected and washed using the same procedure for PLGA-OVA nanoparticles. Finally, about 1.5 ml suspension of cationic PLGA-OVA nanoparticles was obtained. The particle concentration was determined by the microbalance method as described above. For the preparation of PEI-coated PLGA nanoparticles, PVA and PEI were dissolved in HPW to obtain a PVA-PEI solution containing 1.0% (w/v) of PVA and 0.2% (w/v) of PEI, which was then used for the emulsification. Cationic chitosan-coated PLGA nanoparticles loaded with different amounts of OVA were achieved by a similar method for PLGA-OVA nanoparticles (**Table VI-2**). Cationic PLGA-OVA(10%)-chitosan, PLGA-OVA(20%)-chitosan and PLGA-OVA(25%)-chitosan nanoparticles were prepared.

2.2.2 Preparation of PLGA nanoparticles loaded with SIINFEKL

2.2.2.1 Plain PLGA nanoparticles loaded with SIINFEKL

0.2 mg of the fluorescently labeled peptide SIINFEKL was dissolved in 100 μ l of PBS (150mM, pH 7.4). 2 mg/ml of a fluorescently-labeled FAM-SIINFEKL solution was obtained after centrifugation. 50 μ l of the SIINFEKL solution was added to a 1.0 ml solution of 30 mg/ml PLGA in EA. The mixture was ultrasonicated for 30 seconds (Sonotrode MS 72, 20% amplitude) in an ice bath to obtain an emulsion. For plain PLGA nanoparticles loaded with SIINFEKL (PLGA-SIINFEKL), the emulsion was added to 4.0 ml of 1.0% PVA aqueous solution, and was then ultrasonicated for 60 seconds (Sonotrode MS 72, 20% amplitude) in an ice bath. The emulsion was stirred overnight to remove EA. The particles were obtained by centrifugation and washed by HPW twice. Finally, the PLGA-SIINFEKL nanoparticles were re-suspended in HPW under a short ultrasonication (10 seconds). The particle concentration of the obtained suspension was determined by weighing the dry amount of 50 μ l suspension using a microbalance.

2.2.2.2 Cationic PLGA nanoparticles loaded with SIINFEKL

For cationic PLGA nanoparticles loaded with SIINFEKL, the emulsion of SIINFEKL dispersed in PLGA EA solution, as prepared for loading into plain PLGA nanoparticles, was added into 4.0 ml of a acetate buffer (50 mM, pH 4.5) containing 1.0% (w/v) PVA and 0.2% (w/v) chitosan. The mixed solution was then ultrasonicated for 60 seconds (Nr.72, 20% amplitude) in an ice bath. The resulting emulsion was stirred overnight to remove EA. The particles were obtained by centrifugation and washed by HPW. Finally, the cationic PLGA-SIINFEKL-chitosan nanoparticles were re-suspended in HPW and the particle concentration of the obtained suspension was determined by the same previous method.

2.2.3 Determination of ovalbumin loading in PLGA nanoparticles

Sodium dodecyl sulfate (SDS) was dissolved in 0.1 M NaOH to obtain a NaOH-SDS buffer containing 2.0 % (w/v) SDS for dissolving PLGA nanoparticles [184]. 50 µl of OVA-loaded PLGA nanoparticles was dried in a 1.5-ml EP tube at 40 °C overnight. 0.2 ml of the NaOH-SDS buffer was added to dissolve the dry particles. Three repeats for each sample were prepared. The EP tubes were shaken at 20 rpm for about 60 hours at RT (GFL®-3015, Burgwedel, Germany). At last, the tubes were centrifuged at 14 000 rpm for 10 min, the OVA concentration in the supernatant was determined by a protein micro BCA assay (Thermo Scientific, Wilmington, USA) or Nanodrop (Thermo Scientific, Wilmington, USA). The encapsulation efficiency (EE) was calculated as follows:

$$EE = \frac{\text{Measured antigen loading}}{\text{Theoretical antigen loading}} \times 100\% \quad (1)$$

2.2.4 Determination of SIINFEKL loading in PLGA nanoparticles

50 µl suspension of SIINFEKL-loaded PLGA nanoparticles was dried in an EP tube at 40 °C overnight (UL 50, Memmert, Schwabach, Germany). EA and NaOH-SDS extraction methods were used to recover the loaded SIINFEKL. **1) NaOH-SDS extraction:** 0.2 ml of the same NaOH-SDS buffer as described above was added to dissolve the PLGA nanoparticles under gentle shaking for 60 hours at dark. Three repeats for each sample were prepared. The FAM-SIINFEKL concentrations in the supernatants obtained from the tubes after centrifugation (Sigma 4K15 centrifuge, SIGMA Laboratory Centrifuges, Shropshire, UK) were measured by a microplate reader (Fluostar Omega, BMG LABTECH GmbH, Ortenberg, Germany). **2) EA extraction:** Another method for extracting the SIINFEKL was carried out by dissolving PLGA nanoparticles in EA. PBS buffer was added to the EA solution and were then mixed

thoroughly. The mixture was centrifuged to separate the organic phase and aqueous phase. The organic phase was removed and the aqueous phase was then used for concentration determination.

In order to determine concentration of fluorescently-labeled SIINFEKL, a standard curve was needed. A series of FAM-SIINFEKL standards (1 - 20 µg/ml) were prepared. 150 µl of each standard or sample was added into a 96-well plate with flat-bottom wells. The emission at 520 nm under an excitation of 488 nm was recorded using the microplate reader.

2.2.5 Characterisation of OVA/SIINFEKL-loaded PLGA nanoparticles and the microparticles encapsulating the nanoparticles

Dynamic light scattering (DLS)

The hydrodynamic diameter and zeta-potential were determined using a Zetasizer Nano ZS (Malvern Instruments, Herrenberg, Germany). The refractive index (RI) of all nanoparticles used for the size measurement was 1.59. The dispersant phase is water with RI of 1.330 and viscosity of 0.8872 cP. The particle concentration was kept around 0.1-0.2 mg/ml for dynamic light scattering (DLS) measurements.

Scanning electron microscopy (SEM)

Particles were placed on adhesive carbon Leit-Tabs (Plano GmbH, Wetzlar, Germany) and then coated with a thin layer of carbon before the samples were observed using a JEOL JSM-6500F scanning electron microscope (SEM) (Joel Inc., Peabody, USA). Nanoparticles were viewed at a magnification of 40 000 and microparticles were viewed at a magnification of 300.

Confocal Laser Scanning Microscopy (CLSM)

Confocal Laser Scanning Microscope (LSM 510 META, Carl ZEISS, Germany) was used to study the microparticles with encapsulated fluorescent nanoparticles. Argon laser (488 nm) was used as the excitation, corresponding to the emission of BP 505-530 nm. Objectives with magnification of 40, 63 and 100 were used, including Plan-Neofluar 40×/1.3 Oil, Plan-Apochromal 63×/1.4 Oil DIC and Plan-Neofluar 100×/1.3 Oil Ph3. Z-stacking mode was used to observe the distribution of nanoparticles in the microparticles.

2.2.6 Release of ovalbumin from PLGA nanoparticles

The low loading (about 0.18 wt%) of SIINFEKL in PLGA-SIINFEKL nanoparticles can result in difficulties measuring the released peptide. Thus the release experiments were only carried out for plain and cationic PLGA-OVA nanoparticles. 1 ml of 2.0 mg/ml PLGA-OVA nanoparticles in PBS (150 mM, 0.02% NaN₃, pH 7.4) was prepared in an EP tube, which was incubated at 37 °C under 2 rpm shaking. At predetermined time points, the tubes were centrifuged at 14 000 rpm for 10 min (Sigma 4K15 centrifuge, SIGMA Laboratory Centrifuges, Shropshire, UK) before sampling. 0.5 ml of the supernatant was replaced with 0.5 ml of fresh PBS buffer. The particles were re-suspended by a short vortexing or pipetting. The 0.5 ml supernatant of each sample was used to determine the OVA concentration by a protein micro BCA assay (Thermo Scientific, Wilmington, USA). Three repeats of each sample were prepared.

2.2.7 Encapsulation of OVA/SIINFEKL-loaded PLGA nanoparticles into microparticles

Trehalose, mannitol, dextran (10 kDa) and dextran (150 kDa) (TMD) were mixed at a mass ratio of 3:3:3:1 in an 8-ml tube (SARSTEDT, Nuembrecht, Germany). The resulting suspension of the antigen-loaded PLGA nanoparticles from the previous steps was added to the TMD mixture. Highly purified water was added to adjust the solid concentration of the TMD matrix to 35% (w/w). The mixtures of TMD and PLGA nanoparticles (PLGA-NPs) were obtained under stirring at 500 rpm (MR 3001 K, Heidolph, Schwabach, Germany) for about one hour. The TMD/PLGA-NPs suspension was spray-freeze-dried (SFD) using the same method as described in Chapter III. Briefly, the suspensions were sprayed into a liquid nitrogen bath by an ultrasonic atomizing nozzle (120 kHz, Sono-Tek, Milton, USA). The power for spraying was set to 4.5 watts and the flow rate of a peristaltic pump (IsmaTec IPC 78001-20, Wertheim, Germany) to 0.6 ml/min. The sprayed microparticles were collected in vials and transferred to a pre-cooled lyophilizer (Martin Christ EPSILON 2-6D, Harz, Germany). The freeze-drying sequence was carried out by 24 hours of primary drying at -10 °C and 20 hours of secondary drying at 25 °C. The chamber pressure was kept at 0.12 mbar during the whole drying process.

3. Results

3.1 Optimisation of conditions for the preparation of PLGA nanoparticles

3.1.1 Influence of the polyvinyl alcohol (PVA) concentration on the particle size

Emulsification is a common method for the preparation of polymer particles. PVA is a widely used surfactant for the preparation of stable emulsions. Thus we prepared PLGA nanoparticles by an emulsification method using PVA as the stabilizer. The effects of the PVA concentration on the particle size were studied. 0.1 ml of 100 mg/ml ovalbumin (OVA) in PBS (150 mM, pH 7.4) was emulsified in 1.0 ml of 30 mg/ml PLGA in ethyl acetate (EA). The obtained PLGA/OVA emulsion was added to 4 ml of PVA solution for a second emulsification. Finally, OVA-loaded PLGA nanoparticles (PLGA-OVA NPs) containing a theoretical OVA loading of 25% (w/w) were obtained. PVA concentrations of 0.5%, 1%, 2%, 3%, 4% and 5.0% (w/v) were used for the preparation. As shown in Table VI-3, the particle size increases from 198 nm to 708 nm when the PVA concentration increases from 1.0% (w/v) to 5.0% (w/v). The size becomes large when the PVA concentration decreases from 1.0% (w/v) to 0.5% (w/v). Therefore, 1.0% (w/w) of PVA was chosen as the condition for preparing OVA-loaded PLGA nanoparticles with a size around 200 nm.

Table VI-3 Effect of the PVA concentration on the size and PDI of PLGA-OVA nanoparticles

Sample	Z-Ave (d.nm)	PDI	Zeta-potential (mv)
PLGA-OVA-PVA (0.5%) nanoparticles	566±99	0.243±0.025	-(10.6±0.6)
PLGA-OVA-PVA (1%) nanoparticles	198±3	0.256±0.009	-(32.2±2.9)
PLGA-OVA-PVA (2%) nanoparticles	202±2	0.171±0.008	-(26.6±0.4)
PLGA-OVA-PVA (3%) nanoparticles	240±2	0.236±0.012	-(31.3±0.7)
PLGA-OVA-PVA (4%) nanoparticles	281±5	0.163±0.015	-(23.8±0.3)
PLGA-OVA-PVA (5%) nanoparticles	708±45	0.685±0.046	-(21.6±0.3)

3.1.2 Cationisation of PLGA-OVA nanoparticles

Commonly, PEI and chitosan are used to prepare cationic PLGA-OVA nanoparticles [144, 186, 187]. Water-soluble PEI was added into the PVA aqueous solution directly to obtain a solution containing 1.0% (w/w) of PVA and 0.2% (w/w) of PEI. The PEI modified PLGA nanoparticles (PLGA-PEI) PEI have a positive zeta-potential (36.2 mv) after sufficient

washing with HPW, which is an indication that the coating is successful. However, PEI is toxic for humans and this is a major drawback for the use of such systems in drug delivery [200]. Chitosan as a positively charged polysaccharide may be a better choice for cationisation.

Chitosan with medium and low molecular weights as specified in the section of Materials and Methods were chosen to modify PLGA nanoparticles. Chitosan with a medium molecular weight was used to modify the surface of PLGA nanoparticles, but it was not successful. The obtained nanoparticles have a large hydrodynamic size and a negative zeta-potential (**Table VI-4**). The OVA-loaded PLGA nanoparticles were successfully coated by the chitosan with a low molecular weight, showing a zeta-potential of about +40 mv. The chitosan-coated PLGA-OVA nanoparticles containing theoretical OVA loadings of 10 wt% and 20 wt% have a similar size around 200 nm and a narrow size distribution. Therefore, chitosan with a low molecular weight is suitable for cationisation of PLGA nanoparticles.

Table VI-4 Cationic PLGA nanoparticles coated by PEI and chitosan.

Sample	Z-Ave (d.nm)	PDI	Zeta-potential (mv)
PLGA-chitosan (medium)	4855±1345	0.819±0.254	-(20.7±1.7)
PLGA-OVA-chitosan (medium)	2255±111	0.389±0.091	-(31.2±1.1)
PLGA-PEI	368±4	0.173±0.031	36.2±1.3
PLGA-OVA(10%)-chitosan	181±3	0.136±0.012	41.0±0.6
PLGA-OVA(20%)-chitosan	212±3	0.164±0.011	38.7±0.7

3.2 Properties of OVA/SIINFEKL-loaded PLGA nanoparticles

3.2.1 OVA-loaded PLGA nanoparticles

The pure PLGA nanoparticles without protein were prepared as a control. These particles have a Z-average (Z-Ave) size of 121 nm and a PDI of 0.071 (**Table VI-5**), indicating a very narrow size distribution. OVA was loaded into PLGA nanoparticles at theoretical OVA loadings of 10 wt% and 25 wt%. Cationic PLGA-OVA nanoparticles modified by chitosan were also prepared, showing positive zeta-potentials. PLGA nanoparticles containing 10 wt% OVA (PLGA-OVA(10%)) have a size of 211 nm and PLGA-OVA(25%) nanoparticles have a size of 159 nm. The cationic PLGA-OVA(10%) and PLGA-OVA(25%) nanoparticles show a size of about 250 nm and a PDI of about 0.18.

Table VI-5 Plain and cationic OVA-loaded PLGA nanoparticles

Sample	Z-Ave (d.nm)	PDI	Zeta-potential (mv)
PLGA nanoparticles	121 \pm 2	0.071 \pm 0.034	-(24.8 \pm 0.2)
PLGA-OVA(10%) nanoparticles	211 \pm 5	0.172 \pm 0.011	-(14.4 \pm 0.7)
PLGA-OVA(25%) nanoparticles	159 \pm 3	0.140 \pm 0.018	-(13.7 \pm 1.0)
PLGA-OVA(10%)-chitosan nanoparticles	235 \pm 6	0.168 \pm 0.007	31.5 \pm 1.0
PLGA-OVA(25%)-chitosan nanoparticles	256 \pm 5	0.182 \pm 0.022	29.1 \pm 0.6

In order to observe the ovalbumin loaded in PLGA nanoparticles using CLSM, fluorescently labeled ovalbumin (OVA-Alexa488) was used in the formulation. OVA-Alexa488 and OVA were mixed at a mass ratio of 1:50 and the OVA/OVA-Alexa488 mixture was encapsulated in PLGA nanoparticles at a theoretical loading of 10 wt%. As shown in **Figure VI-1**, plain and cationic OVA-loaded PLGA nanoparticles are spheres with diameters of about 100 nm. Their hydrodynamic diameters are 200 - 300 nm, which is larger than the size observed by SEM. A small part of large particles or aggregates exists and increases the Z-Ave size. The OVA-loaded PLGA nanoparticles are dispersed in aqueous solution without distinct aggregation. Only a few big particles were observed in suspension as seen from the CLSM micrographs (**Figure VI-1**). The sizes of big particles or aggregates of small nanoparticles (green spots) are smaller than 1 μ m.

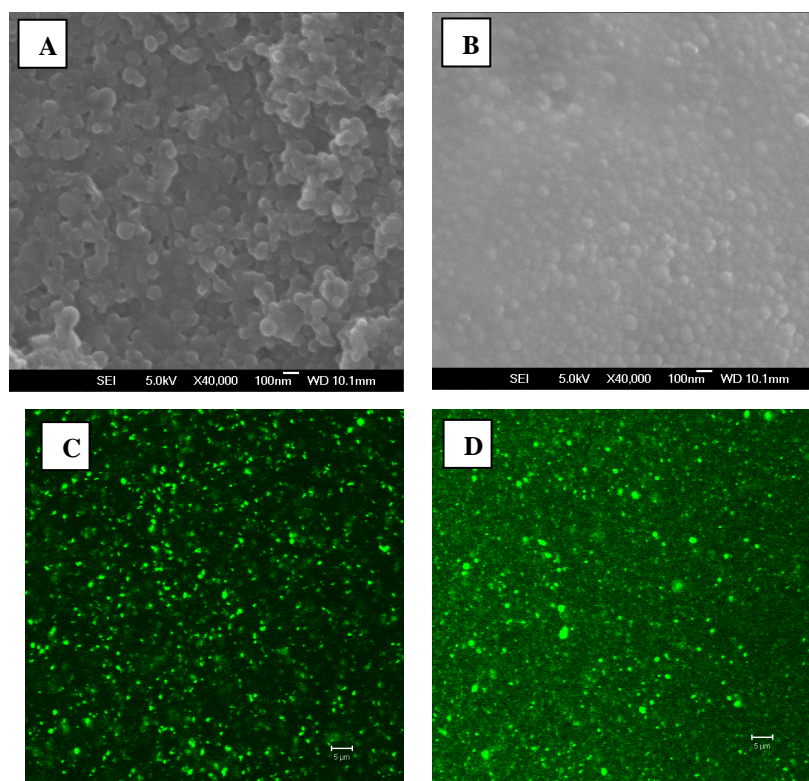


Figure VI-1. Plain and cationic PLGA nanoparticles loaded with OVA/OVA-Alexa. (A) SEM micrograph of PLGA-OVA/OVA-Alexa488 nanoparticles; (B) SEM micrograph of PLGA-OVA(10%)-chitosan nanoparticles; (C) CLSM micrograph of PLGA-OVA/OVA-Alexa488 nanoparticles; (D) CLSM micrograph of PLGA-OVA(10%)-chitosan nanoparticles.

cationic PLGA-OVA/OVA-Alexa488 nanoparticles; **(C)** CLSM micrograph of PLGA-OVA/OVA-Alexa488 nanoparticles suspended in aqueous solution; **(D)** CLSM micrograph of cationic PLGA-OVA/OVA-Alexa488 nanoparticles suspended in aqueous solution. The scale bar of **(A)** and **(B)** is 100 nm, while the scale bar of **(C)** and **(D)** is 5 μ m.

3.2.2 SIINFEKL-loaded PLGA nanoparticles

As SIINFEKL consists of only 8 amino acid units, the SIINFEKL mass is much lower than OVA at the same molar amount. Thus only a small amount of SIINFEKL was used for the encapsulation into PLGA nanoparticles. Theoretically, 0.1 mg of FAM-SIINFEKL was encapsulated in 30 mg of PLGA. The loading amount and efficiency will be described in the following section. The SIINFEKL-loaded PLGA nanoparticles (PLGA-SIINFEKL) have a hydrodynamic size of 114 nm and a PDI of 0.098 (**Table VI-6**), while the cationic ones (PLGA-SIINFEKL-chitosan) have a size of 261 nm and a PDI of 0.268.

Table VI-6 Plain and cationic SIINFEKL-loaded PLGA nanoparticles

Sample Name	Z-Ave (d.nm)	PDI	ZP (mV)
PLGA-SIINFEKL nanoparticles	114 \pm 1	0.098 \pm 0.028	-(35.0 \pm 2.2)
PLGA-SIINFEKL-chitosan nanoparticles	261 \pm 2	0.268 \pm 0.047	50.2 \pm 1.0

SEM observations of the SIINFEKL-loaded nanoparticles are shown in **Figure VI-2**. The fluorescence of PLGA-SIINFEKL nanoparticles is too weak to be observed, due to the small loading (less than 0.33 wt%) of SIINFEKL in the PLGA nanoparticles. The SEM sizes of all the PLGA-SIINFEKL nanoparticles are about 100 nm in diameter.

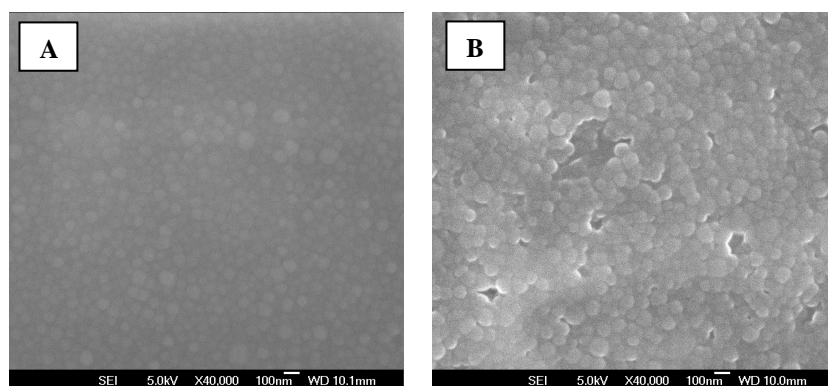


Figure VI-2. Plain and cationic SIINFEKL-loaded PLGA nanoparticles. **(A)** SEM micrograph of PLGA-SIINFEKL nanoparticles; **(B)** SEM micrograph of cationic PLGA-SIINFEKL nanoparticles. The scale bar is 100 nm.

3.3 Loading and encapsulation efficiency of OVA/SIINFEKL in PLGA nanoparticles

3.3.1 PLGA nanoparticles encapsulating ovalbumin

The encapsulation of OVA in PLGA nanoparticles was investigated. OVA-loaded PLGA nanoparticles with theoretical OVA loadings of 10 wt% and 25 wt% were prepared. The theoretical loadings were calculated from the amounts of OVA and PLGA used for the preparation. The OVA concentration (lower than 1 mg/ml) recovered from PLGA nanoparticles is in the low range for measurements using Nanodrop photometry. The BCA assay is a more precise method to detect proteins at low concentrations. As shown in **Table VI-7**, the OVA loadings of PLGA-OVA(10%) and PLGA-OVA(25%) obtained by the BCA assay are 14.5 wt% and 40.1 wt%, respectively, which are very close to the results of Nanodrop determination. The cationic PLGA-OVA(10%)-chitosan and PLGA-OVA(25%)-chitosan nanoparticles show OVA loadings of 9.8 wt% and 23.6 wt% from BCA results, while the ND results show higher OVA loadings and larger variations. The OVA loadings from BCA results were then used to calculate the encapsulation efficiency (EE) of OVA in the PLGA nanoparticles. The EE for plain PLGA-OVA nanoparticles is higher than 100%, which is implausible. The experiments were carefully checked and repeated to make sure that the right EE was obtained. In fact, the EE could be theoretically higher than 100% if the loss of PLGA during the preparation is higher than the loss of OVA. The EE of PLGA-OVA(10%)-chitosan is 98% and the EE of PLGA-OVA(25%)-chitosan is 95%.

Table VI-7 Encapsulation of ovalbumin in PLGA-based nanoparticles

Sample	Theoretical loading (w/w%)	OVA loading (ND) (w/w%)	OVA loading (BCA) (w/w%)	Encapsulation efficiency (%)
PLGA-OVA(10%) NPs	10	13.9±1.0	14.5±2.2	145±22
PLGA-OVA(25%) NPs	25	40.6±5.2	40.1±6.0	160±24
PLGA-OVA(10%)-chitosan NPs	10	12.3±5.2	9.8±3.5	98±35
PLGA-OVA(25%)-chitosan NPs	25	31.7±15.0	23.6±6.4	95±26

The data were obtained by averaging 3 repeats. All the data are shown as the mean and standard deviation (SD), i.e. mean±SD.

3.3.2 PLGA nanoparticles encapsulating SIINFEKL

Now that OVA protein has been shown to be encapsulated in PLGA nanoparticles efficiently, the encapsulation of SIINFEKL needs to be investigated. The concentration of SIINFEKL extracted from the nanoparticles was determined by fluorescence spectroscopy using a

microplate reader. For plain PLGA-SIINFEKL nanoparticles, the SIINFEKL loading extracted by the EA or NaOH-SDS method is about 0.0018 mg per 1 mg of PLGA-SIINFEKL nanoparticles. Their encapsulation efficiency (EE) is about 53.1% (Table VI-8). For the chitosan-coated PLGA-SIINFEKL nanoparticles, the SIINFEKL loading is about 1.0 μ g/mg and the EE is 28.5%, which is distinctly lower than that of PLGA-SIINFEKL nanoparticles. Three independent experiments were carried out.

Table VI-8 Determination of SIINFEKL loaded in PLGA-based nanoparticles

Sample	SIINFEKL loading (EA) (μ g/mg)	SIINFEKL loading (NaOH-SDS) (μ g/mg)	Theoretical SIINFEKL loading (μ g/mg)	EE (%)
PLGA-SIINFEKL	1.79 \pm 0.09	1.77 \pm 0.31	3.33	53.1 \pm 9.2
PLGA-SIINFEKL-chitosan	1.26 \pm 0.47	0.95 \pm 0.13	3.33	28.5 \pm 4.0

The data were obtained by averaging 3 repeats. All the data are shown as the mean and standard deviation (SD), i.e. mean \pm SD.

The true loading EEs for PLGA-SIINFEKL and PLGA-SIINFEKL-chitosan particles are distinctly lower than 100%. Practically, SIINFEKL (Mw, 1320 Da) may diffuse quickly from the organic phase to the aqueous phase during the emulsification step, causing the loss of SIINFEKL. PLGA-SIINFEKL-chitosan particles have a smaller EE than PLGA-SIINFEKL due to the effect of chitosan used during the emulsification step.

3.4 Stability of PLGA nanoparticles during freeze-drying

Nanoparticles in suspension are not suitable for a long-term storage. It is necessary to prepare dry particles using freeze-drying (FD), vacuum-drying, etc. FD as a promising method has been widely used for the preparation of dry protein formulations [201]. FD is also suitable for drying nanoparticles. The freezing step during FD is a process that may compromise the stability of PLGA nanoparticles. The suspensions of PLGA-based nanoparticles in water were frozen and thawed and then the sizes were measured by dynamic light scattering. It is obvious that one freeze-thaw circle induced PLGA nanoparticles to aggregate (Figure VI-3), increasing the hydrodynamic size from 120 nm to 408 nm. For cationic PLGA-chitosan nanoparticles, the size changed from 291 nm to 301 nm after one freeze-thaw circle and increased to 319 nm after the second freeze-thaw circle. The cationic PLGA-PEI nanoparticles are very stable during two freeze-thaw circles. Chitosan was the material chosen to cationise OVA-loaded PLGA nanoparticles. Chitosan-coated PLGA nanoparticles increase

their sizes slightly during one freeze-thaw circle. Therefore, it indicates that chitosan or PEI coating can improve the stability of PLGA nanoparticles.

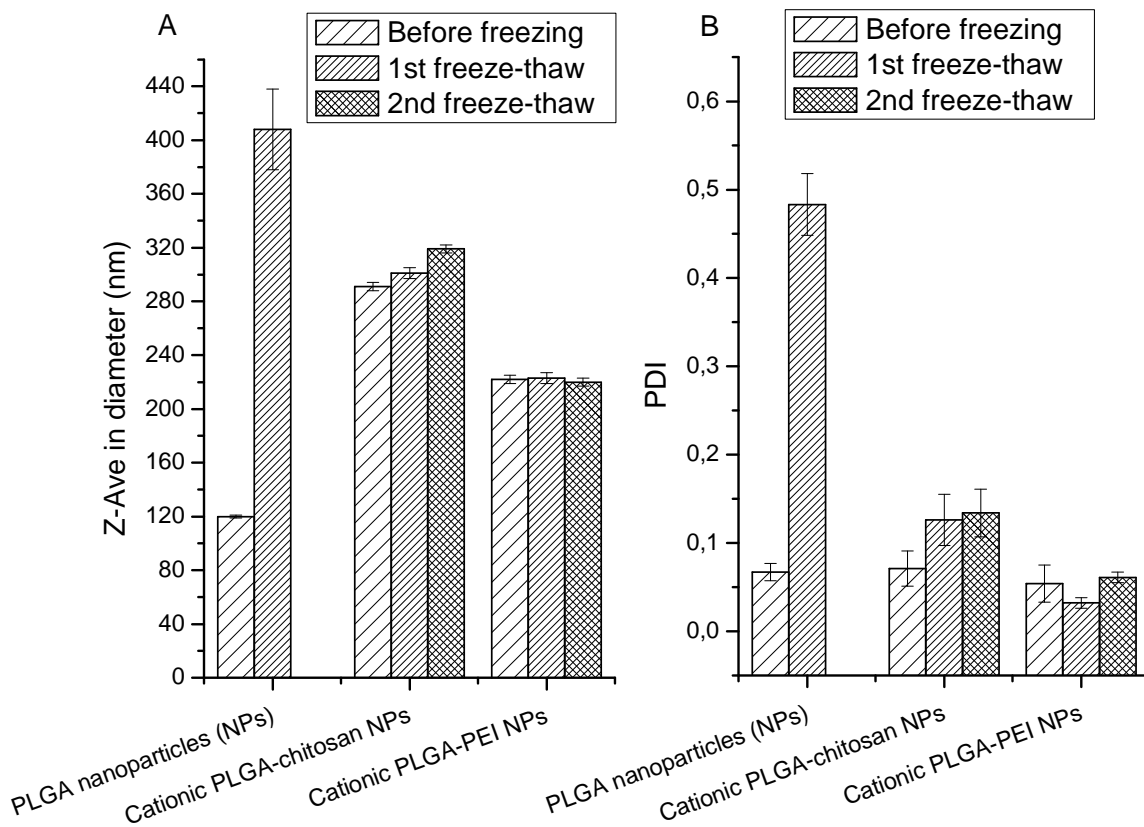


Figure VI-3. Effect of freeze-thaw cycles on the stability of PLGA-based nanoparticles. (A) Z-Ave sizes in diameter; (B) Size distribution (PDI).

In order to improve the stability of nanoparticles during freeze-drying, the addition of lyoprotectants such as trehalose and mannitol is necessary. Trehalose has already been used as a stabiliser of nanoparticles [147]. PLGA-OVA nanoparticles as shown in **Table VI-5** can be refined to obtain a smaller size and better size distribution of particles. The suspension of PLGA-OVA nanoparticles was firstly centrifuged at $5000 \times g$ for 5 min to remove some large particles, the supernatant suspension was then centrifuged at $15000 \times g$ to collect fine PLGA-OVA nanoparticles. Fine PLGA-OVA(10%) and cationic PLGA-OVA(10%)-chitosan nanoparticles were used for the formulation in trehalose. The suspension of OVA-loaded PLGA nanoparticles and 10% (w/v) trehalose aqueous solution were mixed at a dry mass ration of 1/4. There is no change of sizes and zeta-potentials for the PLGA nanoparticles in HPW and those in trehalose solution. The freeze-dried nanoparticles were re-suspended in HPW for DLS measurements. The sizes, PDIs and zeta-potentials of the OVA-loaded PLGA nanoparticles did not change during freeze-drying when 10% (w/v) trehalose was used as the lyoprotectant (**Table VI-9**).

Table VI-9 Stability of OVA-loaded PLGA nanoparticles in aqueous trehalose solution after freeze-drying

Sample	Before freeze-drying			After freeze-drying		
	Z-Ave (d.nm)	PDI	ZP (mv)	Z-Ave (d.nm)	PDI	ZP (mv)
PLGA-OVA(10%) NPs	126±2	0.060±0.016	-(22.9±0.5)	126±1	0.075±0.008	-25.1±0.9
PLGA-OVA(10%)-chitosan NPs	268±1	0.194±0.004	38.1±0.8	283±3	0.167±0.008	38.6±0.5

Trehalose/nanoparticles (NPs) = 4/1 (w/w)

3.5 Sugar-based microparticles encapsulating OVA/SIINFEKL-loaded PLGA nanoparticles

3.5.1 Microparticles encapsulating PLGA-OVA nanoparticles

Plain and cationic PLGA-OVA/OVA-Alexa488 nanoparticles were added to a TMD matrix to obtain a loading of 25 µg/mg. As shown in **Figure VI-4**, most of the microparticles show a size range of 20-30 µm and display shrunken surfaces. There is no distinct difference between the microparticles encapsulating PLGA-OVA/OVA-Alexa488 and PLGA-OVA/OVA-Alexa488-chitosan nanoparticles. The green fluorescence of OVA-Alexa488 is distributed over all microparticles, indicating that encapsulation has been achieved effectively. Both plain and cationic PLGA-OVA nanoparticles are dispersed in the microparticles as observed by CLSM. It is concluded that the surface properties of nanoparticles have no effect on the encapsulation of nanoparticles in TMD microparticles by spray-freeze-drying.

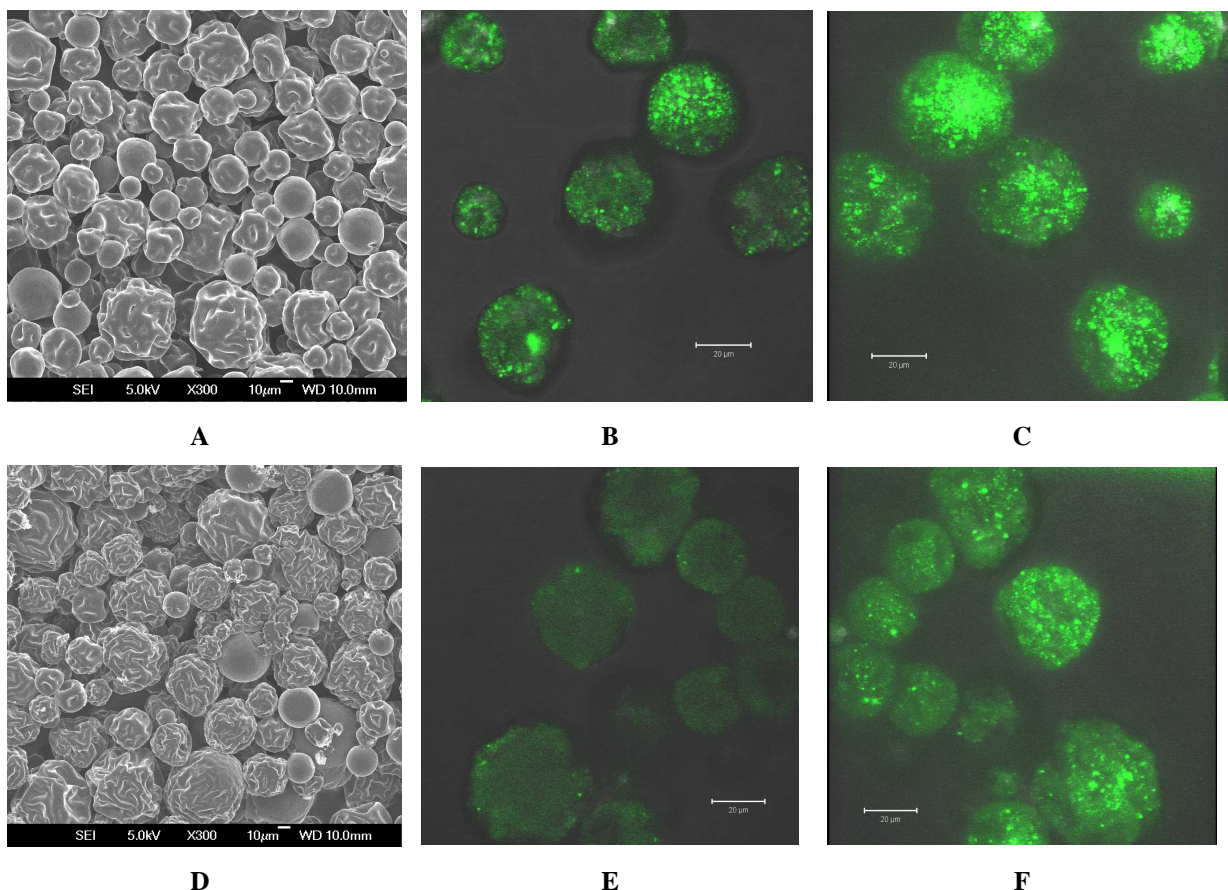


Figure VI-4. TMD microparticles encapsulating OVA-loaded PLGA nanoparticles. SEM micrograph (A), CLSM micrograph (B) and 3D view (C) of TMD/PLGA-OVA/OVA-Alexa488 microparticles; SEM micrograph (D), CLSM micrograph (E) and 3D view (F) of TMD/PLGA-OVA/OVA-Alexa488-chitosan microparticles.

3.5.2 Microparticles encapsulating PLGA-SIINFEKL nanoparticles

In the case of peptide-loaded PLGA nanoparticles, nanoparticles were formulated in TMD microparticles at a concentration of 10 μ g/mg. The SEM micrographs (**Figure VI-5**) show similar particles as the microparticles containing 25 μ g/mg of OVA-loaded PLGA nanoparticles. Weak fluorescence of the microparticles encapsulating PLGA-SIINFEKL nanoparticles was observed. The loading of FAM-SIINFEKL in PLGA nanoparticles is very small (lower than 0.18 wt%), thus the fluorescence intensity of SIINFEKL-loaded PLGA nanoparticles is low, which has also been demonstrated for the PLGA-SIINFEKL nanoparticles in suspension (**Figure VI-2**). However, the results obtained from CLSM micrographs (**Figure VI-5**) show that the plain and cationic PLGA-SIINFEKL nanoparticles have been respectively formulated into microparticles.

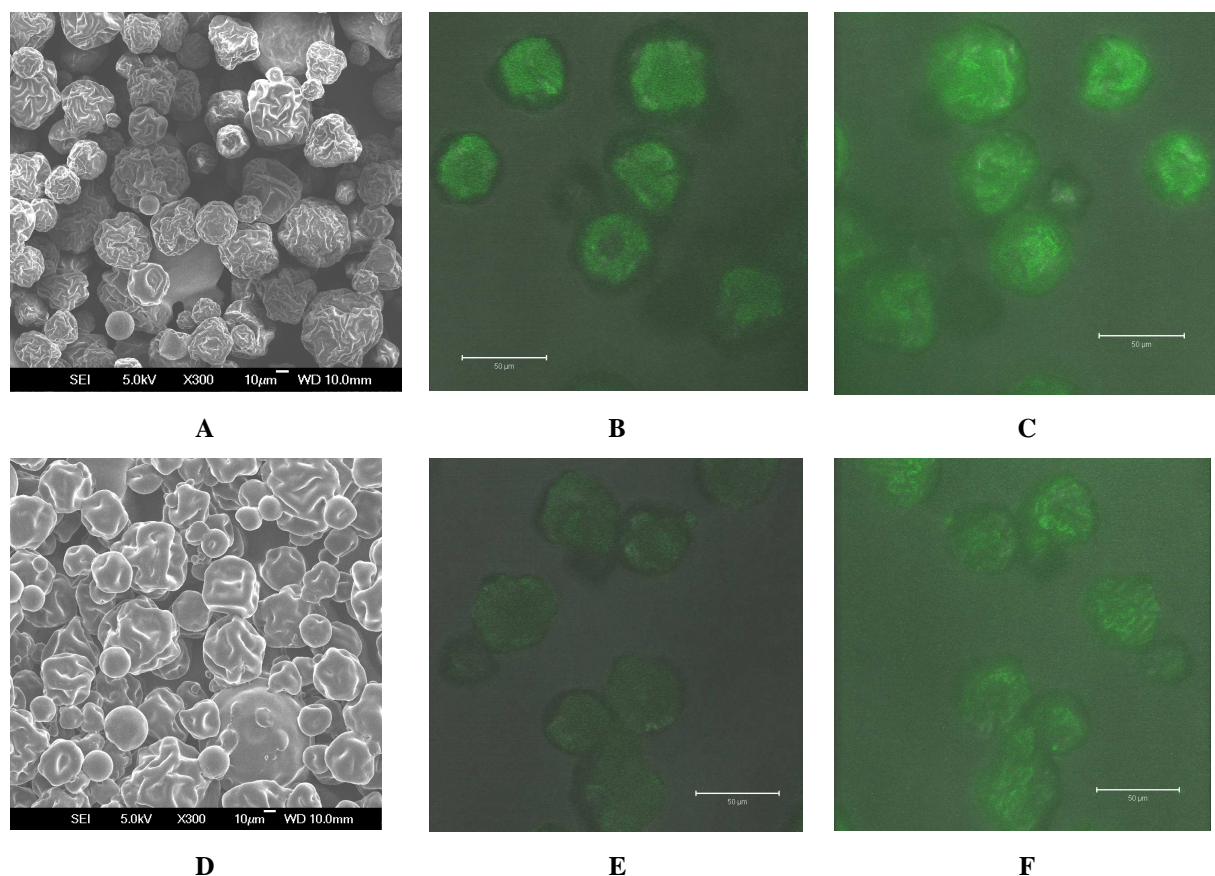


Figure VI-5. TMD microparticles encapsulating SIINFEKL-loaded PLGA nanoparticles. SEM micrograph (A), CLSM micrograph (B) and 3D view (C) of TMD/PLGA-SIINFEKL microparticles; SEM micrograph (D), CLSM micrograph (E) and 3D view (F) of TMD/PLGA-SIINFEKL-chitosan microparticles.

As shown by CLSM observation, OVA-loaded PLGA-based nanoparticles can be encapsulated in the sugar-based microparticles. The stability of PLGA nanoparticles in the formulation is critical for the subsequent application. The sizes of the antigen-loaded PLGA nanoparticles before and after being formulated in TMD microparticles are shown in **Table VI-10**. The dry TMD microparticles containing PLGA-OVA nanoparticles were stored at 4 °C for two months and were then dissolved in HPW for DLS measurements. The size and PDI of the PLGA-antigen nanoparticles in TMD microparticles do not increase after re-suspension in HPW compared to the formulations before spray-freeze-drying. The sizes of PLGA-OVA, PLGA-OVA-chitosan, PLGA-SIINFEKL and PLGA-SIINFEKL-chitosan nanoparticles resuspended from the microparticles are 134 nm, 303 nm, 128 nm and 213 nm, respectively, corresponding zeta-potentials of -19.3 mv, 34.4 mv, -23.6 mv and 19.7 mv. The PLGA-based nanoparticles in the microparticles after storage of two months at 4 °C have almost the same

size and PDI of freshly prepared nanoparticles. Therefore, the formulation of the TMD matrix can stabilise PLGA-based nanoparticles.

Table VI-10 Stability of antigen-loaded PLGA nanoparticles

Sample	Before SFD			Re-suspended		
	Z-Ave (d.nm)	PDI	ZP (mv)	Z-Ave (d.nm)	PDI	ZP (mv)
TMDD/PLGA-OVA	158±2	0.146±0.028	-(15.2±0.4)	134±1	0.135±0.026	-(19.3±1.1)
TMDD/PLGA-OVA-chitosan	349±2	0.249±0.006	38.8±0.3	303±3	0.240±0.011	34.4±1.2
TMDD/PLGA-SIINFEKL	117±2	0.154±0.009	-(25.2±1.6)	128±2	0.191±0.009	-(23.6±2.3)
TMDD/PLGA-SIINFEKL-chitosan	257±2	0.318±0.028	24.9±0.6	213±7	0.280±0.020	19.7±1.3

4. Discussion

4.1 Particle size control and cationisation of PLGA-based nanoparticles

The fabrication methods of PLGA-based nano- and microparticles include emulsification-evaporation [185, 188], emulsification-solvent diffusion [182, 202] and nanoprecipitation [203, 204]. The emulsification-evaporation method was used herein because it has already been proved feasible for loading protein into PLGA particles [185]. The water-in-oil-in-water (W/O/W) double emulsion technique was used to prepare antigen-loaded PLGA nanoparticles [205, 206]. OVA or SIINFEKL in aqueous (water) phase was first emulsified in PLGA in organic phase to obtain the first (1st) emulsion (W/O). The 1st emulsion was then added to a surfactant aqueous (water) solution for the second (2nd) emulsification. The W/O/W double emulsion was finally obtained and particles were formed when the organic solvent evaporated. Dichloride methane is normally used as the organic solvent for dissolving PLGA, but a less toxic solvent, ethyl acetate, was used in this study [206].

Polyvinyl alcohol (PVA) is the surfactant for stabilising the emulsion of PLGA nanoparticles. The particle size of PLGA-OVA(25%) nanoparticles depends on the concentration of PVA. The size increases when the PVA concentration increases at the range of 1% (w/w) and 5% (w/w). The size also increases when the PVA concentration decreases from 1% to 0.5%. Thus, 1% of PVA is the concentration for the smallest PLGA-OVA(25%) nanoparticles. In a study of the preparation of pure PLGA nanoparticles by the emulsification-solvent diffusion method,

authors found that the use of higher PVA concentration (1% - 10%) leads to larger mean particles size (175 nm - 260 nm) [182]. They found that the increase of viscosity of PVA solution when the concentration increases is responsible for the particle size increasing [182]. Even though the method for the preparation of PLGA nanoparticles is different, the tendency of the effect of PVA concentration (no less than 1.0 %) on the particles size is similar. Dynamic viscosity of PVA aqueous solution increases significantly with increasing PVA concentration (0 - 10% (w/v) [207]. During the emulsification process, an emulsion with larger droplets may be formed for higher viscosity solution if the energy for emulsification stays the same. However, the emulsion will not be stable if the PVA concentration is too low, resulting the increasing of the particle size. This explains that the size in the case of 0.5% PVA is distinctly larger than that in the case of 1.0% PVA.

PEI can cationise PLGA nanoparticles as proved in our experiments, but the biocompatibility of PEI is a big issue [200]. Chitosan is the choice for the cationisation of PLGA-based particles [186]. Chitosan with a low molecular weight and a medium molecular weight were used to coat PLGA nanoparticles. It results that the chitosan with a medium molecular weight did not work successfully and the chitosan with a low molecular weight has effectively achieved cationic PLGA nanoparticles. The reason may be explained as follows. Both chitosan can be dissolved in the acetate buffer (50 mM, pH 4.5). The interaction of the chitosan in the aqueous phase and the PLGA in the organic phase may play an important role. For the chitosan with a low molecular weight, the chitosan dissolved in the PVA solution may have strong interaction with the PLGA-ethyl acetate droplets, resulting efficient coatings after the organic solvent is evaporated. The chitosan with a higher molecular weight may reduce the interaction between the chitosan and the PLGA-ethyl acetate droplets, resulting in insufficient coatings.

4.2 OVA/SIINFEKL-loaded PLGA-based nanoparticles in the nano-in-micro particle systems

TMD microparticles containing silica nanoparticles and ovalbumin were studied in Chapter IV. Compared to silica nanoparticles for loading antigens, the antigen loading amount in PLGA nanoparticles is significantly higher. Antigens are mainly encapsulated inside of PLGA nanoparticles. The OVA-loaded or SIINFEKL-loaded plain and cationic PLGA nanoparticles are dispersed in TMD microparticles homogeneously. This indicates that the encapsulation of nanoparticles in microparticles by SFD is suitable for preparing the nano-in-micro particles

containing PLGA-based nanoparticles. Transcutaneous delivery of antigen-loaded PLGA nanoparticles has also been applied on the shaved skin of mice, inducing effective immune responses [199]. The penetration of PLGA nanoparticles on skin is limited due to the biological barrier of skin. Powder injection can accelerate particles into the epidermal or even dermal layer of skin, but there are requirements for the particle size and density [10, 12]. It is very difficult to deliver PLGA nanoparticles (100-1000 nm) into skin by powder injection due to the limitation of the device. A better solution to this problem is to formulate PLGA nanoparticles into microparticles as what was done in this study. Therefore, the TMD microparticles containing antigen-loaded PLGA nanoparticles seem to be a good candidate for the epidermal powder immunisation.

The stability of PLGA nanoparticles is crucial for their application. Freshly prepared antigen-loaded PLGA nanoparticles can be freeze-dried together with trehalose (disaccharide) as the lyoprotectant. In this study it was shown that the properties of PLGA nanoparticles can be preserved when the mass ratio of particles and trehalose in the formulation for freeze-drying is 1/4. It confirms that trehalose can stabilise PLGA nanoparticles after drying [147]. TMD matrix plays a similar role as trehalose for the stabilisation of PLGA nanoparticles. The sizes and zeta-potentials of the antigen-loaded PLGA nanoparticles in TMD microparticles are almost the same as those before spray-freeze-drying.

5. Conclusion

Ovalbumin and SIINFEKL have both been encapsulated in plain and cationic PLGA-based nanoparticles (150 - 300 nm in diameter) by a W/O/W double emulsion technique. Chitosan with a low molecular weight is suitable for cationising PLGA nanoparticles. Plain PLGA-OVA nanoparticles with high OVA loadings and cationic PLGA-OVA-chitosan nanoparticles with OVA loadings of 10 wt% and 24 wt% were obtained. The high loading of OVA enables a sufficient amount of antigens for immunisation. About 0.18 wt% of SIINFEKL was loaded in plain PLGA nanoparticles at an encapsulation efficiency of about 50%, while about 0.10 wt% of SIINFEKL was loaded in cationic PLGA nanoparticles at an encapsulation efficiency of about 30%.

OVA- and SIINFEKL-loaded PLGA nanoparticles have been encapsulated in the sugar-based TMD microparticles, respectively. Each kind of PLGA-antigen nanoparticles can be distributed in TMD microparticles homogeneously. Most of the TMD microparticles

containing PLGA-antigen nanoparticles have a size range of 20 - 30 μm , which meets the size requirement for epidermal powder immunisation. The stability of the antigen-loaded PLGA nanoparticles in TMD microparticles is sufficiently preserved. Furthermore, TMD microparticles containing PLGA nanoparticles enable the delivery of PLGA nanoparticles into skin by ballistic powder injection. From these preliminary studies, the nano-in-micro systems of PLGA nanoparticles in TMD microparticles have the potential to be used for epidermal immunisation via ballistic delivery.

Chapter VII. Final Summary

The work of this thesis is focused on the investigation of skin models mimicking the mechanical properties of human skin and vaccine-loaded microparticles for the development and applications of epidermal powder immunisation (EPI) using a novel device. This project was proposed at the background that a novel, economic and effective device for EPI is being developed by our collaborator. There are two crucial problems that need to be addressed for the design and development of a novel EPI device. One is to deliver vaccine particles into the viable epidermis or upper dermis of skin exactly. The vaccine cannot be efficiently presented to immune cells if its penetration is too small. Pain and bleeding are expected when the vaccine particles penetrate deeply into lower dermis or even hypodermis. For a new established device for EPI, the injection on skin models or *in vitro* skin is a prerequisite before it is applied on animals or later for clinical studies. The other is to prepare appropriate vaccine particles for EPI. Almost all present vaccines on market are supplied in liquid formulations. Dry formulations of vaccines in the form of powder or particles are required for EPI. Appropriate size and density of vaccine particles are very important for their use in EPI.

The studies in this thesis include mainly two parts. The first part is the development of a model skin for the evaluation and optimisation of the novel device for powder injection. This part is described in **Chapter II**. The second part is the fabrication of vaccine-loaded microparticles for EPI. A nanoparticles-in-microparticles (nano-in-micro) system was proposed to prepare vaccine microparticles for EPI. The nano-in-micro concept is described in **Chapter III**. Three embodiments of the nano-in-micro systems for EPI were further investigated using different nanoparticles and vaccines in the formulations. As described in **Chapter IV**, cationic mesoporous silica nanoparticles (MSNP-NH₂) and ovalbumin (OVA) were incorporated into sugar-based microparticles that are aimed for EPI. Influenza H1N1 hemagglutinin (HA) vaccine instead of ovalbumin and MSNP-NH₂ nanoparticles formulated in the microparticles were described in **Chapter V**. Preliminary studies of OVA/SIINFEKL-loaded PLGA nanoparticles for the formulation of TMD microparticles were described in **Chapter VI**. The detailed work of each main chapter is to be summarized further.

In **Chapter II**, the objective was to produce a skin model simulating the mechanical properties of human skin for the evaluation of intradermal powder injection devices. Pig skin

and different films made from gelatin, silicone and agar were prepared and investigated as skin model candidates. The mechanical properties of the skin model candidates were measured with an indentation method using a texture analyser. The indentation results of the films and the biological skin samples suggest that gelatin films plasticised with glycerol are very well suitable for a skin model. The mechanical properties of gelatin-based films can be tailored by changing the glycerol content in the film making it even possible to simulate human skin with different mechanical properties. The reproducibility of the gelatin films can be controlled and the stability during storage is very good. In addition, fluorescently labeled particles in the layered structural model of gelatin at a depth of 400 µm were successfully visualized by CLSM. This is a major advantage for observing the penetration and distribution of fluorescent particles after powder injection, further supporting the feasible applications of the gelatin films for the evaluation of powder injection devices.

Gelatin films were shown as a very good skin model simulating the mechanical properties of human skin, indicating them as a suitable base for powder injection.

In **Chapter III**, the concept of nanoparticles-in-microparticles (nano-in-micro) systems for EPI was proposed and some examples were studied. Sugar-based microparticles (20 - 30 µm in diameter) consisting of trehalose, mannitol, dextran (TMD) were fabricated by spray-freeze-drying. Nanoparticles were incorporated into the matrix by spray-freeze-drying of the mixture of nanoparticles and matrix solution. Nanoparticles including PS, PLGA, gelatin, silica and silk were encapsulated into TMD microparticles, respectively. The sizes of PS and PLGA nanoparticles can be best preserved in the resuspension of TMD microparticles carrying nanoparticles. The size, tap density and velocity of microparticles determine the penetration into skin when the microparticles are used for powder injection. High tap density is vital for the penetration of injected microparticles. The tap density of TMD microparticles can be enhanced by addition of CaCO_3 in the formulation.

In **Chapter IV**, MSNP-NH₂ nanoparticles and ovalbumin were formulated into sugar-based microparticles. Loading of OVA on MSNP-NH₂ was driven by electrostatic interactions. OVA-loaded silica nanoparticles were formulated into TMD microparticles by spray-freeze-drying. The obtained microparticles meet the size requirement for EPI. OVA-loaded MSNP-NH₂ can be homogeneously distributed in the microparticles as demonstrated by confocal microscopy. Furthermore, the silica nanoparticles in the dry microparticles can be re-

dispersed in aqueous solution without obvious aggregation. The recovered ovalbumin shows integrity compared to fresh ovalbumin solution.

In **Chapter V**, concentrated H1N1 HA (1 - 2 mg/ml) and MSNP-NH2 were formulated into TMD microparticles using SFD. The HA content in the TMD microparticles is about 4 μ g/mg. H1N1 HA can be adsorbed on MSNP-NH2 nanoparticles mainly by electrostatic interactions. The H1N1 HA reconstituted from the TMD microparticles maintains the integrity as studied by SDS-PAGE and shows a good binding affinity as proven by western blot. The HA biological activity, studied by the hemagglutinin inhibition (HAI) assay, was not affected during the encapsulation process of HA and MSNP-NH2 nanoparticles into TMD microparticles.

Some preliminary results about PLGA nanoparticles for antigen loadings were described in **Chapter VI**. OVA or SIINFEKL (OVA peptide) was loaded into PLGA nanoparticles by a W/O/W double emulsion technique and the antigen-loaded PLGA nanoparticles were encapsulated into TMD microparticles. Plain PLGA-OVA nanoparticles with OVA loadings of 15 wt% and 40 wt% were obtained and cationic PLGA-OVA-chitosan nanoparticles with OVA loadings of 10 wt% and 24 wt% were obtained. For PLGA-SIINFEKL nanoparticles, about 0.18 wt% of SIINFEKL was loaded in plain PLGA nanoparticles and about 0.10 wt% of SIINFEKL was loaded in cationic PLGA nanoparticles. OVA- and SIINFEKL-loaded PLGA nanoparticles encapsulated in the TMD microparticles have homogeneous distributions and good stability for resuspension in water.

In summary, the studies toward epi- and intra-dermal vaccinations by powder injection were carried out in the thesis. Some positive results in relation to the original objectives have been achieved. Major achievements include two parts: 1) gelatin-based films were found to be an appropriate skin model for the evaluation of epi- and intra-dermal powder injection devices; 2) Nano-in-micro particle systems as particulate vaccines have been demonstrated feasible for epi- and intra-dermal powder immunisation from the formulation point of view. The skin models will facilitate the optimisation of a novel EPI device that is being developed by our collaborator. Furthermore, the applications of the nano-in-micro vaccine particles in animals for epidermal powder immunisation will be interesting for future studies.

Chapter VIII. References

1. Pickering, L. K., Baker, C. J., Freed, G. L., Gall, S. A., Grogg, S. E., Poland, G. A., Rodewald, L. E., Schaffner, W., Stinchfield, P., Tan, L., Zimmerman, R. K., and Orenstein, W. A. (2009) Immunization programs for infants, children, adolescents, and adults: clinical practice guidelines by the Infectious Diseases Society of America, *Clin Infect Dis* 49, 817-840.
2. Haverkate, M., D'Ancona, F., Johansen, K., van der Velden, K., Giesecke, J., and Lopalco, P. L. (2011) Assessing vaccination coverage in the European Union: is it still a challenge?, *Expert Rev Vaccines* 10, 1195-1205.
3. Walsh, S. R., and Dolin, R. (2011) Vaccinia viruses: vaccines against smallpox and vectors against infectious diseases and tumors, *Expert Rev Vaccines* 10, 1221-1240.
4. Giudice, E. L., and Campbell, J. D. (2006) Needle-free vaccine delivery, *Adv Drug Deliv Rev* 58, 68-89.
5. Babiuk, S., Baca-Estrada, M., Babiuk, L. A., Ewen, C., and Foldvari, M. (2000) Cutaneous vaccination: the skin as an immunologically active tissue and the challenge of antigen delivery, *J Control Release* 66, 199-214.
6. Mitragotri, S. (2005) Immunization without needles, *Nat Rev Immunol* 5, 905-916.
7. Glenn, G. M., Kenney, R. T., Hammond, S. A., and Ellingsworth, L. R. (2003) Transcutaneous immunization and immunostimulant strategies, *Immunol Allergy Clin North Am* 23, 787-813.
8. Chen, D., and Payne, L. G. (2002) Targeting epidermal Langerhans cells by epidermal powder immunization, *Cell Res* 12, 97-104.
9. Arora, A., Prausnitz, M. R., and Mitragotri, S. (2008) Micro-scale devices for transdermal drug delivery, *Int. J. Pharm.* 364, 227-236.
10. Chen, D., Maa, Y. F., and Haynes, J. R. (2002) Needle-free epidermal powder immunization, *Expert Rev Vaccines* 1, 265-276.
11. Kendall, M. (2006) Engineering of needle-free physical methods to target epidermal cells for DNA vaccination, *Vaccine* 24, 4651-4656.
12. Kendall, M., Mitchell, T., and Wrighton-Smith, P. (2004) Intradermal ballistic delivery of micro-particles into excised human skin for pharmaceutical applications, *J Biomech* 37, 1733-1741.

13. Kendall, M., Rishworth, S., Carter, F., and Mitchell, T. (2004) Effects of relative humidity and ambient temperature on the ballistic delivery of micro-particles to excised porcine skin, *J Invest Dermatol* 122, 739-746.
14. Agache, P., and Humbert, P. (2004) *Measuring the Skin: non-invasive investigations, physiology, normal constants*, Springer-Verlag, New York.
15. Bos, J. D., Zonneveld, I., Das, P. K., Krieg, S. R., van der Loos, C. M., and Kapsenberg, M. L. (1987) The Skin Immune System (SIS): Distribution and Immunophenotype of Lymphocyte Subpopulations in Normal Human Skin, *J Investig Dermatol* 88, 569-573.
16. Hendriks, F. M., Brokken, D., van Eemeren, J., Oomens, C. W. J., Baaijens, F. P. T., and Horsten, J. (2003) A numerical-experimental method to characterize the non-linear mechanical behaviour of human skin, *Skin Res. Technol.* 9, 274-283.
17. Hendriks, F. M., Brokken, D., Oomens, C. W. J., and Baaijens, F. P. T. (2004) Influence of hydration and experimental length scale on the mechanical response of human skin in vivo, using optical coherence tomography, *Skin Res. Technol.* 10, 231-241.
18. Hendriks, F. M., Brokken, D., Oomens, C. W., Bader, D. L., and Baaijens, F. P. (2006) The relative contributions of different skin layers to the mechanical behavior of human skin in vivo using suction experiments, *Med Eng Phys* 28, 259-266.
19. Pailler-Mattei, C., Bec, S., and Zahouani, H. (2008) In vivo measurements of the elastic mechanical properties of human skin by indentation tests, *Medical Engineering & Physics* 30, 599-606.
20. Kendall, M. A. F., Chong, Y. F., and Cock, A. (2007) The mechanical properties of the skin epidermis in relation to targeted gene and drug delivery, *Biomaterials* 28, 4968-4977.
21. Meyers, M. A., and K.K., C. (1999) *Mechanical Behavior of Materials*, Prentice-Hall.
22. Jachowicz, J., McMullen, R., and Prettypaul, D. (2007) Indentometric analysis of in vivo skin and comparison with artificial skin models, *Skin Res. Technol.* 13, 299-309.
23. Escoffier, C., de Rigal, J., Rochefort, A., Vasselet, R., Leveque, J. L., and Agache, P. G. (1989) Age-related mechanical properties of human skin: an in vivo study, *J Invest Dermatol* 93, 353-357.
24. Agache, P. G., Monneur, C., Leveque, J. L., and De Rigal, J. (1980) Mechanical properties and Young's modulus of human skin in vivo, *Arch Dermatol Res* 269, 221-232.

25. Leveque, J. L., de Rigal, J., Agache, P. G., and Monneur, C. (1980) Influence of ageing on the in vivo extensibility of human skin at a low stress, *Arch Dermatol Res* 269, 127-135.
26. Manschot, J. (1985) The mechanical properties of human skin in vivo, Catholic University of Nijmegen, Nijmegen.
27. Manschot, J. F., and Brakkee, A. J. (1986) The measurement and modelling of the mechanical properties of human skin in vivo--I. The measurement, *J Biomech* 19, 511-515.
28. Grahame, R. (1968) In vivo observations on the elastic properties of human skin, London University, London.
29. Grahame, R., and Holt, P. J. L. (1969) The influence of aging on the in vivo elasticity of human skin, *Gerontologia* 15, 121-139.
30. Barel, A. O., Lambrecht, R., and Clarys, P. (1998) *Mechanical funtion of the skin: state of the art*, Karger, Basel.
31. Diridollou, S., Black, D., Lagarde, J. M., Gall, Y., Berson, M., Vabre, V., Patat, F., and Vaillant, L. (2000) Sex- and site-dependent variations in the thickness and mechanical properties of human skin in vivo, *Int J Cosmet Sci* 22, 421-435.
32. Bader, D. L., and Bowker, P. (1983) Mechanical characteristics of skin and underlying tissues in vivo, *Biomaterials* 4, 305-308.
33. Zhang, M., Zheng, Y. P., and Mak, A. F. (1997) Estimating the effective Young's modulus of soft tissues from indentation tests--nonlinear finite element analysis of effects of friction and large deformation, *Med Eng Phys* 19, 512-517.
34. Sanders, R. (1973) Torsional elasticity of human skin in vivo, *Pflugers Arch* 342, 255-260.
35. H., R. (1950) *Tensile Strength Human Skin*, Marburg-Lahn, Germany.
36. Manschot, J. F., and Brakkee, A. J. M. (1987) Characterisation of in vivo mechanical skin properties independent of measuring configuration, *Bioeng Skin* 3, 1-10.
37. Clark, J. A., Cheng, J. C., and Leung, K. S. (1996) Mechanical properties of normal skin and hypertrophic scars, *Burns* 22, 443-446.
38. Pan, L., Zan, L., and Foster, F. S. (1997) In vivo high frequency ultrasound assessment of skin elasticity, *Proc-IEEE Ultrason Symp* 1082, 1087-1091.
39. Edwards, C., and Marks, R. (1995) Evaluation of biomechanical properties of human skin, *Clin Dermatol* 13, 375-380.

40. Xu, F., Lu, T. J., and Seffen, K. A. (2008) Biothermomechanical behavior of skin tissue, *Acta Mech Sinica-Prc* 24, 1-23.
41. Pan, L., Zan, L., and Foster, F. S. (1998) Ultrasonic and viscoelastic properties of skin under transverse mechanical stress in vitro, *Ultrasound Med Biol* 24, 995-1007.
42. Daly, C. H. (1982) BIOMECHANICAL PROPERTIES OF DERMIS, *J. Invest. Dermatol.* 79, S17-S20.
43. Silver, F. H., Freeman, J. W., and DeVore, D. (2001) Viscoelastic properties of human skin and processed dermis, *Skin Res Technol* 7, 18-23.
44. Jansen, L. H., and Rottier, P. B. (1958) Some mechanical properties of human abdominal skin measured on excised strips: a study of their dependence on age and how they are influenced by the presence of striae, *Dermatologica* 117, 65-83.
45. Dean, H. J., Fuller, D., and Osorio, J. E. (2003) Powder and particle-mediated approaches for delivery of DNA and protein vaccines into the epidermis, *Comp. Immunol. Microbiol. Infect. Dis.* 26, 373-388.
46. Chen, D. X., Endres, R. L., Erickson, C. A., Weis, K. F., McGregor, M. W., Kawaoka, Y., and Payne, L. G. (2000) Epidermal immunization by a needle-free powder delivery technology: Immunogenicity of influenza vaccine and protection in mice, *Nat. Med.* 6, 1187-1190.
47. Drape, R. J., Macklin, M. D., Barr, L. J., Jones, S., Haynes, J. R., and Dean, H. J. (2006) Epidermal DNA vaccine for influenza is immunogenic in humans, *Vaccine* 24, 4475-4481.
48. Roberts, L. K., Barr, L. J., Fuller, D. H., McMahon, C. W., Leese, P. T., and Jones, S. (2005) Clinical safety and efficacy of a powdered Hepatitis B nucleic acid vaccine delivered to the epidermis by a commercial prototype device, *Vaccine* 23, 4867-4878.
49. Raju, P. A., McSloy, N., Truong, N. K., and Kendall, M. A. (2006) Assessment of epidermal cell viability by near infrared multi-photon microscopy following ballistic delivery of gold micro-particles, *Vaccine* 24, 4644-4647.
50. Liu, Y. (2007) Utilization of the venturi effect to introduce micro-particles for epidermal vaccination, *Med Eng Phys* 29, 390-397.
51. Menon, G. K., Brandsma, J. L., and Schwartz, P. M. (2007) Particle-mediated gene delivery and human skin: Ultrastructural observations on stratum corneum barrier structures, *Skin Pharmacol. Physiol.* 20, 141-147.
52. Dehn, J. (1987) A unified theory of penetration, *International Journal of Impact Engineering* 5, 239-248.

53. Mitchell, T. J., Kendall, M. A. F., and Bellhouse, B. J. (2003) A ballistic study of micro-particle penetration to the oral mucosa, *International Journal of Impact Engineering* 28, 581-599.

54. Lir, I., Haber, M., and Dodiuk-Kenig, H. (2007) Skin surface model material as a substrate for adhesion-to-skin testing, *J. Adhes. Sci. Technol.* 21, 1497-1512.

55. Roh, D. H., Kang, S. Y., Kim, J. Y., Kwon, Y. B., Kweon, H. Y., Lee, K. G., Park, Y. H., Baek, R. M., Heo, C. Y., Choe, J., and Lee, J. H. (2006) Wound healing effect of silk fibroin/alginate-blended sponge in full thickness skin defect of rat, *J. Mater. Sci.-Mater. Med.* 17, 547-552.

56. Schramm-Baxter, J., Katrenicik, J., and Mitragotri, S. (2004) Jet injection into polyacrylamide gels: investigation of jet injection mechanics, *J. Biomech.* 37, 1181-1188.

57. Choi, Y. S., Hong, S. R., Lee, Y. M., Song, K. W., Park, M. H., and Nam, Y. S. (1999) Study on gelatin-containing artificial skin: I. Preparation and characteristics of novel gelatin-alginate sponge, *Biomaterials* 20, 409-417.

58. Yannas, I. V., Burke, J. F., Gordon, P. L., and Huang, C. (1977) Multilayer membrane useful as synthetic film, Patent Number: US4060081 A.

59. Lee, S. B., Jeon, H. W., Lee, Y. W., Lee, Y. M., Song, K. W., Park, M. H., Nam, Y. S., and Ahn, H. C. (2003) Bio-artificial skin composed of gelatin and (1-->3), (1-->6)-beta-glucan, *Biomaterials* 24, 2503-2511.

60. Pogue, B. W., and Patterson, M. S. (2006) Review of tissue simulating phantoms for optical spectroscopy, imaging and dosimetry, *J Biomed Opt* 11, 041102.

61. Stachowiak, J. C., von Muhlen, M. G., Li, T. H., Jalilian, L., Parekh, S. H., and Fletcher, D. A. (2007) Piezoelectric control of needle-free transdermal drug delivery, *J. Control. Release* 124, 88-97.

62. Stachowiak, J. C., Li, T. H., Arora, A., Mitragotri, S., and Fletcher, D. A. (2009) Dynamic control of needle-free jet injection, *J. Control. Release* 135, 104-112.

63. Mansy, H. A., Grahe, J. R., and Sandier, R. H. (2008) Elastic properties of synthetic materials for soft tissue modeling, *Physics in Medicine & Biology* 53, 2115-2130.

64. DiMaio, S. P., and Salcudean, S. E. (2002) *Needle Insertion Modelling for the Interactive Simulation of Percutaneous Procedures* Springer Berlin / Heidelberg.

65. Pawley, J. B. (1995) *Handbook of Biological Confocal Microscopy*, Plenum Press, New York.

66. Alvarez-Roman, R., Naik, A., Kalia, Y. N., Fessi, H., and Guy, R. H. (2004) Visualization of skin penetration using confocal laser scanning microscopy, *Eur. J. Pharm. Biopharm.* 58, 301-316.

67. Grams, Y. Y., and Bouwstra, J. A. (2002) A new method to determine the distribution of a fluorophore in scalp skin with focus on hair follicles, *Pharm Res* 19, 350-354.

68. Turner, N. G., and Guy, R. H. (1997) Iontophoretic transport pathways: Dependence on penetrant physicochemical properties, *J. Pharm. Sci.* 86, 1385-1389.

69. Turner, N. G., Ferry, L., Price, M., Cullander, C., and Guy, R. H. (1997) Iontophoresis of poly-L-lysines: the role of molecular weight?, *Pharm Res* 14, 1322-1331.

70. Pygall, S. R., Whetstone, J., Timmins, P., and Melia, C. D. (2007) Pharmaceutical applications of confocal laser scanning microscopy: The physical characterisation of pharmaceutical systems, *Advanced Drug Delivery Reviews* 59, 1434-1452.

71. Brus, C., Santi, P., Colombo, P., and Kissel, T. (2002) Distribution and quantification oligodeoxynucleotide complexes of polyethylenimine in human skin after iontophoretic delivery using confocal scanning laser microscopy, *J. Control. Release* 84, 171-181.

72. Jung, S., Patzelt, A., Otberg, N., Thiede, G., Sterry, W., and Lademann, J. (2009) Strategy of topical vaccination with nanoparticles, *J. Biomed. Opt.* 14.

73. Vauthier, C., and Bouchemal, K. (2009) Methods for the preparation and manufacture of polymeric nanoparticles, *Pharm Res* 26, 1025-1058.

74. De Koker, S., Lambrecht, B. N., Willart, M. A., van Kooyk, Y., Grootenhuis, J., Vervaet, C., Remon, J. P., and De Geest, B. G. (2011) Designing polymeric particles for antigen delivery, *Chem Soc Rev* 40, 320-339.

75. Li, Z. X., Barnes, J. C., Bosoy, A., Stoddart, J. F., and Zink, J. I. (2012) Mesoporous silica nanoparticles in biomedical applications, *Chemical Society Reviews* 41, 2590-2605.

76. Panyam, J., and Labhasetwar, V. (2003) Biodegradable nanoparticles for drug and gene delivery to cells and tissue, *Adv Drug Deliv Rev* 55, 329-347.

77. Look, M., Bandyopadhyay, A., Blum, J. S., and Fahmy, T. M. (2010) Application of nanotechnologies for improved immune response against infectious diseases in the developing world, *Advanced Drug Delivery Reviews* 62, 378-393.

78. Kwon, Y. J., James, E., Shastri, N., and Frechet, J. M. J. (2005) In vivo targeting of dendritic cells for activation of cellular immunity using vaccine carriers based on pH-responsive microparticles, *P Natl Acad Sci USA* 102, 18264-18268.

79. Cruz, L. J., Tacken, P. J., Fokkink, R., Joosten, B., Stuart, M. C., Albericio, F., Torensma, R., and Figdor, C. G. (2010) Targeted PLGA nano- but not microparticles specifically deliver antigen to human dendritic cells via DC-SIGN in vitro, *J. Control. Release 144*, 118-126.

80. Peek, L. J., Middaugh, C. R., and Berkland, C. (2008) Nanotechnology in vaccine delivery, *Advanced Drug Delivery Reviews 60*, 915-928.

81. Reddy, S. T., van der Vlies, A. J., Simeoni, E., Angeli, V., Randolph, G. J., O'Neill, C. P., Lee, L. K., Swartz, M. A., and Hubbell, J. A. (2007) Exploiting lymphatic transport and complement activation in nanoparticle vaccines, *Nat Biotechnol 25*, 1159-1164.

82. Bourquin, C., Wurzenberger, C., Heidegger, S., Fuchs, S., Anz, D., Weigel, S., Sandholzer, N., Winter, G., Coester, C., and Endres, S. (2010) Delivery of Immunostimulatory RNA Oligonucleotides by Gelatin Nanoparticles Triggers an Efficient Antitumoral Response, *J Immunother 33*, 935-944.

83. Florindo, H. F., Pandit, S., Goncalves, L. M., Alpar, H. O., and Almeida, A. J. (2010) Surface modified polymeric nanoparticles for immunisation against equine strangles, *Int J Pharm 390*, 25-31.

84. Verheul, R. J., Slutter, B., Bal, S. M., Bouwstra, J. A., Jiskoot, W., and Hennink, W. E. (2011) Covalently stabilized trimethyl chitosan-hyaluronic acid nanoparticles for nasal and intradermal vaccination, *J. Control. Release 156*, 46-52.

85. Wang, B., Yu, H., Yang, F. R., Huang, M., Ma, J. H., and Tong, G. Z. (2012) Protective efficacy of a broadly cross-reactive swine influenza DNA vaccine encoding M2e, cytotoxic T lymphocyte epitope and consensus H3 hemagglutinin, *Virol J 9*, 127.

86. Boudreau, E. F., Josley, M., Ullman, D., Fisher, D., Dalrymple, L., Sellers-Myers, K., Loudon, P., Rusnak, J., Rivard, R., Schmaljohn, C., and Hooper, J. W. (2012) A Phase 1 clinical trial of Hantaan virus and Puumala virus M-segment DNA vaccines for hemorrhagic fever with renal syndrome, *Vaccine 30*, 1951-1958.

87. Dupuy, L. C., Richards, M. J., Reed, D. S., and Schmaljohn, C. S. (2010) Immunogenicity and protective efficacy of a DNA vaccine against Venezuelan equine encephalitis virus aerosol challenge in nonhuman primates, *Vaccine 28*, 7345-7350.

88. He, Q., Mitchell, A., Morcol, T., and Bell, S. J. D. (2002) Calcium phosphate nanoparticles induce mucosal immunity and protection against herpes simplex virus type 2, *Clin Diagn Lab Immun 9*, 1021-1024.

89. Slowing, I. I., Vivero-Escoto, J. L., Trewyn, B. G., and Lin, V. S. Y. (2010) Mesoporous silica nanoparticles: structural design and applications, *J Mater Chem* 20, 7924-7937.

90. He, Q. J., and Shi, J. L. (2011) Mesoporous silica nanoparticle based nano drug delivery systems: synthesis, controlled drug release and delivery, pharmacokinetics and biocompatibility, *J Mater Chem* 21, 5845-5855.

91. Wan, Y., and Zhao, D. Y. (2007) On the controllable soft-templating approach to mesoporous silicates, *Chem Rev* 107, 2821-2860.

92. Vallet-Regi, M., Balas, F., and Arcos, D. (2007) Mesoporous materials for drug delivery, *Angew Chem Int Edit* 46, 7548-7558.

93. Slowing, I. I., Vivero-Escoto, J. L., Wu, C. W., and Lin, V. S. Y. (2008) Mesoporous silica nanoparticles as controlled release drug delivery and gene transfection carriers, *Advanced Drug Delivery Reviews* 60, 1278-1288.

94. Park, C., Oh, K., Lee, S. C., and Kim, C. (2007) Controlled release of guest molecules from mesoporous silica particles based on a pH-responsive polypseudorotaxane motif, *Angew Chem Int Edit* 46, 1455-1457.

95. Deng, Z. W., Zhen, Z. P., Hu, X. X., Wu, S. L., Xu, Z. S., and Chu, P. K. (2011) Hollow chitosan-silica nanospheres as pH-sensitive targeted delivery carriers in breast cancer therapy, *Biomaterials* 32, 4976-4986.

96. Wilkinson, P. C., and White, R. G. (1966) The role of mycobacteria and silica in the immunological response of the guinea-pig, *Immunology* 11, 229-241.

97. Vallhov, H., Gabrielsson, S., Stromme, M., Scheynius, A., and Garcia-Bennett, A. E. (2007) Mesoporous silica particles induce size dependent effects on human dendritic cells, *Nano Lett* 7, 3576-3582.

98. Vallhov, H., Kupferschmidt, N., Gabrielsson, S., Paulie, S., Stromme, M., Garcia-Bennett, A. E., and Scheynius, A. (2012) Adjuvant Properties of Mesoporous Silica Particles Tune the Development of Effector T Cells, *Small* 8, 2116-2124.

99. Wang, T., Jiang, H., Zhao, Q., Wang, S., Zou, M., and Cheng, G. (2012) Enhanced mucosal and systemic immune responses obtained by porous silica nanoparticles used as an oral vaccine adjuvant: Effect of silica architecture on immunological properties, *Int J Pharm* 436, 351-358.

100. Ginsberg, B. A., Gallardo, H. F., Rasalan, T. S., Adamow, M., Mu, Z. Y., Tandon, S., Bewkes, B. B., Roman, R. A., Chapman, P. B., Schwartz, G. K., Carvajal, R. D., Panageas, K. S., Terzulli, S. L., Houghton, A. N., Yuan, J. D. D., and Wolchok, J. D.

(2010) Immunologic Response to Xenogeneic gp100 DNA in Melanoma Patients: Comparison of Particle-Mediated Epidermal Delivery with Intramuscular Injection, *Clin Cancer Res* 16, 4057-4065.

101. Huang, H. N., Li, T. L., Chan, Y. L., Chen, C. L., and Wu, C. J. (2009) Transdermal immunization with low-pressure-gene-gun mediated chitosan-based DNA vaccines against Japanese encephalitis virus, *Biomaterials* 30, 6017-6025.

102. Lee, P. W., Hsu, S. H., Tsai, J. S., Chen, F. R., Huang, P. J., Ke, C. J., Liao, Z. X., Hsiao, C. W., Lin, H. J., and Sung, H. W. (2010) Multifunctional core-shell polymeric nanoparticles for transdermal DNA delivery and epidermal Langerhans cells tracking, *Biomaterials* 31, 2425-2434.

103. Romani, N., Thurnher, M., Idoyaga, J., Steinman, R. M., and Flacher, V. (2010) Targeting of antigens to skin dendritic cells: possibilities to enhance vaccine efficacy, *Immunol Cell Biol* 88, 424-430.

104. Sparber, F., Tripp, C. H., Hermann, M., Romani, N., and Stoitzner, P. (2010) Langerhans cells and dermal dendritic cells capture protein antigens in the skin: Possible targets for vaccination through the skin, *Immunobiology* 215, 770-779.

105. Dean, H. J., and Chen, D. X. (2004) Epidermal powder immunization against influenza, *Vaccine* 23, 681-686.

106. Maa, Y. F., Shu, C., Ameri, M., Zuleger, C., Che, J., Osorio, J. E., Payne, L. G., and Chen, D. X. (2003) Optimization of an alum-adsorbed vaccine powder formulation for epidermal powder immunization, *Pharm. Res.* 20, 969-977.

107. Maa, Y. F., Ameri, M., Shu, C., Payne, L. G., and Chen, D. X. (2004) Influenza vaccine powder formulation development: Spray-freeze-drying and stability evaluation, *J. Pharm. Sci.* 93, 1912-1923.

108. Rochelle, C., and Lee, G. (2007) Dextran or hydroxyethyl starch in spray-freeze-dried Trehalose/Mannitol microparticles intended as ballistic particulate carriers for proteins, *J. Pharm. Sci.* 96, 2296-2309.

109. Condliffe, J., Schiffter, H. A., Cleveland, R. O., and Coussios, C. C. (2010) An acoustic microscopy technique to assess particle size and distribution following needle-free injection, *J Acoust Soc Am* 127, 2252-2261.

110. Mundargi, R. C., Babu, V. R., Rangaswamy, V., Patel, P., and Aminabhavi, T. M. (2008) Nano/micro technologies for delivering macromolecular therapeutics using poly(D,L-lactide-co-glycolide) and its derivatives, *J. Control. Release* 125, 193-209.

111. Kajjari, P. B., Manjeshwar, L. S., and Aminabhavi, T. M. (2011) Semi-Interpenetrating Polymer Network Hydrogel Blend Microspheres of Gelatin and Hydroxyethyl Cellulose for Controlled Release of Theophylline, *Ind Eng Chem Res* 50, 7833-7840.
112. Ho, J., Huang, Y., Danquah, M. K., Wang, H. T., and Forde, G. M. (2010) Synthesis of biodegradable polymer-mesoporous silica composite microspheres for DNA prime-protein boost vaccination, *European Journal of Pharmaceutical Sciences* 39, 412-420.
113. Schliehe, C., Schliehe, C., Thiry, M., Tromsdorf, U. I., Hentschel, J., Weller, H., and Groettrup, M. (2011) Microencapsulation of inorganic nanocrystals into PLGA microsphere vaccines enables their intracellular localization in dendritic cells by electron and fluorescence microscopy, *J. Control. Release* 151, 278-285.
114. Lell, P. (2004) Needleless injection device with pyrotechnic drive, Patent Number: US 2004/0049151 A1.
115. Lell, P. (2008) Device for injecting a dust-like or powdery substance into a body tissue, Patent Number: EP1599242 B1.
116. Singh, M., Chakrapani, A., and O'Hagon, D. (2007) Nanoparticles and microparticles as vaccine-delivery systems, *Expert Review of Vaccines* 6, 797-808.
117. Leleux, J., and Roy, K. (2013) Micro and nanoparticle-based delivery systems for vaccine immunotherapy: an immunological and materials perspective, *Adv Healthc Mater* 2, 72-94.
118. Mitter, N., Yu, C., Mody, K. T., Popat, A., Mahony, D., and Cavallaro, A. S. (2013) Mesoporous Silica Nanoparticles as antigen carriers and adjuvants for Vaccine Delivery *Nanoscale, 2013, Accepted Manuscript, DOI: 10.1039/C3NR00357D*
119. Gregory, A. E., and Titball R, W. D. (2013) Vaccine delivery using nanoparticles, *Front Cell Infect Microbiol. doi: 10.3389/fcimb.2013.00013.*
120. Boyer, G., Laquieze, L., Le Bot, A., Laquieze, S., and Zahouani, H. (2009) Dynamic indentation on human skin in vivo: ageing effects, *Skin Res Technol* 15, 55-67.
121. Zahouani, H., Pailler-Mattei, C., Sohm, B., Vargiolu, R., Cenizo, V., and Debret, R. (2009) Characterization of the mechanical properties of a dermal equivalent compared with human skin in vivo by indentation and static friction tests, *Skin Res Technol* 15, 68-76.
122. Jachowicz, J., McMullen, R., and Prettypaul, D. (2008) Alteration of skin mechanics by thin polymer films, *Skin Res Technol* 14, 312-319.

123. Achet, D., and He, X. W. (1995) Determination of the Renaturation Level in Gelatin Films, *Polymer* 36, 787-791.

124. Bergo, P., and Sobral, P. J. A. (2007) Effects of plasticizer on physical properties of pigskin gelatin films, *Food Hydrocolloid* 21, 1285-1289.

125. Cao, N., Yang, X. M., and Fu, Y. H. (2009) Effects of various plasticizers on mechanical and water vapor barrier properties of gelatin films, *Food Hydrocolloid* 23, 729-735.

126. Lahm, K., and Lee, G. (2006) Penetration of crystalline powder particles into excised human skin membranes and model gels from a supersonic powder injector, *J. Pharm. Sci.* 95, 1511-1526.

127. Guha, R. A., Shear, N. H., and Papini, M. (2010) Ballistic Impact of Single Particles Into Gelatin: Experiments and Modeling With Application to Transdermal Pharmaceutical Delivery, *J Biomech Eng-T Asme* 132.

128. ASTM. (2007) Standard Practice for Maitaining Constant Relative Huamidity by Means of Aqueous Solutions, *ASTM*.

129. Sneddon, I. N. (1965) The relation between load and penetration in the axiometric Boussinesq problem for a punch of arbitrary profile, *Int. J. Eng. Sci.* 3, 47-57.

130. Herkenne, C., Naik, A., Kalia, Y. N., Hadgraft, J., and Guy, R. H. (2006) Pig ear skin ex vivo as a model for in vivo dermatopharmacokinetic studies in man, *Pharm. Res.* 23, 1850-1856.

131. Barbero, A. M., and Frasch, H. F. (2009) Pig and guinea pig skin as surrogates for human in vitro penetration studies: A quantitative review, *Toxicol in Vitro* 23, 1-13.

132. Schiffter, H., Condliffe, J., and Vonhoff, S. (2010) Spray-freeze-drying of nanosuspensions: the manufacture of insulin particles for needle-free ballistic powder delivery, *J R Soc Interface* 7 Suppl 4, S483-500.

133. Geerligs, M., van Breemen, L., Peters, G., Ackermans, P., Baaijens, F., and Oomens, C. (2011) In vitro indentation to determine the mechanical properties of epidermis, *J. Biomech.* 44, 1176-1181.

134. Pailler-Mattei, C., Pavan, S., Vargiolu, R., Pirot, F., Falson, F., and Zahouani, H. (2007) Contribution of stratum corneum in determining bio-tribological properties of the human skin, *Wear* 263, 1038-1043.

135. Alvarez-Roman, R., Naik, A., Kalia, Y., Guy, R. H., and Fessi, H. (2004) Skin penetration and distribution of polymeric nanoparticles, *J. Control. Release* 99, 53-62.

136. Randolph, G. J., Angeli, V., and Swartz, M. A. (2005) Dendritic-cell trafficking to lymph nodes through lymphatic vessels, *Nat Rev Immunol* 5, 617-628.
137. Bhavsar, M. D., and Amiji, M. M. (2008) Development of novel biodegradable polymeric nanoparticles-in-microsphere formulation for local plasmid DNA delivery in the gastrointestinal tract, *Aaps Pharmscitech* 9, 288-294.
138. Bhavsar, M. D., Tiwari, S. B., and Amiji, M. M. (2006) Formulation optimization for the nanoparticles-in-microsphere hybrid oral delivery system using factorial design, *J. Control. Release* 110, 422-430.
139. LEE, Y.-S., Johnson, P. J., Philip T. Robbins, and Bridson, R. (2013) Production of nanoparticles-in-microparticles by a double emulsion method: A comprehensive study, *Eur. J. Pharm. Biopharm.* 83, 168-173.
140. Wanakule, P., Liu, G. W., Fleury, A. T., and Roy, K. (2012) Nano-inside-micro: Disease-responsive microgels with encapsulated nanoparticles for intracellular drug delivery to the deep lung, *J. Control. Release* 162, 429-437.
141. Gomez-Gaete, C., Fattal, E., Silva, L., Besnard, M., and Tsapis, N. (2008) Dexamethasone acetate encapsulation into Trojan particles, *J. Control. Release* 128, 41-49.
142. Sham, J. O. H., Zhang, Y., Finlay, W. H., Roa, W. H., and Lobenberg, R. (2004) Formulation and characterization of spray-dried powders containing nanoparticles for aerosol delivery to the lung, *Int. J. Pharm.* 269, 457-467.
143. Ohashi, K., Kabasawa, T., Ozeki, T., and Okada, H. (2009) One-step preparation of rifampicin/poly(lactic-co-glycolic acid) nanoparticle-containing mannitol microspheres using a four-fluid nozzle spray drier for inhalation therapy of tuberculosis, *J. Control. Release* 135, 19-24.
144. Takashima, Y., Saito, R., Nakajima, A., Oda, M., Kimura, A., Kanazawa, T., and Okada, H. (2007) Spray-drying preparation of microparticles containing cationic PLGA nanospheres as gene carriers for avoiding aggregation of nanospheres, *Int. J. Pharm.* 343, 262-269.
145. Wieber, A., Selzer, T., and Kreuter, J. (2011) Characterisation and stability studies of a hydrophilic decapeptide in different adjuvant drug delivery systems: A comparative study of PLGA nanoparticles versus chitosan-dextran sulphate microparticles versus DOTAP-liposomes, *Int. J. Pharm.* 421, 151-159.
146. Wang, G., Pan, L., Zhang, Y., Wang, Y., Zhang, Z., Lu, J., Zhou, P., Fang, Y., and Jiang, S. (2011) Intranasal delivery of cationic PLGA nano/microparticles-loaded

FMDV DNA vaccine encoding IL-6 elicited protective immunity against FMDV challenge, *PLoS One* 6, e27605.

147. Mattheolabakis, G., Lagoumartzis, G., Panagi, Z., Papadimitriou, E., Partidos, C. D., and Avgoustakis, K. (2010) Transcutaneous delivery of a nanoencapsulated antigen: Induction of immune responses, *Int. J. Pharm.* 385, 187-193.

148. Sarti, F., Perera, G., Hintzen, F., Kotti, K., Karageorgiou, V., Kammona, O., Kiparissides, C., and Bernkop-Schnurch, A. (2011) In vivo evidence of oral vaccination with PLGA nanoparticles containing the immunostimulant monophosphoryl lipid A, *Biomaterials* 32, 4052-4057.

149. Fuchs, S., Winter, G., and Coester, C. (2010) Ultrasonic resonator technology as a new quality control method evaluating gelatin nanoparticles, *J Microencapsul* 27, 242-252.

150. Fuchs, S., Kutscher, M., Hertel, T., Winter, G., Pietzsch, M., and Coester, C. (2010) Transglutaminase: New insights into gelatin nanoparticle cross-linking, *J Microencapsul* 27, 747-754.

151. Hofer, M., Winter, G., and Myschik, J. (2012) Recombinant spider silk particles for controlled delivery of protein drugs, *Biomaterials* 33, 1554-1562.

152. Xia, T. A., Kovochich, M., Liong, M., Meng, H., Kabehie, S., George, S., Zink, J. I., and Nel, A. E. (2009) Polyethyleneimine Coating Enhances the Cellular Uptake of Mesoporous Silica Nanoparticles and Allows Safe Delivery of siRNA and DNA Constructs, *Ac Nano* 3, 3273-3286.

153. Deng, Y. B., Winter, G., and Myschik, J. (2012) Preparation and validation of a skin model for the evaluation of intradermal powder injection devices, *Eur. J. Pharm. Biopharm.* 81, 360-368.

154. Mollet, H., and Grubenmann, A. (2001) Manufacture and Properties of Colloidal Suspensions and Dispersions, In *Formulation Technology* (Mollet, H., and Grubenmann, A., Eds.), pp 131-180, WILEY-VCH, Weinheim.

155. Teunissen, M. B. (1992) Dynamic nature and function of epidermal Langerhans cells in vivo and in vitro: a review, with emphasis on human Langerhans cells, *Histochem J* 24, 697-716.

156. Etzl, E. E., Winter, G., and Engert, J. (2013) Toward intradermal vaccination: preparation of powder formulations by collapse freeze-drying, *Pharm Dev Technol.*

157. Larsson, L. (1988) *Immunocytochemistry: Theory and Practice.*, CRC. Boca Raton, 77-83, 224-225.

158. Ho, J., Al-Deen, F. M. N., Al-Abboodi, A., Selomulya, C., Xiang, S. D., Plebanski, M., and Forde, G. M. (2011) N,N '-Carbonyldiimidazole-mediated functionalization of superparamagnetic nanoparticles as vaccine carrier, *Colloid Surface B* 83, 83-90.
159. Khlebtsov, B. N., Khanadeev, V. A., and Khlebtsov, N. G. (2008) Determination of the size, concentration, and refractive index of silica nanoparticles from turbidity spectra, *Langmuir* 24, 8964-8970.
160. Farnsworth, A., Cyr, T. D., Li, C., Wang, J., and Li, X. (2011) Antigenic stability of H1N1 pandemic vaccines correlates with vaccine strain, *Vaccine* 29, 1529-1533.
161. Weijers, M., Barneveld, P. A., Cohen Stuart, M. A., and Visschers, R. W. (2003) Heat-induced denaturation and aggregation of ovalbumin at neutral pH described by irreversible first-order kinetics, *Protein Sci* 12, 2693-2703.
162. Coenen, F., Tolboom, J. T., and Frijlink, H. W. (2006) Stability of influenza sub-unit vaccine. Does a couple of days outside the refrigerator matter?, *Vaccine* 24, 525-531.
163. Amorij, J. P., Huckriede, A., Wilschut, J., Frijlink, H. W., and Hinrichs, W. L. (2008) Development of stable influenza vaccine powder formulations: challenges and possibilities, *Pharm Res* 25, 1256-1273.
164. Bell, K. N., Hogue, C. J., Manning, C., and Kendal, A. P. (2001) Risk factors for improper vaccine storage and handling in private provider offices, *Pediatrics* 107, E100.
165. Feshchenko, E., Rhodes, D. G., Felberbaum, R., McPherson, C., Rininger, J. A., Post, P., and Cox, M. M. (2012) Pandemic influenza vaccine: characterization of A/California/07/2009 (H1N1) recombinant hemagglutinin protein and insights into H1N1 antigen stability, *BMC Biotechnol* 12, 77.
166. Athmaram, T. N., Saraswat, S., Santhosh, S. R., Singh, A. K., Suryanarayana, W. S., Priya, R., Gopalan, N., Parida, M., Rao, P. V., and Vijayaraghavan, R. (2011) Yeast expressed recombinant Hemagglutinin protein of novel H1N1 elicits neutralising antibodies in rabbits and mice, *Virol J* 8, 524.
167. Hirst, G. K. (1942) The Quantitative Determination of Influenza Virus and Antibodies by Means of Red Cell Agglutination, *J Exp Med* 75, 49-64.
168. Kommareddy, S., Bonificio, A., Gallorini, S., Baudner, B., Singh, M., and O'Hagan, D. (2013) Preparation of highly concentrated influenza vaccine for use in novel delivery approaches, *J Pharm Sci* 102, 866-875.

169. Maa, Y. F., Ameri, M., Shu, C., Payne, L. G., and Chen, D. (2004) Influenza vaccine powder formulation development: spray-freeze-drying and stability evaluation, *J Pharm Sci* 93, 1912-1923.

170. Luykx, D. M., Casteleijn, M. G., Jiskoot, W., Westdijk, J., and Jongen, P. M. (2004) Physicochemical studies on the stability of influenza haemagglutinin in vaccine bulk material, *Eur J Pharm Sci* 23, 65-75.

171. Amorij, J. P., Meulenaar, J., Hinrichs, W. L., Stegmann, T., Huckriede, A., Coenen, F., and Frijlink, H. W. (2007) Rational design of an influenza subunit vaccine powder with sugar glass technology: preventing conformational changes of haemagglutinin during freezing and freeze-drying, *Vaccine* 25, 6447-6457.

172. Lu, J. M., Wang, X., Marin-Muller, C., Wang, H., Lin, P. H., Yao, Q., and Chen, C. (2009) Current advances in research and clinical applications of PLGA-based nanotechnology, *Expert Rev Mol Diagn* 9, 325-341.

173. Giteau, A., Venier-Julienne, M. C., Aubert-Pouessel, A., and Benoit, J. P. (2008) How to achieve sustained and complete protein release from PLGA-based microparticles?, *Int. J. Pharm.* 350, 14-26.

174. Panyam, J., Zhou, W. Z., Prabha, S., Sahoo, S. K., and Labhasetwar, V. (2002) Rapid endo-lysosomal escape of poly(DL-lactide-co-glycolide) nanoparticles: implications for drug and gene delivery, *Faseb J* 16.

175. Sah, H., Thoma, L. A., Desu, H. R., Sah, E., and Wood, G. C. (2013) Concepts and practices used to develop functional PLGA-based nanoparticulate systems, *Int J Nanomedicine* 8, 747-765.

176. LUPRON DEPOT®, <http://www.endofacts.com>.

177. Sandostatin® LAR Depot, <http://www.us.sandostatin.com/index.jsp>.

178. Indications and Usage for Zoladex, <http://www.drugs.com/pro/zoladex.html>.

179. VIVITROL®, <http://www.vivitrol.com>.

180. Danhier, F., Ansorena, E., Silva, J. M., Coco, R., Le Breton, A., and Preat, V. (2012) PLGA-based nanoparticles: An overview of biomedical applications, *J. Control. Release* 161, 505-522.

181. Demento, S. L., Cui, W. G., Criscione, J. M., Stern, E., Tulipan, J., Kaech, S. M., and Fahmy, T. M. (2012) Role of sustained antigen release from nanoparticle vaccines in shaping the T cell memory phenotype, *Biomaterials* 33, 4957-4964.

182. Tsukada, Y., Hara, K., Bando, Y., Huang, C. C., Kousaka, Y., Kawashima, Y., Morishita, R., and Tsujimoto, H. (2009) Particle size control of poly(DL-lactide-co-glycolide) nanospheres for sterile applications, *Int. J. Pharm.* 370, 196-201.

183. Cheng, F. Y., Wang, S. P. H., Su, C. H., Tsai, T. L., Wu, P. C., Shieh, D. B., Chen, J. H., Hsieh, P. C. H., and Yeh, C. S. (2008) Stabilizer-free poly(lactide-co-glycolide) nanoparticles for multimodal biomedical probes, *Biomaterials* 29, 2104-2112.

184. Sah, H. K. (1997) A new strategy to determine the actual protein content of poly(lactide-co-glycolide) microspheres, *J. Pharm. Sci.* 86, 1315-1318.

185. Kang, F., and Singh, J. (2001) Effect of additives on the release of a model protein from PLGA microspheres, *Aaps Pharmscitech* 2, 30.

186. Kumar, M. N. V. R., Bakowsky, U., and Lehr, C. M. (2004) Preparation and characterization of cationic PLGA nanospheres as DNA carriers, *Biomaterials* 25, 1771-1777.

187. Wischke, C., Borchert, H. H., Zimmermann, J., Siebenbrodt, I., and Lorenzen, D. R. (2006) Stable cationic microparticles for enhanced model antigen delivery to dendritic cells, *J. Control. Release* 114, 359-368.

188. Zhang, X. Y., Sun, M. Z., Zheng, A. P., Cao, D. Y., Bi, Y. Q., and Sun, J. X. (2012) Preparation and characterization of insulin-loaded bioadhesive PLGA nanoparticles for oral administration, *European Journal of Pharmaceutical Sciences* 45, 632-638.

189. Zeng, P., Xu, Y., Zeng, C. H., Ren, H., and Peng, M. L. (2011) Chitosan-modified poly(D,L-lactide-co-glycolide) nanospheres for plasmid DNA delivery and HBV gene-silencing, *Int. J. Pharm.* 415, 259-266.

190. Guo, C. Q., and Gemeinhart, R. A. (2008) Understanding the adsorption mechanism of chitosan onto poly(lactide-co-glycolide) particles, *Eur. J. Pharm. Biopharm.* 70, 597-604.

191. Yuan, X. D., Shah, B. A., Kotadia, N. K., Li, J. A., Gu, H., and Wu, Z. Q. (2010) The Development and Mechanism Studies of Cationic Chitosan-Modified Biodegradable PLGA Nanoparticles for Efficient siRNA Drug Delivery, *Pharm. Res.* 27, 1285-1295.

192. Shau, M. D., Shih, M. F., Lin, C. C., Chuang, I. C., Hung, W. C., Hennink, W. E., and Cherng, J. Y. (2012) A one-step process in preparation of cationic nanoparticles with poly(lactide-co-glycolide)-containing polyethylenimine gives efficient gene delivery, *European Journal of Pharmaceutical Sciences* 46, 522-529.

193. Besheer, A., Vogel, J., Glanz, D., Kressler, J., Groth, T., and Mader, K. (2009) Characterization of PLGA Nanospheres Stabilized with Amphiphilic Polymers:

Hydrophobically Modified Hydroxyethyl Starch vs Pluronics, *Mol Pharmaceut* 6, 407-415.

194. Yang, M., Lai, S. K., Wang, Y. Y., Zhong, W. X., Happe, C., Zhang, M., Fu, J., and Hanes, J. (2011) Biodegradable Nanoparticles Composed Entirely of Safe Materials that Rapidly Penetrate Human Mucus, *Angew Chem Int Edit* 50, 2597-2600.

195. Prasad, S., Cody, V., Saucier-Sawyer, J. K., Fadel, T. R., Edelson, R. L., Birchall, M. A., and Hanlon, D. J. (2012) Optimization of Stability, Encapsulation, Release, and Cross-Priming of Tumor Antigen-Containing PLGA Nanoparticles, *Pharm. Res.* 29, 2565-2577.

196. Kazzaz, J., Singh, M., Uguzzoli, M., Chesko, J., Soenawan, E., and O'Hagan, D. T. (2006) Encapsulation of the immune potentiators MPL and RC529 in PLG microparticles enhances their potency, *J. Control. Release* 110, 566-573.

197. Met, O., Buus, S., and Claesson, M. H. (2003) Peptide-loaded dendritic cells prime and activate MHC-class I-restricted T cells more efficiently than protein-loaded cross-presenting DC, *Cell Immunol* 222, 126-133.

198. Nagata, T., Toyota, T., Ishigaki, H., Ichihashi, T., Kajino, K., Kashima, Y., Itoh, Y., Mori, M., Oda, H., Yamamura, H., Taneichi, M., Uchida, T., and Ogasawara, K. (2007) Peptides coupled to the surface of a kind of liposome protect infection of influenza viruses, *Vaccine* 25, 4914-4921.

199. Taneichi, M., Ishida, H., Kajino, K., Ogasawara, K., Tanaka, Y., Kasai, M., Mori, M., Nishida, M., Yamamura, H., Mizuguchi, J., and Uchida, T. (2006) Antigen chemically coupled to the surface of liposomes are cross-presented to CD8+ T cells and induce potent antitumor immunity, *J Immunol* 177, 2324-2330.

200. Yoon, C. S., Jung, H. S., Kim, T. K., Kwon, M. J., Kim, M. K., Lee, M., Koh, K. S., Rhee, B. D., and Park, J. H. (2008) Comparison of the efficiency and toxicity of sonoporation with branched polyethylenimine-mediated gene transfection in various cultured cell lines, *J Drug Target* 16, 773-779.

201. Wang, W. (2000) Lyophilization and development of solid protein pharmaceuticals, *Int J Pharm* 203, 1-60.

202. Murakami, H., Kobayashi, M., Takeuchi, H., and Kawashima, Y. (1999) Preparation of poly(DL-lactide-co-glycolide) nanoparticles by modified spontaneous emulsification solvent diffusion method, *Int. J. Pharm.* 187, 143-152.

203. Govender, T., Stolnik, S., Garnett, M. C., Illum, L., and Davis, S. S. (1999) PLGA nanoparticles prepared by nanoprecipitation: drug loading and release studies of a water soluble drug, *J. Control. Release* 57, 171-185.
204. Luz, P. P., Magalhaes, L. G., Pereira, A. C., Cunha, W. R., Rodrigues, V., and Silva, M. L. A. E. (2012) Curcumin-loaded into PLGA nanoparticles, *Parasitol Res* 110, 593-598.
205. Mao, S. R., Xu, J., Cai, C. F., Germershaus, O., Schaper, A., and Kissel, T. (2007) Effect of WOW process parameters on morphology and burst release of FITC-dextran loaded PLGA microspheres, *Int. J. Pharm.* 334, 137-148.
206. Meng, F. T., Ma, G. H., Qiu, W., and Su, Z. G. (2003) W/O/W double emulsion technique using ethyl acetate as organic solvent: effects of its diffusion rate on the characteristics of microparticles, *J Control Release* 91, 407-416.
207. Krise, K. M., Hwang, A. A., Sovic, D. M., and Milosavljevic, B. H. (2011) Macro- and microscale rheological properties of poly(vinyl alcohol) aqueous solutions, *J Phys Chem B* 115, 2759-2764.

List of Presentations and Publications

Articles and Patents

1. **Y. Deng**, G. Winter, J. Myschik. Preparation and validation of a skin model for the evaluation of intradermal powder injection devices. *Eur. J. Pharm. Biopharm.*, **2012**, 81(2): 360-368.
2. **Y. Deng**, G. Winter, J. Myschik. Encapsulation of antigen-loaded silica nanoparticles into microparticles for intradermal powder injection. *In manuscript*.
3. **Y. Deng**, G. Winter, J. Myschik. Microparticles with dense materials and drug/antigen-loaded nanoparticles for intradermal delivery. *Submitted*, 2013.

Poster Presentations

1. **Y. Deng**, G. Winter, J. Myschik. Preparation and investigation of gelatin films as a skin model for the development of epidermal immunisation by powder injection. APV 8th World Meeting on Pharmaceutics, Biopharmaceutics and Pharmaceutical Technology, March 19-22, **2012**, Istanbul, Turkey.
2. **Y. Deng**, G. Winter, J. Myschik. Encapsulation of antigen-loaded silica nanoparticles into microparticles for intradermal powder injection. 2013 AAPS National Biotechnology Conference, May 20-22, **2013**, San Diego, USA.

Curriculum Vitae

Personal Details

Name: Yibin Deng
Date of Birth: 16.08.1982
Place of Birth: Yushan, Jiangxi
Nationality: Chinese
Marital Status: Single

Education

9/2009 – 7/2013 **Ludwig-Maximilians-University Munich**
Department of Pharmacy, Pharmaceutical Technology and Biopharmaceutics
Ph.D. in the group of **Prof. Dr. Gerhard Winter**
Dissertation: Investigation on the Administration of Dry Vaccines via Epidermal Powder Injection

9/2006 – 7/2009 **Fudan University, Shanghai**
Department of Macromolecular Science
M.Sc. in the group of **Prof. Dr. Ping Zhou**,
Dissertation: Interaction of *Bombyx mori* Silk Fibroin with Mn(II)
Studied Using Magnetic Resonance Methods and Biosynthesis of Amyloid- β 42 Peptide

9/2002 – 7/2006 **Sun Yat-Sen University, Guangzhou**
College of Chemistry and Chemical Engineering
B.Sc. in Material Chemistry (major), GPA Rank: 2/60
International Economy and Trade (minor)
Thesis: Synthesis of Anilido-Imino Chromium Complexes and Their Catalytic Behavior toward Ethylene and Norbornene